The Dissertation Committee for Patrick Kevin Meazell II Certifies that this is the approved version of the following Dissertation:

Gas hydrate reservoirs of the deepwater Gulf of Mexico: characterization and consequences

Committee:

Peter B. Flemings, Supervisor

Jacob Covault

David Mohrig

Lori Summa

Gas hydrate reservoirs of the deepwater Gulf of Mexico: Characterization and Consequences

by

Patrick Kevin Meazell II

Dissertation

Presented to the Faculty of the Graduate School of

The University of Texas at Austin

in Partial Fulfillment

of the Requirements

for the Degree of

Doctor of Philosophy

The University of Texas at Austin

December 2021

Abstract

Gas hydrate reservoirs of the deepwater Gulf of Mexico: characterization and consequences

Patrick Kevin Meazell II, Ph.D.

The University of Texas at Austin, 2021

Supervisor: Peter B. Flemings

Gas hydrate is found in cold, high-pressure, marine sediments around the world. Hydrate is important as a carbon sink, a natural geohazard, and a valuable economic resource. I use classic sedimentologic analyses, well log analysis, X-ray CT, seismic stratigraphy, pore pressure estimation, and basin modeling to elucidate the geologic conditions within highly-saturated, natural gas hydrate reservoirs in the deepwater northern Gulf of Mexico.

I begin with the characterization of the channel-levee hydrate reservoir in GC-955 with grain size experiments, lithofacies mapping. Hydrate is found in thin-bedded layers of sandy silt that increase in net-to-gross and mean grainsize downhole. I use these results to interpret deposition of overbank sediment gravity flows from a deepwater bypass channel as it becomes increasingly confined by the levees it builds. Next, I use 3D seismic data to identify the relationship between similar channel-levee systems and venting seafloor gas mounds in the Terrebonne Basin of the Walker Ridge protraction area. I estimate the pore pressures, and show that below the hydrate phase boundary, free gas in

the levees builds to a critical pressure and creates hydraulic fractures to the seafloor. I describe a conceptual model by which the venting process perturbs the hydrate stability zone, leading to further venting from shallower positions and the formation of distinct rows of gas mounds on the seafloor. Finally, I combine geomechanical properties of the GC-955 reservoir with the structure of the Terrebonne Basin system to show that the pressure estimates are well within reason. Together, these studies provide new insights into where hydrate is found, and how hydrate systems can both control and in turn be controlled by fluid flow, pressure, and stress in the deepwater environment.

Table of Contents

Chapter 1: Introduction 1

Future research 4

References 6

Chapter 2: Sedimentology and stratigraphy of a deepwater gas hydrate reservoir in the northern Gulf of Mexico 8

Abstract 8

2.1 Introduction 9

2.2 Geologic setting and previous work 12

2.3 Data and Methods 16

2.4 Results 21

2.4.1 Lithofacies description 21

2.4.2 Silty clay 21

2.4.3 Interbedded sandy silt and clayey silt 28

2.5 Lithofacies Interpretation 33

2.5.1 Silty clay 33

2.5.2 Sandy silt and clayey silt 33

2.6 Discussion 37

2.6.1 Evolution of the Levee 37

2.6.2 Core-Log Comparison 42

2.6.3 Grain Size Comparison 43

2.6.4 Clayey silt vs. silty clay 43

2.6.5 The Bounding Units of the Hydrate Reservoir 44

2.7 Conclusions 46

Acknowledgments 47

References.....47

Chapter 3: The evolution of seafloor venting from hydrate-sealed gas reservoirs 57

Abstract.....57

3.1 Introduction.....58

3.2 Geological Setting and Previous Work.....62

3.2.1 The Terrebonne Basin.....62

3.2.2 Reservoir Characterization 63

3.2.3 Seafloor Vents.....63

3.3 Methods and Data 66

3.3.1 Well logs 66

3.3.2 Seismic data 66

3.3.3 Mapping.....67

3.4 Observations and Interpretations 69

3.4.1 The Green sand 69

3.4.2 The Orange sand 70

3.4.3 The Blue sand 72

3.4.4 Gas mounds.....74

3.4.5 Hydrate stability zone 78

3.4.6 Relationship of sands to gas mounds.....81

3.4.7 Pressure conditions 82

3.5 Discussion.....85

3.5.1 Pressure controls.....85

3.5.2 Evolution of the venting system 86
3.5.3 Implications of a dynamic hydrate seal 89
3.6 Conclusions....90
Acknowledgements....91
Funding 92
References....92
Chapter 4: Rapid sedimentation in the deepwater GOM: implications for subsurface temperature, overpressure, hydrate formation, and venting 97
Abstract....97
4.1 Introduction....97
4.2 Background Geology 99
4.3 Data and Methods 102
4.3.1 Seismic data 102
4.3.2 Sand maps 103
4.3.2 Basin Model....105
4.3.3 Geomechanical properties of the mudrock 105
4.3.4 Model conditions 107
4.4 1D models....110
4.4.1 1D Overpressure 110
4.4.2 1D Temperature 112
4.5 2D Models....112
4.5.1 2D Temperature 112
4.4.5 2D Pressure 118
4.4.5 2D Gas and hydrate model....120

4.6 Discussion 125
4.6.1 Pressure 125
4.6.2 Venting locations 126
4.6.3 Three sands 127
4.7 Conclusions 129
References 129
Appendices 133
Appendix A: Grain size experiment data 133
Appendix B: Supplemental figures from Chapter 3 166
Appendix B1. Well logs for WR313-H 167
Appendix B2. Well logs for WR313-G 168
Appendix B3. Seismic profile of the Blue row of gas mounds 169

Chapter 1: Introduction

Methane hydrate is a naturally occurring, inorganic crystalline solid composed of a methane molecule trapped inside a cage-like structure of water molecules (Sloan and Koh, 2007). Methane hydrate is also referred to methane clathrate, gas hydrate, or simply hydrate. In popular culture, it is even referred to as "Fire Ice" (e.g., Cussler, 2003) due to the fact that it is both frozen solid and combustible; it dissociates into liquid water and burning methane gas in the presence of a flame.

Hydrate is important for a variety of reasons. Hydrate is part of the global carbon cycle, and sequesters 5-22% of the world's organic carbon (Ruppel and Kessler, 2017). Hydrate is a drilling hazard that can destabilize the seafloor (McConnell et al., 2012). Hydrate is an energy-dense mineral that may be exploited in the future (Boswell et al., 2020; Frye et al., 2012).

Hydrate is found in low-temperature, high-pressure environments with methane and water, such as below permafrost in the Arctic (Yoneda et al., 2021), and in deep ocean basins worldwide (e.g., Boswell et al., 2012; Crutchley et al., 2018; Ito et al., 2015; Paganoni et al., 2018; Shukla et al., 2018). Due to high porosity and intrinsic permeability, deepwater hydrate-bearing sands hold particular importance as potentially economically recoverable reservoirs (Boswell et al., 2020). However, these systems are not stable at normal surface conditions, making them difficult to study. As a result, many questions about the petrophysical and geological conditions of such reservoirs remain.

The goal of this dissertation is to better understand the geology of deepwater, coarse-grained hydrate reservoirs. I use a grain- to basin-scale approach, starting with classic sedimentologic experiments on core samples to characterize a deepwater clastic reservoir with high concentrations of hydrate. I then apply the results from the small-scale studies to applications at the reservoir-, and eventually basin-scale.

In Chapter 2, I examine the levee architecture of a Pleistocene deepwater channel system that has been literally frozen in time. I describe the sedimentology and stratigraphy of a coarse-grained, highly-saturated hydrate reservoir in the shallow subsurface outboard of the Sigsbee Escarpment, in the Green Canyon protraction area of the northern Gulf of Mexico. Before this study, shallow, coarse-grained, non-lithified, deepwater channel systems were notoriously difficult to study. Due to changes in pressure and temperature, hydrate within conventional, non-pressure cores dissociates when brought to the surface; this process severely degrades the core and erases sedimentary fabric, which can complicate interpretations of hydrate presence and depositional environment. Through the technology of pressure coring, we are able to observe and analyze hydrate-bearing cores at near in-situ pressure and temperature conditions. I use these analyses to interpret pore fluid and depositional environment within a thinly-bedded turbidite system.

The key results of Chapter 2 include the lithologic characterization of the reservoir, using X-Ray CT scans, geophysical logs, and traditional grain-size analysis. I find that the reservoir is composed of decimeter- to -meter scale layers of sandy silt, interbedded with clayey silt. I show that hydrate is lithology-dependent; it is found predominantly in the coarser-grained sandy silt. I use stratigraphic and sedimentologic relationships to show

that the thinbed reservoir was deposited on the levees of a bypass channel system by overspilling sediment gravity flows.

In Chapter 3, I describe what happens when the frozen (i.e., hydrate-saturated) reservoir melts (i.e., dissociates) and erupts at the surface. I explore the connection of dipping gas and hydrate reservoirs to seafloor vents in the Terrebonne Basin, located in the Walker Ridge protraction area of the northern Gulf of Mexico. This location is ~100 miles from the Chapter 2 study area, and at similar seafloor depths and depositional environment. I use mapping of 3D seismic data to show that three rows of venting seafloor mounds are rooted in the three major hydrate-bearing sands. By tying the seafloor vents to the sandy reservoirs via fluid escape pipes, I am able to estimate the pore pressures within the gas and hydrate sands.

I find that the leak point for the sands is not the crest of the sands, but rather the hydrate seal at the gas-hydrate interface. The stratigraphically shallowest sand is more overpressured than the deeper sands due to the relative position of the leak point to the seafloor. I describe a conceptual model of venting for dipping gas + hydrate systems, whereby pore pressures build at the base of the hydrate stability zone until they reach the least principal stress and vent to the surface via hydraulic fracturing. The venting process melts updip hydrate, which raises the base of the hydrate stability zone, increases the gas column, and creates a new, shallower, and more-easily bypassed hydrate seal. I show how in a 2D perspective, this process can extend to the seafloor and empty the hydrate reservoir.

In Chapter 4, I investigate the causes of the eruption from the hydrate reservoir. First, I extend the mapping of the Terrebonne Basin sands to the north, where they reach depths of greater than 7000 meters. I apply the sedimentological and geomechanical properties of the hydrate reservoir and seal from Chapter 2 to the geology and structure of the dipping sands and mudrock of Chapter 3, and I use basin modeling to investigate the evolution of pressures and stresses within the Terrebonne Basin to understand the contribution of hydrate to the overpressure of gas + hydrate reservoirs.

Key findings of Chapter 4 include the discovery that rapid sedimentation in the northern Terrebonne Basin has resulted in almost 4 Mpa of water-phase overpressure. The addition of gas + hydrate further increase pore pressures to the point of lithostatic stress, and likely failure via hydraulic fracturing. I show how the position of base of the hydrate stability zone controls pore pressure in dipping sands that cross the hydrate phase boundary. The results of Chapter 4 support the pore pressure estimates from Chapter 3.

Ultimately, this dissertation describes hydrate reservoirs at multiple scales, and it shows how they evolve in a dynamic depositional environment. It is my hope that this research will be utilized by scientists seeking to understand the potential of other hydrate systems to serve as both a reservoir as well as a seal for methane and carbon dioxide.

FUTURE RESEARCH

This dissertation has explored gas hydrate reservoirs from several viewpoints, including sedimentology, seismic stratigraphy, and basin modeling. Research into gas hydrates will continue in the future, aided by the growing enthusiasm in regards to the

feasibility of production from hydrates (Konno et al., 2017; Okinaka et al., 2020; Ye et al., 2020) as well as the ability for hydrates to sequester substantial amounts of CO2 (Darnell et al., 2017).

Future drilling and pressure coring is scheduled to take place in the Terrebonne Basin, and will provide invaluable data in regards to the geomechanical properties of the reservoir and surrounding mudrock. These properties can be used to refine the basin model in Chapter 4 in order to better understand the geologic evolution of the gas-hydrate system in the Terrebonne Basin. In addition, pressurized cores will provide a fantastic sedimentologic data set that can be used to further elucidate the depositional environment of the hydrate sands in the Terrebonne Basin, similar to study of the Green Canyon system in Chapter 2.

Additionally, the conceptual model from Chapter 3 could be improved with a numerical model similar to those used to understand the venting process elsewhere (Darnell and Flemings, 2015; Smith et al., 2014). This is complex problem due to the thermodynamic, salinity, and pressure changes that arise when hydrate dissociates and gas moves into the hydrate stability zone. The results of such a study could help to both quantify the amount of gas released, and better understand the time frame required for the venting location to move updip within the gas-hydrate sands.

REFERENCES

Boswell, R., Collett, T. S., Frye, M., Shedd, W., McConnell, D. R., and Shelander, D., 2012, Subsurface gas hydrates in the northern Gulf of Mexico: Marine and Petroleum Geology, v. 34, no. 1, p. 4-30.

Boswell, R., Hancock, S., Yamamoto, K., Collett, T., Pratap, M., and Lee, S.-R., 2020, 6 - Natural Gas Hydrates: Status of Potential as an Energy Resource, *in* Letcher, T. M., ed., Future Energy (Third Edition), Elsevier, p. 111-131.

Crutchley, G. J., Kroeger, K. F., Pecher, I. A., and Gorman, A. R., 2018, How tectonic folding influences gas hydrate formation: New Zealand's Hikurangi subduction margin: Geology, v. 47, no. 1, p. 39-42.

Cussler, C., 2003, Fire Ice, Penguin.

Darnell, K., Flemings, P., and DiCarlo, D., 2017, Subsurface injection of combustion power plant effluent as a solid-phase carbon dioxide storage strategy: Geophysical Research Letters, v. 44, no. 11, p. 5521-5530.

Darnell, K. N., and Flemings, P. B., 2015, Transient seafloor venting on continental slopes from warming-induced methane hydrate dissociation: Geophysical Research Letters, v. 42, no. 24, p. 10,765-710,772.

Frye, M., Shedd, W., and Boswell, R., 2012, Gas hydrate resource potential in the Terrebonne Basin, Northern Gulf of Mexico: Marine and Petroleum Geology, v. 34, no. 1, p. 150-168.

Ito, T., Komatsu, Y., Fujii, T., Suzuki, K., Egawa, K., Nakatsuka, Y., Konno, Y., Yoneda, J., Jin, Y., Kida, M., Nagao, J., and Minagawa, H., 2015, Lithological features of hydrate-bearing sediments and their relationship with gas hydrate saturation in the eastern Nankai Trough, Japan: Marine and Petroleum Geology, v. 66, p. 368-378.

Konno, Y., Fujii, T., Sato, A., Akamine, K., Naiki, M., Masuda, Y., Yamamoto, K., and Nagao, J., 2017, Key findings of the world's first offshore methane hydrate production test off the coast of Japan: Toward future commercial production: Energy & Fuels, v. 31, no. 3, p. 2607-2616.

McConnell, D. R., Zhang, Z., and Boswell, R., 2012, Review of progress in evaluating gas hydrate drilling hazards: Marine and Petroleum Geology, v. 34, no. 1, p. 209-223.

Okinaka, N., Boswell, R., Collett, T., Yamamoto, K., and Anderson, B., 2020, Progress toward the establishment of an extended duration gas hydrate reservoir response test on the Alaska North Slope: extended abstracts, ICHGH 10.

Paganoni, M., Cartwright, J. A., Foschi, M., Shipp, C. R., and Van Rensbergen, P., 2018, Relationship between fluid-escape pipes and hydrate distribution in offshore Sabah (NW Borneo): Marine Geology, v. 395, p. 82-103.

Ruppel, C. D., and Kessler, J. D., 2017, The interaction of climate change and methane hydrates: Reviews of Geophysics, v. 55, no. 1, p. 126-168.

Shukla, K., Collett, T., Kumar, P., Yadav, U., Boswell, R., Frye, M., Riedel, M., Kaur, I., and Vishwanath, K., 2018, National Gas Hydrate Program expedition 02: Identification of gas hydrate prospects in the Krishna-Godavari Basin, offshore India: Marine and Petroleum Geology.

Sloan, E. D., and Koh, C., 2007, Clathrate hydrates of natural gases, CRC press.

Smith, A. J., Flemings, P. B., Liu, X., and Darnell, K., 2014, The evolution of methane vents that pierce the hydrate stability zone in the world's oceans: Journal of Geophysical Research: Solid Earth, v. 119, no. 8, p. 6337-6356.

Ye, J.-l., Qin, X.-w., Xie, W.-w., Lu, H.-l., Ma, B.-j., Qiu, H.-j., Liang, J.-q., Lu, J.-a., Kuang, Z.-g., and Lu, C., 2020, The second natural gas hydrate production test in the South China Sea: China Geology, v. 3, no. 2, p. 197-209.

Yoneda, J., Jin, Y., Muraoka, M., Oshima, M., Suzuki, K., Walker, M., Otsuki, S., Kumagai, K., Collett, T. S., and Boswell, R., 2021, Multiple physical properties of gas hydrate-bearing sediments recovered from Alaska North Slope 2018 Hydrate-01 Stratigraphic Test Well: Marine and Petroleum Geology, v. 123, p. 104748.

Chapter 2: Sedimentology and stratigraphy of a deepwater gas hydrate reservoir in the northern Gulf of Mexico[1]

ABSTRACT

We interpret the sedimentologic evolution of a deepwater channel-levee deposit in Green Canyon block 955 (GC 955) (deepwater Gulf of Mexico) by analyzing hydrate-bearing pressure cores and non-pressure cores collected during Expedition UT-GOM2-1 that preserve remarkable sedimentary structures. The levee is composed of alternating beds of sandy silt and clayey silt that range from millimeters to meters in thickness. We interpret that each couplet of sandy silt and clayey silt records a single turbidity current flow where the upper part of the flow overtops the levee and is deposited along its flank. The sandy silt is coarser, its beds are thicker, and the fraction of sandy silt to clayey silt (net-to-gross) is greater near the base of the levee. We interpret that as the levee grew, the channel depth increased and a smaller fraction of the flow overtopped the levee. An increase in net-to-gross, both at the base and near the top of the cored section may record an increase in the size of turbidity current flows or a decrease in the relative height of the levee. Based on the limited core recovery, we infer that the lithology of the bounding unit immediately above the hydrate-bearing unit is thinner-bedded and has lower net-to-gross than the hydrate reservoir. The bounding unit below the hydrate-bearing interval is

[1] This chapter was published as Meazell, P.K., Flemings, P.B., Santra, M., and Johnson, J. (2020), Sedimentology and stratigraphy of a deep-water gas hydrate reservoir in the northern Gulf of Mexico. *AAPG Bulletin*, vol. 104, no. 9. DOI: 10.1306/05212019027
I performed the grain size analyses, core logging, and log analyses, and prepared the manuscript for publication. Peter Flemings edited the manuscript and provided valuable feedback on the manuscript. Manasij Santra provided valuable feedback in regards to sediment deposition and overall clarity. Joel Johnson conducted petrographic smear slide analyses.

similarly thinner-bedded, yet contains high saturations of hydrate. This study illuminates the lithologic architecture of leveed-channel turbidite reservoirs at a grain- to core-scale and provides insight into how lithology controls hydrate distribution and concentration.

2.1 INTRODUCTION

Deepwater channel-levee systems are conduits for the movement of massive amounts of sediment to the deep ocean (Covault and Graham, 2010). These depositional systems have been studied in outcrop (Beaubouef, 2004; Figueiredo et al., 2010; Gardner et al., 2003; Hansen et al., 2017a; Hodgson et al., 2011; Kane and Hodgson, 2011) and with seismic data (Deptuck et al., 2003; Hansen et al., 2017b) and coupled to cores and geophysical logs (Enunwa et al., 2005; Hackbarth and Shew, 1994). Studies of near-seafloor channel levee systems show these systems evolve from an initial period of incision to levee growth and vertical aggradation (Deptuck et al., 2003; Hodgson et al., 2011; Sawyer et al., 2007).

The sedimentology of near-surface channel-levee systems has been the focus of numerous scientific research cruises. IODP Expedition 308 documented fine-grained, thin bedded turbidites within the Brazos-Trinity slope system (Prather et al., 2012) and the eastern levee of Southwest Pass Canyon of the Gulf of Mexico (Sawyer et al., 2009). DSDP Leg 96 documented muddy, thin bedded, turbidites within the levee of the Pleistocene Mississippi Fan (Pickering et al., 1986). Thick levees of the Einstein channel in Viosca Knoll, northern Gulf of Mexico, were found to be similarly fine-grained, with a net-to-gross and bed thickness that decreases upwards to the top of the levees (Hackbarth

and Shew, 1994). ODP Leg 155 found the levees of the recent Amazon Channel to be composed of alternating mud and silt laminae (Hiscott et al., 1997; Piper and Deptuck, 1997).

The levee deposits are a substantial volumetric element of channel-levee systems. They are formed by the overspilling of turbidity currents (Beaubouef, 2004; Hansen et al., 2015; Morris et al., 2014; Piper and Normark, 2001; Sawyer et al., 2007; Walker, 1978). While often finer-grained and with less porosity and permeability than channel fill (Cronin et al., 2000), the lithology of deepwater levees is commonly coarse enough to contain substantial porosity and permeability (Browne and Slatt, 1997). As such, levees are important reservoirs of productive conventional petroleum systems (Kendrick, 2000). Within the Gulf of Mexico, petroleum has been produced from fine-grained interbedded sand and mud levees at the Ram-Powell (Clemenceau, 1995; Clemenceau et al., 2000), Magnolia (Jobe, 2010; Jobe et al., 2012; Kane et al., 2012; McCarthy et al., 2005; Weissenburger and Borbas, 2004), and Tahoe (Enunwa et al., 2005; Kendrick, 2000) fields.

Deepwater channel levee systems are also reservoirs for methane hydrate, an ice-like crystalline solid that consists of methane locked inside a cage structure of water molecules (Sloan, 2003). Methane hydrate is found at low temperatures and high pressures in the presence of methane gas and water. Deposits of methane hydrate are ubiquitous in the slope environment of most continental margins (Kvenvolden, 1988); however, the most favorable occurrence type for potential energy extraction are those that occur as high saturation pore-fill within sand and silt-rich sediments (Boswell et al., 2014). Therefore, the study of potentially productive marine hydrate reservoirs has focused on near-surface

channel-levee systems and the associated turbidite sands of the deepwater. Recent studies of turbidite-hosted marine hydrate have occurred in the Krishna-Godavari Basin (Boswell et al., 2018; Oshima et al., 2019; Shukla et al., 2018), the Ulleung Basin (Ryu et al., 2013), the Nankai Trough (Fujii et al., 2008; Ito et al., 2015; Noguchi et al., 2011), and the Gulf of Mexico (Boswell et al., 2012b; Collett et al., 2014; Frye et al., 2012).

The UT-GOM2-1 Hydrate Pressure Coring Expedition was funded by the Department of Energy Award DE-FE0023919, and advised by the United States Geological Survey (USGS) and the Bureau of Ocean Energy Management (BOEM). As part of this program, two holes were drilled into the levee of a methane hydrate-bearing Pleistocene submarine channel in Green Canyon Block 955 (GC 955) in the deepwater Gulf of Mexico (Flemings et al., 2017). Pressure cores of the hydrate-bearing interval were recovered (Thomas et al., 2020) and we observed that the presence of hydrate strengthened the non-lithified sediment making it possible to image and study gas hydrate-bearing core that is commonly difficult to retrieve. We use physical measurements, grain size data, and x-ray mineralogic analysis of pressure cores and conventional, non-pressurized cores to elucidate the depositional process responsible for the creation of the hydrate reservoir. This paper documents the sedimentology and lithostratigraphy of the hydrate-bearing interval of the channel-levee system at GC 955. The results of this study can be compared with seismic interpretation (Portnov et al., 2020; Santra et al., 2020), depressurization experiments (Phillips et al., 2020), and pressure coring analyses (Flemings et al., 2020; Thomas et al., 2020).

2.2 GEOLOGIC SETTING AND PREVIOUS WORK

Green Canyon block 955 is immediately basinward of the Sigsbee escarpment, at the mouth of the Green Canyon reentrant (Figure 1). The seafloor is at a depth of 1975 -2250 m and gently dips to the southeast. The area is heavily affected by salt tectonics and diapirism (Portnov et al., 2018), which has created abundant faulting and a salt-cored anticline (Figure 2). The supra-salt section contains a major N-S trending channel-levee system (Santra et al., in press), which has been interpreted as a Pleistocene-aged sediment fairway related to the Mississippi Fan system by Weimer (1990).

The GC 955 channel-levee system was first described by McConnell (2000) in an analysis of shallow hazards in this region that used seismic reflection data. In 1999, drilling of the first industry well in GC 955 confirmed the presence of sand within the shallow subsurface (McConnell et al., 2010). Later evaluation led to the identification of gas chimneys and shallow gas deposits associated with the channel system (Heggland, 2004; Meldahl et al., 2001). Further geophysical analysis led to the identification of a strong positive reflector above the shallow gas (Figure 2, inset), which was interpreted to record the upper boundary of potential hydrate-bearing sediments (McConnell et al., 2010). Several locations associated with the channel levee system within GC 955 were identified as prospective hydrate targets (Hutchinson et al., 2009; Hutchinson et al., 2008; Ruppel et al., 2008), of which, three holes (I001, H001, and Q001) were drilled in 2009 as part of the Joint Industry Project II (Boswell et al., 2012a; Boswell et al., 2012b; Collett and Boswell, 2012). Logging while drilling (LWD) data confirmed the presence of hydrate within

coarse-grained reservoirs among all three holes (Guerin et al., 2010). No core was obtained during this drilling program.

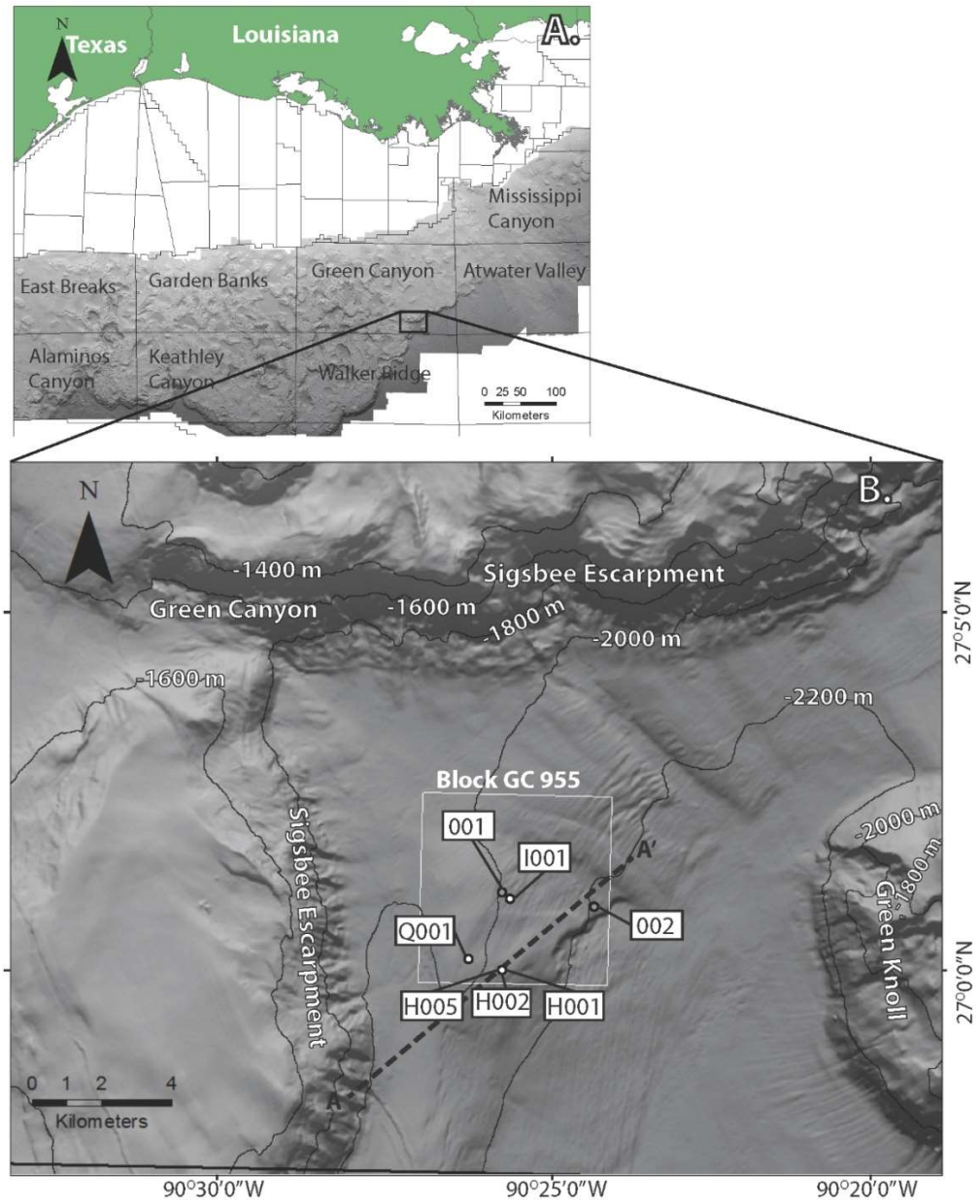

Figure 1. A. The study area (black box) is within Block 955 of the Green Canyon protraction area at the base of the Sigsbee escarpment. B. Bathymetric map of the study area, showing the location of industry wells (001 and 002), JIP II holes (H001, I001, and Q001), and the two UT-GOM2-1 holes (H002, H005). The black dashed line is the location of seismic section A-A' (Figure 2). Contour lines are in meters below sea level.

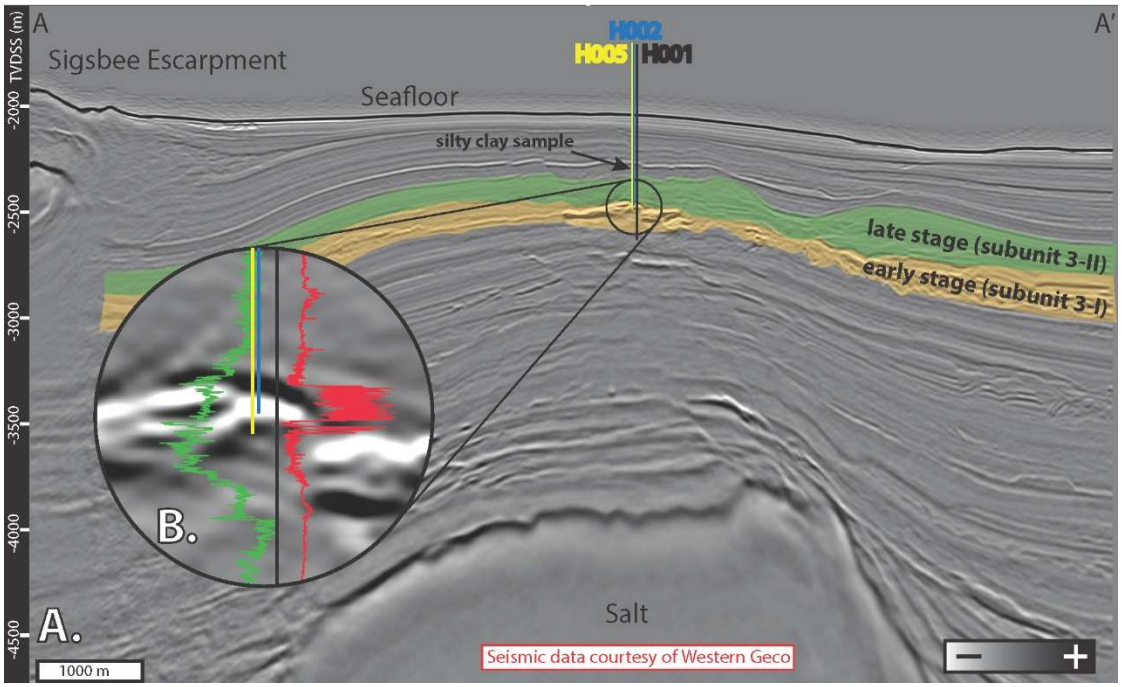

Figure 2. A. Seismic section A-A' across the study area (located in Fig. 1). The original JIP II H001 hole (black) as well as the UT-GOM2-1 H002 (blue) and H005 (yellow) holes targeted the high amplitude reflectors of the shallow subsurface directly above a salt anticline. These holes encountered hydrate within the early stage channel (subunit 3-I) and finer grained, water-bearing sediments within the late stage channel (subunit 3-II). B. Zoomed in detail of well penetrations. The strong positive (black) over negative (white) was interpreted as hydrate-bearing sediments. Gamma ray (green) and resistivity (red) are from the 2009 JIP II H001 hole. The high resistivity and low gamma are interpreted to record the presence of hydrocarbons within a coarse-grained reservoir.

The H001 hole intersected a zone of high resistivity and low gamma ray (Figure 3), which was interpreted as a hydrate-bearing channel levee deposit of fine to very fine sand beds 0.15-1.2 m thick interbedded with clay beds 0.15-0.6 m thick (Boswell et al., 2012b). Low gamma ray and low resistivity readings may record the presence of water-bearing sands directly above and below the hydrate reservoir; however, these readings might also record borehole washout, which is recorded by high caliper readings (Figure 3 B). A

similar lithologic succession was encountered at the nearby Q001 hole (Figure 1), but possible gas flow prevented completing the hole to depth (Boswell et al., 2012b).

Santra et al. (2020), used recently reprocessed 3D seismic data to interpret that the channel system is composed of two units: an early stage, bypass system with coarse-grained levees and no channel fill (subunit 3-I), and a later stage with fine grained levees and coarse fill (subunit 3-II) (Figure 2). The levee reservoir of subunit 3-I is compartmentalized by gravitational failure surfaces (Santra et al., 2020). The overlying subunit 3-II (Figure 2) is composed of largely mud.

Through well log and geophysical analysis, the early stage (subunit 3-I) of the channel-levee system at GC 955 has been interpreted as a hydrate reservoir with potential water-bearing zones immediately above and below (Boswell et al., 2012b). Due to the limited resolution of seismic and LWD data, the fine-scale lithologic composition and architecture of the hydrate-bearing interval and the nature of the bounding units above and below the main hydrate reservoir were unknown.

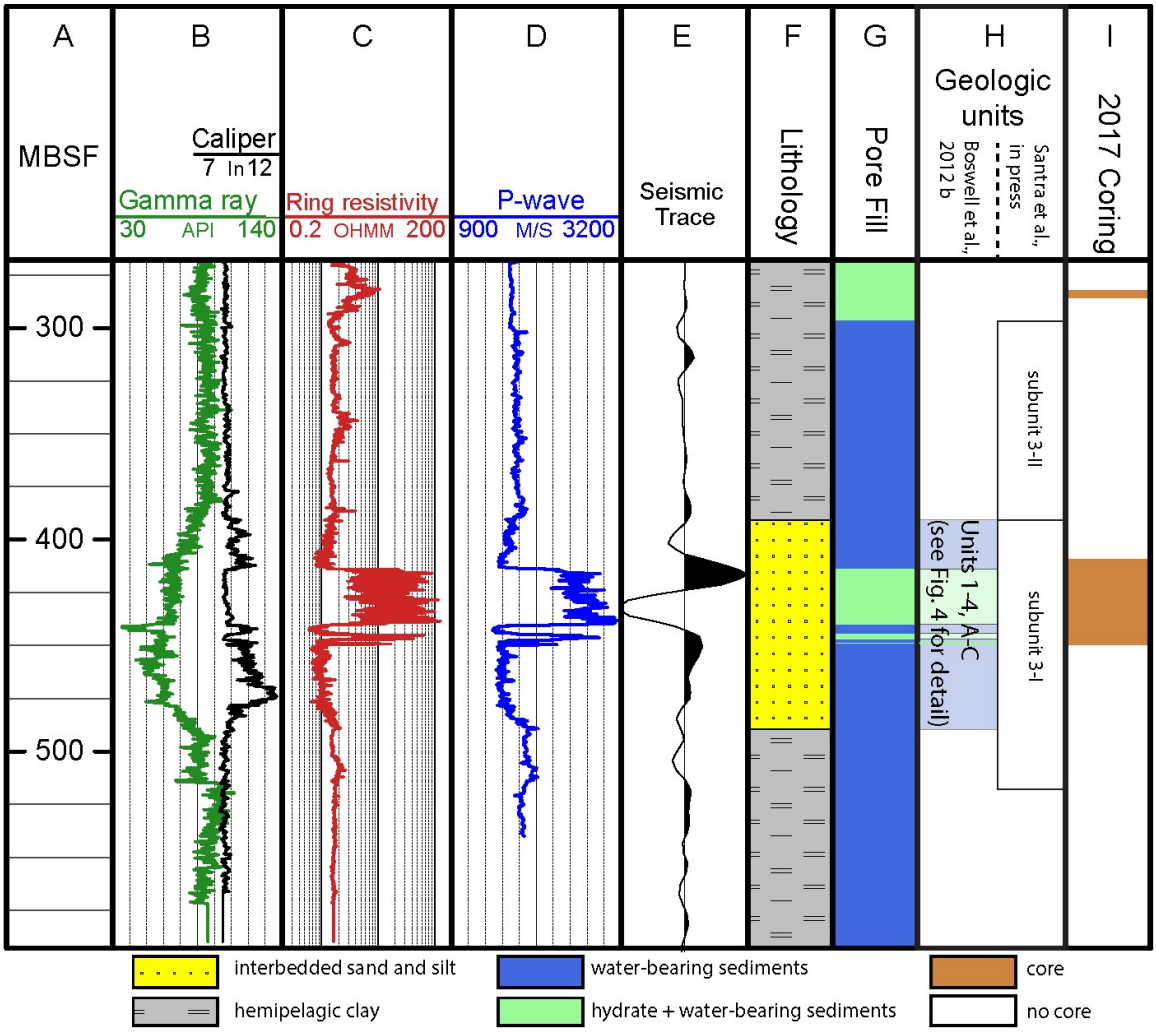

Figure 3. LWD logs from the 2009 JIP GC 955 H001 hole (Guerin et al., 2010) that was twinned and pressure-cored during the 2017 UT-GOM2-1 expedition. The presence of hydrate within a clastic reservoir was inferred from the high resistivity, high sonic velocity, low gamma ray interval from 414-450 mbsf. A. Depth in meters below seafloor. B.-D. LWD logs from the 2009 JIP expedition. E. Seismic trace from the H001 location. F. Lithology interpreted from LWD logs. G. Pore fill. H. Nomenclature of geologic units from Boswell et al. (2012b) on the left and Santra et al., (2020) on the right. For greater detail of Unit 1 – Unit 4, see Figure 4. I. Intervals cored during the 2017 UT-GOM2-1 expedition. For greater detail of core recovery, see Figure 4.

2.3 Data and Methods

We use the naming convention from Boswell et al. (2012b) to identify the geologic units of the hydrate reservoir. The high resistivity, high p-wave intervals (units A, B, and

C in Figure 4) are interpreted as high saturations of hydrate in interbedded sand and mud. The low resistivity, low p-wave intervals (units 1, 2, 3, and 4 in Figure 4) are interpreted as water-bearing units that bound the hydrate reservoir.

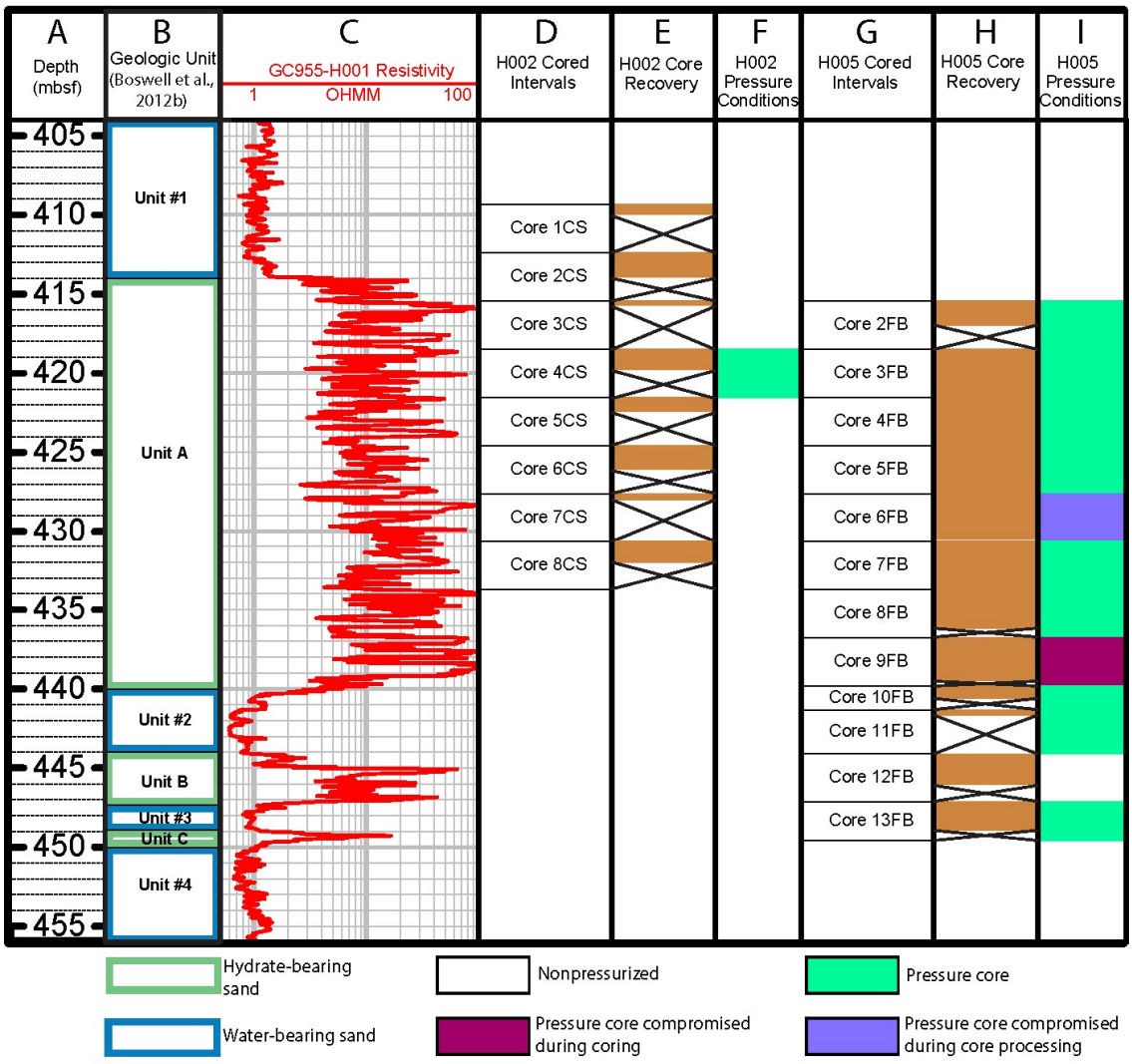

Figure 4. Core recovery during The University of Texas-Gulf of Mexico 2-1 (UT-GOM2-1) Hydrate Pressure Coring Expedition from holes H002 and H005. (A) Depth in meters below seafloor (mbsf). (B) Geologic units from Boswell et al. (2012b). (C) Ring resistivity from GC 955-H001. (D) H002 cored intervals. (E) Core recovery of H002. (F) Pressure conditions from core recovered from H002. (G) H005 cored intervals. (H) Core recovery of H005. (I) Pressure conditions from core recovered from H005. The H002 hole had low recovery, with only one core maintaining pressure (Thomas et al., 2020), whereas H005 had better recovery through the high-resistivity zone of unit A (cores 2FB-10FB), with low recovery in the upper and lower bounding units (core 1CS-1 in unit 1 and core 11FB in unit 2, respectively) (Thomas et al., 2020).

At GC 955, two holes were drilled within 15 meters (49.2 feet) of the hole GC955-H001 (Figure 2) in order to obtain pressure cores from the main hydrate reservoir of unit A (414-440 mbsf in Figure 4) as well as the contacts at the base and above the reservoir. Core recovery was low for the first hole and but was high in the second hole (H002 and H005, respectively in Figure 4). Core recovery was highest within unit A (414-440 mbsf in Figure 4), and lower within the bounding units (unit 1 and unit 2 in B of Figure 4). More information on the drilling and pressure coring operations may be found in the initial report (Flemings et al., 2018), Thomas et al. (2020), and Flemings et al. 2020).

Upon recovery, non-destructive physical measurements of the pressure cores were made with the Pressure Core Analysis and Transfer System (PCATS) (Schultheiss et al., 2011). Analyses included P-wave velocity measurement (every 0.5 cm), gamma density measurements, and 2D/3D X-ray imaging. The p-wave velocity was calculated from the pulse travel time measured by two 500 kHz acoustic transducers with a precision of +/- 1.5 m s^{-1} and accuracy of +/- 5 m s^{-1} (Schultheiss et al., 2011). Gamma attenuation was measured every 0.5 cm using gamma photons from a Cs-137 source, and then calibrated to density (Schultheiss et al., 2011). Linear 2D X-ray images were collected at a resolution of 112 µm/pixel. 3D X-ray CT data were collected at the same voxel resolution of 112 µm per side. Each core was scanned every 0.8°, totaling 400 images per core. This CT data was then used to construct 5 cm thick slab images that were used for the identification and measurement of sedimentary structures. Beds were measured at 0.5 cm resolution. All X-ray images are positive, therefore the higher attenuation, denser material appears darker than the lower attenuation, less dense material in images.

Following PCATS analyses, sections of the pressure core at least 10 cm in length were depressurized (Phillips et al., 2020). After depressurization, subsamples were collected for grain size experiments. Particle size distribution was analyzed using the hydrometer method following Germaine and Germaine (2009). 35-70 grams of homogenized sediment was thoroughly mixed with water and 5 g of a dispersing agent. At the end of the experiment, the sediment was poured through a 63 um sieve to separate the sand fraction from the fines. Grain size was classified based on a modified version of the Udden-Wentworth grain size scale (Wentworth, 1922), with cut-offs for clay at < 2 um, and sand at > 63 um. The grain size by hydrometer method was compared to the laser diffraction particle size analysis used to report on the grain size of cored sediments (Flemings et al., 2020). The Shepard nomenclature (Shepard, 1954) was used to classify and name each sample based on relative sand, silt, and clay content. Sorting was determined using the inclusive graphic standard deviation methodology of Folk (1980). Sediments from non-pressure cores were examined visually and in smear slide under a petrographic microscope per ODP and IODP protocols (e.g. Tréhu et al. (2003)). Small samples were collected by toothpick for microscopic description of the lithology. Smear slides were prepared on glass slides, dried on a hotplate, and cured under a UV light. Percent estimates of the major lithologic and biogenic components were estimated and reported in the GOM-2-1 Initial report (Flemings et al., 2018).

Mineralogical analysis of the whole rock and the clay fraction (less than 2 micron sized) was conducted by X-ray powder diffraction at the James Hutton Limited Analytical Laboratories. Quantitative analysis of mineral content was performed by a normalized full

pattern reference intensity ratio method. Uncertainty is dependent on the relative concentration and is reported as $\pm x^{\wedge 0.35}$, where x is the concentration in weight percent. Compositionally, sediment samples were classified based on the relative percent of the clay fraction and mineralogy of the silt to sand fraction as described by Pettijohn et al. (2012).

2.4 RESULTS

2.4.1 Lithofacies description

We defined lithofacies based on physical properties and named them based on the dominant grain size. This classification separates muds that are far above the hydrate reservoir (silty clay sample) from interbedded sandy silts (sandy silt) and silty muds (clayey silt) within the hydrate reservoir interval.

2.4.2 Silty clay

One pressure core was collected from 130 meters above the reservoir at 282 mbsf at the H005 location, (Figure 2). It has a p-wave velocity of ~1700 m/s, a density of 2.0 g/cm2 and a relatively high X-ray attenuation. In X-ray, this core appears mostly homogenous, with no sedimentary structures or signs of bioturbation (Figure 5 A). Thin, near-vertical fractures of low-attenuation material are found throughout the core (Figure 5 A). This core is interpreted to be composed of entirely the same lithologic unit. The one sample analyzed for particle size distribution has 57% clay-sized particles, 43% silt-sized particles, and negligible sand with a D 0.50 grain size of 1.4 μm and sorting coefficient of 3.0 (Figure 6, Table 1). This lithofacies is defined as a poorly-sorted silty clay (Figure 7).

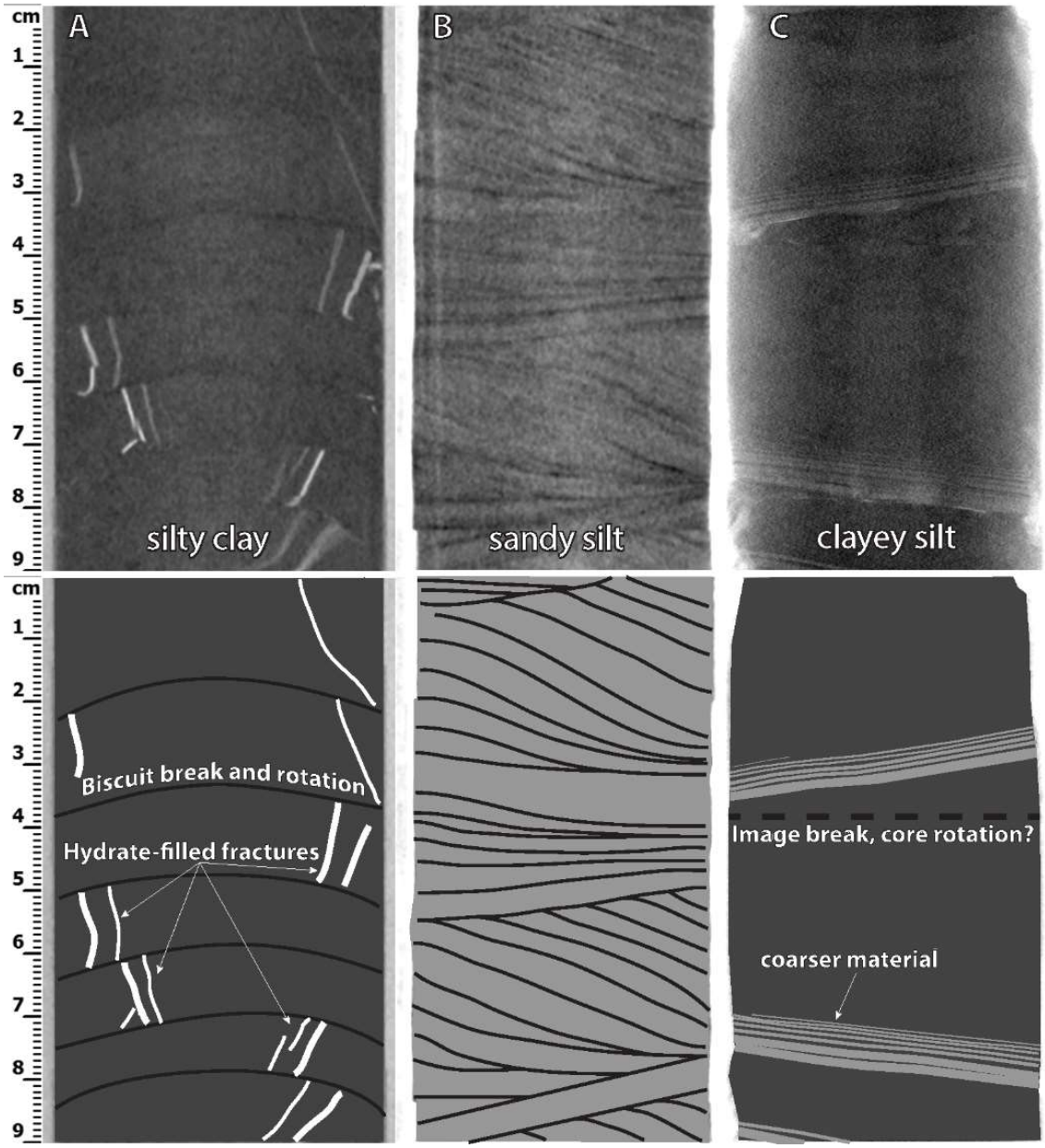

Figure 5. Xray-CT of the 3 lithofacies (upper) and interpreted features (lower). A. The structureless silty clay from 130 m above the hydrate reservoir (core H005-01FB, 26-35 cm). B. The sandy silt (core H005-02FB, 65-74 cm) has abundant ripple lamination, with individual sets up to 3 cm thick. C. The clayey silt has zones of dark, structureless sediment as well as regular, sub-mm planar lamination of lighter material (core H005-04FB, 96-105 cm).

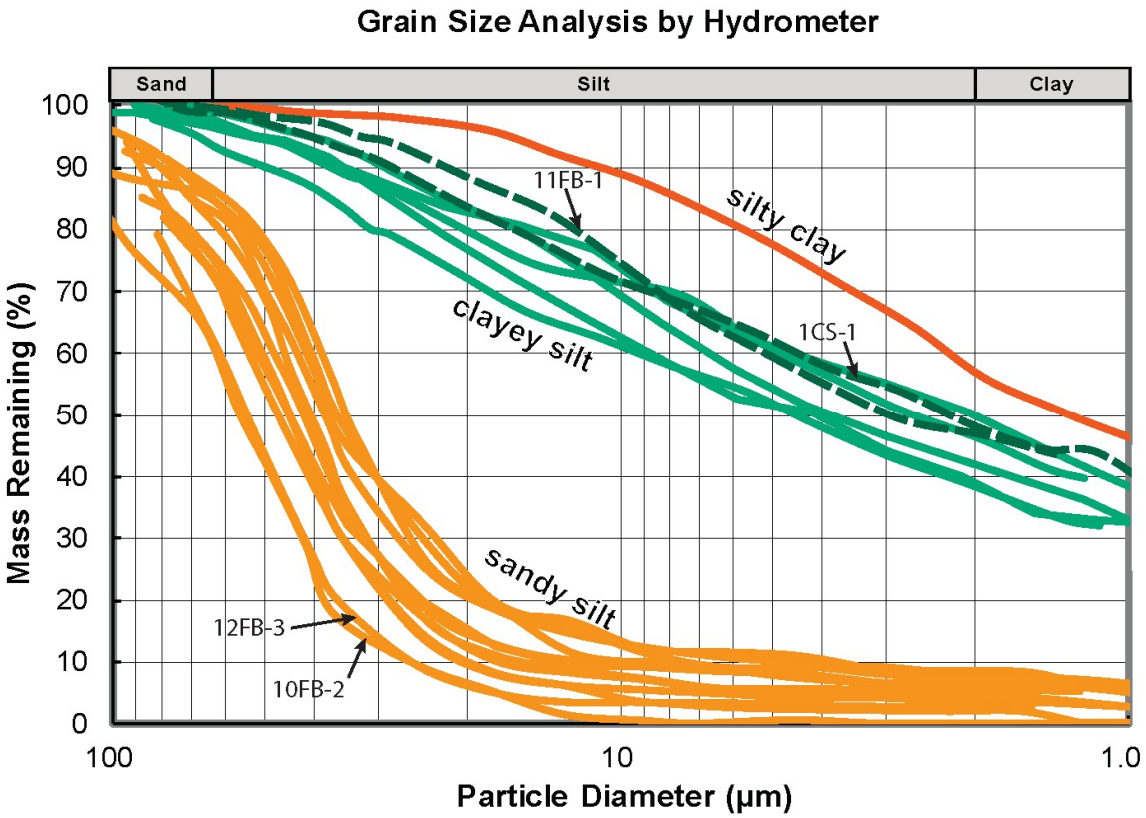

Figure 6. Particle size distribution for the 3 lithofacies based on hydrometer analysis. Grain size was classified based on a modified version of the Udden-Wentworth grain size scale (Wentworth, 1922), with cut-offs for clay at < 2 um, and sand at > 63 um. The steep angle of sandy silt from 90-20 um indicates better sorting than the silty clay and clayey silt. The coarsest-grained samples (10FB-2 and 12FB-3) are from near the base of the drilled interval. The darker, dashed lines represent sediment samples from the bounding layers above (1CS-1) and below (11FB-1) unit A (Figure 4).

The bulk mineralogy of the silty clay is dominated by illite-smectite, quartz, and plagioclase, with accessory minerals including calcite, potassium feldspar, and dolomite (Table 2). Trace amounts of amphibole, siderite, pyrite, halite, and kaolinite are also present. The clay fraction (less than 2 microns) is composed of 72% interlayered illite & smectite, 14% illite, 10% chlorite, and 4% kaolinite (Table 3).

Hole	Core-Section	Depth in section (top) (cm)	Depth in section (bottom) (cm)	Length (cm)	Top depth (mbsf)	Bottom depth (mbsf)	Depth uncertainty (m)	Lithofacies	D 0.50	% Sand	% Silt	% Clay	Sorting (φ)
H005	1FB-3	163	184	21	284.18	284.39	-	SC	1.4	0	43.1	56.9	2.95
H005	3FB-2	117.3	132.7	15.4	419.66	419.82	-	CS	4.6	6.5	55.1	38.4	3.98
H005	3FB-3	132.7	159.2	26.5	419.82	420.08	-	SS	45	28	66.2	5.8	1.58
H005	4FB-2	12.7	38.5	25.8	421.67	421.92	-	SS	45	29	68.2	2.8	0.90
H005	4FB-3	38.5	53.3	14.8	421.92	422.07	-	CS	2.8	3	50.3	46.7	3.56
H005	4FB-4	53.3	65	11.7	422.07	422.19	-	SS	40	18	77.3	4.7	1.13
H005	7FB-1	0	18.6	18.6	430.68	430.87	-	SS	46	25	71.5	3.5	1.16
H005	7FB-4	178.2	194.8	16.6	432.46	432.63	-	SS & CS	30	16	59.2	24.8	4.00
H005	9FB-2	18	138	120	436.96	438.16	-	SS	45	24	72.2	3.8	1.01
H005	10FB-2	0	32	32	439.83	440.15	+ 1.05	SS	55	38	60	2	0.78
H005	11FB-1	0	27	27	441.35	441.62	+/- 1.52	CS	2.9	0.5	52.3	47.2	3.84
H002	1CS-1	-	-	-	409.35	412.39	+/- 1.52	CS	2.3	0.4	51.5	48.1	3.17
H002	3CS-1	-	-	-	415.44	418.49	-	SS	38	17	74.5	8.5	1.65
H002	6CS-5	-	-	-	424.59	427.63	+/- 1.52	SS	48	30	67.3	2.7	0.97
H002	8CS-4	3	6	3	430.71	430.74	-	CS	3.9	1	56.4	42.6	2.40
H002	8CS-4	13	15	2	430.81	430.83	-	CS	2	1	49.3	49.7	3.11
H002	8CS-4	18	21	3	430.86	430.89	-	SS	37	16.2	77.7	6.1	1.42
H002	8CS-4	39	41	2	431.07	431.09	-	SS	37	18.3	73.7	8	1.79
H005	12FB-1	1	6	5	444.41	444.46	-	CS	3	0.9	60.4	38.7	3.07
H005	12FB-3	106	113	7	445.46	445.53	-	SS	56	40.8	59.2	0	0.88

Silty Clay (SC) Average	1.4	0.0	43.1	56.9	3.0
Sandy Silt (SS) Average	44.7	25.8	69.8	4.4	1.2
Clayey Silt (CS) Average	3.1	1.9	53.6	44.5	3.3

Table 1. Results of particle size analysis by hydrometer method.

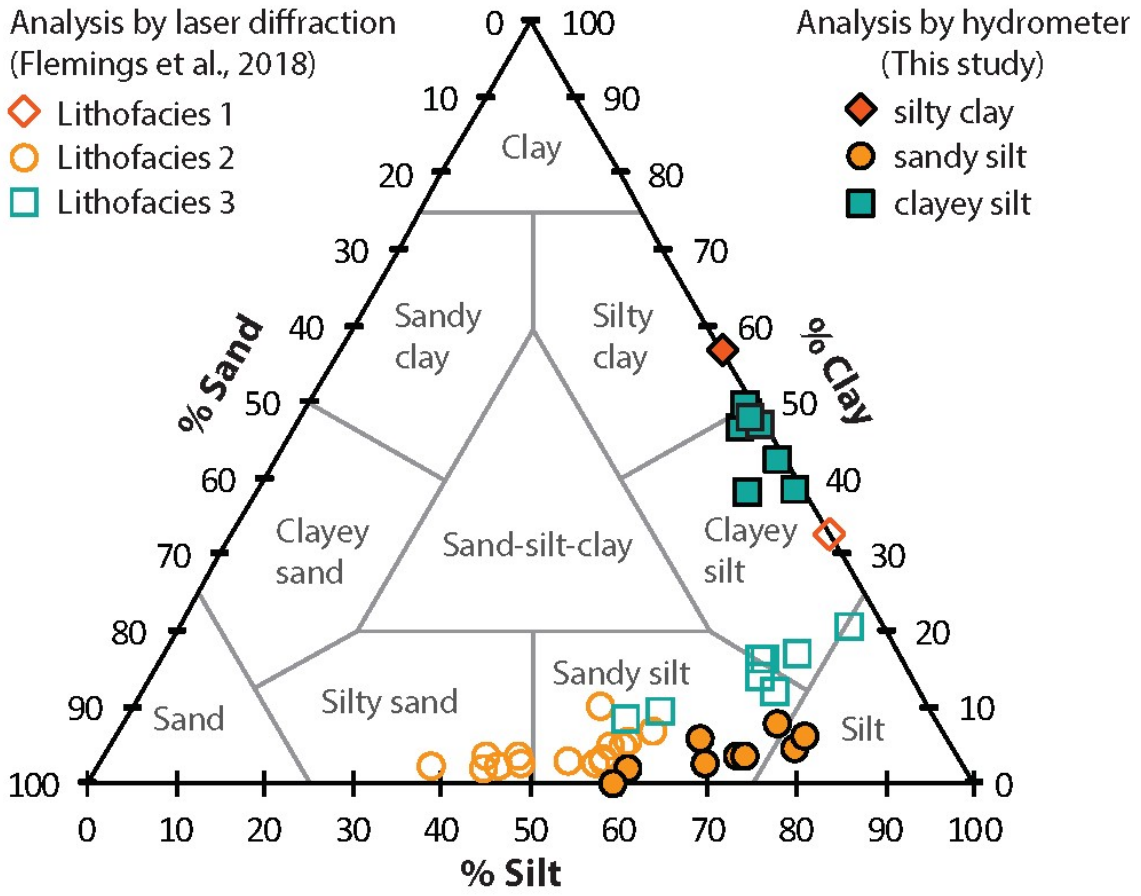

Figure 7. Sedimentological classification of the lithofacies based on the Shepard scale (Shepard, 1954). Grain size was classified based on a modified version of the Udden-Wentworth grain size scale (Wentworth, 1922), with cut-offs for clay at < 2 um, and sand at > 63 um. Analysis by hydrometer (closed symbols) shows that all samples from the main hydrate reservoir are composed of sandy silt and clayey silt, and one sample of from the upper mud is silty clay. Analysis by laser diffraction (open symbols) (Flemings et al., 2018) produced substantially coarser results than those analyzed by the hydrometer method (closed symbols).

Core section	Lithofacies	Quartz	Plagioclase	K-feldspar	Amphibole	Calcite	Dolomite	Siderite	Pyrite	Anatase	Halite	Illite + Smectite	Chlorite	Kaolinite
1FB-3	SC	20	15.9	8.4	1.8	11.7	8.4	0.8	0.4	0	0.7	26.9	2.9	2.1
3FB-3	SS	47.6	20.9	8.4	1.3	5.9	9.7	0.2	0	0	0.1	5.9	0	0
4FB-2	SS	46.7	22.3	8	1	6.1	9.7	0.2	0	0	0	6	0	0
3FB-2	CS	34.4	18.7	7.4	1.3	8.4	10.7	0.5	0.3	0	2	15.2	0.8	0.3
4FB-3	CS	25.6	15	6.5	1.4	9.7	9.3	0.9	0.2	0.1	0.9	25.8	1.2	3.4
Silty Clay (SC) avg		20	15.9	8.4	1.8	11.7	8.4	0.8	0.4	0	0.7	26.9	2.9	2.1
Sandy Silt (SS) avg		47.15	21.6	8.2	1.15	6	9.7	0.2	0	0	0.05	5.95	0	0
Clayey Silt (CS) avg		30	16.85	6.95	1.35	9.05	10	0.7	0.25	0.05	1.45	20.5	1	1.85

Table 2. Bulk rock mineralogy (weight %) of lithofacies-specific samples as determined by quantitative powdered XRD. All samples are from hole H005. See Table 1 for the exact location of each core section.

Core section	Lithofacies	Chlorite	Kaolinite	Illite	Mixed layer Illite + Smectite	% Expandability
1FB-3	SC	10	4	14	72	75
3FB-3	SS	3	2	10	85	75
4FB-2	SS	3	2	9	86	75
3FB-2	CS	5	3	15	77	75
4FB-3	CS	6	4	13	77	75
Silty Clay (SC)		10	4	14	72	75
Sandy Silt (SS) avg		3	2	9.5	85.5	75
Clayey Silt (CS) avg		5.5	3.5	14	77	75

Table 3. Results of XRD analysis of the less than 2 micron fraction of lithofacies-specific samples, reported in weight percent. The high % expandability is interpreted as a high smectite-illite ratio. All samples are from hole H005. See Table 1 for the exact location of each core section.

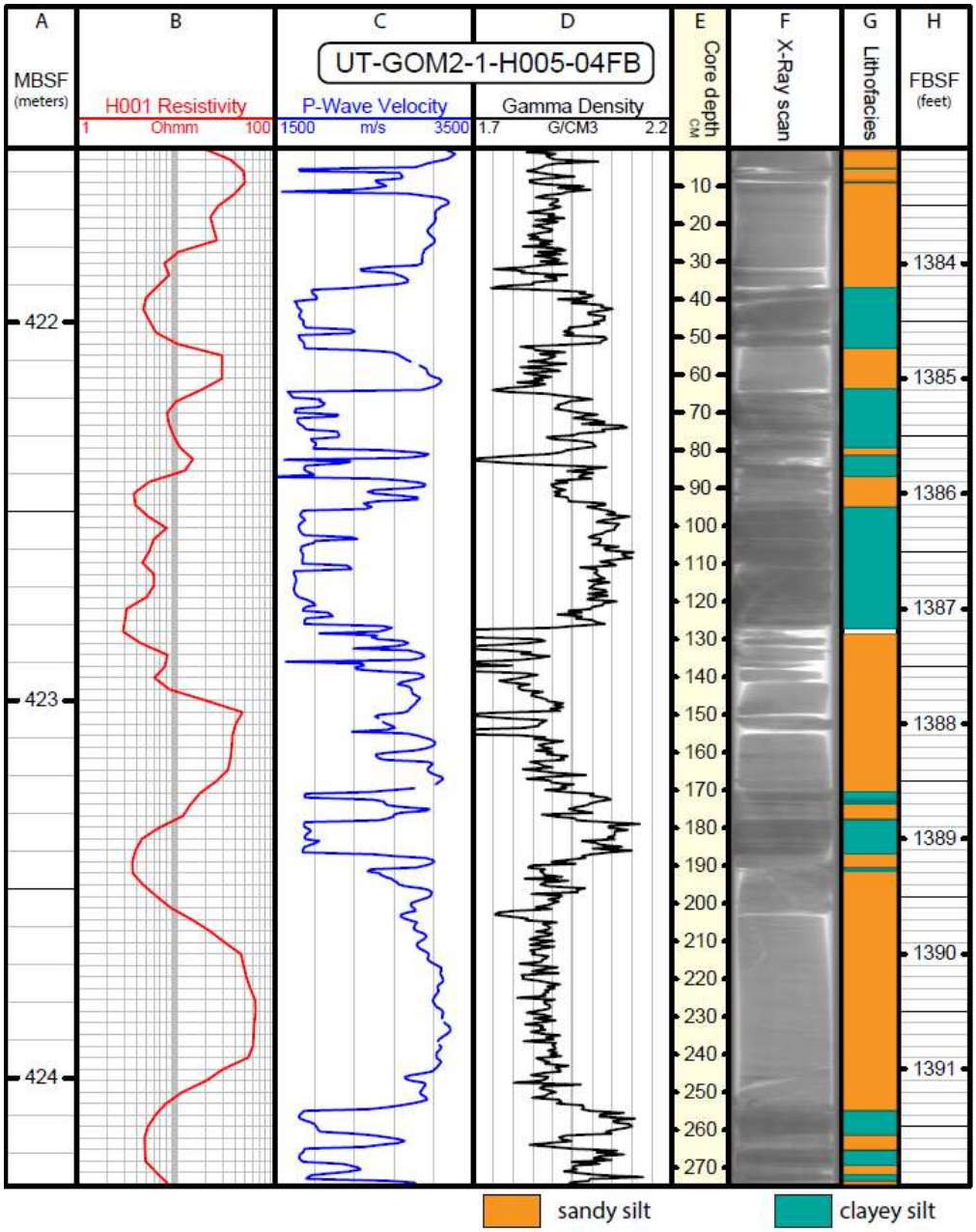

Figure 8. Comparison of resistivity from the 2009 JIP II expedition (Guerin et al., 2010) to PCATS analysis of the top 275 cm of pressure core H005 4FB (total length 315 cm). A. Depth in meters below seafloor. B. Ring resistivity from the LWD log at the H001 hole (Guerin et al., 2010). C. P-wave velocity from pressure core analysis of H005 4FB. D. Gamma density from pressure core analysis of H005 4FB. E. Core depth of H005 4FB. F. Pressure core X-Ray scan of core H005 4FB. G. Distribution of lithofacies within core 4FB. The sandy silt has a lower density, higher p-wave velocity, and lower X-ray attenuation (lighter-colored). The clayey silt has a higher density, lower p-wave velocity, and a higher X-ray attenuation (darker colored). H. Depth in ft below seafloor.

2.4.3 Interbedded sandy silt and clayey silt

X-ray scans of pressure cores from the hydrate reservoir reveal two interbedded lithologies: a lighter-colored, less-attenuated lithofacies, and a darker-colored, more-attenuated lithofacies (Figure 8). The median grain size (D 0.50) for the lighter-colored, less-attenuated lithofacies is 35-55 μm (Figure 6). While two of the samples lie in the silt regime, most of the samples are sandy silts (Figure 7); therefore, we have termed this lithofacies as "sandy silt". The sandy silt lithofacies has a p-wave velocity of 2500-3500 m/s, a density of 1.85-1.95 g/cm^2, and low X-ray attenuation (Figure 8). Ripple cross lamination sets with relief up to 3 cm are abundant (Figure 9 A. 264-267 cm; Figure 5 B). In the failed pressure cores, the sandy silt is darker in shallower cores (1CS-1 and 2CS-2 in Figure 10) and lighter in deeper cores (8CS-4 in Figure 10); the deeper cores contain more sand than the shallower cores. Bubbles are sometimes found in sandy silt in the failed pressure cores (e.g. 35-45 cm in 2CS-2 in Figure 10). The sandy silt is well-sorted with almost 90% of the mass fraction lying between 20 and 100 microns (Figure 6).

The sandy silt lithofacies is composed of primarily quartz and plagioclase, with accessory minerals including potassium feldspar, dolomite, illite-smectite, and calcite (Table 2). Trace amounts of amphibole, siderite, and halite are also present. In smear slides, most grains are angular and composed of quartz, detrital carbonate, and feldspar (Figure 11 A). The clay fraction (less than 2 microns) from X-ray diffraction is composed of mostly smectite with minor amounts of illite, chlorite, and kaolinite (Table 3). The sandy silt lithofacies is classified as a lithic arkose.

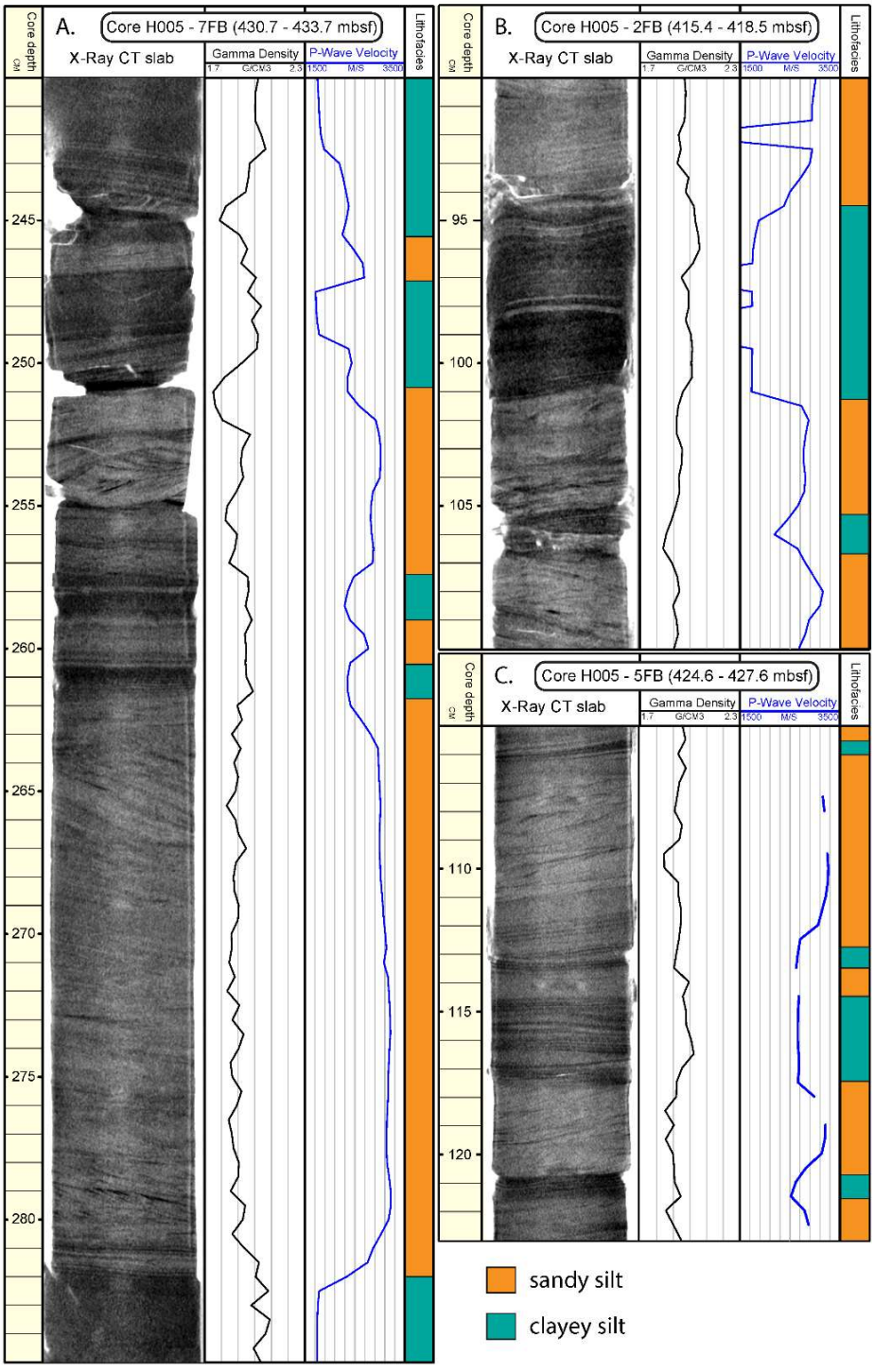

Figure 9. The sandy silt and clayey silt are interbedded at the sub-cm scale. The upward transition from sandy silt to clayey silt is often gradational, while the upward contact from the clayey silt to the sandy silt is sharp.

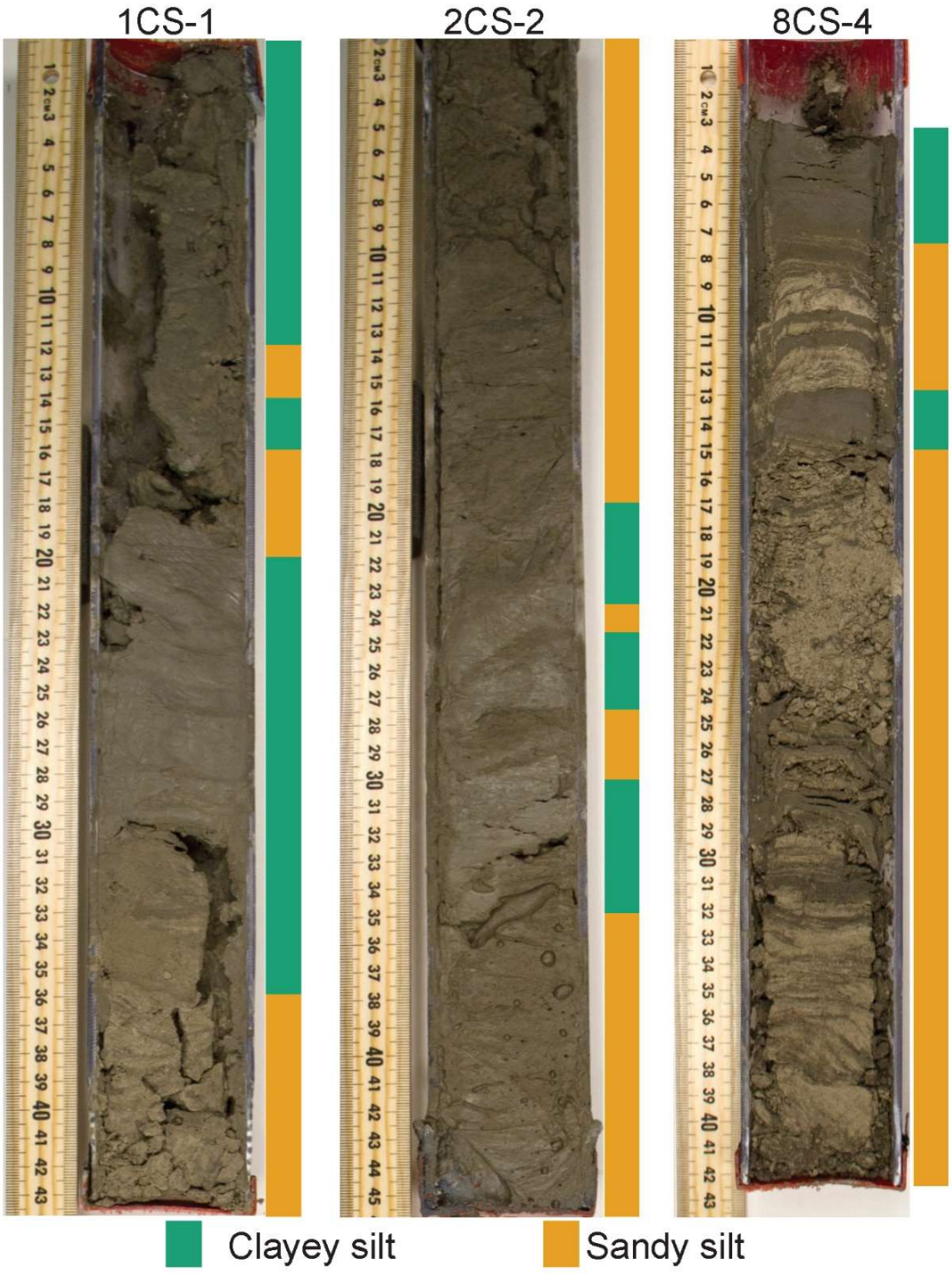

Figure 10. Photographs of split, non-pressure cores from H002. 1CS-1 is from unit 1, immediately above the hydrate reservoir (Figure 4). 2CS-2 spans the boundary of unit 1 and unit A. 8CS-4 is from unit A.

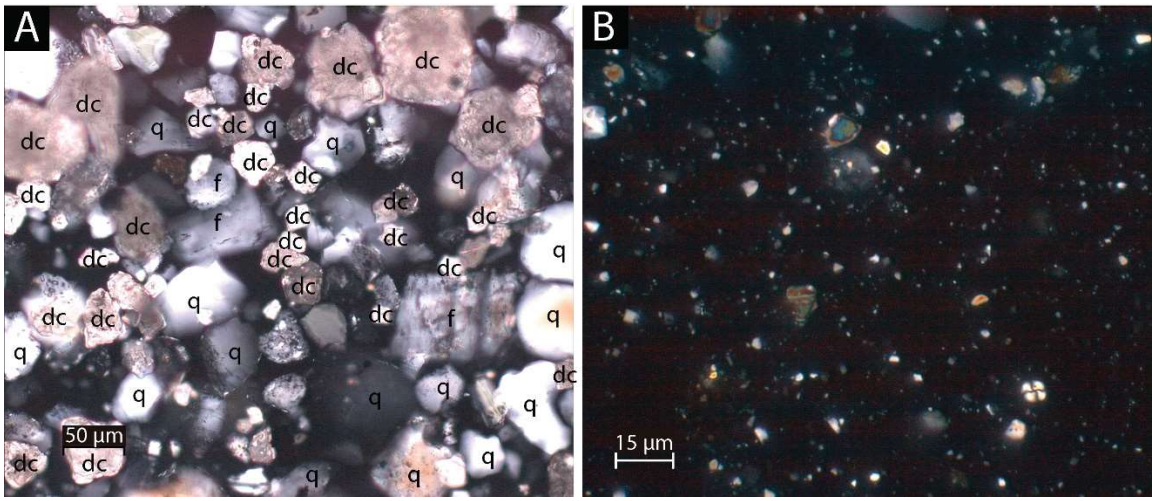

Figure 11. Photomicrographs of representative lithologic units from H002, core 2CS. A. The sandy silt is composed of angular quartz (q), detrital carbonate (dc), and feldspar (f). B. The clayey silt contains a composition similar to the sandy silt, but at much smaller grain sizes, and with minor amounts of biogenic grains.

The darker colored, higher-attenuated interbedded lithofacies (Figure 8) is a classified as a clayey silt (Figure 7) with less than 10% sand-sized particles and 40-50% clay-sized particles (Figure 6, Table 1). It has a lower p-wave velocity (1600-2400 m/s), higher density (2.0-2.1 g/cm^2), and higher X-ray attenuation than the sandy silt (Figure 8). The median grain size (D 0.50) for the clayey silt lithofacies is 2.0-4.6 µm. This lithofacies is more poorly-sorted than the silty clay or sandy silt lithofacies, with an average sorting coefficient of 3.3 (Table 1).

The clayey silt is dominated by quartz, plagioclase, and interlayered illite-smectite (Table 2). Accessory minerals include calcite, potassium feldspar, and dolomite are also present. Trace amounts of chlorite, amphibole, siderite, pyrite, halite, and kaolinite are also present. In smear slides, the mineralogy of this lithofacies is similar to that of the sandy silt lithofacies, with rare biogenic grains present (Figure 10 B). X-ray diffraction

results show that the clay fraction is composed of mostly smectite with interlayered illite, and less than 10% chlorite and kaolinite (Table 3). The clayey silt lithofacies is classified as a lithic wacke.

The clayey silt generally appears structureless in non-pressure cores (Figure 10). However, in X-ray CT scans, laminae are observed in some locations, composed of alternating light (low density) and dark (high density) layers (Figure 5 C). The layered interval is commonly less than 1 cm thick, with laminae a few millimeters thick that often thin upward (Figure 5 C). The low attenuation (low density) layers may be composed of coarser material with higher hydrate saturation that are analogous to sediments of the sandy silt lithofacies. Three samples of the clayey silt that did not have the laminae were analyzed for particle size (see 8CS-4 3-6 cm, 11FB-1, and 12FB-1 in Table 1). All samples of the clayey silt lithofacies contain less clay than the silty clay (Figure 6).

The upward transition from the sandy silt lithofacies to the clayey silt lithofacies is sometimes gradual (Figure 9 A. 261-265 cm), and other times sharp (Figure 9 B. 101 cm). In contrast, the upward transition from the clayey silt lithofacies to the sandy silt lithofacies is most often sharp (Figure 9 A. 282 cm; B. 94 cm, 105 cm; C. 121 cm). Thin planar laminae of lower density (light) layers interbedded with higher density (darker) material, and corresponding intermediate p-wave velocities are sometimes found where the contact is gradual (Figure 9 A. 261-263 cm, 278-282 cm; C. 112-116 cm).

2.5 LITHOFACIES INTERPRETATION

2.5.1 Silty clay

The silty clay lithofacies is interpreted to be a mud formed by hemipelagic sedimentation or very distal turbidity currents. The lack of sedimentary structures and the small grain size indicate that the silty clay was deposited in a very low energy system. It is homogenous, and has a clay mass fraction of ~60% dominated by interlayered smectite and illite. Its composition is similar to other shallow muds encountered on the Gulf of Mexico slope (e.g., Sawyer et al., 2009, site 1322), which are interpreted to record distal deposition relative to a submarine channel. Thin, vertical fractures of low attenuation material found throughout the x-ray images (Figure 5 A) are interpreted to be hydrate-filled fractures (Flemings et al., 2018).

2.5.2 Sandy silt and clayey silt

We interpret that the sandy silt and clayey silt were sourced by an overspilling turbidity current that flowed down the channel axis and deposited sediment on the levees. The turbidity current was stratified, with a higher concentration of coarser material near the base and only finer material near the top. The head of the turbidity current was large enough to suspend clay, silt, and fine sand well above the height of the levee (Figure 12). The thickness of the spillover flow was much less than the thickness of the flow within the channel, resulting in a sudden decrease in the height and energy of the turbidity current away from the channel. Initial overspilling flow energy was high enough to transport fine silt and sand as bedload, forming ripples and cross bedding in the sandy silt (Figure 5 B). Stacked patterns of ripple lamination that we observe in our cores reach up to ~90 cm,

indicating rapid sediment fallout from sustained flows (see, Jobe et al., 2012). Thin clay drapes may show that the flows, while persistent, had repeated periods of localized low energy. Thin planar laminae within the sandy silt may record increased flow (upper plane bed) or decreased flow (lower plane bed) suggesting waxing and waning of individual flows. Such deposits are commonly found in the submarine channel levee environment (Hansen et al., 2017a; Jobe et al., 2012; Kane and Hodgson, 2011).

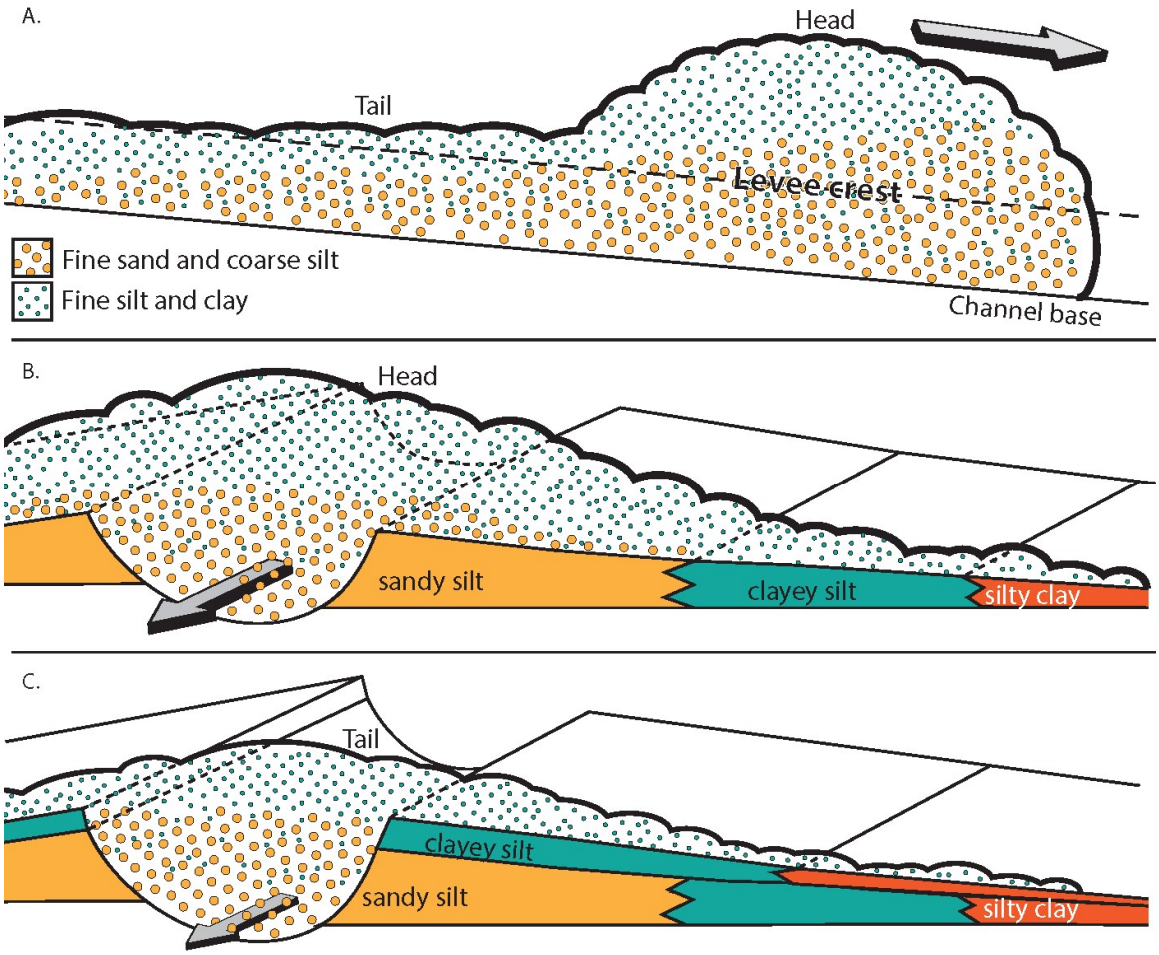

Figure 12. Depositional model for turbidite channel levee at GC-955. A. Longitudinal view of stratified turbidity current. B. The sandy silt is deposited on the levees proximal to the channel as the head of the bypassing turbidity current spills over the levees. The finer-grained clayey silt and silty clay are deposited more distally. C. After the head passes, the tail of the turbidity current deposits clayey silt proximally and silty clay distally.

In pressure cores, the sandy silt is always found with high sonic velocities (VP) and low densities (Figure 9), which are interpreted as pore-filing hydrate with a high saturation. The presence of bubbles in non-pressure cores supports the interpretation of pore-filing hydrate within the sandy silt. Phillips et al. (2020) describe how hydrate saturations in the sandy silt range from 79-93%. The presence of gas hydrate in the pore spaces increases

the bulk modulus and holds the unlithified sediment together, thereby increasing the measured compressional p-wave velocity (Chand et al., 2004; Winters et al., 2007). The high density and moderately low VP readings of the clayey silt (Figure 9) are interpreted to record mud with a low to negligible amount of hydrate, which was confirmed by subsequent depressurization experiments (Phillips et al., 2020).

The clay mineral composition in the sandy silt and the clayey silt (Table 3) are virtually indistinguishable. Additionally, a gradual transition is often present between the sandy silt and the clayey silt (e.g. Figure 9. A. 255-282 cm; C. 105-120 cm). Therefore, we interpret that the two lithologic units are related, and originated from the deposition of sediment gravity flows at differing energy conditions. One possible mechanism is that the succession of the sandy silt to clayey silt describes a single turbidity current in the main channel (Figure 12). The sandy silt is deposited near the levee crest when the head of the turbidity current, which had higher energy and more suspended coarser sediments higher in the section, spills over the levee. After the head passes, the lower energy tail of the flow supplied the finer grained sediments present in the clayey silt. The steady decrease in energy of a single turbidity current results in a deposit of rippled sandy silt that grades into laminations of fine silt and clay and ultimately clayey silt (Figure 13). The thin interbedded silts present in the clayey silt may represent shear sorting of silt and mud as flow from a waning turbidity current (Stow and Bowen, 1978; Stow and Bowen, 1980). Alternatively, the finer-grained beds (clayey silt) may have been deposited by smaller or lower-energy turbidity currents compared to those responsible for the deposition of the coarser-grained beds (sandy silt).

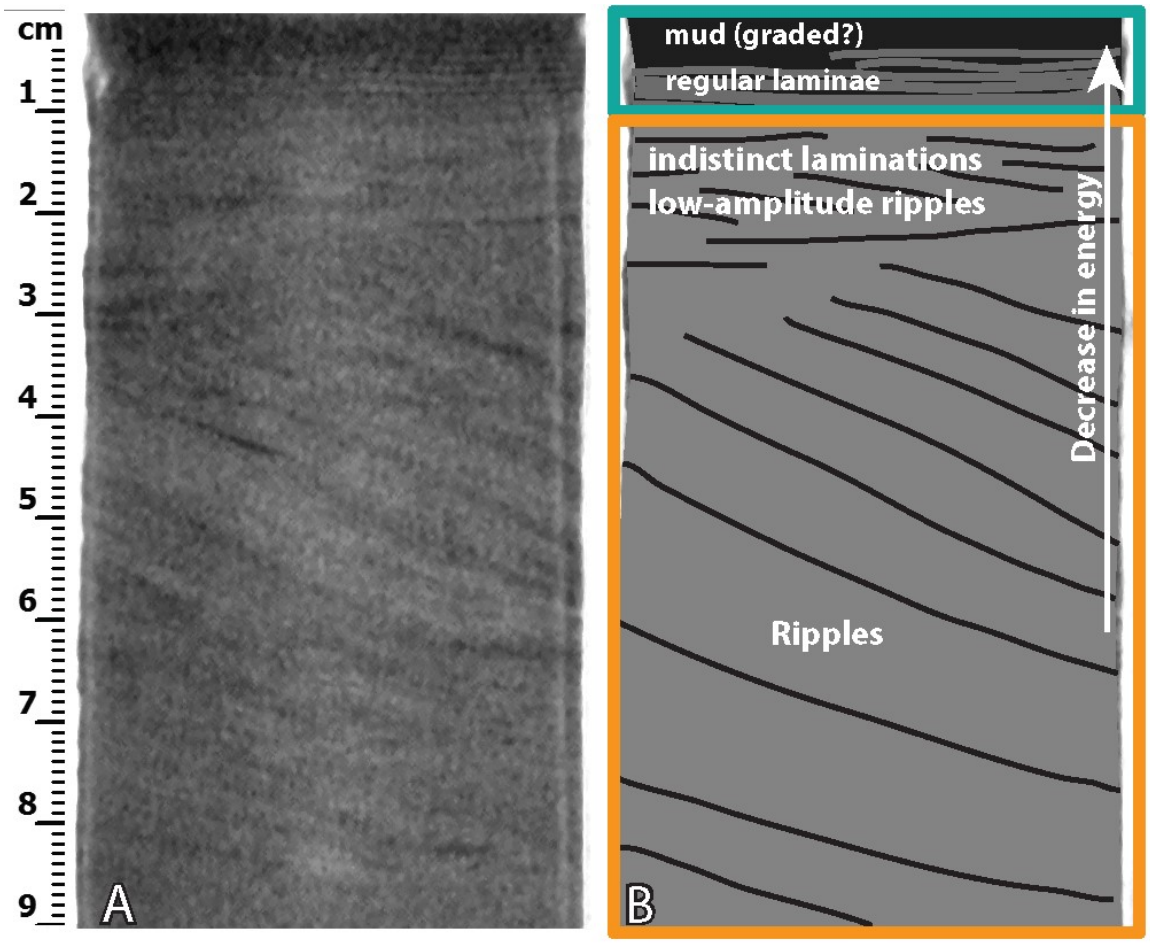

Figure 13. A complete stratigraphic succession resulting from a single, waning turbidity current, as described by Figure 11. A. X-ray-CT scan of H005-7FB. B. Interpretation of sedimentary structures of sandy silt (yellow box) that grades into clayey silt (green box).

2.6 Discussion

2.6.1 Evolution of the Levee

Based on the recovered intact core, there are 163 beds of sandy silt that comprise 72% (17.04 meters) of the total thickness. In turn, there are 148 beds of clayey silt that comprise 28% (6.51 meters) of the total section. We define the net-to-gross value as the

ratio of the thickness of sandy silt to the sum of the thicknesses of the sandy silt and clayey silt. Thus, the total net-to-gross is 72%.

Within any particular pressure core, the net-to-gross varies (Figure 9). At the base of the deepest cored section, the net-to-gross is 73-75% within the section spanning unit B, unit #3, and unit C (445-450 mbsf in Figure 14). Net to gross is highest (97%) and both average and maximum thickness of sandy silt is greatest at the base of unit A (Figure 14 F, G, and H). Within unit A, net-to-gross declines upward to 59% (FB 4, 422-425 mbsf in Figure 14). The average bed thickness also decreases upward in this interval, from 19.0 cm at the base of unit A to 5.7 cm in core FB 5. The maximum thickness of the sandy silt follows a similar pattern, decreasing from 95.6 cm at the base of unit A to 26 cm in core FB 5 (Figure 14 H). Above 422 m, the net-to-gross and the sandy silt bed thickness sharply increase once again, reaching values of 82% net-to-gross and 12.0 cm average thickness at the top of unit A before decreasing to 48% net-to-gross and 6.3 cm average thickness in unit #1 (Figure 14 F-H). The net-to-gross follows similar patterns to those seen in the 2009 LWD data (Guerin et al., 2010), and interestingly, the highest peaks in resistivity correspond to the highest net-to-gross (416 mbsf, 428.5 mbsf, and 439 mbsf in Figure 14 D and F). P-wave and resistivity values are high at the base of unit A, and decrease upwards to approximately 425 mbsf. Above this, the resistivity values increase once again to 416 mbsf, and then decrease to the top of unit A. Over the same interval, gamma ray values increase from 52 API at the base of unit A to 58 API at 422 mbsf, and then decrease to 45 API at 416 mbsf. Overall, these trends show an overall decrease of hydrate-bearing coarse-grained sediments over unit A.

The upward decrease in net-to-gross, average sandy silt bed thickness, and maximum bed thickness of the sandy silt is interpreted to record the progressive building of the levee by turbidity currents (Figure 15). Turbidity currents are stratified, with sediment concentration and coarse sediment fraction decreasing upwards (Hansen et al., 2015; Peakall et al., 2000; Straub et al., 2011). Initially, the levees are small and the channel relief (R), as measured from the base of the channel to the top of the levee is low (Figure 15 A). As each sequential turbidity current overspills the levee, sediment is deposited and the levee grows, increasing R. As the levee grows in height and R is increased, subsequent turbidity currents are increasingly confined and spill progressively less coarse sediment over the levees (Figure 15 B). This results in the gradual fining-upwards pattern and upward decrease of sand deposited on the levee, similar to the patterns of Figure 14 described above. This succession is characteristic of other such channel levee systems (Beaubouef, 2004; Piper and Normark, 2001; Straub and Mohrig, 2008; Walker, 1978).

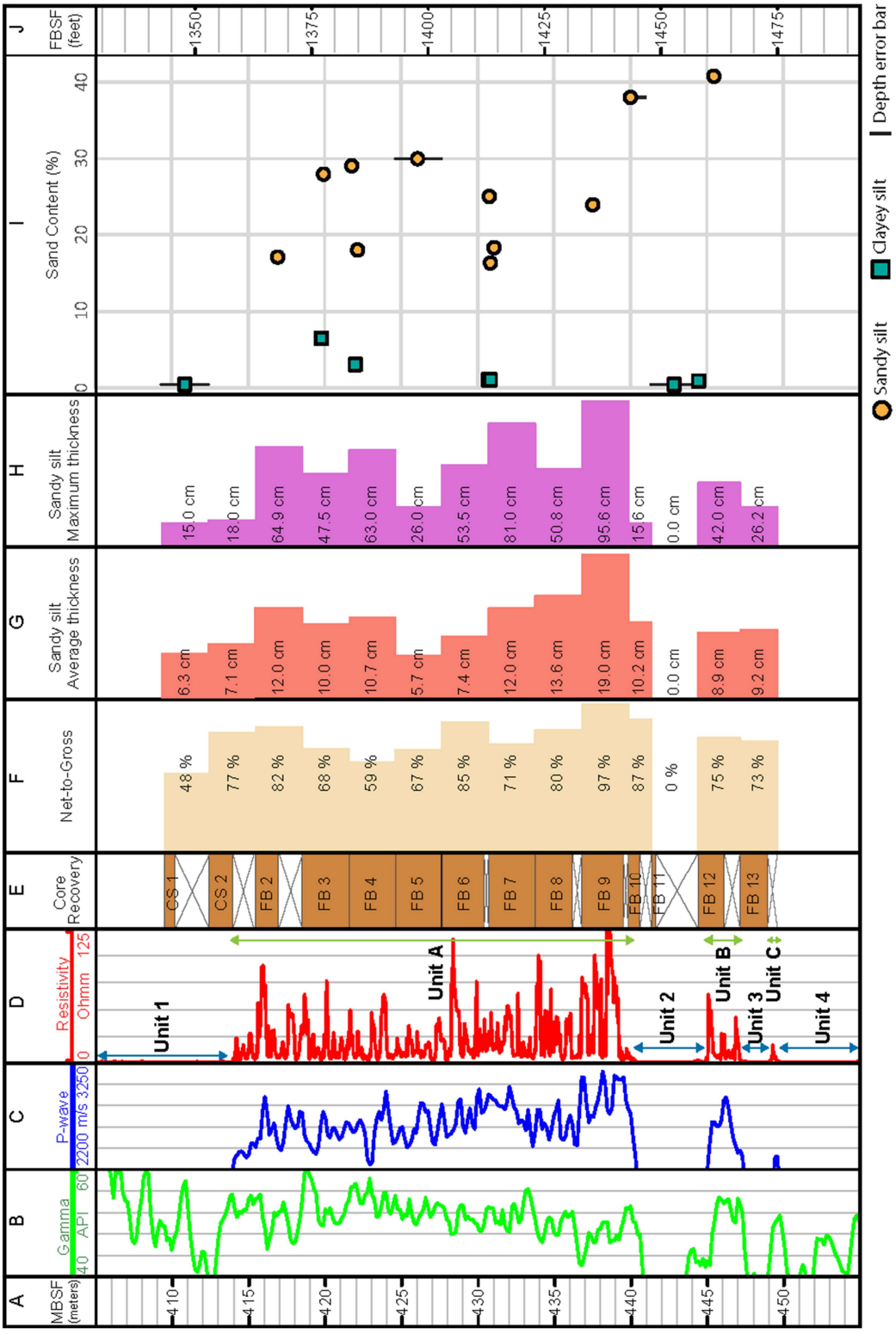
A
MBSF (meters)
B
Gamma
40 API 60
C
P-wave
2200 m/s 3250
D
Resistivity
0 Ohmm 125
E
Core Recovery
F
Net-to-Gross
G
Sandy silt Average thickness
H
Sandy silt Maximum thickness
I
Sand Content (%)
0 10 20 30 40
J
FBSF (feet)
1350 1375 1400 1425 1450 1475
410 415 420 425 430 435 440 445 450
Unit 1
Unit A
Unit 2
Unit B
Unit 3
Unit C
Unit 4
CS 1 CS 2 FB 2 FB 3 FB 4 FB 5 FB 6 FB 7 FB 8 FB 9 FB 10 FB 11 FB 12 FB 13
48 % 77 % 82 % 68 % 59 % 67 % 85 % 71 % 80 % 97 % 87 % 0 % 75 % 73 %
6.3 cm 7.1 cm 12.0 cm 10.0 cm 10.7 cm 5.7 cm 7.4 cm 12.0 cm 13.6 cm 19.0 cm 10.2 cm 0.0 cm 8.9 cm 9.2 cm
15.0 cm 18.0 cm 64.9 cm 47.5 cm 63.0 cm 26.0 cm 53.5 cm 81.0 cm 50.8 cm 95.6 cm 15.6 cm 0.0 cm 42.0 cm 26.2 cm
Sandy silt
Clayey silt
Depth error bar

Figure 14. (Previous page) Synthesis of LWD, stratigraphic, and sedimentologic data. A. Depth in meters below seafloor. B. LWD Gamma ray log from H001. C. LWD Compressional velocity log from H001 hole. D. LWD Ring resistivity from H001 hole plotted on linear scale (Guerin et al., 2010) and geological units from Boswell et al. (2012b). E. Core recovery from H002 (CS 1 and CS 2) and H005 (FB 2 – FB 13). F. Net-to-gross per core from H002 (CS 1 and CS 2) and H005 (FB 2 – FB 13). G. Average bed thickness of sandy silt per core from H002 (CS 1 and CS 2) and H005 (FB 2 – FB 13). H. Maximum thickness of any bed of sandy silt per core from H002 (CS 1 and CS 2) and H005 (FB 2 – FB 13). I. Percent sand from grain size measurements of H002 and H005 samples (Table 1). Green dots are samples of sandy silt and red squares are samples of clayey silt. Vertical black lines show the estimated depth of samples where the exact position is not precisely known. J. Depth in feet below seafloor.

The upward sharp increase in the average bed thickness of the sandy silt between cores 4FB and 5FB (Figure 14) record a possible increase in the intensity of the turbidity currents feeding the system. Alternatively, this transition records a relative decrease of the levee height. Such an abrupt change in net-to-gross and sandy silt bed thickness may be the result of levee collapse, as described by Santra et al. (2020), whereby oversteepening of the levee causes gravitational failure, and the internal levee slides toward the channel axis. As a result, channel relief (R) is reduced, the turbidity currents are less confined, and there is more overspill of coarse-grained sediments, leading to another episode of progressive thinning of turbidite deposits. Post-collapse, the levee begins to build again with subsequent overspilling turbidity currents.

The basal part of the cored section (unit 2, unit B, and unit 3) is thinner bedded. However, this is not the base of the entire levee (subunit 3-I), and this section may be composed of smaller or lower energy turbidity currents. Alternatively, the fine-bedded character may represent overspill when the vertical relief of the levee was high, before a phase of gravitational failure as discussed by Santra et al. (2020).

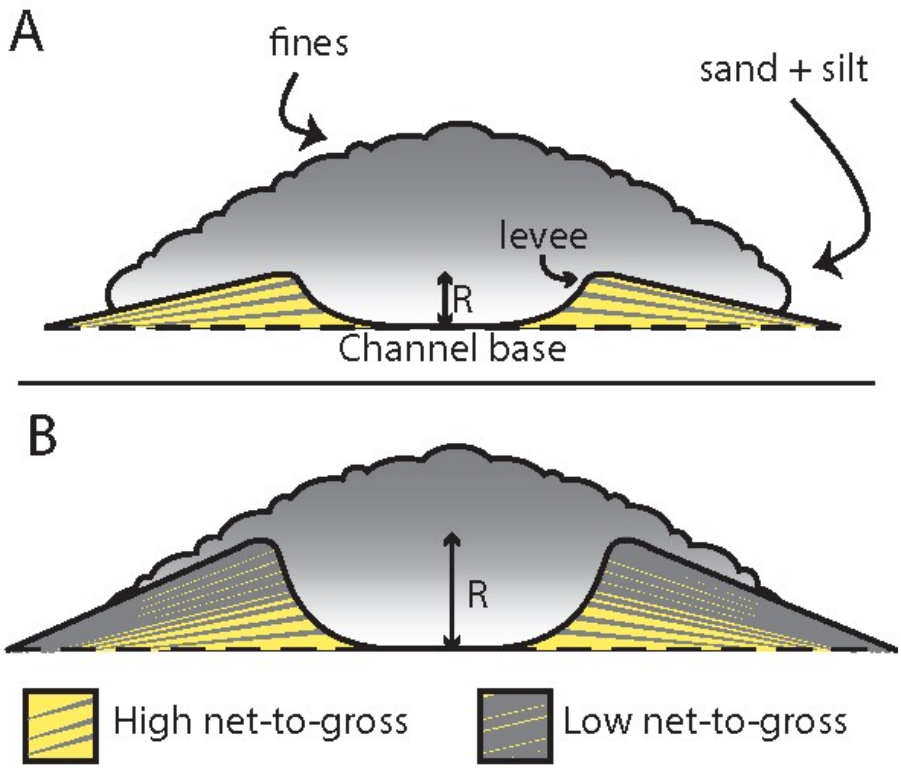

Figure 15. Cartoon evolution of the channel at GC 955. Flow of the turbidity current is into or out of the page for all images. A. Early in the channel evolution, the vertical relief between the channel base and the top of the levees (R) was low, and the lower, sand-rich part of the turbidity current spilled over the levee and deposited coarse-grained sediments. B. As the levees grew, the vertical relief between the channel base and the top of the levees (R) increased. The turbidity currents were increasingly confined, and less coarse-grained material was deposited on the levees, leading to an upward decrease in net-to-gross.

2.6.2 Core-Log Comparison

The 2009 LWD resistivity data from GC 955 H001 and the 2017 pressure core data from H005 record very similar lithologies even though they were drilled 15 meters apart and have very different resolution (Figure 8). The vertical resolution of the LWD ring resistivity is 5-8 cm (Lee and Collett, 2012). These data appear to accurately record the core properties when the individual bed thicknesses are greater than 20 cm. However,

when the beds are thinner than 20 cm, the resistivity values are clearly averaging the different lithologies present at the boundary. The fact that individual beds are present within both H001 and H005 suggests that the beds as thin as 10 cm (3.94 inches) are laterally continuous for at least 15 meters (49.2 ft).

2.6.3 Grain Size Comparison

Flemings et al. (2018) provided the initial measurements of grain size as measured by laser diffraction. In this study, we conducted grain size analysis via the hydrometer method on subsamples from the same cores, and found the fine-silt and clay fraction to be greater than the results provided by the laser diffraction method for each lithofacies (Figure 7). Such discrepancies are common (Di Stefano et al., 2010; Ferro and Mirabile, 2009; Wen et al., 2002), and we attribute this difference to variations in the shape and density of individual mineral clasts. The silty clay and clayey silt show the largest difference between methods, most likely due to the high fraction of non-spherical clay particles. The sandy silt is less affected, but is still observed to be finer when measured via hydrometer versus the laser hydrometer method (Figure 7).

2.6.4 Clayey silt vs. silty clay

The clayey silt is composed of both clayey silt and thin laminae of coarser-grained material (Figure 5) whereas the silty clay contains only clay and silt. There is a notable difference in particle size between the silty clay and the clayey silt (Figure 6). One interpretation is that the difference in particle size between the silty clay and the clayey silt is due solely to the inclusion of coarse laminae in the clayey silt (Figure 5) and that the

mudrock in the two lithofacies is identical. However, we sampled just the mud portion in the clayey silt (see 8CS-4 3-6 cm, 11FB-1, and 12FB-1 in Table 1), and found it also to be coarser-grained than the silty clay. We interpret that they are distinct lithologies and that the slightly coarser grained clayey silt is deposited more proximally to the levee channel than the finer-grained silty clay (Figure 11).

2.6.5 The Bounding Units of the Hydrate Reservoir

We have wondered since the 2009 LWD drilling what distinguishes the non-hydrate bearing units (units 1, 2, and 3 in Figure 4) from the hydrate-bearing reservoir units (units A, B, and C in Figure 4). Boswell et al. (2012 b) suggested two possible interpretations. Based on the low gamma ray values, the first interpretation is that the bounding units are water-bearing sands with less mud than the hydrate reservoir. The second interpretation is that the bounding units are finer-grained, with a reduced permeability and increased capillary entry pressure that inhibited hydrate formation.

To test these hypotheses, we analyzed the particle size distribution at one location from unit #1 above the hydrate reservoir and one location from unit #2 below the reservoir (Figure 13, samples 1CS-01 and 11FB-1 in Table 1). These samples were clayey silt (dashed lines in Figure 6) with <2% sand content (Figure 13); however, these single samples may not be indicative of the overall lithology of the unit. When we cored these intervals, the recovery was low, and the ball valve did not seal within unit #1 (Thomas et al., this volume); we interpret that this was because much of the sediment was washed out during drilling. Of the sediment recovered, thin beds of sandy silt averaging 6.3-7.1 cm

were found in non-pressured cores CS 1 from unit 1 and CS 2 (Figure 10). When compared to unit A, the net-to-gross and sandy silt bed thickness of unit 1 is low (Figure 14). We interpret that the low net-to-gross and thin bedded architecture of unit 1 created difficulties in drilling that led to washout and poor log response within this unit.

The majority of core FB 13 is from unit 3 (Figure 14), which was originally interpreted as water-bearing with no hydrate based on LWD logs (Boswell et al., 2012b). Therefore, we expected this core to contain inappreciable amounts of hydrate. However, within the PCATS analysis of FB 13, we find numerous beds of sandy silt with low density, high p-wave, and low attenuation lithofacies, interpreted as hydrate (Figure 16). Lithologically, unit 3 is similar to unit 1, with thinner silty sand beds and a lower net-to-gross than that of unit A. It is possible that the low net-to-gross and thin bedded character of unit #3 was difficult to drill during the original 2009 expedition, resulting in washout and poor log quality that affected the initial interpretation. It is therefore possible that all of the "water-bearing units" are in fact composed of thin bedded, hydrate-bearing, low net-to-gross sandy silt interbedded with clayey silt.

Alternatively, it is also possible that the stratigraphy is not consistent between the H001, H002, and H005 holes. However, this idea is contradicted by the correlation of hydrate-bearing layers between H001 and H005 (Figure 8), and H002 and H005 (Thomas et al., 2020). Another explanation may be that hydrate saturation is patchy throughout the reservoir for other reasons, as observed recently in the Nankai Trough, where individual beds were correlated between holes, but hydrate saturation varied (Tamaki et al., 2017).

2.7 CONCLUSIONS

We described the sedimentology and stratigraphy of an unlithified deepwater channel-levee hydrocarbon reservoir at the grain to bed scale, and provided a depositional model for the system. The hydrate reservoir at GC 955 is composed of interbedded sandy silt and clayey silt. As observed from pressure cores, the sandy silt intervals always contain high p-wave values interpreted as gas hydrate in high concentrations. Net-to-gross is greatest near the base of the cored interval and decreases upwards, supporting the interpretation of LWD data from the 2009 JIP II campaign. We have described a simple depositional model to explain the interbedded stacking patterns of coarser and finer grained sediment. In our model, overspilling, stratified turbidity currents build levees of interbedded sandy silt and clayey silt that shows a fining-upwards trend. We have also provided a model for the evolution of the channel system at GC 955 based on our sedimentologic analyses whereby an increase in channel relief causes a decrease in net-to-gross as the levees grow. The lower bounding unit is composed of thin bedded, hydrate-bearing sandy silt. The upper bounding unit is composed of low net-to-gross, thin bedded sandy silt that may contain hydrate. The scale of vertical reservoir heterogeneity that is observed here is impossible to capture in seismic and log data due to the discrepancy in vertical resolution between seismic, log, and core data. Interbedded hydrate-rich sandy silts range in thickness from less than 1 cm to nearly 100 cm, and such heterogeneity may be inherent in many deepwater levee reservoirs.

ACKNOWLEDGMENTS

This material is based upon work supported by the Department of Energy under Award Number DE-FE0023919. This report was prepared as an account of work sponsored by an agency of the United States Government. Neither the United States Government nor any agency thereof, nor any of their employees, makes any warranty, express or implied, or assumes any legal liability or responsibility for the accuracy, completeness, or usefulness of any information, apparatus, product, or process disclosed, or represents that its use would not infringe on privately owned rights. Reference herein to any specific commercial product, process, or service by trade name, trademark, manufacturer, or otherwise does not necessarily constitute or imply its endorsement, recommendation, or favoring by the United States Government or any agency thereof. The views and opinions of authors expressed herein to not necessarily state or reflect those of the United States Government or any agency thereof.

REFERENCES

Beaubouef, R., 2004, Deep-water leveed-channel complexes of the Cerro Toro Formation, Upper Cretaceous, southern Chile: AAPG bulletin, v. 88, p. 1471-1500.

Boswell, R., T. S. Collett, M. Frye, W. Shedd, D. R. McConnell, and D. Shelander, 2012a, Subsurface gas hydrates in the northern Gulf of Mexico: Marine and Petroleum Geology, v. 34, p. 4-30.

Boswell, R., M. Frye, D. Shelander, W. Shedd, D. R. McConnell, and A. Cook, 2012b, Architecture of gas-hydrate-bearing sands from Walker Ridge 313, Green canyon 955, and Alaminos canyon 21: northern deepwater Gulf of Mexico: Marine and Petroleum Geology, v. 34, p. 134-149.

Boswell, R., K. Yamamoto, S.-R. Lee, T. Collett, P. Kumar, and S. Dallimore, 2014, Methane hydrates, Future Energy (Second Edition), Elsevier, p. 159-178.

Boswell, R., J. Yoneda, and W. F. Waite, 2018, India National Gas Hydrate Program Expedition 02 summary of scientific results: Evaluation of natural gas-hydrate-bearing pressure cores: Marine and Petroleum Geology http://doi.org/10.1016/j.marpetgeo.2018.10.020.

Browne, G. H., and R. M. Slatt, 1997, Thin-bedded slope fan (channel-levee) deposits from New Zealand: an outcrop analog for reservoirs in the Gulf of Mexico.

Chand, S., T. A. Minshull, D. Gei, and J. M. Carcione, 2004, Elastic velocity models for gas-hydrate-bearing sediments—A comparison: Geophysical Journal International, v. 159, p. 573-590.

Clemenceau, G. R., 1995, Ram/Powell Field: Viosca Knoll Block 912, Deepwater Gulf of Mexico, *in* R. D. J. Winn, J. M. Armentrout, ed., Turbidites and associated deep-water facies: SEPM Core Workshop 20, p. 95-129.

Clemenceau, G. R., J. Colbert, and D. Edens, 2000, Production Results from Levee-Overbank Turbidite Sands at Ram/Powell Field, Deepwater Gulf of Mexico, *in* P. Weimer, ed., Deep-Water Reservoirs of the World, SEPM Society for Sedimentary Geology.

Collett, T. S., and R. Boswell, 2012, Resource and hazard implications of gas hydrates in the Northern Gulf of Mexico: Results of the 2009 Joint Industry Project Leg II Drilling Expedition: Marine and Petroleum Geology, v. 34, p. 1-3.

Collett, T. S., R. Boswell, J. R. Cochran, P. Kumar, M. Lall, A. Mazumdar, M. V. Ramana, T. Ramprasad, M. Riedel, K. Sain, A. V. Sathe, and K. Vishwanath, 2014, Geologic implications of gas hydrates in the offshore of India: Results of the National Gas Hydrate Program Expedition 01: Marine and Petroleum Geology, v. 58, p. 3-28.

Collett, T. S., M. Riedel, J. R. Cochran, R. Boswell, P. Kumar, and A. Sathe, 2008, Indian continental margin gas hydrate prospects: results of the Indian National Gas Hydrate Program (NGHP) expedition 01: Proc. 6 th Int. Conf. Gas Hydrates, Vancouver. https://circle.ubc.ca/bitstream/handle/2429/1035/5365.pdf.

Covault, J. A., and S. A. Graham, 2010, Submarine fans at all sea-level stands: Tectono-morphologic and climatic controls on terrigenous sediment delivery to the deep sea: Geology, v. 38, p. 939-942.

Cronin, B. T., A. Hurst, H. Celik, and I. Türkmen, 2000, Superb exposure of a channel, levee and overbank complex in an ancient deep-water slope environment: Sedimentary Geology, v. 132, p. 205-216.

Deptuck, M. E., G. S. Steffens, M. Barton, and C. Pirmez, 2003, Architecture and evolution of upper fan channel-belts on the Niger Delta slope and in the Arabian Sea: Marine and Petroleum Geology, v. 20, p. 649-676.

Di Stefano, C., V. Ferro, and S. Mirabile, 2010, Comparison between grain-size analyses using laser diffraction and sedimentation methods: Biosystems engineering, v. 106, p. 205-215.

Enunwa, C., J. L. Razzano III, A. Ramgulam, P. B. Flemings, T. Ertekin, and Z. T. Karpyn, 2005, Tahoe Field Case Study—Understanding Reservoir Compartmentalization in a Channel-Levee System: Gulf Coast Association of Geologic Societies Transactions, v. 55, p. 152-162.

Ferro, V., and S. Mirabile, 2009, Comparing particle size distribution analysis by sedimentation and laser diffraction method: Journal of Agricultural Engineering, v. 40, p. 35-43.

Figueiredo, J. J., D. M. Hodgson, S. S. Flint, and J. P. Kavanagh, 2010, Depositional environments and sequence stratigraphy of an exhumed Permian mudstone-dominated submarine slope succession, Karoo Basin, South Africa: Journal of Sedimentary Research, v. 80, p. 97-118.

Flemings, P., S. Phillips, R. Boswell, T. S. Collett, A. Cook, T. Dong, M. Frye, G. Guerin, D. Goldberg, M. Holland, J. Jang, P. Meazell, J. Morrison, J. O'Connell, T. Pettigrew, E. Petrou, P. Polito, A. Portnov, M. Santra, P. Schultheiss, Y. Seol, W. Shedd, E. Solomon, C. Thomas, W. F. Waite, and K. You, 2020, Pressure coring a high-saturation coarse-grained methane hydrate reservoir in the northern Gulf of Mexico: AAPG bulletin.

Flemings, P., S. Phillips, T. S. Collett, A. Cook, R. Boswell, and t. U.-G.-E. Scientists, 2018, Expedition Summary, UT-GOM2-1 Hydrate Pressure Coring Expedition Report, Austin, TX, University of Texas Institute for Geophysics, TX.

Flemings, P. B., R. Boswell, T. S. Collett, A. E. Cook, D. Divins, M. Frye, G. Guerin, D. S. Goldberg, A. Malinverno, and K. Meazell, 2017, GOM2: Prospecting, Drilling and Sampling Coarse-Grained Hydrate Reservoirs in the Deepwater Gulf of Mexico: Proceeding of ICGH-9, p. 10.

Folk, R. L., 1980, Petrology of sedimentary rocks, Hemphill Publishing Company.

Frye, M., W. Shedd, and R. Boswell, 2012, Gas hydrate resource potential in the Terrebonne Basin, Northern Gulf of Mexico: Marine and Petroleum Geology, v. 34, p. 150-168.

Fujii, T., T. Saeki, T. Kobayashi, T. Inamori, M. Hayashi, O. Takano, T. Takayama, T. Kawasaki, S. Nagakubo, and M. Nakamizu, 2008, Resource assessment of methane hydrate in the eastern Nankai Trough, Japan: Offshore technology conference.

Gardner, M. H., J. M. Borer, J. J. Melick, N. Mavilla, M. Dechesne, and R. N. Wagerle, 2003, Stratigraphic process-response model for submarine channels and related features from studies of Permian Brushy Canyon outcrops, West Texas: Marine and Petroleum Geology, v. 20, p. 757-787.

Germaine, J. T., and A. V. Germaine, 2009, Geotechnical laboratory measurements for engineers, John Wiley & Sons.

Guerin, G., A. Cook, S. Mrozewski, T. Collett, and R. Boswell, 2010, Gulf of Mexico Gas Hydrate Joint Industry Project Leg II: Green Canyon 955 LWD operations and results.

Gupta, L. P., W. Tanikawa, Y. Hamada, T. Hirose, N. Ahagon, T. Sugihara, N. Abe, S. Nomura, Y. Masaki, and H. Y. Wu, 2018, Examination of gas hydrate-bearing deep ocean sediments by X-ray Computed Tomography and verification of physical property measurements of sediments: Marine and Petroleum Geology.

Hackbarth, C. J., and R. D. Shew, 1994, Morphology and stratigraphy of a Mid-Pleistocene turbidite leveed channel from seismic, core and log data, northeastern Gulf of Mexico, *in* P. Weimer, A. H. Bouma, and B. F. Perkins, eds., Submarine Fans and Turbidite Systems—Sequence Stratigraphy, Reservoir Architecture and Production Characteristics Gulf of Mexico and International, Houston, Texas, SEPM Society for Sedimentary Geology, v. 15, p. 127 - 133, doi: https://doi.org/10.5724/gcs.94.15.

Hagedorn, A. R., and R. J. Blackwell, 1972, Summary of Experience with Pressure Coring, Fall Meeting of the Society of Petroleum Engineers of AIME, San Antonio, Texas, Society of Petroleum Engineers, p. 10.

Hansen, L., R. Callow, I. Kane, and B. Kneller, 2017a, Differentiating submarine channel-related thin-bedded turbidite facies: Outcrop examples from the Rosario Formation, Mexico: Sedimentary Geology, v. 358, p. 19-34.

Hansen, L., M. Janocko, I. Kane, and B. Kneller, 2017b, Submarine channel evolution, terrace development, and preservation of intra-channel thin-bedded turbidites: Mahin and Avon channels, offshore Nigeria: Marine Geology, v. 383, p. 146-167.

Hansen, L. A., R. H. Callow, I. A. Kane, F. Gamberi, M. Rovere, B. T. Cronin, and B. C. Kneller, 2015, Genesis and character of thin-bedded turbidites associated with submarine channels: Marine and Petroleum Geology, v. 67, p. 852-879.

Heggland, R., 2004, Definition of geohazards in exploration 3-D seismic data using attributes and neural-network analysis: AAPG bulletin, v. 88, p. 857-868.

Hiscott, R. N., F. R. Hall, and C. Pirmez, 1997, Turbidity-current overspill from the Amazon Channel: texture of the silt/sand load, paleoflow from anisotropy of magnetic susceptibility, and implications for flow processes: Proceedings -Ocean Drilling Program Scientific Results, p. 53-78.

Hodgson, D. M., C. N. Di Celma, R. L. Brunt, and S. S. Flint, 2011, Submarine slope degradation and aggradation and the stratigraphic evolution of channel–levee systems: Journal of the Geological Society, v. 168, p. 625-628.

Holland, M., P. Schultheiss, and J. Roberts, 2019, Gas hydrate saturation and morphology from analysis of pressure cores acquired in the Bay of Bengal during expedition NGHP-02, offshore India: Marine and Petroleum Geology, v. 108, p. 407-423.

Holland, M., P. Schultheiss, J. Roberts, and M. Druce, 2008, Observed gas hydrate morphologies in marine sediments: 6th International Conference on Gas Hydrates, Chevron, Vancouver, BC, Canada, p. 6-10.

Hutchinson, D., R. Boswell, T. Collett, J. C. Dai, O. Dugan, M. Frye, D. Mcconnell, K. Rose, W. Shedd, and D. Shel, 2009, Gulf of Mexico gas hydrate joint industry project leg II: green canyon 955 site selection.

Hutchinson, D. R., D. Shelander, J. Dai, D. McConnell, W. Shedd, M. Frye, C. Ruppel, R. Boswell, E. Jones, and T. Collett, 2008, Site selection for DOE/JIP gas hydrate drilling in the northern Gulf of Mexico: International Conference on Gas Hydrates.

Inada, N., and K. Yamamoto, 2015, Data report: Hybrid Pressure Coring System tool review and summary of recovery result from gas-hydrate related coring in the Nankai Project: Marine and Petroleum Geology, v. 66, p. 323-345.

Ito, T., Y. Komatsu, T. Fujii, K. Suzuki, K. Egawa, Y. Nakatsuka, Y. Konno, J. Yoneda, Y. Jin, M. Kida, J. Nagao, and H. Minagawa, 2015, Lithological features of hydrate-bearing sediments and their relationship with gas hydrate saturation in the eastern Nankai Trough, Japan: Marine and Petroleum Geology, v. 66, p. 368-378.

Jobe, Z. R., 2010, Multi-scale architectural evolution and flow property characterization of channelized turbidite systems, Doctoral dissertation: Stanford University, Stanford, California, 218 p.

Jobe, Z. R., D. R. Lowe, and W. R. Morris, 2012, Climbing-ripple successions in turbidite systems: depositional environments, sedimentation rates and accumulation times: Sedimentology, v. 59, p. 867-898.

Kane, I. A., and D. M. Hodgson, 2011, Sedimentological criteria to differentiate submarine channel levee subenvironments: exhumed examples from the Rosario Fm.(Upper Cretaceous) of Baja California, Mexico, and the Fort Brown Fm.(Permian), Karoo basin, S. Africa: Marine and Petroleum Geology, v. 28, p. 807-823.

Kane, I. A., D. T. McGee, and Z. R. Jobe, 2012, Halokinetic effects on submarine channel equilibrium profiles and implications for facies architecture: conceptual model illustrated with a case study from Magnolia Field, Gulf of Mexico: Geological Society, London, Special Publications, v. 363, p. 289-302.

Kendrick, J. W., 2000, Turbidite Reservoir Architecture in the Northern Gulf of Mexico Deepwater: Insights from the Development of Auger, Tahoe, and Ram/Powell Fields, *in* P. Weimer, ed., Deep-Water Reservoirs of the World, Houston, Texas, SEPM Society for Sedimentary Geology, p. 450-468.

Kvenvolden, K. A., 1988, Methane hydrate—a major reservoir of carbon in the shallow geosphere?: Chemical geology, v. 71, p. 41-51.

Lee, M. W., and T. S. Collett, 2012, Pore- and fracture-filling gas hydrate reservoirs in the Gulf of Mexico Gas Hydrate Joint Industry Project Leg II Green Canyon 955 H well: Marine and Petroleum Geology, v. 34, p. 62-71.

McCarthy, P., J. Brand, B. Paradiso, J. Ezekwe, N. Wiltgen, A. Bridge, R. Willingham, and M. Bogaards, 2005, Using Geostatistical Inversion of Seismic And Borehole Data to Generate Reservoir Models For Flow Simulations of Magnolia Field, Deepwater Gulf of Mexico, SEG Technical Program Expanded Abstracts, Houston, Texas, Society of Exploration Geophysicists, p. 1351-1354.

McConnell, D. R., 2000, Optimizing deepwater well locations to reduce the risk of shallow-water-flow using high-resolution 2D and 3D seismic data. Proceedings of Offshore Technology Conference, Houston, Texas, USA, OTC-11973, DOI: 10.4043/11973-MS.

McConnell, D. R., T. S. Collett, R. Boswell, M. Frye, W. W. Shedd, R. S. Dufrene, P. D. Godfriaux, S. Mrozewski, G. Guerin, A. Cook, and E. Jones, 2010, Gulf of

Mexico Gas Hydrate Joint Industry Project Leg II: Initial Results from the Green Canyon 955 Site, Proceedings of Offshore Technology Conference, Houston, Texas, USA, OTC-20801-MS, DOI: 10.4043/20801-MS.

Meldahl, P., R. Heggland, B. Bril, and P. de Groot, 2001, Identifying faults and gas chimneys using multiattributes and neural networks: The Leading Edge, v. 20, p. 474-482.

Morris, E. A., D. M. Hodgson, R. L. Brunt, and S. S. Flint, 2014, Origin, evolution and anatomy of silt-prone submarine external levées: Sedimentology, v. 61, p. 1734-1763.

Noguchi, S., N. Shimoda, O. Takano, N. Oikawa, T. Inamori, T. Saeki, and T. Fujii, 2011, 3-D internal architecture of methane hydrate-bearing turbidite channels in the eastern Nankai Trough, Japan: Marine and Petroleum Geology, v. 28, p. 1817-1828.

Oshima, M., K. Suzuki, J. Yoneda, A. Kato, M. Kida, Y. Konno, M. Muraoka, Y. Jin, J. Nagao, and N. Tenma, 2019, Lithological properties of natural gas hydrate–bearing sediments in pressure-cores recovered from the Krishna–Godavari Basin: Marine and Petroleum Geology, v. 108, p. 439-470.

Peakall, J., B. McCaffrey, and B. Kneller, 2000, A process model for the evolution, morphology, and architecture of sinuous submarine channels: Journal of Sedimentary Research, v. 70, p. 434-448.

Pettijohn, F. J., P. E. Potter, and R. Siever, 2012, Sand and sandstone, New York, Springer Science & Business Media, 553 p.

Phillips, S., P. Flemings, M. Holland, P. Schultheiss, W. F. Waite, J. Jang, E. Petrou, and H. Hammon, 2020, Extremely high concentrations of methane hydrate in a deepwater silt reservoir from the northern Gulf of Mexico (Green Canyon 955): AAPG bulletin.

Pickering, K., J. Coleman, M. Cremer, L. Droz, B. Kohl, W. Normark, S. O'Connell, D. Stow, and A. Meyer-Wright, 1986, A high sinuosity, laterally migrating submarine fan channel-levee-overbank: results from DSDP Leg 96 on the Mississippi Fan, Gulf of Mexico: Marine and Petroleum Geology, v. 3, p. 3-18.

Piper, D. J., and M. Deptuck, 1997, Fined-grained turbidites of the Amazon Fan: facies characterization and interpretation: PROCEEDINGS-OCEAN DRILLING PROGRAM SCIENTIFIC RESULTS, p. 79-108.

Piper, D. J., and W. R. Normark, 2001, Sandy fans-from Amazon to Hueneme and beyond: AAPG bulletin, v. 85, p. 1407-1438.

Portnov, A., A. E. Cook, M. Heidari, D. E. Sawyer, M. Santra, and M. Nikolinakou, 2018, Salt-driven evolution of a gas hydrate reservoir in Green Canyon, Gulf of Mexico: AAPG Bulletin, this volume.

Prather, B. E., C. Pirmez, C. D. Winker, M. Deptuck, and D. Mohrig, 2012, Stratigraphy of linked intraslope basins: Brazos-Trinity system western Gulf of Mexico: Application of the principles of seismic geomorphology to continental-slope and base-of-slope systems: Case studies from seafloor and near-seafloor analogues: SEPM, Special Publication, v. 99, p. 83-109.

Ruppel, C., R. Boswell, and E. Jones, 2008, Scientific results from Gulf of Mexico gas hydrates Joint Industry Project Leg 1 drilling: introduction and overview: Marine and Petroleum Geology, v. 25, p. 819-829.

Ryu, B.-J., T. S. Collett, M. Riedel, G. Y. Kim, J.-H. Chun, J.-J. Bahk, J. Y. Lee, J.-H. Kim, and D.-G. Yoo, 2013, Scientific results of the Second Gas Hydrate Drilling Expedition in the Ulleung Basin (UBGH2): Marine and Petroleum Geology, v. 47, p. 1-20.

Santra, M., P. Flemings, and K. Meazell, 2020, Evolution of Gas Hydrate-bearing Deepwater Channel-Levee System in Abyssal Gulf of Mexico – Levee Growth and Deformation: AAPG bulletin.

Sawyer, D. E., P. B. Flemings, R. C. Shipp, and C. D. Winker, 2007, Seismic geomorphology, lithology, and evolution of the late Pleistocene Mars-Ursa turbidite region, Mississippi Canyon area, northern Gulf of Mexico: AAPG bulletin, v. 91, p. 215-234.

Sawyer, D. E., R. Jacoby, P. Flemings, and J. T. Germaine, 2009, Data report: Particle size analysis of sediments in the Ursa Basin, IODP Expedition 308 Sites U1324 and U1322, northern Gulf of Mexico: Proc. IODP| Volume, p. 2.

Schultheiss, P., M. Holland, J. Roberts, Q. Huggett, M. Druce, and P. Fox, 2011, PCATS: pressure core analysis and transfer system: Proceedings of the 7th International Conference on Gas Hydrates (ICGH 2011), Edinburgh, UK, p. 17-21.

Shepard, F. P., 1954, Nomenclature based on sand-silt-clay ratios: Journal of Sedimentary Research, v. 24, p. 151-158.

Shukla, K., T. Collett, P. Kumar, U. Yadav, R. Boswell, M. Frye, M. Riedel, I. Kaur, and K. Vishwanath, 2018, National Gas Hydrate Program expedition 02:

Identification of gas hydrate prospects in the Krishna-Godavari Basin, offshore India: Marine and Petroleum Geology, v. 108, p. 167-184.

Sloan, E. D., 2003, Fundamental principles and applications of natural gas hydrates: Nature, v. 426, p. 353.

Stow, D. A. V., and A. J. Bowen, 1978, Origin of lamination in deep sea, fine-grained sediments: Nature, v. 274, p. 324.

Stow, D. A. V., and A. J. Bowen, 1980, A physical model for the transport and sorting of fine-grained sediment by turbidity currents: Sedimentology, v. 27, p. 31-46.

Straub, K. M., and D. Mohrig, 2008, Quantifying the morphology and growth of levees in aggrading submarine channels: Journal of Geophysical Research: Earth Surface, v. 113.

Straub, K. M., D. Mohrig, J. Buttles, B. McElroy, and C. Pirmez, 2011, Quantifying the influence of channel sinuosity on the depositional mechanics of channelized turbidity currents: A laboratory study: Marine and Petroleum Geology, v. 28, p. 744-760.

Tamaki, M., T. Fujii, and K. Suzuki, 2017, Characterization and prediction of the gas hydrate reservoir at the second offshore gas production test site in the eastern Nankai trough, Japan: Energies, v. 10, p. 1678.

Thomas, C., S. Phillips, P. Flemings, M. Santra, H. Hammon, T. S. Collett, A. Cook, T. Pettigrew, M. Holland, and P. Schultheiss, 2020, Pressure-coring operations durin Expedition UT-GOM2-1 in Green Canyon Block 955, northern Gulf of Mexico: AAPG bulletin.

Tréhu, A. M., F. R. Rack, and M. E. Torres, 2003, Proceedings of the Ocean Drilling Program [electronic resource].: drilling gas hydrates on Hydrate Ridge, Cascadia Continental Margin; covering leg 204 of the cruises of the drilling vessel JOIDES Resolution; Victoria, British Columbia, Canada, to Victoria, British Columbia, Canada; 7 July-2 September 2002. Initial reports, Texas A&M University.

Walker, R. G., 1978, Deep-water sandstone facies and ancient submarine fans: models for exploration for stratigraphic traps: AAPG Bulletin, v. 62, p. 932-966.

Weimer, P., 1990, Sequence stratigraphy, facies geometries, and depositional history of the Mississippi Fan, Gulf of Mexico (1): AAPG bulletin, v. 74, p. 425-453.

Weissenburger, K., and T. Borbas, 2004, Fluid properties, phase and compartmentalization: Magnolia field case study, deepwater Gulf of Mexico, USA: Geological Society, London, Special Publications, v. 237, p. 231-255.

Wen, B., A. Aydin, and N. S. Duzgoren-Aydin, 2002, A comparative study of particle size analyses by sieve-hydrometer and laser diffraction methods: Geotechnical Testing Journal, v. 25, p. 434-442.

Wentworth, C. K., 1922, A scale of grade and class terms for clastic sediments: The journal of geology, v. 30, p. 377-392.

Winters, W. J., W. F. Waite, D. Mason, L. Gilbert, and I. Pecher, 2007, Methane gas hydrate effect on sediment acoustic and strength properties: Journal of Petroleum Science and Engineering, v. 56, p. 127-135.

Chapter 3: The evolution of seafloor venting from hydrate-sealed gas reservoirs[2]

ABSTRACT

We use 3D seismic data to show that three rows of seafloor gas mounds can be traced downward to leak points that lie at the hydrate-gas contact within three individual dipping coarse-grained sand bodies in the Terrebonne Basin, Walker Ridge block 313, northern Gulf of Mexico. We predict the overpressure within the sand bodies by assuming that the gas pressure at the vent points equal the least principal stress. We interpret that free gas accumulates at the base of the hydrate stability zone, trapped by the overlying sand which has a high methane hydrate saturation. The free gas accumulates until the gas pressure at the base of the hydrate stability zone reaches the least principal stress in the overlying mudrock, whereupon hydraulic fractures form and fluids are vented to the surface. The warm rising fluids and perhaps localized exothermic formation of hydrate raise the local salinity and temperature. This process progressively shifts the base of the hydrate stability zone to shallower depths and dissociates the hydrate seal within the sand, which creates new leak points and results in the observed migration of the seafloor vents. Within the southwest corner of the Terrebonne Basin, this process has repeated multiple times within the Blue, Orange, and Green sands. This study shows how the hydrate stability zone can influence the location of fluid expulsion and in turn be affected by the warm, rising, saline fluids sealed by hydrate.

[2] This chapter has been submitted to Earth and Science Planetary Letters. I performed the analyses and wrote the manuscript. Peter Flemings edited the manuscript and provided valuable feedback.

3.1 INTRODUCTION

Fluid expulsion is a common occurrence within sedimentary basins (Judd and Hovland, 2009). Seafloor vents connect subsurface aquifers and hydrocarbon reservoirs with the ocean, and contribute vast quantities of methane to the ocean, and lesser amounts to the atmosphere (Foschi et al., 2020; Kvenvolden and Rogers, 2005). As such, they are an important piece of the global carbon cycle, contributing as much as 20 Tg of methane to the ocean per year, with minor amounts reaching the atmosphere (Etiope, 2012).

On the seafloor, the venting of fluids is often manifested as pockmarks, cold seeps, and mud volcanoes (Cartwright et al., 2007; Ceramicola et al., 2018; Loher et al., 2018; Roberts, 2001; Talukder, 2012). Due to the presence of methane-rich, migrating fluids, seafloor chemosynthetic communities thrive in these environments (Ceramicola et al., 2018; Loher et al., 2018; Roberts et al., 2010). In seismic reflection data, the subsurface root zones of vents are characterized by zones of reduced reflector continuity that connect seafloor features to deeper hydrocarbon reservoirs (Cartwright and Santamarina, 2015).

Seafloor vents are an important indicator of the pressures and stresses in subsurface systems (Andresen, 2012), and the identification of fluid expulsion features has long guided petroleum exploration (Judd and Hovland, 2009; Seldon and Flemings, 2005). Elevated pore pressures are commonly found in the reservoirs that source deepwater vents (Reilly and Flemings, 2010; Seldon and Flemings, 2005; Tréhu et al., 2004; Van Rensbergen et al., 2005), and are often inferred to drive these vents. In particular, a documented mechanism to drive fluid flow is the presence of permeable beds trapped within overpressured shales: where the overburden is thin relative to the permeable beds,

the pore pressure approaches the least principal stress causing hydraulic fracturing and ultimately venting to the seafloor (Flemings, 2021). In the absence of pre-existing faults or fractures, venting begins at the crest of the permeable bed.

Methane hydrate is an ice-like compound composed of a single methane molecule trapped inside a cage of water molecules (Sloan Jr and Koh, 2007). Due to high pressures, low temperatures, and the presence of methane, hydrate is commonly found both on the seafloor and within the sediments near deepwater vents (Flemings et al., 2003; Paganoni et al., 2018; Roberts, 2001), and deepwater hydrate sequesters a significant amount of the global carbon budget (Ruppel and Kessler, 2017). Due to increasing temperatures with depth, hydrate is only stable within the uppermost 10's to 100's of meters of sediment beneath the seafloor. The Base of the Hydrate Stability Zone (BHSZ) is the deepest point at which hydrate is stable. Beneath the BHSZ, free gas is stable, and thick layers of gas have been interpreted from seismic data within the Makran accretionary prism (Sain et al., 2000) the Niger Delta (Hovland et al., 1997), the Krishna-Godavari Basin (Dewangan et al., 2021), and offshore New Zealand (Crutchley et al., 2018). Gas-rich fluids have been observed rising from such deepwater reservoirs, bypassing the hydrate stability zone and venting at the surface (Gay et al., 2007; Liu and Flemings, 2006; Smith et al., 2014; Tréhu et al., 2004). These deepwater reservoirs are often low-relief (e.g., Gay et al., 2007; Liu and Flemings, 2006; Tréhu et al., 2004), or rise up against the flanks of a diapir (e.g., Smith et al., 2014b), and they are sealed by low permeability mudrock.

As opposed to typical low-permeability mudrock seals, a seal composed of highly-concentrated hydrate will dissociate due to changes in pressure, temperature, or salinity;

the hydrate seal can become a free gas reservoir from depressurization, warming, or increasing salinity. Dipping, gas- and hydrate-saturated sand bodies that cross the base of the hydrate stability zone in the Terrebonne Basin, northern Gulf of Mexico (Fig. 1) provide the perfect opportunity to investigate the sealing capacity of concentrated hydrate as well as the effects that rising fluids exhibit on these hydrate seals.

In this paper, we demonstrate how natural methane hydrate systems impact fluid venting at the surface. We use 3D seismic interpretation to explore the interaction between venting overpressured reservoirs and the hydrate stability zone. We map three sand units in the deepwater Gulf of Mexico and use the seismic response and well logs to infer fluid presence within these reservoirs, and estimate pore pressures within the basin. We show that in the Terrebonne Basin, fluids are leaking from three discrete sand bodies precisely at the hydrate-gas interface at the base of the hydrate stability zone. We describe how the venting of warm, saline fluids has modified the hydrate seal, resulting in the stepwise-shoaling of leak points and the formation of rows of seafloor mounds.

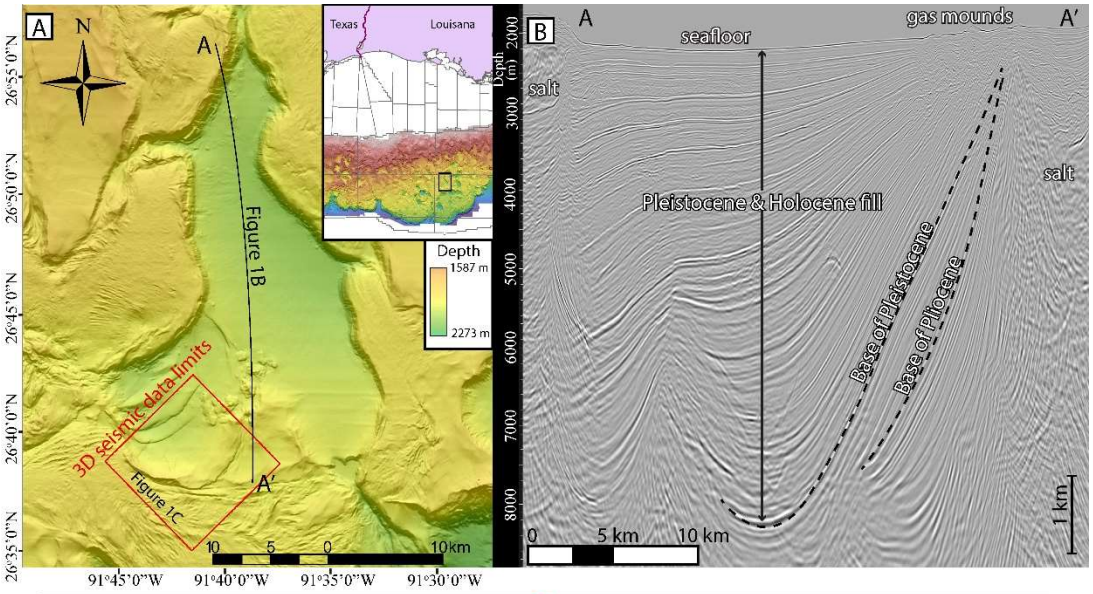
A
N
A
Figure 1B
A'
3D seismic data limits
Figure 1C
Texas
Louisana
Depth (m)
Depth
1587 m
2273 m
10 5 0 10km
26°55'0"N
26°50'0"N
26°45'0"N
26°40'0"N
26°35'0"N
91°45'0"W
91°40'0"W
91°35'0"W
91°30'0"W
B
A
A'
seafloor
gas mounds
salt
salt
Pleistocene & Holocene fill
Base of Pleistocene
Base of Pliocene
0 5 km 10 km
1 km

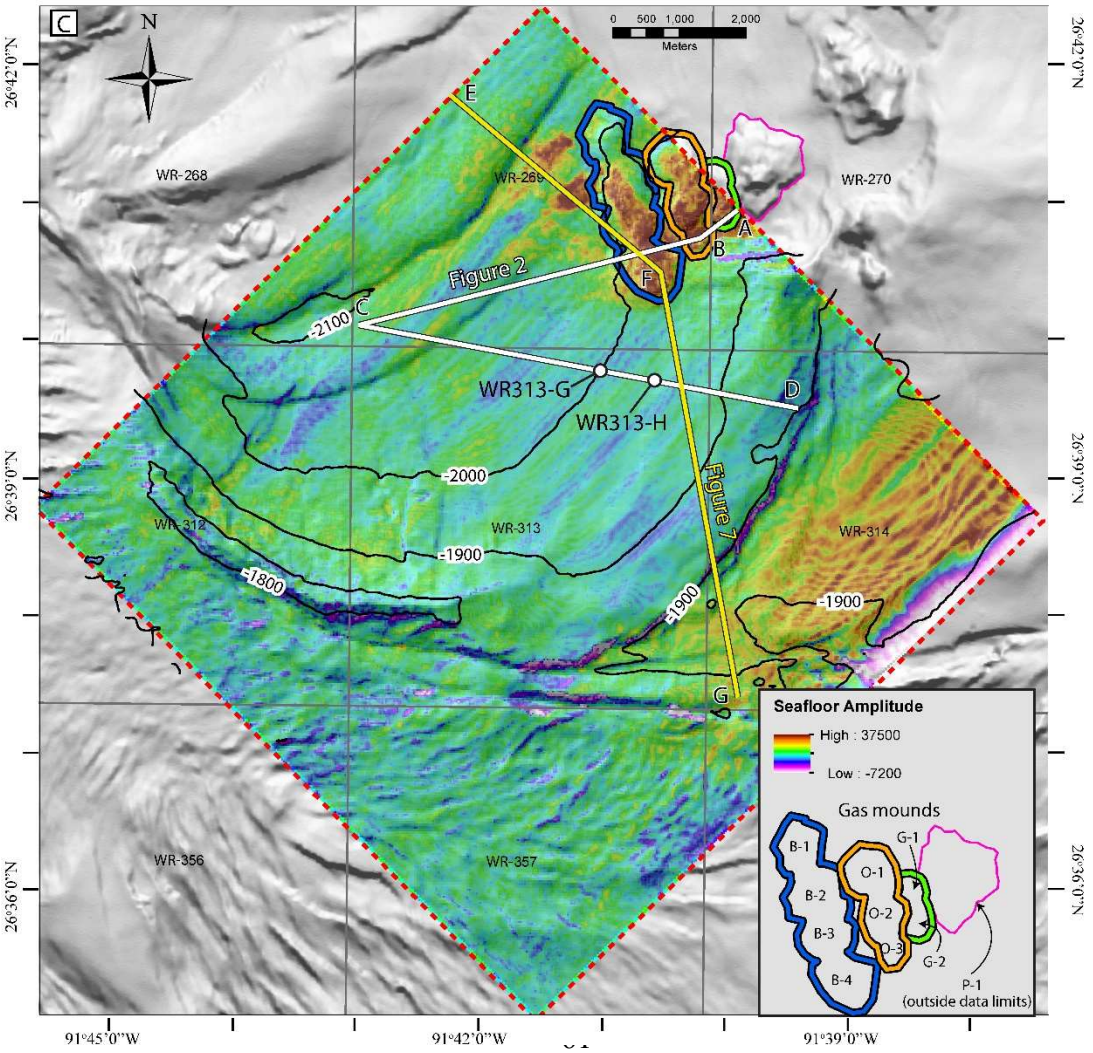
C
N
0 500 1,000 2,000
Meters
E
WR-268
WR-269
WR-270
A
B
F
Figure 2
C
-2100
WR313-G
WR313-H
D
-2000
WR-312
WR-313
WR-314
-1900
-1800
-1900
-1900
Figure 7
G
WR-356
WR-357
Seafloor Amplitude
High : 37500
Low : -7200
Gas mounds
B-1
B-2
B-3
B-4
O-1
O-2
O-3
G-1
G-2
P-1
(outside data limits)
26°42'0"N
26°39'0"N
26°36'0"N
91°45'0"W
91°42'0"W
91°39'0"W

Figure 1. (Previous page) Overview of the Terrebonne Basin. A. Bathymetry of the Terrebonne Basin. Circular, positive relief features in the south are seafloor gas mounds. B. North-south seismic line of the Terrebonne Basin. Strata dip to the north, where they reach depths of 8000 m. A discontinuous BSR (bottom-simulating reflector) indicates the presence of gas and hydrate in sand bodies. C. Seafloor amplitude map of southwestern Terrebonne basin, with positive amplitudes displayed as blue to red, and negative amplitudes displayed as white to purple. Three rows of gas mounds (outlined by Blue, Orange, and Green polygons) are imaged as strong positive amplitude reflectors, with amplitudes increasing to the southeast. Several more gas mounds are imaged to the northwest, outside of our 3D seismic data set.

3.2 Geological Setting and Previous Work

3.2.1 The Terrebonne Basin

The Terrebonne Basin is a salt-withdrawal minibasin in the northwestern region of the Walker Ridge protraction area in the northern Gulf of Mexico, with seafloor depths ranging from 1700-2250m (Fig. 1A). Salt underlies and bounds the elongate basin and beneath the seafloor, Pliocene and Pleistocene strata dip to the north to depths as great as 8 km (Fig. 1B). In the southern Terrebonne basin, seafloor mounds are found overlying dipping sand bodies where the sands are structurally high (Fig. 1A & 1B).

Within the southern Terrebonne Basin, McConnell and Kendall (2002) identified a discontinuous Bottom-Simulating Reflector (BSR) and interpreted it to represent the point at which multiple gas- and hydrate-bearing sand layers cross the BHSZ. Two gas hydrate exploration holes in block WR313 in 2009 confirmed the presence of hydrate in these dipping layers (Boswell et al., 2012a; Boswell et al., 2012b; Collett and Boswell, 2012; Frye et al., 2012).

3.2.2 Reservoir Characterization

Three sand-rich reservoir units were inferred by logging while drilling (LWD) and termed the Blue, Orange, and Green sands (Boswell et al., 2012a; Boswell et al., 2012b; Collet et al., 2012). High hydrate-saturations of 75-90% were interpreted above the BSR in the Blue and Orange sands (Collett et al., 2012). The Green sand was only penetrated beneath both hydrate and free gas; however, both gas and hydrate are interpreted from seismic data to be present updip of the BSR (Boswell et al., 2012b; Frye et al., 2012). Free gas is also interpreted to exist within the Blue, Orange, and Green sands below the hydrate stability zone (Frye et al., 2012; McConnell and Kendall, 2002; McConnell et al., 2012). Above the BSR, high sonic velocities suggest that the sands contain only water and hydrate; No free gas was detected within the hydrate stability zone (Boswell et al., 2012b; Collett et al., 2012).

3.2.3 Seafloor Vents

McConnell and Kendall (2002) originally described the ~800m diameter vents as "Giant gas mounds," and mention that 99% of the hydrocarbons expelled were composed of methane. Positive amplitude seismic anomalies were found blanketing the seafloor on top of and adjacent to the mounds (McConnell and Kendall, 2002; Roberts et al., 2010a). Roberts et al. (2010a) investigated the gas mounds in WR 270 (labeled P-1 in Fig. 2) via ROV, and confirmed the presence of chemosynthetic communities, carbonate hardgrounds, and active expulsion at the surface of the gas mounds. A single rock sample collected from the top of the mound contains silt-sized quartz grains, which are interpreted to have been

transported from the subsurface to the seafloor via the venting of fluids (Roberts et al., 2010).

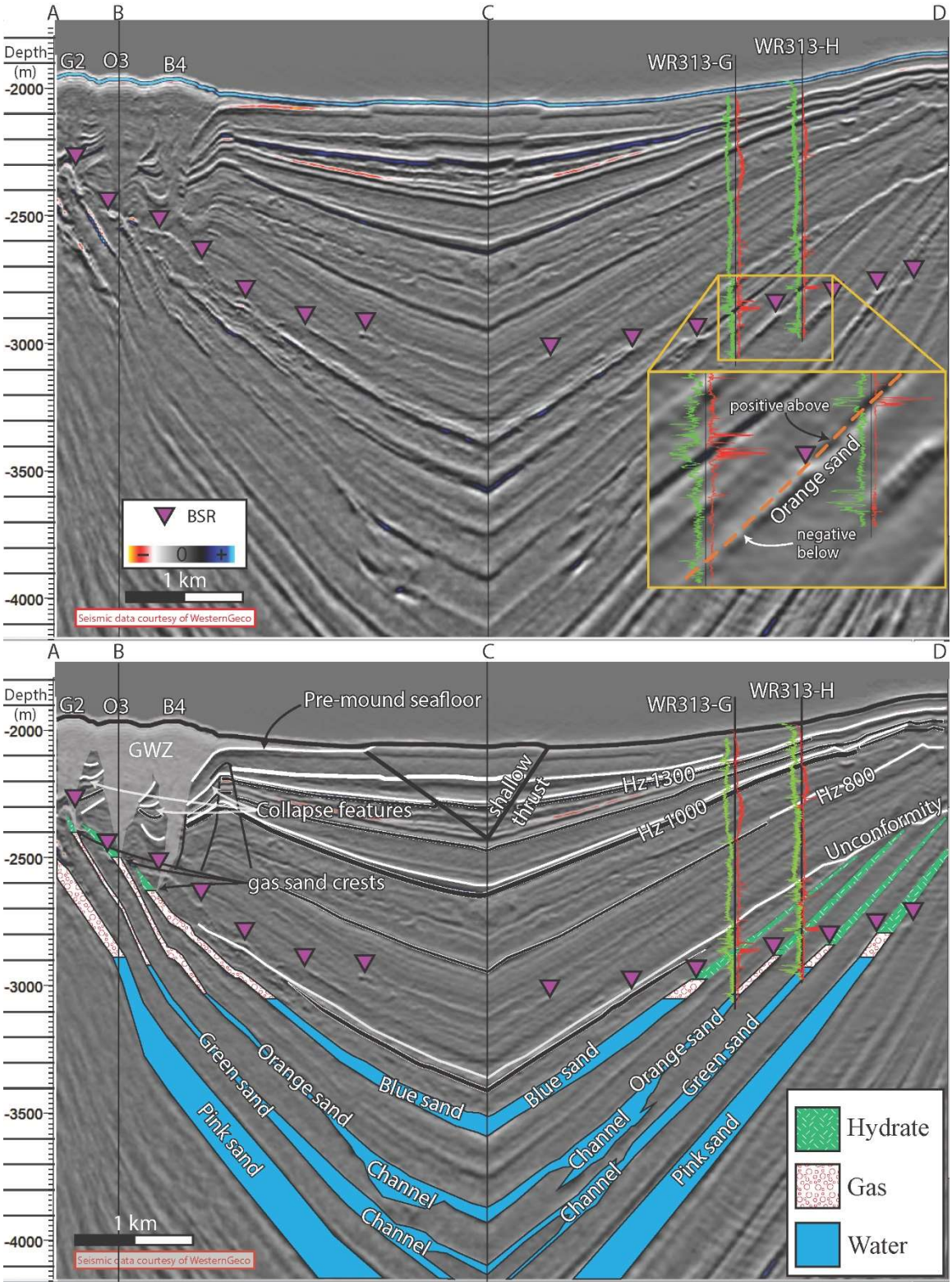
A
B
C
D
Depth (m)
-2000
-2500
-3000
-3500
-4000
G2
O3
B4
WR313-G
WR313-H
positive above
Orange sand
negative below
BSR
0
1 km
Seismic data courtesy of WesternGeco
Pre-mound seafloor
GWZ
Collapse features
shallow thrust
gas sand crests
Hz-1300
Hz-1000
Hz-800
Unconformity
Green sand
Orange sand
Blue sand
Pink sand
Channel
Hydrate
Gas
Water

Figure 2. (Previous page) Uninterpreted (Top) and Interpreted (Bottom) seismic cross section of the gas mounds and major sand units in the SW Terrebonne basin, including Gamma Ray (green) and resistivity (red) well logs from the WR313-G and WR313-H wells. A discontinuous bottom simulating reflector (BSR, purple triangles) is found across the Terrebonne basin, and rises in the vicinity of the gas mounds. Hydrate was found in the Blue and Orange sands above the BSR (Boswell et al., 2009b). The inset displays the mapping strategy, whereby the sands were mapped on the positive (black) reflector above the BSR, and on the negative reflector (white) below the BSR. An abrupt dimming of the negative reflector with depth is interpreted as the gas-water contact (GWC). Conical shaped gas wipeout zones (GWZ) are found below each gas mound, and terminate at the crestal position of gas within each sand. Additional well logs for the reservoir section of WR313-G and WR313-H are included in Appendix B.

3.3 METHODS AND DATA

3.3.1 Well logs

We use logging-while-drilling (LWD) data from the WR313-G and WR313-H wells to interpret lithology and pore fill. A standard suite of well logs, including Gamma Ray, resistivity, sonic velocity, and density have been used to infer a range of reservoir properties such as porosity and hydrate saturation (Collett et al., 2012; Cook et al., 2012; Lee and Collett, 2012). Well logs were processed onboard by Schlumberger personnel, and corrected for hole size, collar size, and type of drilling fluid. Density data have been corrected for the shallow section (0-60 mbsf) where quality is low due to increased borehole diameter (Hillman et al., 2017). The well logs for WR313-G and WR313-H are included in Appendix B.

3.3.2 Seismic data

We make use of commercial 3D seismic reflection data for the mapping and interpretation of the subsurface geology. The geographic limits of the data subset is shown as a red diamond in Figures 1A and 2. This seismic data set was acquired in 2006-2007

from a 4 Tuned Bolt airgun array marine survey with streamers at 12 m depth and 120 m between streamers. The sample rate of the data is 2 ms. Data processing followed an industry standard workflow including a water velocity correction, residual multiple attenuation, seismic interference noise elimination, high-resolution sediment flood, and Kirchoff migration. All seismic data is zero-phase and in North American polarity, where the seafloor is represented by the peak of a positive reflection.

3.3.3 Mapping

The Terrebonne Basin was one of the first locations where it was documented that hydrate-filled sands are imaged with a positive polarity seismic reflector, whereas underlying gas-filled sands are imaged with a negative polarity reflector. For example, the Orange sand is imaged as a strong positive reflection above the BSR (interpreted as the base of the hydrate stability zone), whereas this sand is imaged as a negative reflection below the BSR (Fig. 2, inset). The drilling results (Appendix B) documented that above the BSR, the strong positive reflections associated with the sands are correlated with very high sonic velocities interpreted as hydrate within the sands (Boswell et al., 2012b; Collett et al., 2012).

From these observations arose the basic strategy of mapping the presence of hydrate in sands by mapping on a positive polarity seismic reflection at the top of the sand above the BSR, and on a negative polarity event at the top of the sand below the BSR (e.g. Frye et al., 2012; McConnell and Kendall, 2002; McConnell et al., 2012). We used this approach to generate maps of the Green, Orange, and Blue sands (Fig. 3, 4, and 5,

respectively) and from these maps interpreted the distribution of water, free gas, and hydrate within each sand body. These maps are similar to those presented by Boswell et al. (2012) and Frye et al. (2012).

We assume the BSR represents the pressure-, temperature-, and salinity-dependent phase boundary that marks the base of the hydrate stability zone. We mapped the discontinuous BSR on the strong, negative amplitude (opposite of the seafloor) reflection (purple triangles in Fig. 2). We interpolated the base of the hydrate stability zone between these points, assuming that similar conditions are present in the areas between the BSR. We calculated the thickness of the hydrate stability zone by subtracting the total vertical depth of the interpolated base of hydrate stability from the total vertical depth of the seafloor.

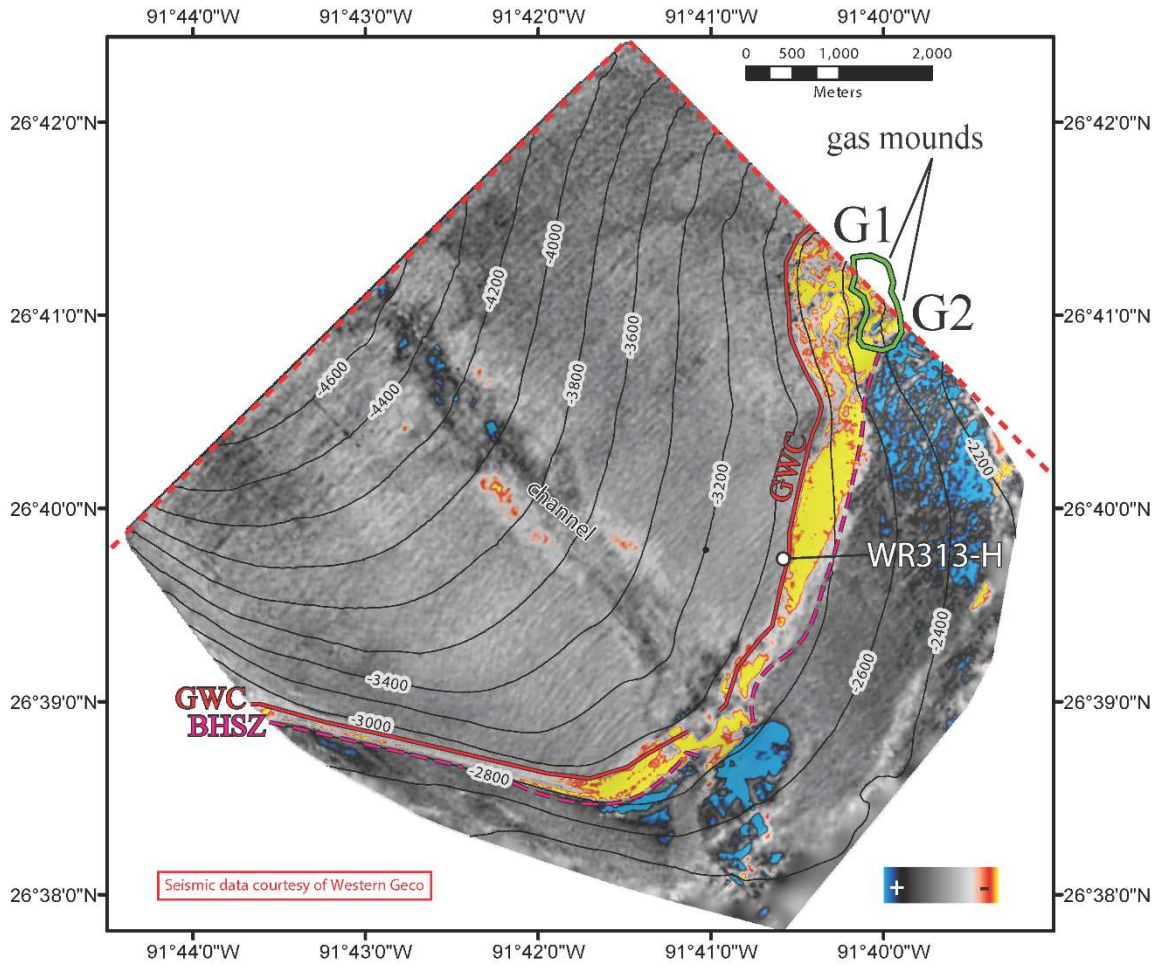

Figure 3. Amplitude map of the Green sand, with outlines of the surficial gas mounds overlain. Blue-dark grey = hydrate-bearing sands; red-yellow = gas-bearing sands; light grey-white = water-bearing sands. A southeast-trending channel cuts across the sand, but the gas-water contact (GWC) is at the same depth throughout the study area. The base of the hydrate stability zone, as interpreted by a bottom-simulating reflector, conforms to structure in the SW, but cuts across contours in the N & E, and leads directly to mound G2.

3.4 Observations and Interpretations

3.4.1 The Green sand

The Green sand dips to the northwest with a synclinal geometry; a southeast trending, 700-1000-meter-wide low amplitude zone within it is interpreted as a submarine

channel (Fig. 3). Bright amplitude zones on both sides of the channel are interpreted as coarse-grained levees (Boswell et al., 2012b; Frye et al., 2012).

The boundary between the positive amplitudes (blue and black to dark grey) and the negative amplitudes (light grey to red and yellow) marks the base of the hydrate stability zone (BHSZ in Fig. 3). To the south of channel, the BHSZ parallels the structural contours at 2800 m (dashed pink line in Fig. 3). However, northeast of the channel, the BHSZ rises, crossing the structural contours, reaching a depth of 2400 m just beneath the mound G2 (located in Fig. 1C).

Immediately below the base of the hydrate stability zone, there is a zone of strong, negative polarity amplitudes that we interpret as free gas. At the base of the free gas zone, an abrupt decrease in amplitude that conforms to structure is observed on both sides of the channel at 2930 m. We interpret this as a gas-water contact (GWC in Fig. 3); our interpretation is supported by log data from WR313-H (Appendix B1), which found low gamma ray and low resistivities interpreted as water-saturated sand in the low amplitude zone immediately downdip of the bright zone interpreted as gas. On the SW flank, we observe a gas column of 150 m. On the NE flank, the column of gas grows to height of 520 m beneath the gas mounds (Fig. 2 & 3).

3.4.2 The Orange sand

The Orange sand also dips to the northwest with a synclinal geometry (Fig. 4). Similar to the Green sand, a southeast trending, 700-1000-meter wide, low-amplitude zone

is interpreted to record a submarine channel, and separates bright amplitude zones interpreted as coarse-grained levees on both sides (Boswell et al., 2012b; Frye et al., 2012).

The boundary between the positive amplitudes (blue and black to dark grey) and the negative amplitudes (light grey to red and yellow) marks the base of the hydrate stability zone (BHSZ in Fig. 4). To the south of channel, the BHSZ parallels the structural contours at 2950 m (dashed pink line, Fig. 4). However, northeast of the channel, the BHSZ rises (crossing the structural contours) reaching a depth of 2500 m just beneath the mound O3 (located in Fig. 1C).

The presence of patchy high-amplitude zones (yellow to red) near the hydrate stability zone with low amplitudes below (grey) suggest the presence of free gas with a gas-water contact at different depths on either side of the channel. On the SW flank, we observe a gas column of 250 m. On the NE flank, the gas column is 530 m thick beneath the gas mounds (Fig. 2 & 4). The interpreted fluid contacts are supported by LWD log data from the two holes drilled in 2009 as part of JIP. Above the base of the hydrate stability zone in WR313-H, low gamma ray values and high sonic velocity and resistivity measurements (Appendix B1) are interpreted to indicate the presence of gas hydrate within sand. Downdip and below the base of the hydrate stability zone, low sonic velocity and resistivity measurements indicate the presence of water in sand in WR313-G (Appendix B2). Patchy, very high amplitude zones in the north (Fig. 4) are interpreted as stratigraphic traps either presently or previously filled with free gas.

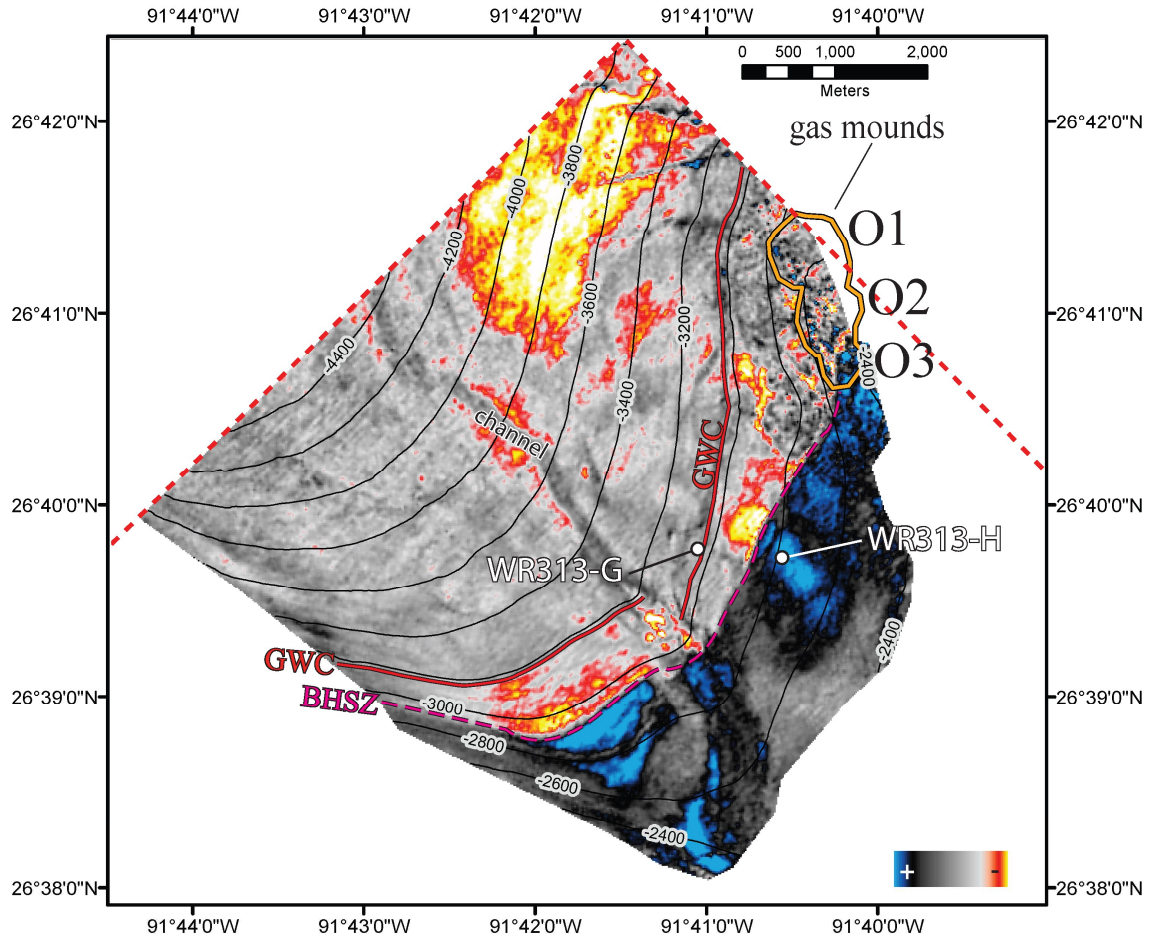

Figure 4. Amplitude map of the Orange sand, with outlines of the surficial gas mounds overlain. Blue-dark grey = hydrate-bearing sands; red-yellow = gas-bearing sands; light grey-white = water-bearing sands. A southeast-trending channel separates two gas-water contacts at different depths on different sides of the channel. The base of the hydrate stability zone, as interpreted by a bottom-simulating reflector, conforms to structure in the SW, but cuts across contours in the E, and leads directly to mound O3.

3.4.3 The Blue sand

The Blue sand also dips to the northwest with a synclinal geometry, but unlike the other mapped sands, there is not a clearly defined channel (Fig. 5). Compared to the other sands, the Blue sand is more poorly developed and therefore more poorly defined in seismic imaging. While overall the Blue sand is thicker, it has a lower net-to-gross and is

interpreted as distal sedimentation from a channel outside of our seismic data (Boswell et al., 2012b).

The boundary between the positive amplitudes (blue and black to dark grey) and the negative amplitudes (light grey to red and yellow) marks the base of the hydrate stability zone (pink dashed line in Fig. 5). In the east, the BHSZ parallels the structural contours at 3000 m (Fig. 5). However, in a similar fashion as to the other sands, the BHSZ rises 300 m near the gas mounds, reaching a depth of 2700 m just beneath the mound B4 (Fig. 5), while the seafloor only rises by ~100 m. Our interpretation of the BHSZ is supported by two wells that penetrated the Blue sand above the BHSZ (Appendix B), and found low gamma ray values and high sonic velocity and resistivity measurements that are interpreted as gas hydrate within coarse-grained sediment (Boswell et al., 2012b).

Below the base of the hydrate stability zone we observe very bright, negative amplitudes (yellow and red) beneath the gas mounds, which we interpret as free gas within the Blue sand (Fig. 5). Downdip, these amplitudes lose strength and abruptly dim out. We interpret this sudden decrease in amplitudes as marking the depth of the gas-water contact at 3050 m. In the west, we observe similar, though weaker negative amplitudes (red) that dim at ~3800 m. It is possible that this represents either a paleo gas-water-contact or stratigraphic variability, where brighter areas are more sand prone, and dimmer areas are more mud prone. It is also possible that the Blue sand is composed of two separate reservoirs that are divided by a flow restricting mud in the dim dark grey area central to the basin.

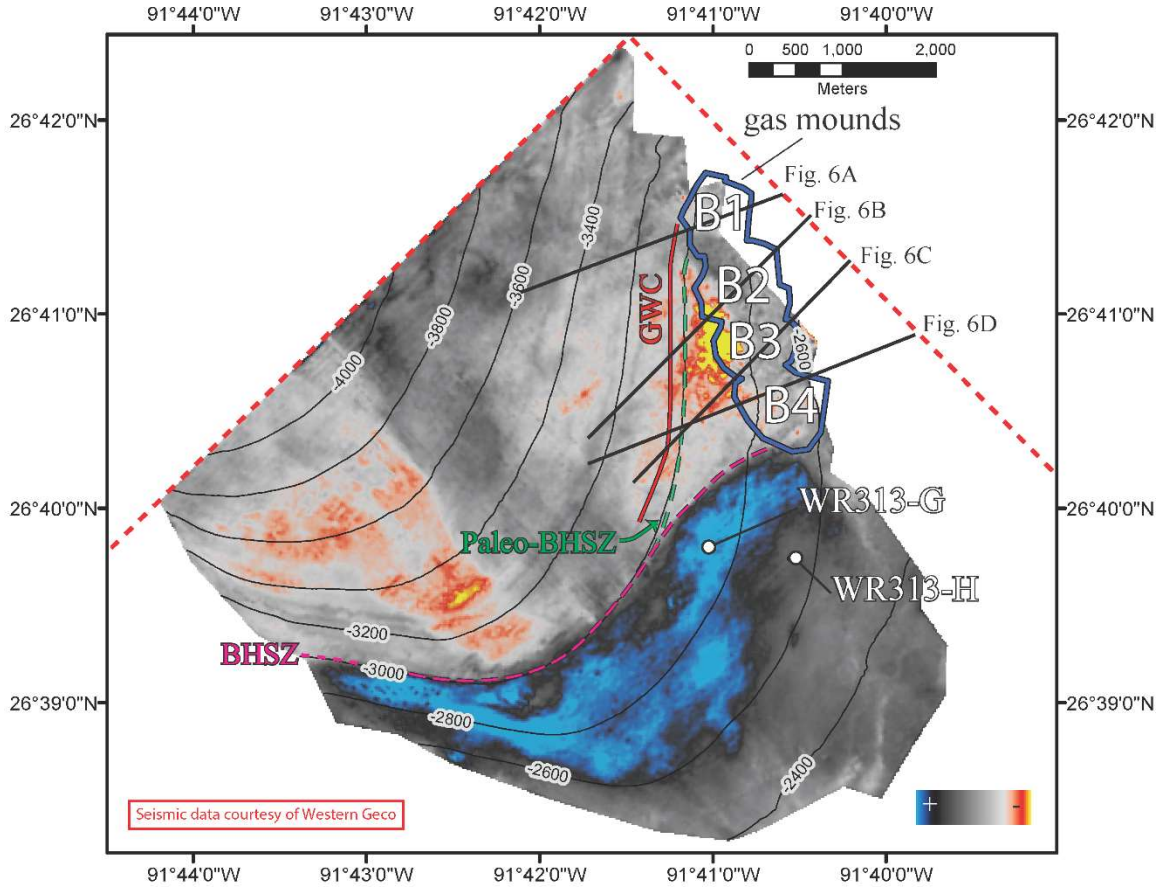

Figure 5. Amplitude map of the Blue sand. Blue-dark grey = hydrate-bearing sands; red-yellow = gas-bearing sands; light grey-white = water-bearing sands. The seafloor position of the eastern row of gas mounds is projected onto the maps, outlined in blue. The Base of hydrate stability zone (BHSZ) follows depth contours in the west and south, but becomes much shallower in the vicinity of the mounds, and leads directly to the center of mound B4. The dashed green line represents the expected BHSZ for the Blue sand, which points directly to the northernmost mound (B1).

3.4.4 Gas mounds

On the surface, the seafloor gas mounds are imaged as three adjacent rows of positive, high-amplitude, seismic anomalies trending in a NW-SE direction (Fig. 1C). The mounds rise approximately 100 m above the seafloor (Fig. 2). We do not observe

onlapping relationships from which we could infer the relative age of these mounds (Appendix B3).

Below the surface, a cone-shaped gas wipeout zone (GWZ in Fig. 2), defined as a blank seismic response, extends downwards 600-800 meters from the mounds. These blank zones connect the Blue, Orange, and Green sands with discrete overlying mounds (Fig. 2). At the root of the GWZ's, each sand is imaged by a strong negative polarity reflector (Fig. 2, Fig. 6, Fig. 7), implying the presence of a low-density phase such as free gas. We label the point at which the gas-sand meets the GWZ as the "gas crest" (Fig. 2), and we interpret that this is the leak point for the sands. The western-most row of gas mounds (B1 through B4 in Fig. 5) are the most clearly imaged in the subsurface (Fig. 6). Here, the gas wipeout zone extends 880 m downward to the Blue sand gas crest at the northern most location B1 (Fig. 6A). Moving southward along this row, the gas wipeout zone becomes progressively shallower (Fig 6B-C), and only extends 630 meters downward at location B4 (Fig. 6D).

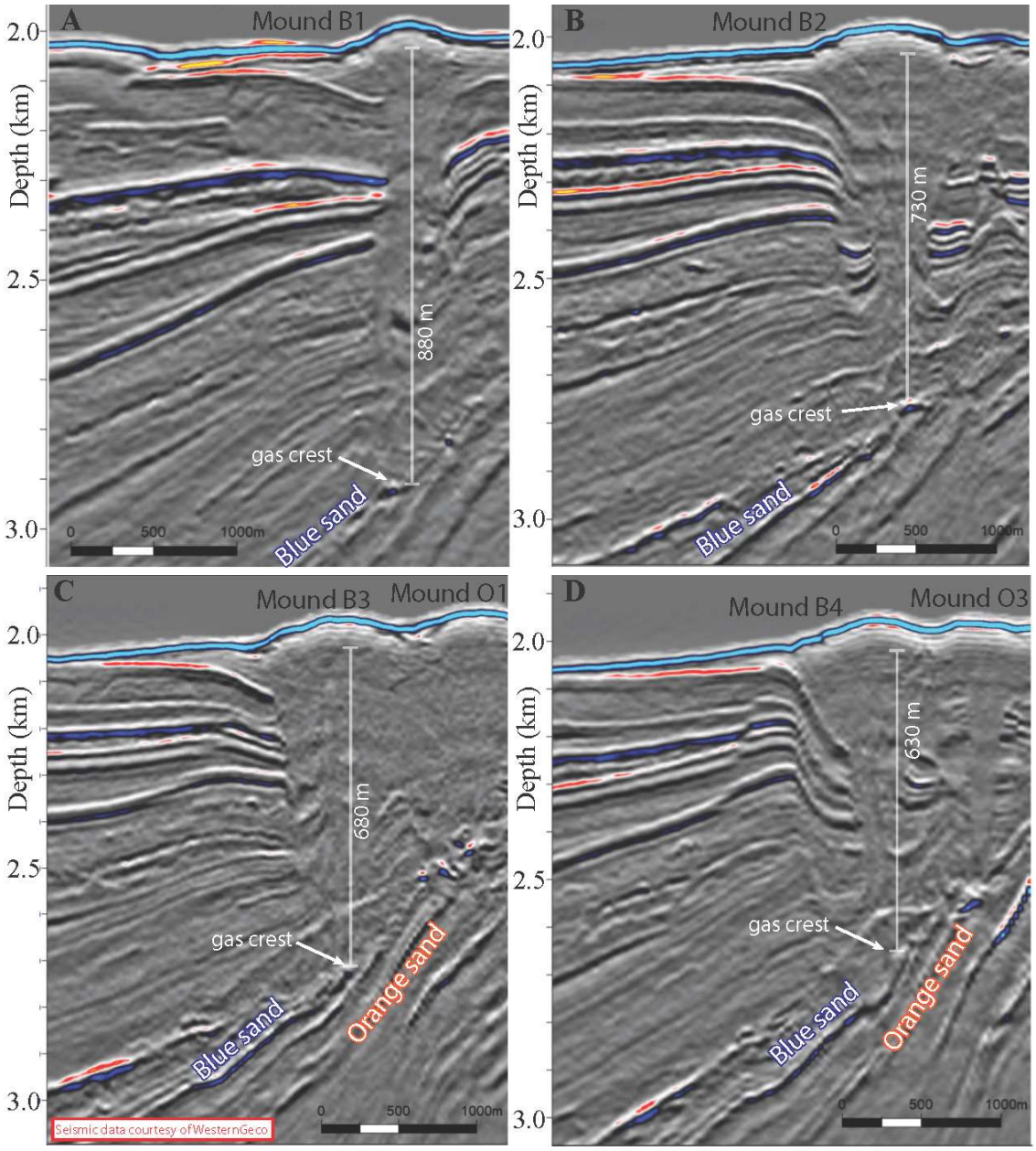

Figure 6. Seismic cross sections of gas mounds. A blank seismic response connects the gas mounds to individual sands below. The depth from the paleo seafloor to the crest of the gas sands is greatest in the northern mounds, and decreases with each mound to the south. See Figure 5 for location of each cross section. A. Cross section of mound B1. B. Cross section of mound B2. C. Cross section of mounds B3 and O1. D. Cross section of mounds B4 and O3. These seismic lines are located in Figure 5.

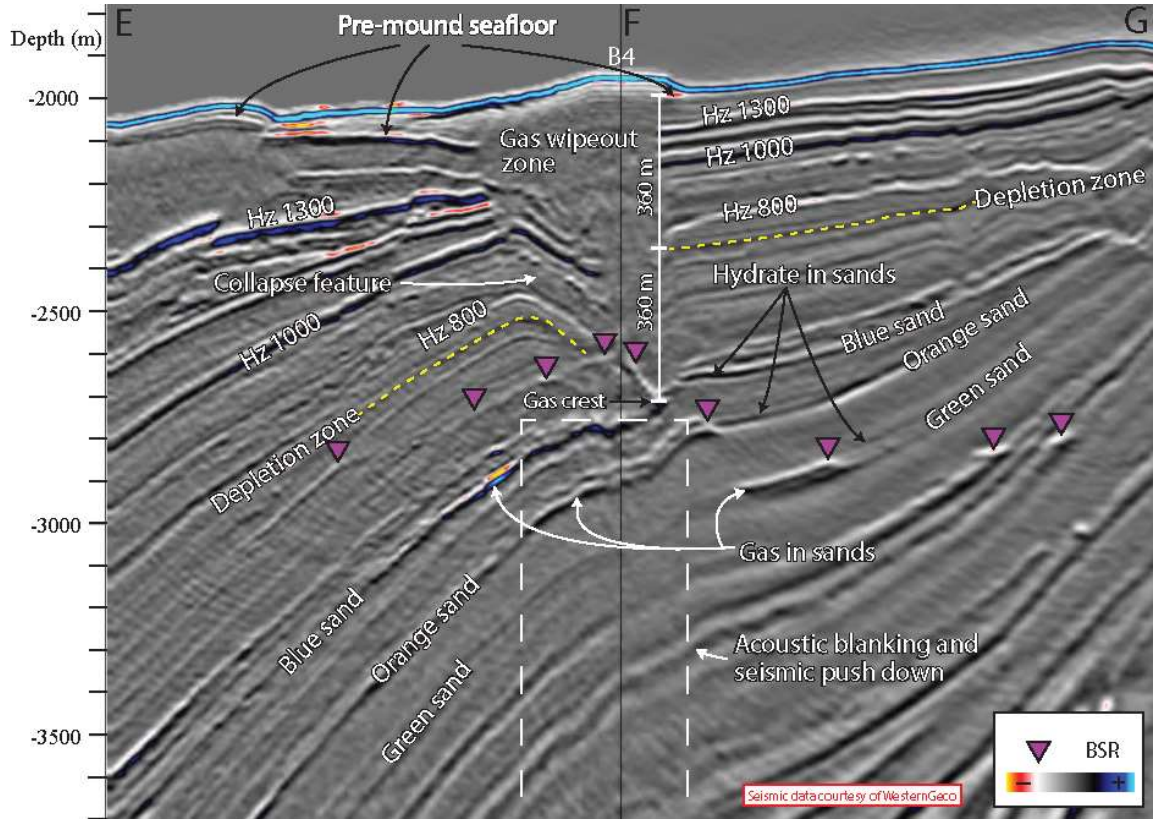

Figure 7. The base of the hydrate stabity zone is warped upwards below mound B4 and imaged by a pluming bottom-simulating reflector (BSR). The area beneath the mound is poorly imaged due to acoustic blanking and seismic pushdown, suggesting the presence of gas above. Fluids from the Blue sand are venting to the seafloor via the gas wipeout zone at the BSR. Directly updip from this leakpoint, we interpret the presence of hydrate in the Blue sand based on the positive acoustic impedence of the Blue sand reflector. A collapse feature is imaged beneath the mound and dips toward the center of the mound. The location for this cross section is shown in Figure 2.

Beneath the edges of the mounds, several stratal reflectors (Hz 800 – Hz 1300) dip steeply toward the center of the blank zone (Fig 7). Sometimes these reflectors are completely detached, with intact 100m-thick blocks that appear to have sunk up to 220 m. (Fig. 7). We interpret that these are collapse features that have resulted from the fluidization and removal of underlying sediment during venting of fluids from below.

Immediately below the collapse features is a depletion zone composed of non-hydrate bearing mudrock as imaged by the Gamma Ray and resistivity logs from the nearby exploration wells (Appendix B). The vertical distance between the seafloor and the top of the depletion zone is roughly the same as the vertical distance from the gas crest within the sand and the top of the depletion zone (Fig. 7). We interpret that in the area of the gas mounds, the sediment within the depletion zone was mobilized by the venting, rising fluids, and deposited onto the pre-mound seafloor. The removal of sediment from within the depletion zone led to subsidence, and formation of the collapse features in a manner similar to the that of calderas found at mud volcanoes (Kopf, 2008; Rudolph et al., 2011). In addition to authigenic carbonate, hydrate, and chemosynthetic communities, the gas mounds in the Terrebonne Basin are also formed from the extruded, fine-grained material of the depletion zone. Structurally and compositionally, the gas mounds in the Terrebonne Basin are therefore similar to seafloor mounds (Benjamin and Huuse, 2017) and mud volcanoes (Evans et al., 2007) found in other overpressured sedimentary basins.

3.4.5 Hydrate stability zone

The thickness of the hydrate stability zone ranges from 100m to 1000m (Fig. 8). It is thickest in the center of the basin, and thins around the edges (Fig 8A). We interpret that the thinning of the hydrate stability zone in the south and east is the result of increased thermal gradient due to highly conductive, shallow salt, in a manner similar to that observed near salt structures in the Kwanza Basin (Serié et al., 2017). We interpret the anomalously thin hydrate stability zone in the north is related to the presence of warm,

possibly saline upward fluid flow beneath the gas mounds. In this area, the hydrate stability zone is thinnest directly beneath the southern Orange and Green mounds, where a pluming BSR rises sharply towards the seafloor (Fig. 8B).

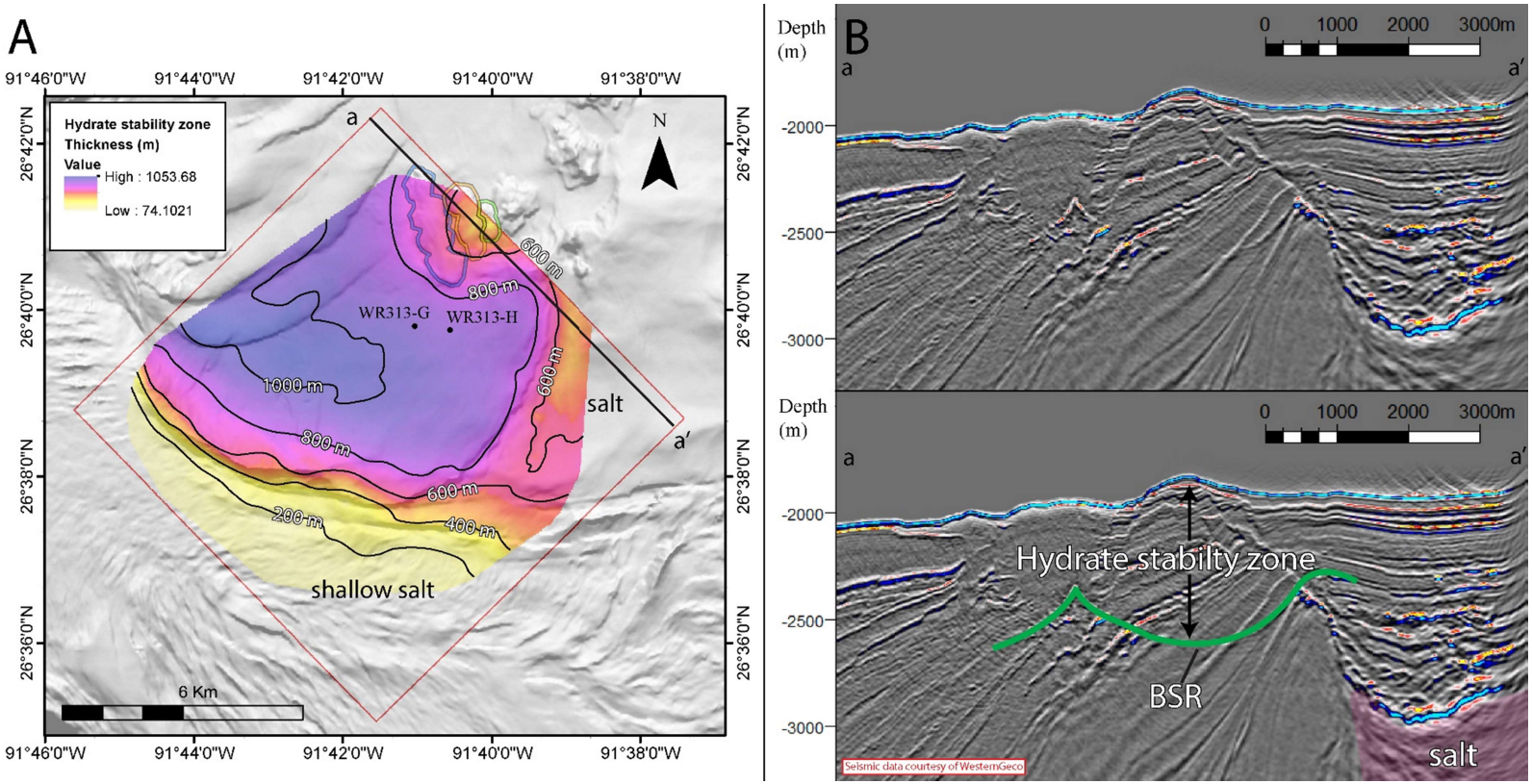
A
91°46'0"W
91°44'0"W
91°42'0"W
91°40'0"W
91°38'0"W
26°42'0"N
26°40'0"N
26°38'0"N
26°36'0"N
Hydrate stability zone
Thickness (m)
Value
High : 1053.68
Low : 74.1021
a
a′
N
WR313-G
WR313-H
600 m
800 m
1000 m
800 m
600 m
600 m
200 m
400 m
salt
shallow salt
6 Km
B
Depth (m)
0
1000
2000
3000m
-2000
-2500
-3000
Hydrate stabilty zone
BSR
salt
Seismic data courtesy of WesternGeco

Figure 8. (Previous page) A. The hydrate stability zone is thickest in the center of the basin, and thins drastically along the edges in the presence of shallow salt and the gas mounds. B. Uninterpreted (top) and interpreted (below) cross section showing a pluming BSR and thinning of the hydrate stability zone near the gas mounds in the north and shallow salt in the east.

3.4.6 Relationship of sands to gas mounds

We interpret that the three rows of gas mounds are rooted in the three hydrate-bearing sands because the gas wipeout zones terminate at the Green, Orange, and Blue sands (Fig. 2, 6, 7). The western-most row of gas mounds (B1-B4) is sourced from the stratigraphically shallowest (Blue) sand, the middle row of gas mounds (O1-O3) is sourced from the Orange sand, and the eastern-most row of gas mounds (G1-G2) is sourced from the stratigraphically deepest Green sands.

Recent venting is recorded by a pluming BSR, where the base of the hydrate stability zone is warped upwards below the southwestern vents (Fig. 7, 8). This is interpreted to represent localized areas where the hydrate stability zone is perturbed by rising fluids that are warmer, and, or, more saline than the surrounding rock. Because the BSR is shallowest beneath the mounds in the south, we interpret that these are the most recently active vents and that the northernmost mounds are the oldest (B1, O1, G1). McConnell and Kendall (2002) also suggested that the mounds to the south are the youngest based on the location of the highest surface amplitudes. We envision that before the mounds formed, the BHSZ was continuous along contours across the basin, similar to the position of the BSR in the southwest today. Sequential venting of each row of gas mounds (starting at B1, O1, and G1) progressively pushed the BSR to a shallower position, until the base of the hydrate stability zone reached the position where we observe it today.

3.4.7 Pressure conditions

We interpret that at the vent locations, pore pressures within the sands are converging on the least principal stress and inducing natural hydraulic fractures that are allowing the fluids to vent to the seafloor. This process has been documented in numerous locations including Hydrate Ridge (Tréhu et al., 2004), Blake Ridge (Flemings et al., 2003), the Gulf of Mexico (Reilly and Flemings, 2010; Seldon and Flemings, 2005), and offshore Brazil (Naruk et al., 2019). We estimate the gas and water pressure within the sand bodies. We assume that the gas pressure (u_g) at the vent location equals the least principal stress (σ_h):

$$u_g = \sigma_h \qquad \text{Eq. 1.}$$

We assume that the capillary pressure (u_{cgw}, the difference between the gas pressure (u_g) and the water pressure(u_w)), at the vent location is equal to the buoyancy force of the gas, or:

$$u_{cgw} = u_g - u_w = (\rho_w - \rho_g)gh \qquad \text{Eq. 2.}$$

g is the force of acceleration from gravity and h is the gas column height. At the gas-water contact, we assume $u_{cgw} = 0$.

Finally, we assume that the least principal stress is proportional to the water pressure in the sand.

$$\sigma_h = K_0(\sigma_v - u_w) + u_w \qquad \text{Eq. 3}$$

K_0 is the commonly termed the effective stress ratio and is found to range from 0.6 to 0.8 (Ladd et al., 1977).

We calculated the overburden stress (σ_v) by integrating the corrected bulk density log (Hillman et al., 2017) at WR313-G. We calculated the hydrostatic pressure by assuming a density of salt water (1.025 g/cm^3). Using the ideal gas law, we calculate the gas density to be 0.24965 g/cm^3, 0.25136 g/cm^3, and 0.25256 g/cm^3, for the Blue, Orange, and Green sand reservoirs, respectively, based on a temperature gradient of 18.1^{o}C/km, and pressures within the center of the gas reservoir.

Equations 1, 2, and 3 are solved simultaneously for the pore water pressure (u_w). The results for each reservoir are illustrated in Figure 9. We find a water-phase overpressure of 9.07 MPa for the Blue sand, 4.79 MPa for the Orange sand, and 2.85 MPa for the Green sand (Fig. 9).

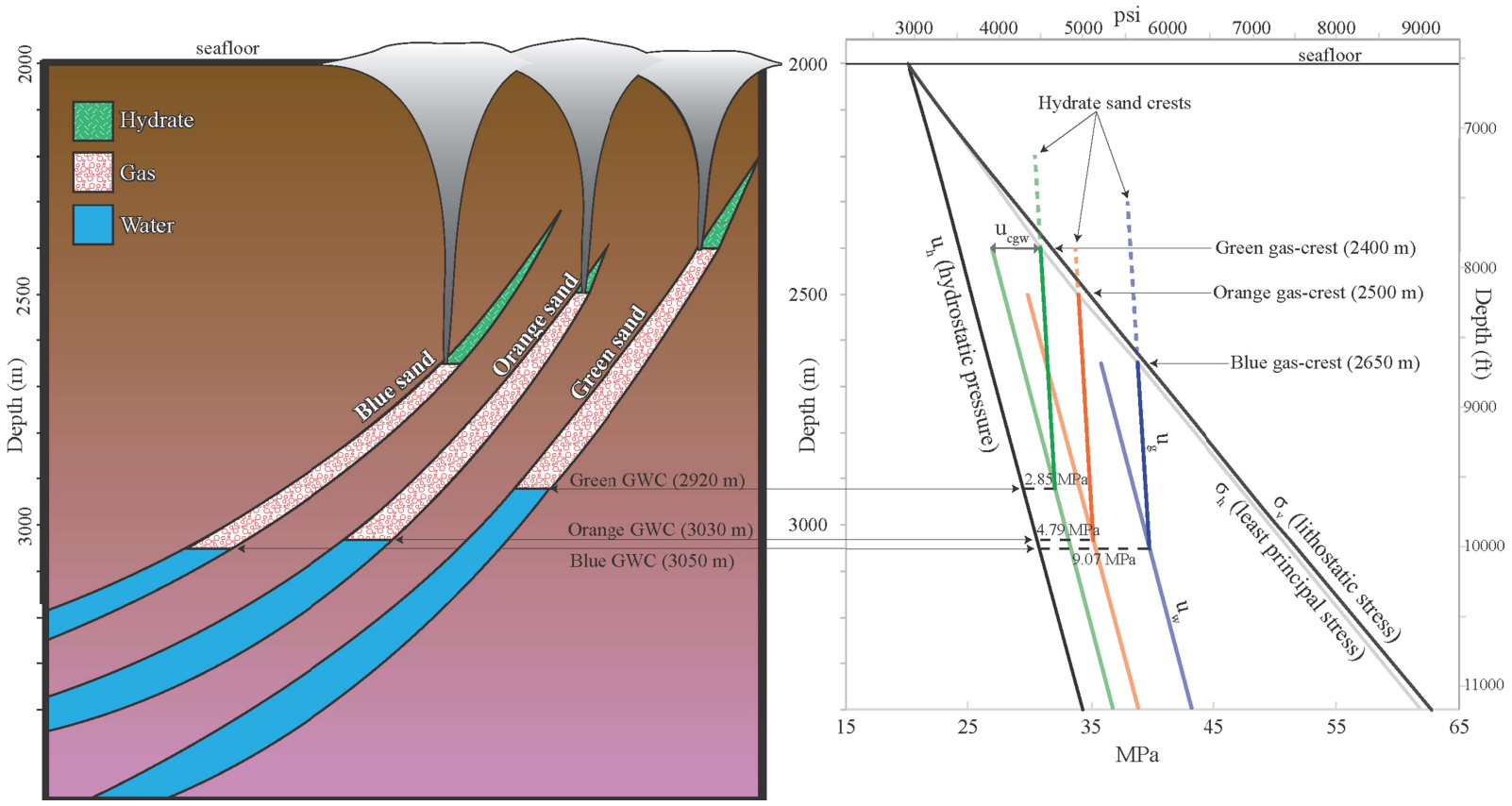
seafloor
Hydrate
Gas
Water
Blue sand
Orange sand
Green sand
Green GWC (2920 m)
Orange GWC (3030 m)
Blue GWC (3050 m)
Depth (m)
2000
2500
3000
psi
3000
4000
5000
6000
7000
8000
9000
seafloor
Hydrate sand crests
u_{cgw}
u_h (hydrostatic pressure)
Green gas-crest (2400 m)
Orange gas-crest (2500 m)
Blue gas-crest (2650 m)
u_g
2.85 MPa
4.79 MPa
9.07 MPa
u_w
σ_h (least principal stress)
σ_v (lithostatic stress)
Depth (ft)
7000
8000
9000
10000
11000
15
25
35
45
55
65
MPa

Figure 9. Pressure conditions within the dipping hydrate sands. The cartoon on the left is an idealized representation of the southernmost gas mounds, similar to Figure 2. The stratigraphically shallowest Blue sand is at greatest overpressure, while the deepest Green sand is at the lowest overpressure; This is due to the position of the gas crest within each sand relative to the seafloor.

3.5 DISCUSSION

3.5.1 Pressure controls

We interpret that fluids are venting from the Blue, Orange, and Green reservoirs at the gas-hydrate contact, which is the shallowest position of the hydrate-gas contact and the position where the gas column is thickest and the overburden is thinnest (Fig. 2, 8). As a result, the gas pressure converges on the least principal stress in the overlying mudrock, resulting in hydraulic fracturing and the expulsion of gas to the seafloor.

All three of the sands have similarly sized gas columns beneath the hydrate; however, they exhibit different overpressures. The Blue sand is the shallowest sand stratigraphically, yet is estimated to have the greatest overpressure (Fig. 9). The deeper sands have greater lateral extent and reach higher on the structure (Fig. 2), thereby having a greater overburden than the shallower sands. Seal failure occurs when the pore pressure converges on the least principal stress where overburden is thinnest. There is less overburden at the gas crest of the Green sand than at the same point for the Blue sand. Therefore, a lower pore pressure is required to reach the critical point at the Green sand than at the Blue sand. As a result, the Blue sand requires greater water pressure to reach the failure limit. While nonintuitive, this geometry and stress regime whereby the

shallower sand is under greater overpressure than the deeper sand, is not unique, and has been studied at other vent sites in the Gulf of Mexico (e.g. Seldon and Flemings, 2002).

Vertical expulsion at the hydrate-gas contact implies that it is easier for the gas to fracture the overlying seal than it is to migrate updip through the hydrate-bearing reservoir. We interpret that hydrate preferentially fills the largest pores available in the sand (e.g. Clennell et al., 1999), creating high concentrations of hydrate at the BHSZ, which results in capillary sealing at the hydrate-gas interface. Because the gas cannot enter the remaining small pores in the reservoir, the gas pressures builds until it hydraulically fractures the overlying mudrock directly at the hydrate-gas interface. The hydrate-bearing sands are interpreted to have a hydrate saturation of 80-90% based on log data (Collett et al., 2012) and Fang et al. (2020) show that in a similar hydrate reservoir, sands with this hydrate concentration will have a capillary entry pressure that results in a gas pressure that exceeds the fracture pressure.

3.5.2 Evolution of the venting system

We developed the following model to describe successive mound growth (Fig. 10). Initially, gas migrates updip through the sands by buoyancy until it reaches the base of the hydrate stability zone, at which point it forms high concentrations of gas hydrate (Fig. 10A). Once sufficient quantities of hydrate form, gas hydrate creates a seal at the gas-hydrate interface and precludes gas from rising further within the sand. As a result, gas pressure builds up below the seal until it reaches a critical pressure, upon which fractures dilate from the gas crest up to the seafloor, and fluid expulsion begins (Fig. 10B). The

warm rising fluids elevate the temperature in the surrounding sediments both vertically and laterally. As gas rises into the hydrate stability zone, hydrate forms and the exothermic reaction adds to the increase in temperature. Locally the BHSZ is now shallower than the regional BHSZ, and hydrate within the sand updip of the gas crest begins to dissociate (Fig. 10C). The impact of this is two-fold: First, the melting of the hydrate moves the seal to an updip position within the sand and creates a new gas crest; Second, because the new crest is shallower and with less overburden, a smaller amount of gas is required to reach the critical point of failure leading to the next generation of mound growth. With continued gas charge from depth, a new gas mound will now form above the new gas crest, and the process will start again (Fig. 10D). This process will result in a series of gas mounds from progressively shallower leak points determined by the local BHSZ, similar to our observations in the Terrebonne Basin. Since the seal is migrating closer to the surface with each expulsion, the gas pressures required to achieve venting become lower with each episode.

This model provides a conceptual view of how the venting location will move updip. However, it remains unclear as to why there appear to be distinct periods of venting before periodic shifts to the new updip locations. One possibility would be that the rate of venting outpaces the rate of gas recharging the reservoir, so that reservoir pressures drop to the point where the hydraulic fractures close. The heat related to the venting process continues to melt nearby hydrate while the gas pressure once again builds up, leading to the next venting episode.

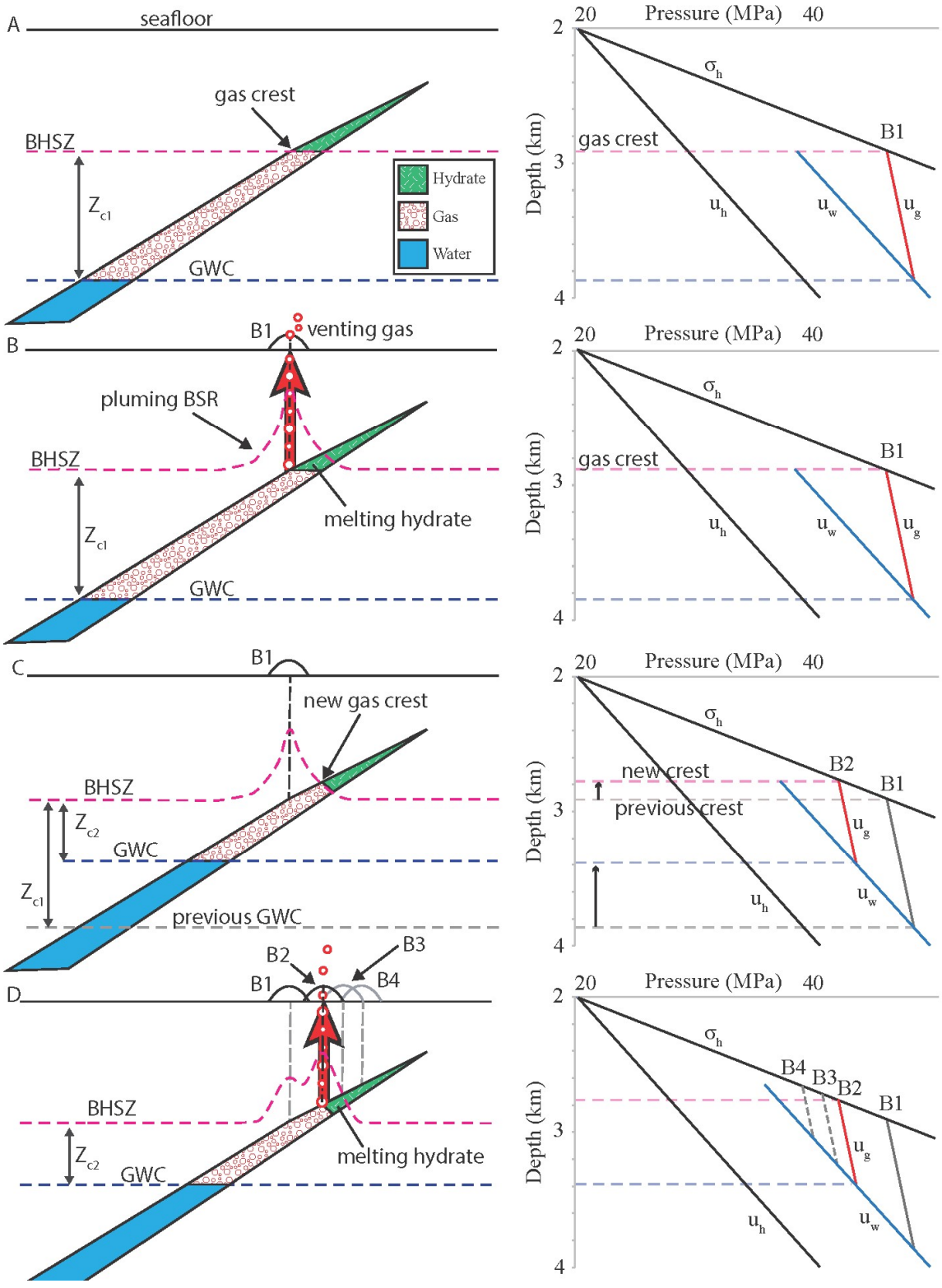
A
seafloor
gas crest
BHSZ
Z_{c1}
GWC
Hydrate
Gas
Water
B
B1
venting gas
pluming BSR
BHSZ
Z_{c1}
melting hydrate
GWC
C
B1
new gas crest
BHSZ
Z_{c2}
GWC
Z_{c1}
previous GWC
D
B2
B3
B1
B4
BHSZ
Z_{c2}
GWC
melting hydrate
20
Pressure (MPa)
40
2
3
4
Depth (km)
σ_h
gas crest
B1
u_h
u_w
u_g
new crest
previous crest
B2
B4
B3

Figure 10. Evolution of gas mounds. The leak point migrates up dip with time (A-D). Upward fluid migration causes the hydrate stability boundary to shift upward due to heat advected by rising fluids, heat generated by gas forming hydrate, and/or elevated salinity generated by hydrate formation. GWC = Gas-water contact. A. Gas builds up within a dipping sand at the Base of Hydrate Stability Zone (BHSZ). Z_{c1} is the height of the gas column required to reach critical pressure and breach the seal. B. Critical pressure is reached, and fluid expulsion begins. Warm rising fluids raise the local BHSZ in a lateral position. C. Updip hydrate dissociates, and a new gas crest is created at a shallower position. D. Pressure builds up again, and a new leak point is established at the new gas crest. A new gas mound is formed above an updip position in the sand. Due to a decrease in overburden at the updip position, a smaller gas column (Z_{g2}) is required to breach the seal and initiate fluid expulsion. Each successive eruption of fluid pushes the BHSZ to shallower depths within the hydrate sands.

Perturbations to the hydrate stability zone are crucial to the process outlined in the model above. The pluming BSR observed below the gas mounds (Fig. 7, 8) is a direct observation of the dynamics of a shifting hydrate stability zone. Similar anomalies have been observed in the Lower Congo Basin (Gay et al., 2007), offshore Angola (Serié et al., 2017), and elsewhere in the Gulf of Mexico (Shedd et al., 2012; Smith et al., 2014). These phenomena are often explained by the effects of warm and salty fluids rising from depths; however, hydrate formation may cause similar effects. As gas enters the hydrate stability zone, the exothermic formation of hydrate will increase heat and salinity within the system (Liu and Flemings, 2006). The upward warping of the BSR in the Terrebonne Basin is likely due to a combination of these effects.

3.5.3 Implications of a dynamic hydrate seal

5-22% of the world's organic carbon is trapped as gas hydrate (Ruppel and Kessler, 2017) and most of this massive carbon reservoir lies in the deep ocean. This layer interacts with the Earth's ocean and, occasionally, the atmosphere. The size of this reservoir and its

dynamic nature has focused the community on the role of the hydrate system in the carbon cycle. In many locations above concentrated methane hydrate deposits, methane vents into the overlying ocean where it is either oxidized, resulting in potential for ocean acidification, or, under very rare occasions, the methane reaches the atmosphere.

We show how methane bypasses the hydrate stability zone and is vented at the seafloor through hydraulic fracturing and we show how hydrate acts as an ephemeral reservoir that first stores and then releases methane at the seafloor. Drastic bottom-water warming is not needed to initiate dissociation and venting from gas hydrate reservoirs. Instead, within dipping, hydrate-sealed reservoirs, an initial venting episode from naturally built up critical pressure may lead to further venting episodes as the dissociated hydrate forms a new, shallower crest with a reduced overburden. This implies a dynamic evolution, whereby hydrate reservoirs are both created and destroyed through geological time.

3.6 CONCLUSIONS

Within the dipping sands of the Terrebonne Basin, gas is trapped below the base of hydrate stability by a seal of highly concentrated gas hydrate. Each of the three sets of sands is connected to an overlying row of seafloor mounds that have been created by fluid expulsion. We estimate the pore pressures within the sands by interpreting the presence of gas in seismic data and assuming that expulsion occurs when a critical pressure is reached. The stratigraphically shallower sands are more overpressured than the deeper sands as a result of the stratigraphically deeper sands extending closer to the seafloor. The leak point for these sands is not the crest of the sand, but rather the pressure-, temperature-, and

salinity-dependent point at the base of the hydrate stability zone, where the gas pressures are highest. Pore pressures in the sands build until they converge on the least principal stress, at which point natural hydraulic fractures connect to the seafloor and fluids escape.

The formation of hydrate, as well as the warm and salty escaping fluids alter the position of the hydrate stability zone nearby. This process melts updip hydrate, and creates a new shallower seal in the sand above which a new seafloor mound will be created when critical pressure is once again reached. The result is that a significant amount of the methane stored as hydrate is expelled to the ocean floor. This model may be applied to understanding the genesis and orientation of rows of seafloor gas mounds, as well as the pressures and stresses within other high-relief, deepwater basins with gas and hydrate-bearing sands.

The interplay between adjoining gas and hydrate reservoirs is complex. Hydrate reservoirs are both created and then destroyed through geologic time just by the process of gas charging and venting. Hydrate dissociation does not just depend on temperature perturbations, but may occur naturally from the venting of connected, critically pressured gas reservoirs. This suggests that the role of hydrates in the carbon cycle is even more dynamic than previously envisioned.

ACKNOWLEDGEMENTS

We thank Christian Berndt and Mads Huuse for their constructive reviews that helped to improve the quality of the manuscript, and Lawrence Coogin for editorial handling. We also thank Western Geco for access to the 3D seismic data.

FUNDING

This material is based upon work supported by the Department of Energy under Award Number and DE-FE0023919. This report was prepared as an account of work sponsored by an agency of the United States Government. Neither the United States Government nor any agency thereof, nor any of their employees, makes any warranty, express or implied, or assumes any legal liability or responsibility for the accuracy, completeness, or usefulness of any information, apparatus, product, or process disclosed, or represents that its use would not infringe on privately owned rights. Reference herein to any specific commercial product, process, or service by trade name, trademark, manufacturer, or otherwise does not necessarily constitute or imply its endorsement, recommendation, or favoring by the United States Government or any agency thereof. The views and opinions of authors expressed herein to not necessarily state or reflect those of the United States Government or any agency thereof.

REFERENCES

Andresen, K. J., 2012, Fluid flow features in hydrocarbon plumbing systems: What do they tell us about the basin evolution?: Marine Geology, v. 332, p. 89-108.

Benjamin, U. K., and Huuse, M., 2017, Seafloor and buried mounds on the western slope of the Niger Delta: Marine and Petroleum Geology, v. 83, p. 158-173.

Boswell, R., Collett, T. S., Frye, M., Shedd, W., McConnell, D. R., and Shelander, D., 2012a, Subsurface gas hydrates in the northern Gulf of Mexico: Marine and Petroleum Geology, v. 34, no. 1, p. 4-30.

Boswell, R., Frye, M., Shelander, D., Shedd, W., McConnell, D. R., and Cook, A., 2012b, Architecture of gas-hydrate-bearing sands from Walker Ridge 313, Green canyon 955, and Alaminos canyon 21: northern deepwater Gulf of Mexico: Marine and Petroleum Geology, v. 34, no. 1, p. 134-149.

Cartwright, J., Huuse, M., and Aplin, A., 2007, Seal bypass systems: AAPG Bulletin, v. 91, no. 8, p. 1141-1166.

Cartwright, J., and Santamarina, C., 2015, Seismic characteristics of fluid escape pipes in sedimentary basins: Implications for pipe genesis: Marine and Petroleum Geology, v. 65, p. 126-140.

Ceramicola, S., Dupré, S., Somoza, L., and Woodside, J., 2018, Cold seep systems, Submarine geomorphology, Springer, p. 367-387.

Clennell, M. B., Hovland, M., Booth, J. S., Henry, P., and Winters, W. J., 1999, Formation of natural gas hydrates in marine sediments: 1. Conceptual model of gas hydrate growth conditioned by host sediment properties: Journal of Geophysical Research: Solid Earth, v. 104, no. B10, p. 22985-23003.

Collett, T. S., and Boswell, R., 2012, Resource and hazard implications of gas hydrates in the Northern Gulf of Mexico: Results of the 2009 Joint Industry Project Leg II Drilling Expedition: Marine and Petroleum Geology, v. 34, no. 1, p. 1-3.

Collett, T. S., Lee, M. W., Zyrianova, M. V., Mrozewski, S. A., Guerin, G., Cook, A. E., and Goldberg, D. S., 2012, Gulf of Mexico Gas Hydrate Joint Industry Project Leg II logging-while-drilling data acquisition and analysis: Marine and Petroleum Geology, v. 34, no. 1, p. 41-61.

Cook, A. E., Anderson, B. I., Rasmus, J., Sun, K., Li, Q., Collett, T. S., and Goldberg, D. S., 2012, Electrical anisotropy of gas hydrate-bearing sand reservoirs in the Gulf of Mexico: Marine and Petroleum Geology, v. 34, no. 1, p. 72-84.

Crutchley, G. J., Kroeger, K. F., Pecher, I. A., and Gorman, A. R., 2018, How tectonic folding influences gas hydrate formation: New Zealand's Hikurangi subduction margin: Geology, v. 47, no. 1, p. 39-42.

Dewangan, P., Sriram, G., Kumar, A., Mazumdar, A., Peketi, A., Mahale, V., Reddy, S. S. C., and Babu, A., 2021, Widespread occurrence of methane seeps in deep-water regions of Krishna-Godavari basin, Bay of Bengal: Marine and Petroleum Geology, v. 124, p. 104783.

Etiope, G., 2012, Climate science: Methane uncovered: Nat. Geosci., v. 5, p. 373-374.

Evans, R. J., Davies, R. J., and Stewart, S. A., 2007, Internal structure and eruptive history of a kilometre-scale mud volcano system, South Caspian Sea: Basin Research, v. 19, no. 1, p. 153-163.

Fang, Y., Flemings, P. B., Daigle, H., Phillips, S. C., Meazell, P. K., and You, K., 2020, Petrophysical properties of the Green Canyon Block 955 hydrate reservoir inferred from reconstituted sediments: Implications for hydrate formation and production: AAPG Bulletin, v. 104, no. 9, p. 1997-2028.

Flemings, P. B., 2021, A Concise Guide to Geopressure: Origin, Prediction, and Applications, Cambridge University Press.

Flemings, P. B., Liu, X., and Winters, W. J., 2003, Critical pressure and multiphase flow in Blake Ridge gas hydrates: Geology, v. 31, no. 12, p. 1057-1060.

Foschi, M., Cartwright, J. A., MacMinn, C. W., and Etiope, G., 2020, Evidence for massive emission of methane from a deep-water gas field during the Pliocene: Proceedings of the National Academy of Sciences, v. 117, no. 45, p. 27869-27876.

Frye, M., Shedd, W., and Boswell, R., 2012, Gas hydrate resource potential in the Terrebonne Basin, Northern Gulf of Mexico: Marine and Petroleum Geology, v. 34, no. 1, p. 150-168.

Gay, A., Lopez, M., Berndt, C., and Séranne, M., 2007, Geological controls on focused fluid flow associated with seafloor seeps in the Lower Congo Basin: Marine Geology, v. 244, no. 1, p. 68-92.

Hovland, M., Gallagher, J., Clennell, M., and Lekvam, K., 1997, Gas hydrate and free gas volumes in marine sediments: Example from the Niger Delta front: Marine and Petroleum Geology, v. 14, no. 3, p. 245-255.

Judd, A., and Hovland, M., 2009, Seabed fluid flow: the impact on geology, biology and the marine environment, Cambridge University Press.

Kopf, A. J., 2008, Making calderas from mud: Nature Geoscience, v. 1, no. 8, p. 500-501.

Kvenvolden, K. A., and Rogers, B. W., 2005, Gaia's breath—global methane exhalations: Marine and Petroleum Geology, v. 22, no. 4, p. 579-590.

Lee, M., and Collett, T., 2012, Pore-and fracture-filling gas hydrate reservoirs in the Gulf of Mexico gas hydrate joint industry project leg II Green Canyon 955 H well: Marine and Petroleum Geology, v. 34, no. 1, p. 62-71.

Liu, X., and Flemings, P. B., 2006, Passing gas through the hydrate stability zone at southern Hydrate Ridge, offshore Oregon: Earth and Planetary Science Letters, v. 241, no. 1-2, p. 211-226.

Loher, M., Marcon, Y., Pape, T., Römer, M., Wintersteller, P., dos Santos Ferreira, C., Praeg, D., Torres, M., Sahling, H., and Bohrmann, G., 2018, Seafloor sealing, doming, and collapse associated with gas seeps and authigenic carbonate structures at Venere mud volcano, Central Mediterranean: Deep Sea Research Part I: Oceanographic Research Papers, v. 137, p. 76-96.

McConnell, D. R., and Kendall, B. A., 2002, Images of the Base of Gas Hydrate Stability, Northwest Walker Ridge, Gulf of Mexico, Offshore Technology Conference: Houston, Texas, Offshore Technology Conference, p. 10.

McConnell, D. R., Zhang, Z., and Boswell, R., 2012, Review of progress in evaluating gas hydrate drilling hazards: Marine and Petroleum Geology, v. 34, no. 1, p. 209-223.

Naruk, S. J., Solum, J. G., Brandenburg, J. P., Origo, P., and Wolf, D. E., 2019, Effective stress constraints on vertical flow in fault zones: Learnings from natural CO2 reservoirs: AAPG Bulletin, v. 103, no. 8, p. 1979-2008.

Paganoni, M., Cartwright, J. A., Foschi, M., Shipp, C. R., and Van Rensbergen, P., 2018, Relationship between fluid-escape pipes and hydrate distribution in offshore Sabah (NW Borneo): Marine Geology, v. 395, p. 82-103.

Reilly, M. J., and Flemings, P. B., 2010, Deep pore pressures and seafloor venting in the Auger Basin, Gulf of Mexico: Basin Research, v. 22, no. 4, p. 380-397.

Roberts, H. H., 2001, Fluid and gas expulsion on the northern Gulf of Mexico continental slope: mud-prone to mineral-prone responses: Washington DC American Geophysical Union Geophysical Monograph Series, v. 124, p. 145-161.

Roberts, H. H., Feng, D., and Joye, S. B., 2010, Cold-seep carbonates of the middle and lower continental slope, northern Gulf of Mexico: Deep Sea Research Part II: Topical Studies in Oceanography, v. 57, no. 21, p. 2040-2054.

Rudolph, M. L., Karlstrom, L., and Manga, M., 2011, A prediction of the longevity of the Lusi mud eruption, Indonesia: Earth and Planetary Science Letters, v. 308, no. 1, p. 124-130.

Ruppel, C. D., and Kessler, J. D., 2017, The interaction of climate change and methane hydrates: Reviews of Geophysics, v. 55, no. 1, p. 126-168.

Sain, K., Minshull, T. A., Singh, S. C., and Hobbs, R. W., 2000, Evidence for a thick free gas layer beneath the bottom simulating reflector in the Makran accretionary prism: Marine Geology, v. 164, no. 1, p. 3-12.

Seldon, B., and Flemings, P. B., 2005, Reservoir pressure and seafloor venting: Predicting trap integrity in a Gulf of Mexico deepwater turbidite minibasin: AAPG bulletin, v. 89, no. 2, p. 193-209.

Serié, C., Huuse, M., Schødt, N. H., Brooks, J. M., and Williams, A., 2017, Subsurface fluid flow in the deep-water Kwanza Basin, offshore Angola: Basin Research, v. 29, no. 2, p. 149-179.

Shedd, W., Boswell, R., Frye, M., Godfriaux, P., and Kramer, K., 2012, Occurrence and nature of “bottom simulating reflectors” in the northern Gulf of Mexico: Marine and Petroleum Geology, v. 34, no. 1, p. 31-40.

Sloan Jr, E. D., and Koh, C. A., 2007, Clathrate hydrates of natural gases, CRC press.

Smith, A. J., Flemings, P. B., Liu, X., and Darnell, K., 2014, The evolution of methane vents that pierce the hydrate stability zone in the world's oceans: Journal of Geophysical Research: Solid Earth, v. 119, no. 8, p. 6337-6356.

Talukder, A. R., 2012, Review of submarine cold seep plumbing systems: leakage to seepage and venting: Terra Nova, v. 24, no. 4, p. 255-272.

Tréhu, A. M., Flemings, P. B., Bangs, N. L., Chevallier, J., Gràcia, E., Johnson, J. E., Liu, C. S., Liu, X., Riedel, M., and Torres, M. E., 2004, Feeding methane vents and gas hydrate deposits at south Hydrate Ridge: Geophysical Research Letters, v. 31, no. 23.

Van Rensbergen, P., Depreiter, D., Pannemans, B., Moerkerke, G., Van Rooij, D., Marsset, B., Akhmanov, G., Blinova, V., Ivanov, M., and Rachidi, M., 2005, The El Arraiche mud volcano field at the Moroccan Atlantic slope, Gulf of Cadiz: Marine Geology, v. 219, no. 1, p. 1-17.

Chapter 4: Rapid sedimentation in the deepwater GOM: implications for subsurface temperature, overpressure, hydrate formation, and venting

ABSTRACT

Rapid sedimentation and the formation of methane hydrate within permeable, dipping layers combine to elevate pore pressures that converge on the least principal stress in the Terrebonne Basin on the northern Gulf of Mexico, USA. We use geologic mapping of public 2D seismic data and geomechanical properties of similar hydrate reservoirs to model the evolution of pressure and temperature in the Terrebonne Basin

in Petromod 2020. We find that due to rapid sedimentation, present-day pore pressures in dipping sands may be nearly 4 MPa. With the addition of biogenic gas, hydrate within the sands restricts fluid flow and may increase fluid overpressure by greater than twofold to 9.3 MPa. The buildup of pore pressure leads to negative effective stress and venting at the gas-to-hydrate phase boundary. This study shows how in addition to rapid sedimentation, the hydrate phase boundary exhibits remarkable control over pore pressures in high-relief deepwater basins.

4.1 INTRODUCTION

Elevated pore pressures are common in the subsurface Gulf of Mexico (Finkbeiner et al., 2001; Reilly and Flemings, 2010; Seldon and Flemings, 2005). Increases in pore pressure can arise from compressive stress, changes in the volume of fluid or rock matrix, or buoyancy and fluid movement (Osborne and Swarbrick, 1997). In rapidly forming basins, elevated pore pressures are driven by disequilibrium compaction; the sedimentation

rate outpaces the draining of pore fluids, resulting in pore pressures greater than hydrostatic (Osborne and Swarbrick, 1997).

The presence of a dipping, permeable sand layer within overpressured, low-permeability, mudrock can redistribute basin-wide pore pressures (England et al., 1987; Gao and Flemings, 2017; Flemings et al., 2002; Yardley and Swarbrick, 2000). The pressure gradient within the mudrock is greater than that within the dipping sand layer, and this pressure differential drives fluid flow from deep in the basin into the permeable layer at its base, and out near its crest.

When pore pressures within the dipping sand rise to the point whereby they converge on the least principle stress, venting to the seafloor is initiated via hydraulic fracturing (Cartwright et al., 2007; Reilly and Flemings, 2010). In the absence of preexisting faults or fractures, venting will occur at the crest of the permeable layer.

In high-pressure and low-temperature environments such as deepwater marine systems, fluid expulsion features are commonly associated with methane hydrate (e.g., Crutchley et al., 2010; Dewangan et al., 2021; Loher et al., 2018; Paganoni et al., 2018; Serié et al., 2017). Methane hydrate is an energy-dense ice-like crystalline solid composed of a single methane molecule trapped inside a cage of water molecules (Sloan and Koh, 2007). Due to increasing subsurface temperatures with depth, methane hydrate is only found in the upper 100's of meters of subsurface sediment. The maximum depth at which hydrate can exist is the Base of the Hydrate Stability Zone (BHSZ); below this point methane and water will coexist separately as gas and water. In porous media, methane

hydrate reduces permeability and restricts fluid flow (Clennell et al., 1999). In nature, methane hydrate is common in the deepwater shallow subsurface (Boswell et al., 2014).

While there is a clear connection between hydrate and venting in deepwater basins, we do not fully understand the role of methane hydrate in the generation of elevated pore pressures. Meazell and Flemings (In revision) illustrate the connection between gas- and hydrate-bearing sands to seafloor vents in the Terrebonne Basin, northern Gulf of Mexico, and they predict elevated pore pressures in the shallow subsurface that arise from a highly-concentrated hydrate restricting fluid flow at the gas-to-hydrate phase boundary.

To better understand the role of hydrate in the generation of overpressure, we broaden the studies of the subsurface Terrebonne Basin. We extend the mapping of permeable sands in the Terrebonne Basin with 2D public seismic data. We investigate the compressibility and compaction of similarly-aged, deepwater sediments, and we create a 2D basin model in PetroMod 2020 to explore the impact of hydrate on overpressure and fluid flow. We use these results to explore the evolution of temperature and pore pressures in response to rapid sedimentation and a dynamic hydrate phase boundary.

4.2 Background Geology

The Terrebonne Basin is a salt-withdrawal mini-basin located in the Walker Ridge province of the northern Gulf of Mexico, approximately 150 miles southwest of New Orleans. The water depth ranges from 1900-2200 meters. Within the northern part of the basin, there has been little public research; however, the southwestern flank of the basin (red box in Fig 1) has been the focus for numerous studies of gas hydrate (Boswell et al.,

2012a; Frye et al., 2012; Hillman et al., 2017; McConnell and Kendall, 2002) and seafloor cold seeps (Roberts et al., 2010a; Roberts et al., 2010b).

In the southern basin, three Pleistocene sands are found in the shallow subsurface (Boswell et al., 2012b; Frye et al., 2012). These sands are bowl-shaped, and they dip towards the north (Meazell and Flemings, In revision). We use publicly available 2D seismic reflection data from the BOEM to extend our geologic interpretation of the sand bodies to the full extent of the basin to the north.

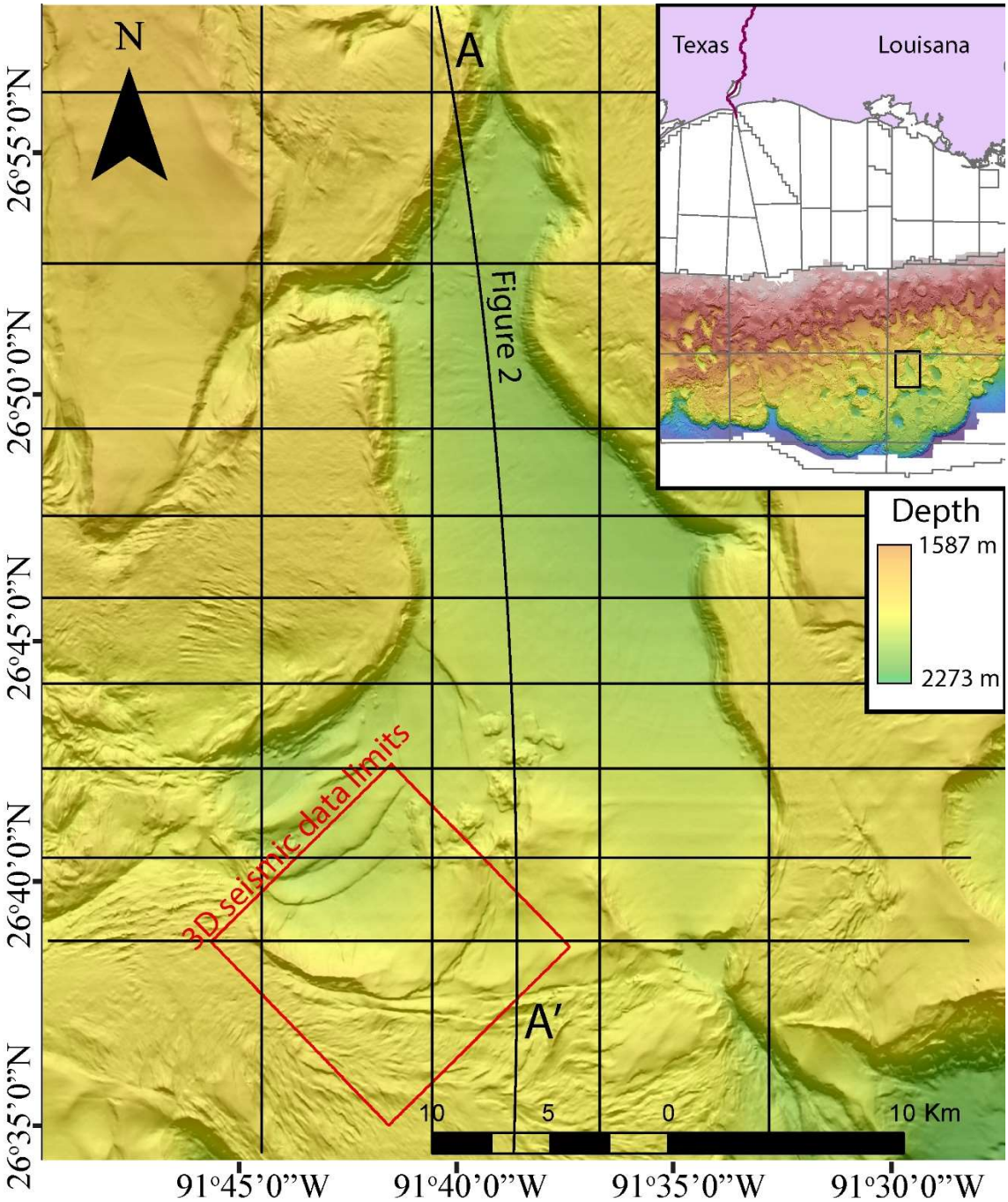

Figure 1. Overview of the Terrebonne Basin. A. Bathymetry of the Terrebonne Basin. The red diamond is the extent of our 3D seismic data set. Black lines are 2D seismic sections.

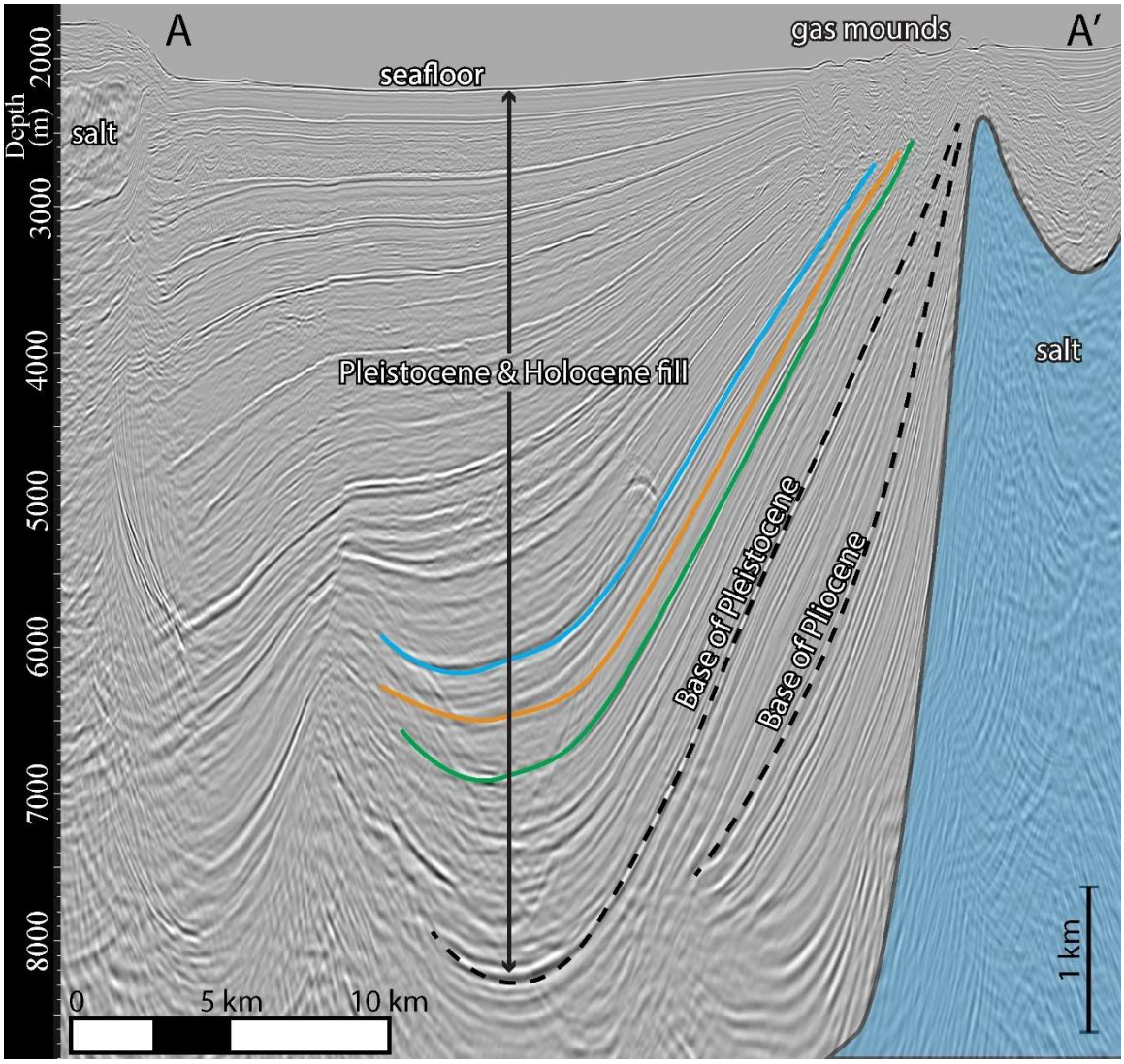

Figure 2. Strata in the Terrebonne Basin dip to the north, reaching depths up to 8,000 meters below sealevel. Blue, orange, and green lines represent the respective mapped sands in the basin. Time lines for the base of the Pleistocene and Pliocene are inferred from micropaleontological data from WR313-001. Seismic data provided by ION Geophysical.

4.3 Data and Methods

4.3.1 Seismic data

The seismic data sets include a 3D, depth-converted seismic cube in the southwest (red box in Fig. 1), several publicly available 2D seismic lines (black lines in Fig. 1), and

a 2D industry seismic line in time and depth spanning the basin from north to south provided by Ion Geophysical (Fig. 2, located in Fig. 1).

4.3.2 Sand maps

The Blue, Green, and Orange sands in the south continue into the northern Terrebonne Basin (Fig. 3). The sands all have a similar structure; they are shallowest in the south and dip to the west-northwest and north. The deepest part of the sands is in the northeast, where the sand bodies are bowl-shaped. The Blue sand is stratigraphically the shallowest, and reaches minimum and maximum depth of 2200 m and 7300 m, respectively (Fig. 3A). The Orange sand reaches a minimum and maximum depth of 2400 m and 7800 m, respectively (Fig. 3B). The Green sand is stratigraphically the deepest, and reaches a minimum and maximum depth of 2450 and 8000 m, respectively (Fig. 3C). In the north, the sands onlap onto a deep salt diapir. In the south, the sands are capped by an angular unconformity as they rise near the seafloor. Poor imaging due to a shallow salt canopy obscures the eastern and western limits of the sands, where they may reach greater depths.

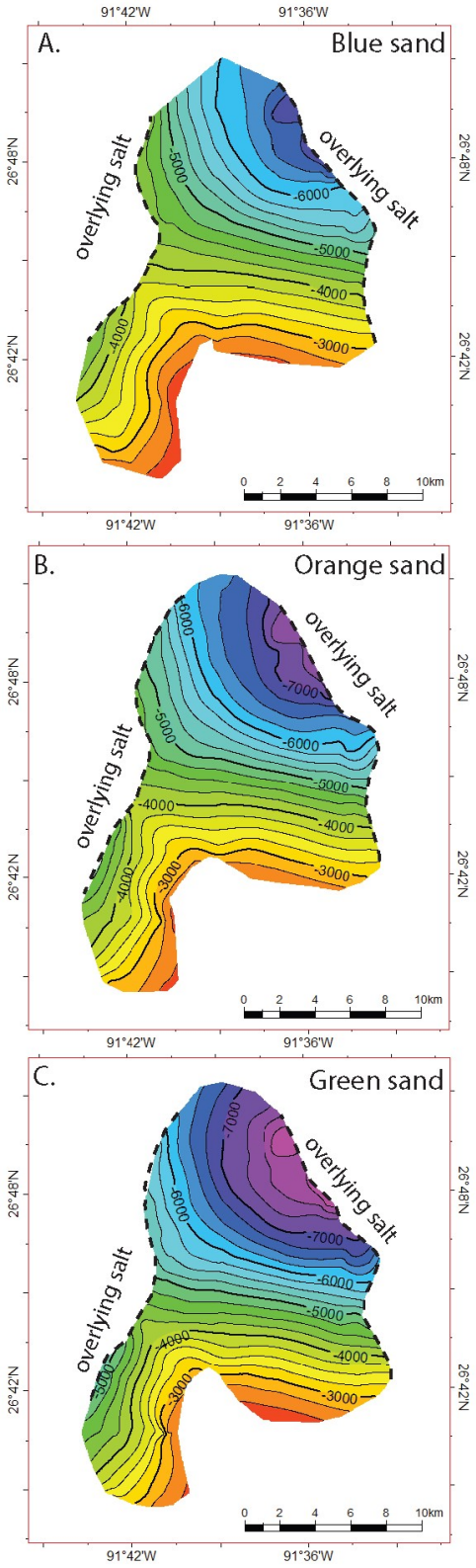
A.
Blue sand
overlying salt
overlying salt
-5000
-6000
-5000
-4000
-3000
-4000
-4000
91°42'W
91°36'W
26°48'N
26°42'N
0 2 4 6 8 10km
B.
Orange sand
overlying salt
overlying salt
-6000
-7000
-5000
-6000
-5000
-4000
-4000
-4000
-3000
-3000
C.
Green sand
overlying salt
overlying salt
-7000
-6000
-7000
-6000
-5000
-4000
-4000
-3000
-3000

Figure 3. (Previous page) Structure maps of the major sands within the Terrebonne basin. Contour lines are 250 m. A. Structure of the Blue sand. B. Structure of the Orange sand. C. Structure of the green sand.

4.3.2 Basin Model

We use PetroMod 2020 to model the evolution of the Terrebonne Basin. PetroMod models the successive deposition and burial of geologic layers with specific boundary conditions (Hantschel and Kauerauf, 2009). This model assumes that compression is uniaxial and compaction is related to effective stress. In PetroMod, compressibility and permeability control fluid flow and the formation of pressure. To calculate pore pressure, PetroMod uses the following equation:

$$\frac{m_v}{1-\phi}\frac{\delta u}{\delta t} - \nabla \cdot \frac{k}{\mu} \cdot \nabla u = \frac{m_v}{1-\phi}\frac{\delta u_l}{\delta t} \qquad \text{Eq. 1}$$

Where ϕ is porosity, ∇u is the overpressure gradient, μ is viscosity, and u_l is lithostatic potential (lithostatic pressure – hydrostatic pressure).

In our model, the boundary conditions include a constant seafloor depth, open sides for lateral flow, and no fluid flow at the base (Fig 4). The seafloor depth is kept constant, and the seafloor temperature is fixed at 4° C. We apply a constant basal heat flow of 45mW/m^2. Pore pressures in our model are not limited by lithostatic stress.

4.3.3 Geomechanical properties of the mudrock

We compare two different lithologies from the northern Gulf of Mexico, Eugene Island (EI) mudrock, and clayey silt from GC-955. The Eugene Island mudrock was deposited in outer neritic depths (Alexander and Flemings, 1995). The GC-955 clayey silt

was deposited by distal overbank sediment gravity flows (Meazell et al., 2020). For the Eugene Island mudrock, we use porosity and permeability measurements from Geofluids (2015). For the GC-955 clayey silt, we use porosity and permeability relationships from Fang et al. (2020).

The compaction and consolidation of low permeability mudrock is a major driver of elevated pore pressures (Flemings 2021). Consolidation is controlled by permeability (k), compressibility (m_v), and the coefficient of consolidation (c_v). To calculate compressibility (m_v), we use the following equation:

$$m_v = \frac{1}{1+e}\frac{\partial e}{\partial \sigma_v'} \qquad \text{Eq. 2}$$

Where e is the void ratio, and σ_v' is the vertical effective stress.

Clayey silt is slightly less compressible than the Eugene Island mudrock (Fig. 4A). When effective stress is less than 5 MPa, the clayey silt is less permeable than the EI mudrock (Fig. 4B). The permeability of the clayey silt decreases with increasing effective stress, but to much less of a degree than the decrease observed in the permeability of the EI mudrock.

The sandy silt is much less compressible than the two mudrocks, but has a much higher permeability (Fig 4). For this sediment, permeability does not change much with effective stress, and we do not expect much compaction during burial.

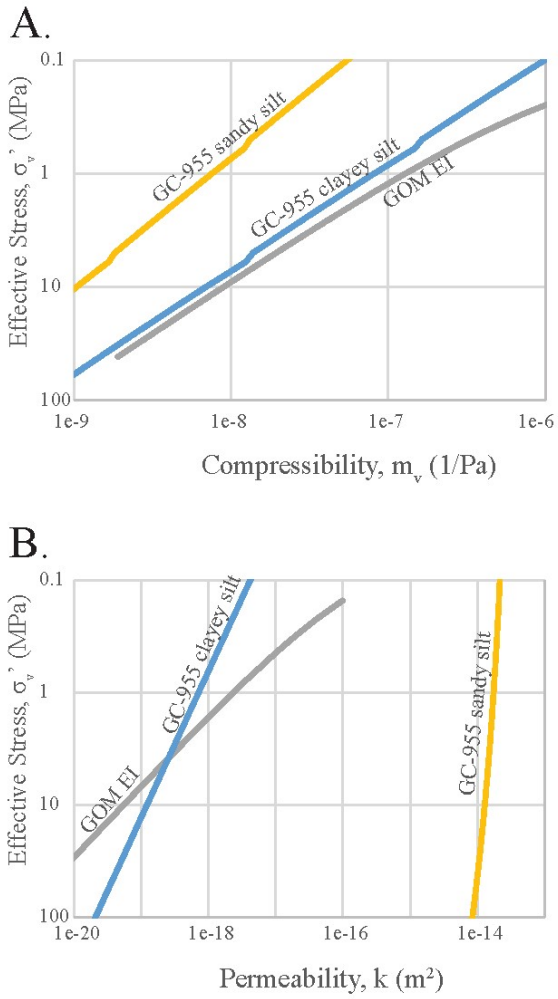

Figure 4. Compaction trends for the GC-955 and Eugene Island sediments.

4.3.4 Model conditions

The model starts with a near-horizontal seafloor upon which sediment is added. The geometry of our model (Figure 5), including the extent and depths of sands, mudrock, and salt, comes from the results of our mapping in 2D and 3D (Fig 3) and approximates the geometry in Figure 2.

For the ages in our model, we use a single Lower Pleistocene (Calabrian) marker 750 m below our mapped sands of interest (Frye et al., 2012). We assume that the sands have a maximum age of 1.5 Ma and minimum age of 0.7 Ma, and we assume that all deposition above the sands occurred during constant sedimentation from 0.7 Ma to present. Below the sands, the majority of sediment in the Terrebonne Basin is Middle Pleistocene to Pliocene; therefore we assign ages of 1.5 – 4 Ma for the mudrock below the sand. These dates are somewhat arbitrary; however, they are similar to a previous analysis suggesting that the majority of sediment below the sands in the Terrebonne Basin is from the Pliocene to the Middle Pleistocene (Frye et al., 2012). Stratigraphic ages are displayed in Figure 5, and the geometric evolution of the basin model is displayed in Figure 6.

Based on these age assumptions, from the start of basin deposition (4 Ma) to the sand layer (1.5 Ma), the accumulation rate was 0.00108 m/yr at location A and 0.00097 m/yr at location B. Above the sand, the accumulation rate was 0.00714 m/yr at location A and 0.00043 m/yr at location B.

For our gas + hydrate models, we add 2% TOC to the sand layers and assign a hydrogen index of 300 mgHC/gTOC. We use a Middleburg biogenic kinetics to generate methane in the shallow subsurface sand.

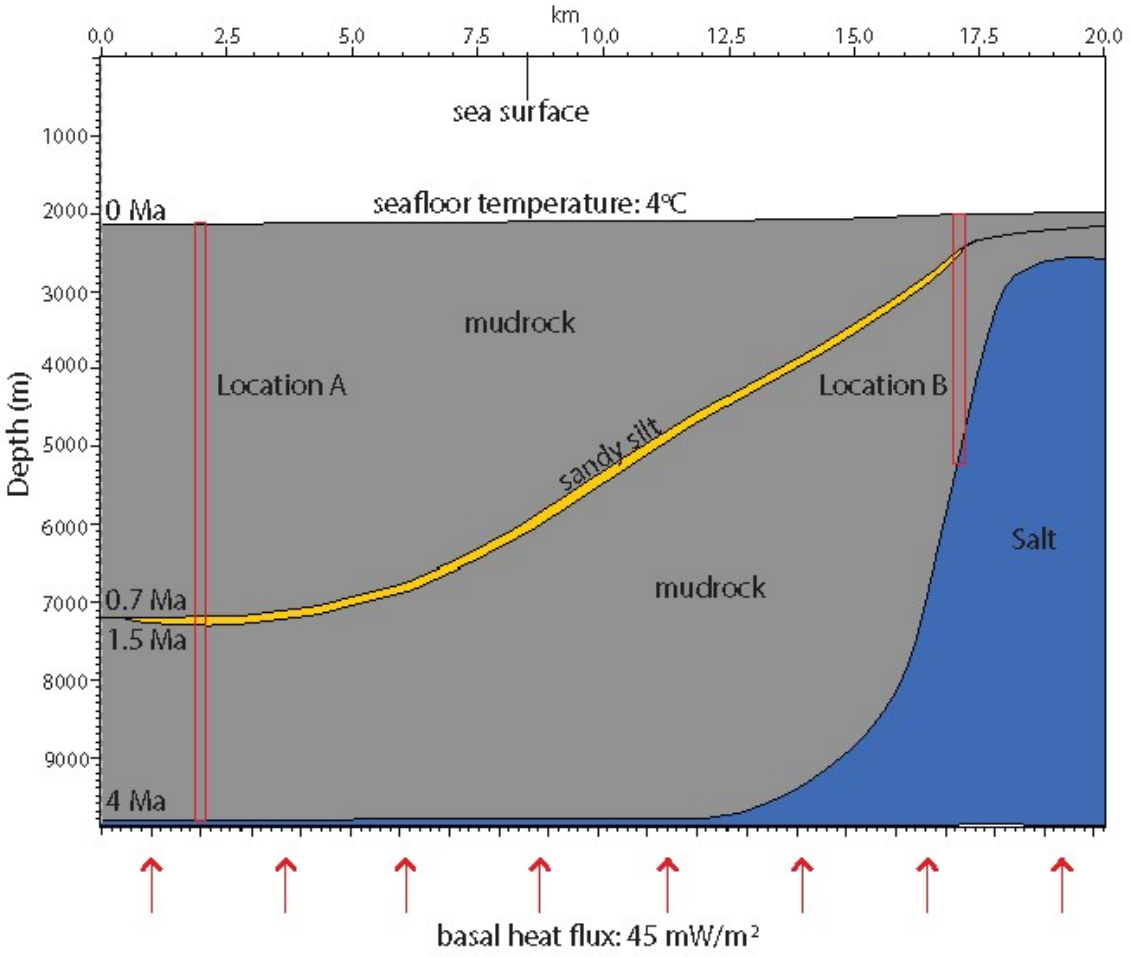

Figure 5. 2D Basin model conditions. Time lines are displayed on the left. The sandy silt layer is deposited by 0.7 Ma, and undergoes constant sedimentation until it reaches the present-day geometry at 0 Ma. The locations for the 1D basin models in Figure 7 are displayed in the red boxes.

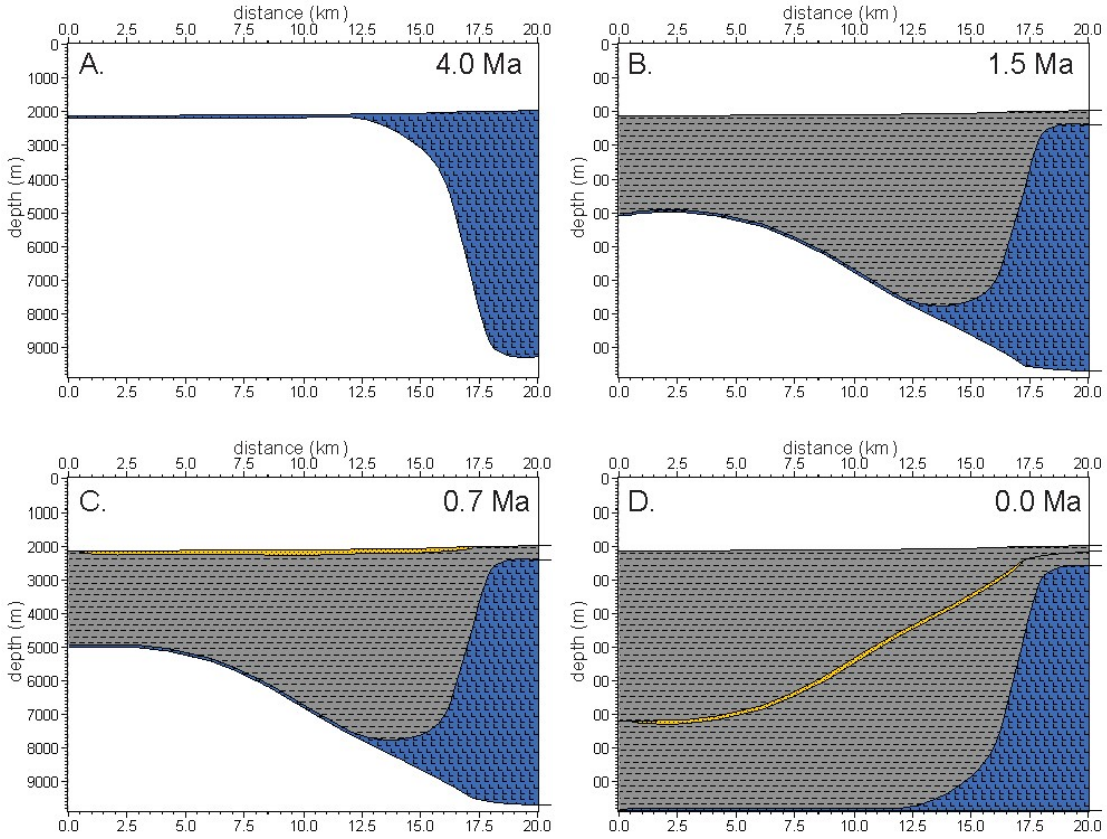

Figure 6. Geometric evolution of the basin model. A. Deposition of the underlying mudrock begins at 4.0 Ma. B. Deposition of the underburden is complete at 1.5 Ma. C. Deposition of the permeable layer is complete at 0.7 Ma, and deposition of the overlying mudrock begins. D. Basin evolution is complete present day.

4.4 1D MODELS

4.4.1 1D Overpressure

We begin with a simple 1D model of the Terrebonne Basin from the seafloor to the top of salt in two areas: deep in the basin center (Fig. 7A), and shallow near the basin edge (Fig.7B). In the center of the basin, 5000 m of sediment has been deposited in 700,000 years. As a result of the rapid sedimentation in the deep basin, the majority of the overburden has not had a chance to drain, resulting in water-phase pressures that are near

the lithostatic stress (Fig 7A). Near the basin edge, only 300 m of sediment has been deposited over the same amount of time. This much lower accumulation rate has resulted in pore pressures near hydrostatic pressure (Fig 7B).

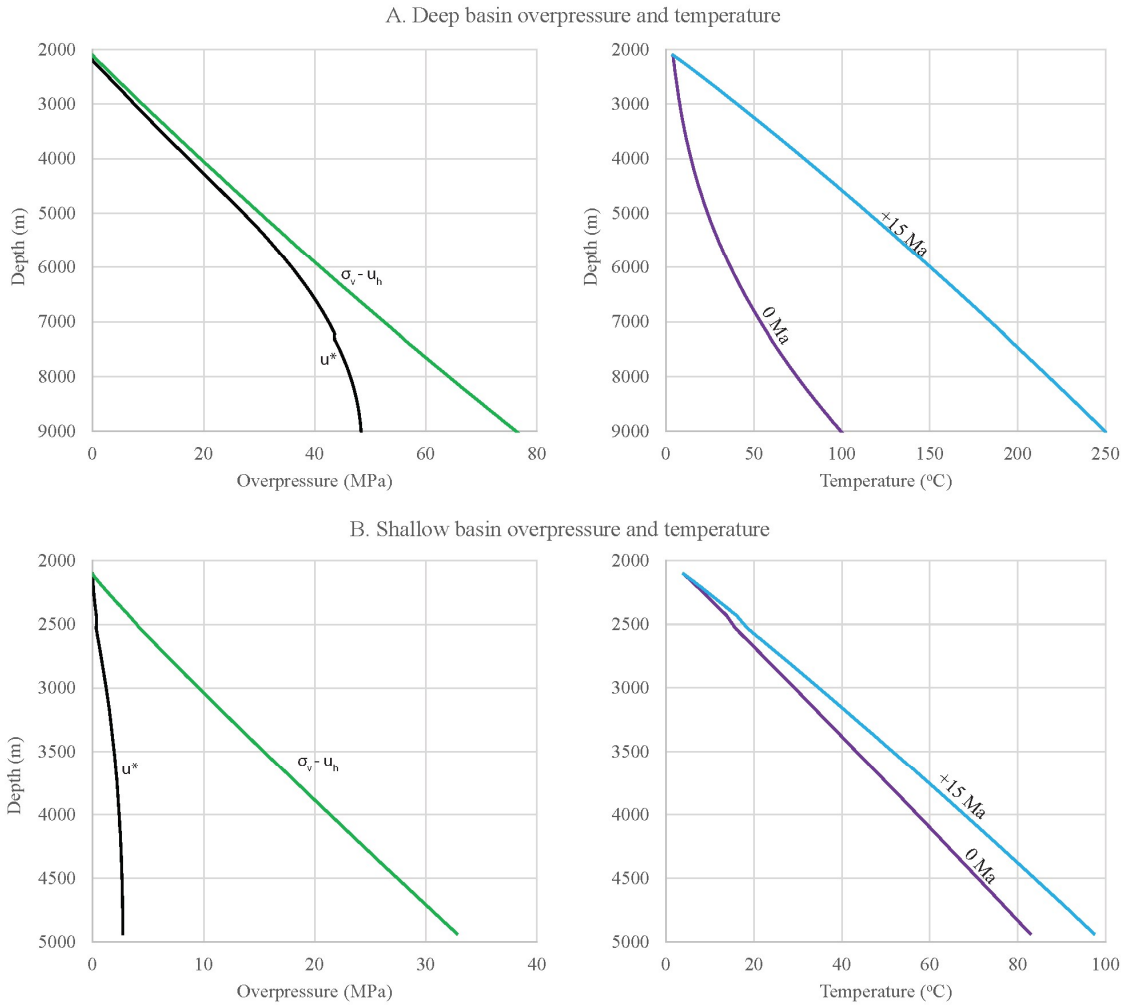

Figure 7. Overpressure and temperature plots for 1D sedimentation models in the deep (A) and shallow (B) sections of the Terrebonne Basin. The location for the models is displayed in Figure 5. u* = overpressure; u_h = hydrostatic pressure; σ_v = lithostatic stress. The temperature plots include subsurface temperatures for the present-day (purple line) and +15 Ma into the future (blue line).

4.4.2 1D Temperature

The temperature profiles vary greatly between the 1D model locations. In the deep part of the basin, the temperature increases with depth gradually near the seafloor, and much faster towards the base of the section (Fig 7A). In the shallow section of the basin, the temperature increases in a much more linear trend (Fig 7B). The discrepancy between the two temperature profiles is due to the sedimentation rate. The shallow section underwent slow deposition and has reached an equilibrium temperature (Fig 7B), whereas the deeper section has had an enormous amount of cold sediment deposited, and heat flow from the base has not had a chance to catchup to the sedimentation rate, resulting in the curved temperature profile where the gradient increases with depth (Fig 7A). Heat is absorbed by the cold, rapidly deposited sediment, thereby decreasing the heat flow towards the surface.

4.5 2D MODELS

We continue our model into the 2D space approximating the geology of the Terrebonne Basin. In this model, a permeable sand layer connects the deep left side of the basin with the shallow right side of the basin (Fig 5). The sand is deposited parallel to the seafloor, but differential sedimentation rates cause the sand to dip progressively more to the left (Fig 6). The right side of the basin is underlain by a tall salt diapir that maintains high-relief from 1.5 Ma to present (Fig 6). We first explore the evolution of pressures and temperatures of the basin with no hydrocarbons.

4.5.1 2D Temperature

Figure 8 shows the evolution of the temperature in the basin. The highest temperatures are found near the base of the salt. During basin evolution we observe overall temperatures decreasing in the basin center, and increasing at the basin edge near the salt.

As a result, the isotherms dip toward the basin center the north, in the same direction as the sand. Within the top 2 km of sediment, the temperatures range from less than 10 C to 40 C at present day (Fig 8C).

Heat flow is varied throughout the basin (Fig 9). On the left, where sedimentation is high, heat flow is low. The rapid deposition of cold mudrock outpaces the flow of heat from below. Higher subsurface temperatures are found on the right side at the basin edge, likely as a result of the lower sedimentation rate and the underlying shallow salt. Salt wicks heat from deep below and releases it near the surface (Mello et al., 1995; Portnov et al., 2020). We observe an increase in heat flow at the top of the salt and extending 1.5 km towards the basin center (Fig. 9). This result supports the interpretation of Meazell and Flemings (In revision) that heat from the adjacent salt thins the hydrate stability zone near the edges of the basin.

The position of the base of the hydrate stability zone is directly influenced by temperature. The thickness of the hydrate stability zone changes throughout basin development (Fig. 8). It starts thin, and later thickens toward the basin center. As the dip of the sand body increases, a greater amount of the sand body crosses the phase boundary from hydrate-stable, to gas and water stable. This results in a sand body that is half above, and half below the base of the hydrate stability zone by 0.5 Ma (Fig. 8B), and mostly below the base of the hydrate stability zone at 0.25 Ma (Fig. 8C). At present-day, the entire sand is below the hydrate stability, with the exception of the crest of the sand at the basin edge near the salt (Fig. 8D). From 0.5 Ma to present, the hydrate phase boundary moves updip in the sand from the basin center to near the basin edge.

The basin center is cold due to the rapid deposition of cold mud outpacing the basal heatflow. By continuing the model into the future, we can observe the degree to which the present-day system is out thermal equilibrium (Fig 10). At 15 million years after present day, the left side of the basin has warmed up, and the isotherms are again near parallel to the seafloor (Fig. 10B), resulting in a temperature profile similar to that observed near the start of rapid deposition (Fig. 8A). Near the salt, temperatures remain elevated. At +15 Ma, the entire sand body including the crest is below the base of the hydrate stability zone, and any hydrate within the sands would be dissociated into free gas.

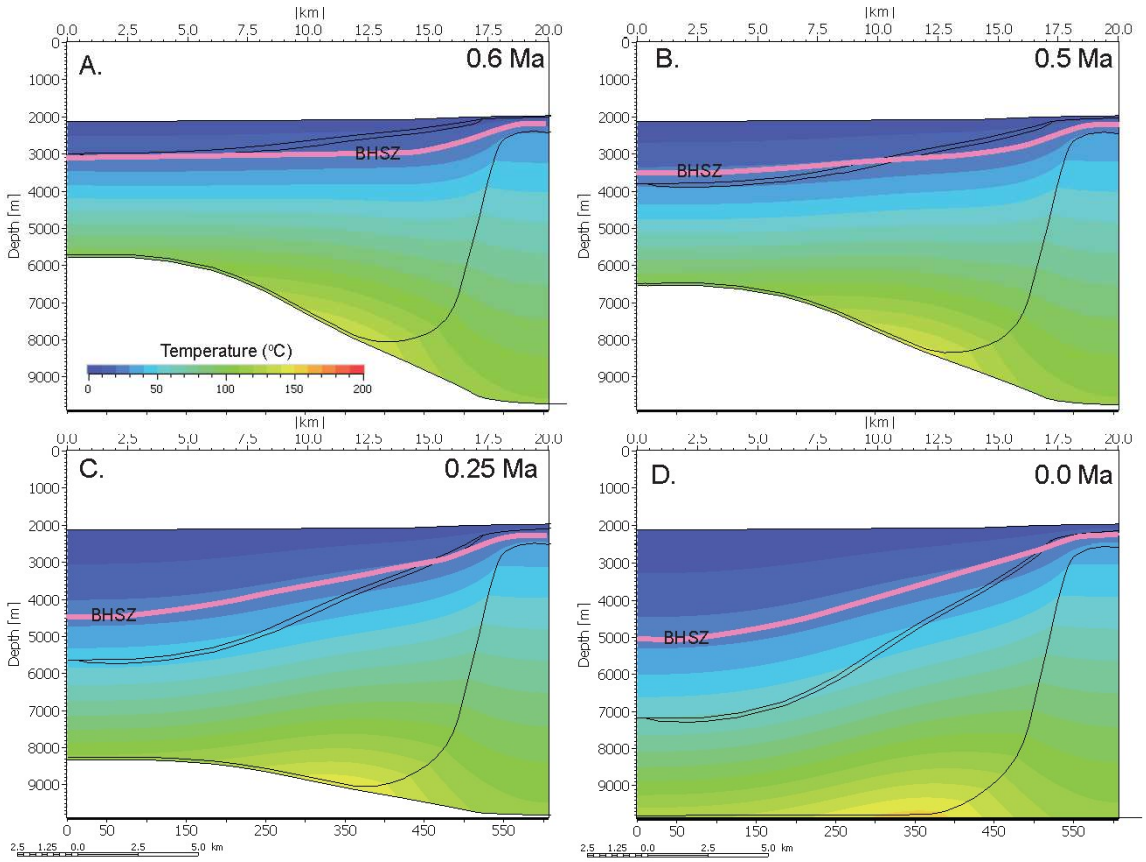

Figure 8. Temperature evolution of the Terrebonne Basin from 0.6 Ma to present. The highest temperatures are at the toe of the salt, and the lowest temperatures are found in the center of the basin. After 0.6 Ma, the sand begins to dip beneath the Base of the Hydrate Stability Zone (pink line - BHSZ). By 0.25 Ma (C), the majority of the sand is beneath the BHSZ.

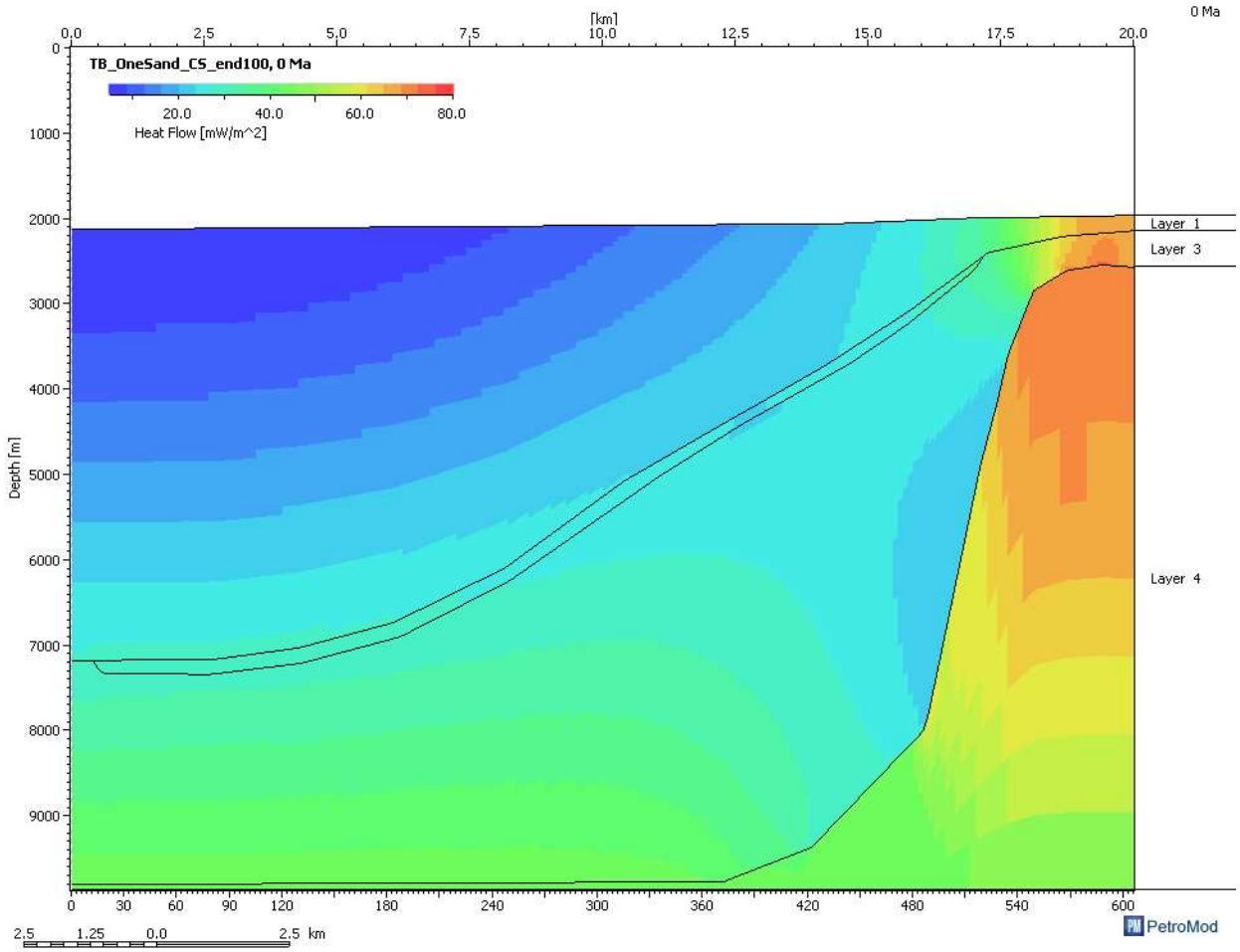

Figure 9. Present day vertical heat flow is affected by rapid sedimentation and nearby salt. On the left, vertical heat flow is suppressed by the deposition of cold mudrock. Above the salt, vertical heat flow is nearly double the basal heat flow input.

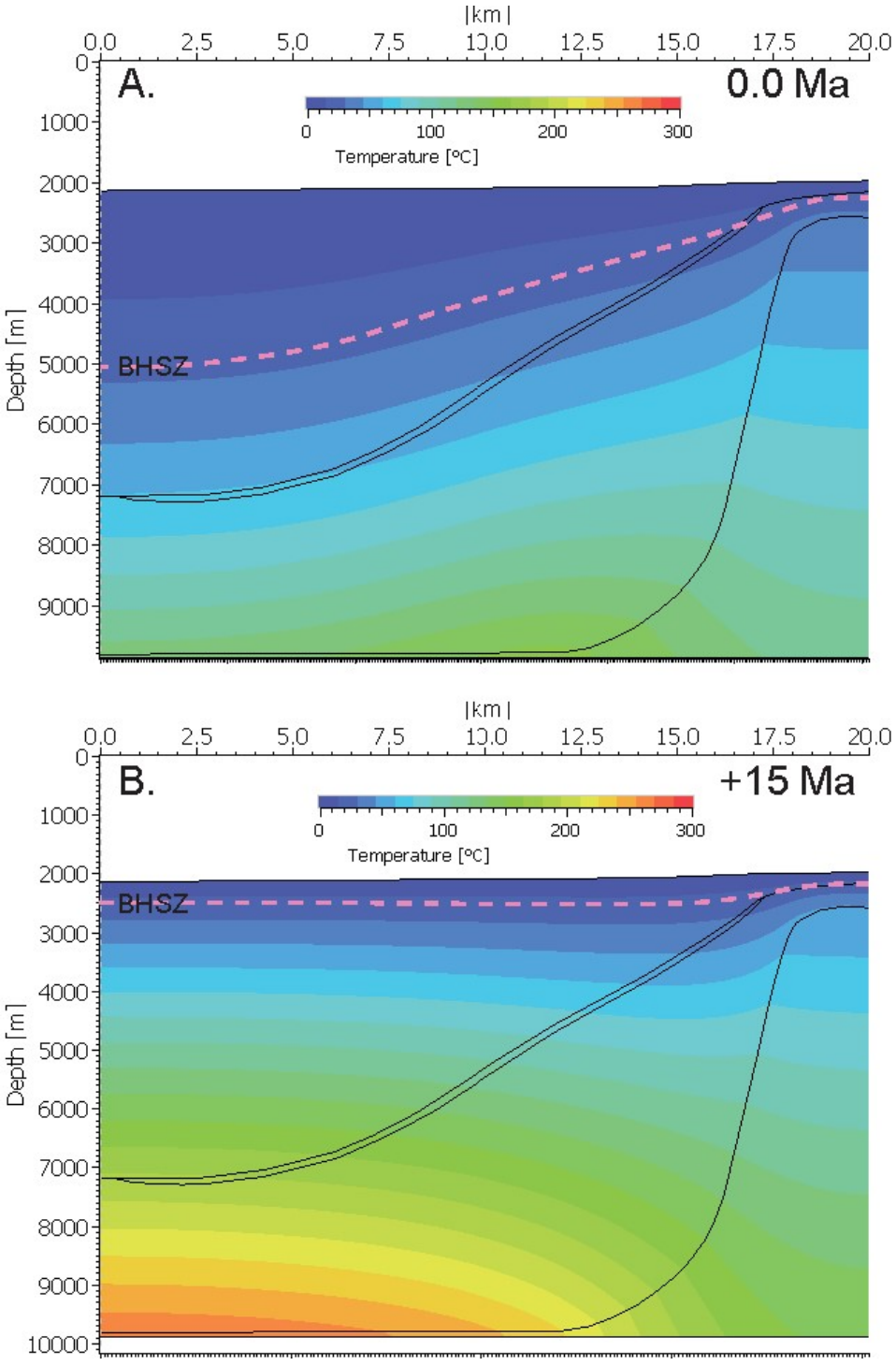

Figure 10. Present and future temperatures. (A) At present, basin temperatures are low and isotherms dip to the left. (B) At +15 Ma, the basin has warmed substantially and isotherms away from the salt are near parallel to the seafloor.

4.4.5 2D Pressure

Figure 11 shows the evolution of overpressure within our model. Early in the model, there is low overpressure, with values ranging from near hydrostatic in the upper 1000 m, to 4.5 MPa in the deepest part of the basin (Fig 11A). The low basin-wide overpressures are due to the low sedimentation rate of the deeper mudrock, which has been draining fluid pressure from the start of deposition at 4 Ma to the end of the sand deposition at 0.7 Ma.

As rapid deposition of the overlying mudrock begins to fill the basin, overpressures grow throughout the basin (Fig 11B). Strikingly, the greatest overpressures are found not at the deepest point of the basin, but rather in the center of both the upper and lower mudrock between 4-6 km. The sand layer has a low overpressure of 2.2 MPa throughout the basin, and overpressures within the mudrock near the sand share similar values. The highly-permeable, dipping sand layer is draining water from the adjoining mudrock and releasing it near the surface on the right side of the model.

As deposition of the overlying mudrock continues, overpressure continues to develop above the sand, where present-day overpressure values reach 17 MPa (Fig 11C). Below the sand, overpressure in the underlying mudrock has dissipated from 10 MPa to 3.7 MPa and matching the overpressure of the dipping sand layer. The sand layer continues to drain both overlying and underlying mudrocks. The underlying mudrock has an overpressure lower than that of the overlying mudrock because the lower mudrock is older, was deposited slower, and has been draining for much longer than the overlying mudrock.

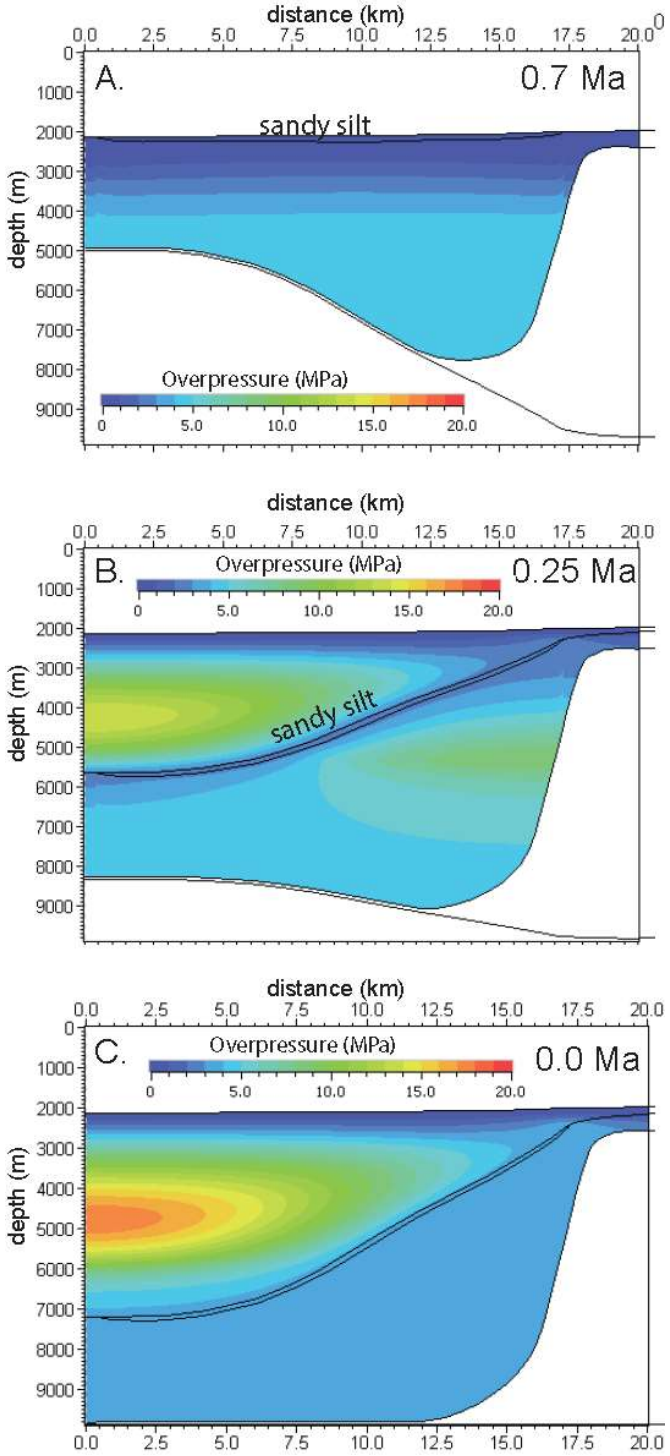

Figure 11. Overpressure evolution of the basin with a single, dipping, water-only sand and a sand crest at 400 mbsf. Overpressure of the sand remains low during deposition (A) and slowly builds to 2.6 MPa at 0.25 Ma (B). At 0.0 Ma (C), we observe overpressure of 3.7 MPa.

4.4.5 2D Gas and hydrate model

We now explore the temperature and pore pressures within the single dipping sand model with the addition of methane gas and hydrate. Figure 12 shows the present-day temperature profile of the basin, which is nearly identical to the non-hydrate model (Fig 8C). Isotherms dip to the left, in the same direction as the sand. Within the top 2 km of sediment, the temperatures range from less than 10 C to 40 C. Higher temperatures are found at the basin edge, near the shallow salt in the south.

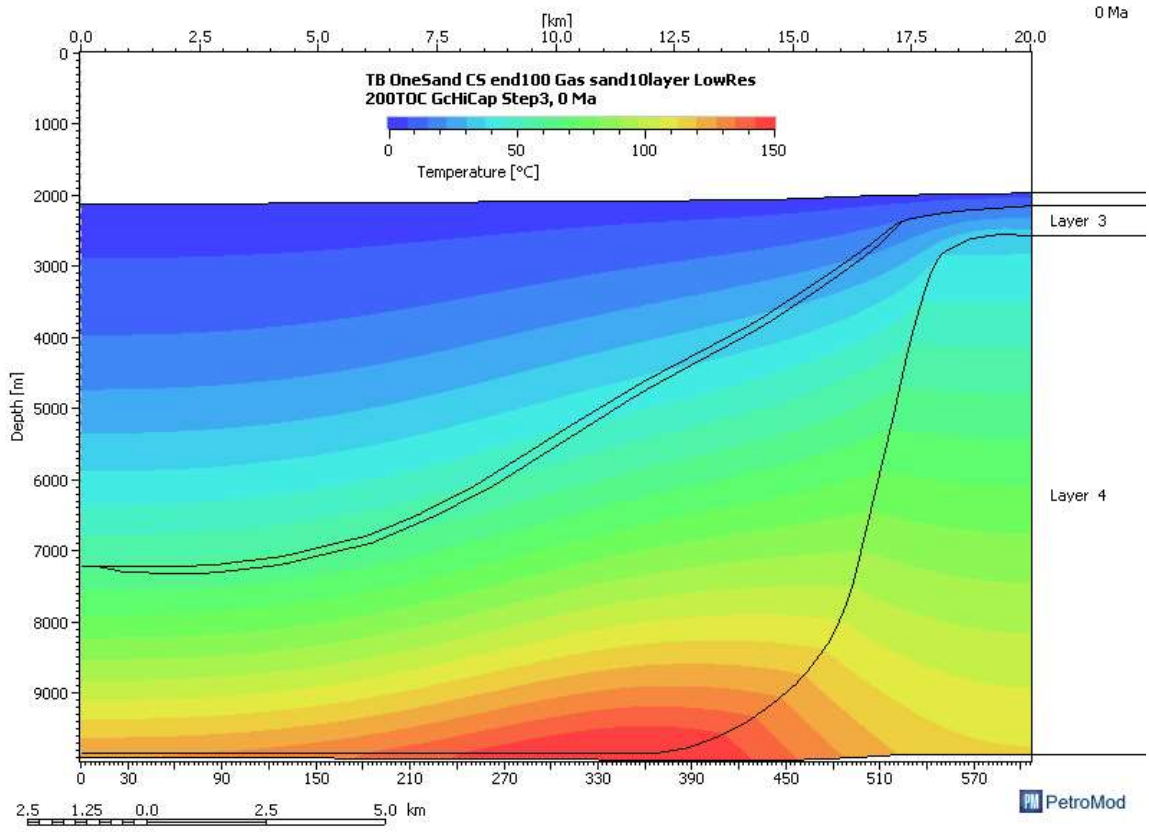

Figure 12. The present-day temperature of the gas + hydrate model is identical to the water-only model (Fig 8C).

Figure 13 shows the present-day overpressure of the gas + hydrate model. Overpressure ranges from zero MPa near the seafloor, to more than 20 MPa in the center

of the basin. The crest of the dipping sand body has a water-phase overpressure of 3.7 MPa; however, there is a sharp contact at 2800 m, below which the sand has an overpressure of 9.3 MPa. The addition of gas and hydrate has increased basin wide overpressures by 5.6 MPa.

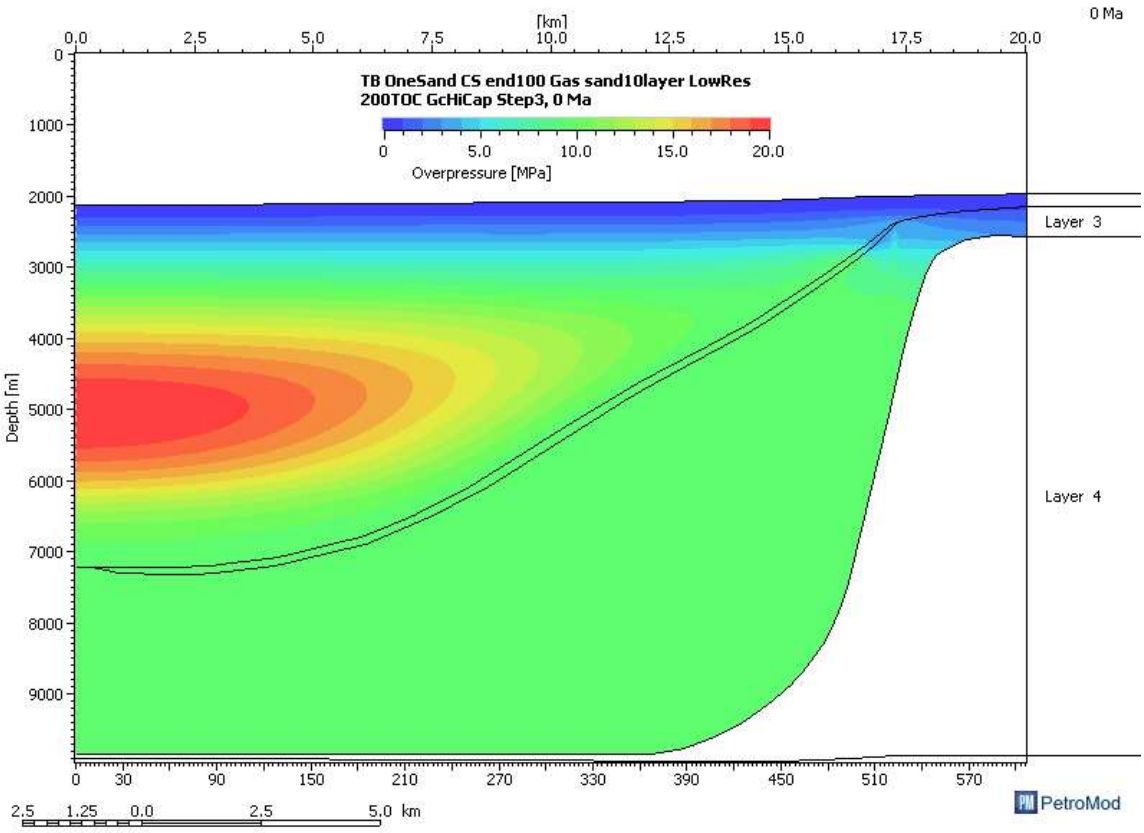

Figure 13. Overpressure of the gas hydrate model. At the crest of the sand, overpressure is 3.7 Mpa, the same value as that of the water-only model. However, below 2800 m an overpressure of 9.3 Mpa is observed in the dipping sand body as well as the surrounding mudrock.

As a result of the pressure, temperature, and presence of methane, high concentrations of gas hydrate are observed in the dipping sand layer (Fig 14). The highest concentrations of hydrate are found near the base of the hydrate stability zone, where

hydrate occupies >90% of the available pore space. Shallower within the sand, hydrate concentrations range from 20-50% of the available pore space.

Beneath the base of hydrate stability, a 100 m thick column of free gas is present within the sand (Fig 15). The gas is created through the process of hydrate recycling (Crutchley et al., 2019; Nole et al., 2018); as the sand layer becomes buried and dips beneath the base of the hydrate stability zone, hydrate within the sand dissociates and gas flows upwards until it reaches the hydrate stability zone. This gas is trapped by a hydrate seal at the phase boundary, and no gas is found within the hydrate stability zone. The buoyancy effect of this gas increases the pore pressure of the sand by 1.0 Mpa, and pushes the fluid pressure beyond the lithostatic stress (Fig 16).

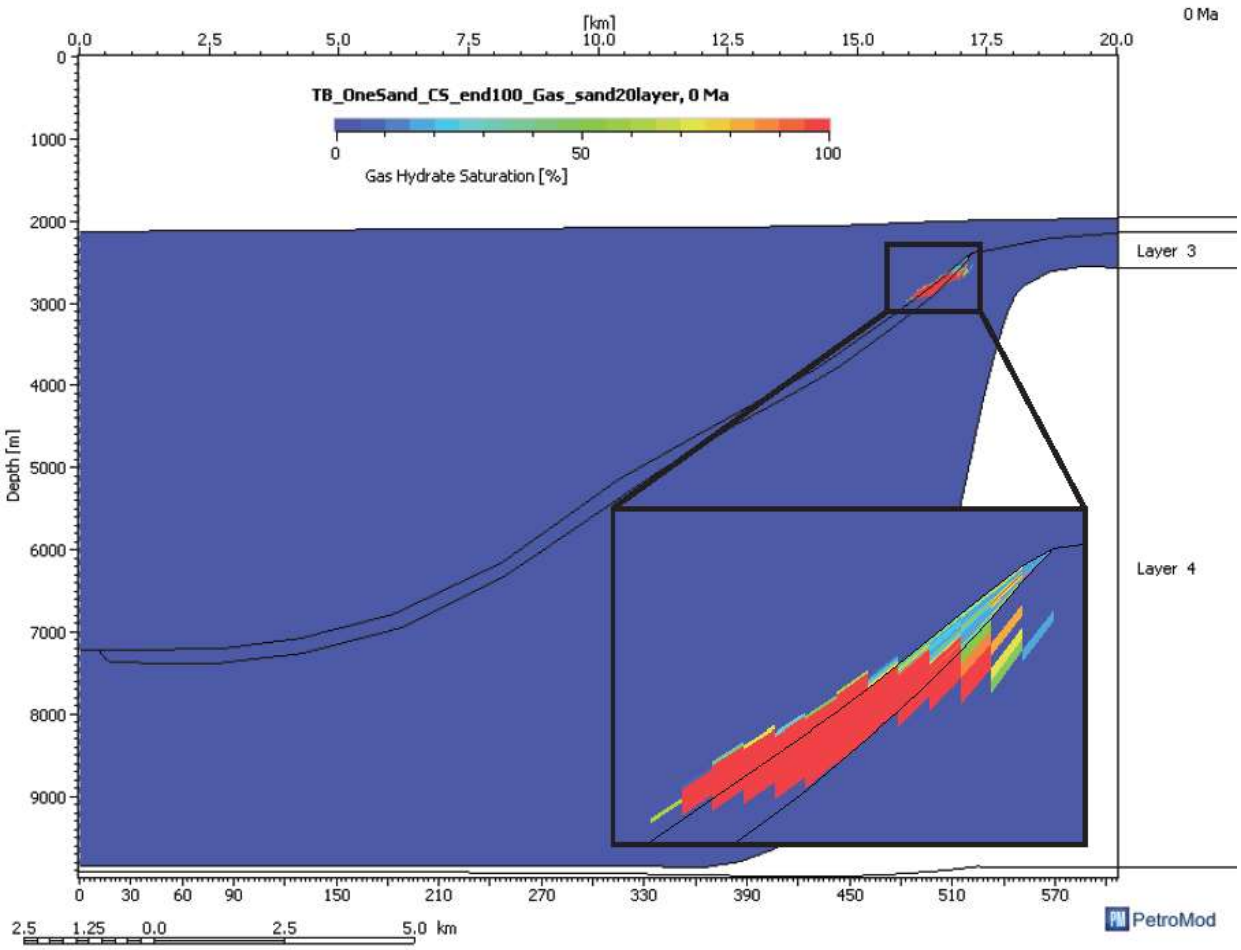

Figure 14. Hydrate saturation in single dipping sand. The highest hydrate saturations are near the base of hydrate stability, and a patchy, low concentrations of hydrate are within the shallow crest.

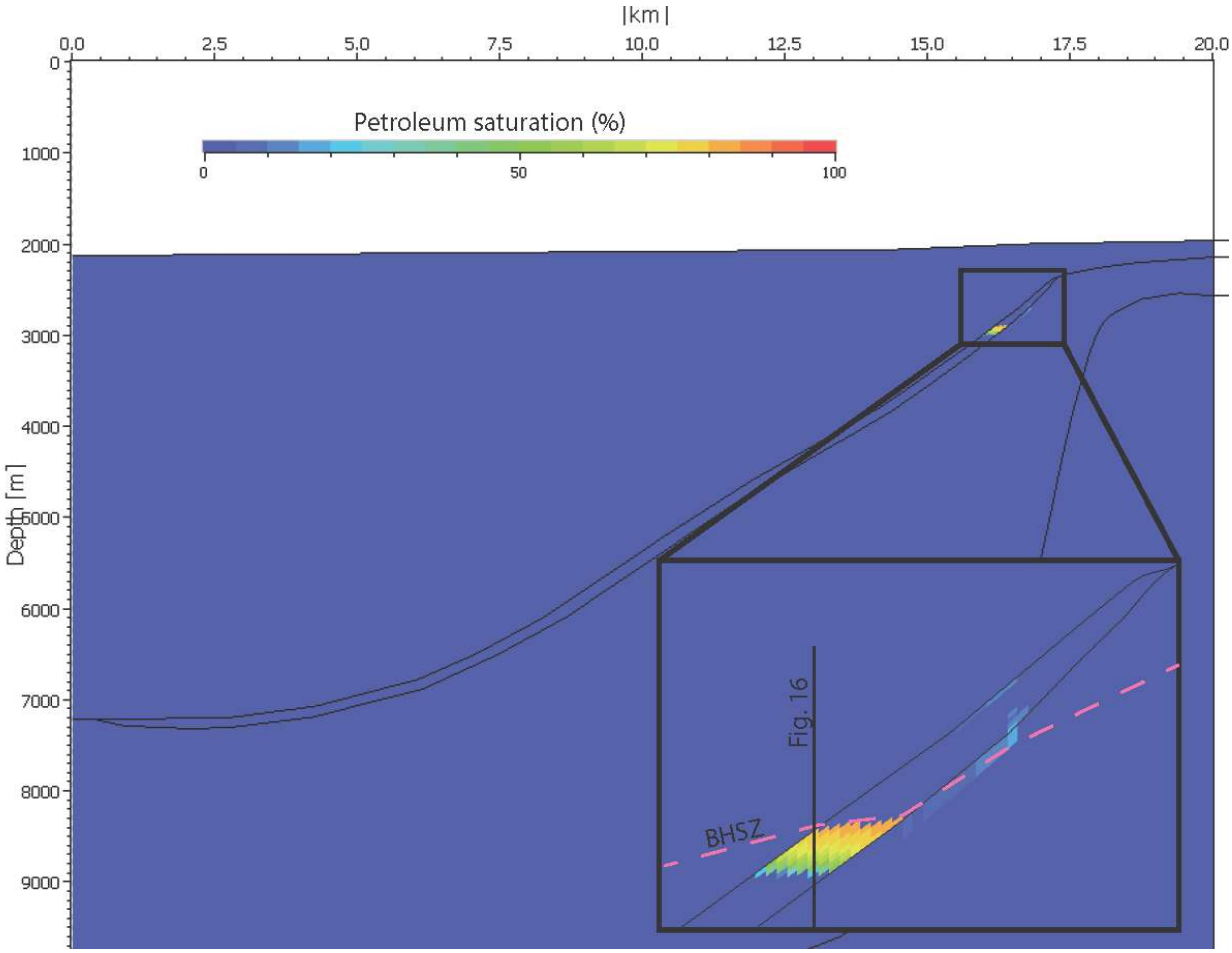

Figure 15. Gas saturation in single dipping sand. We observe a gas column of 200 m directly below the base of hydrate stability.

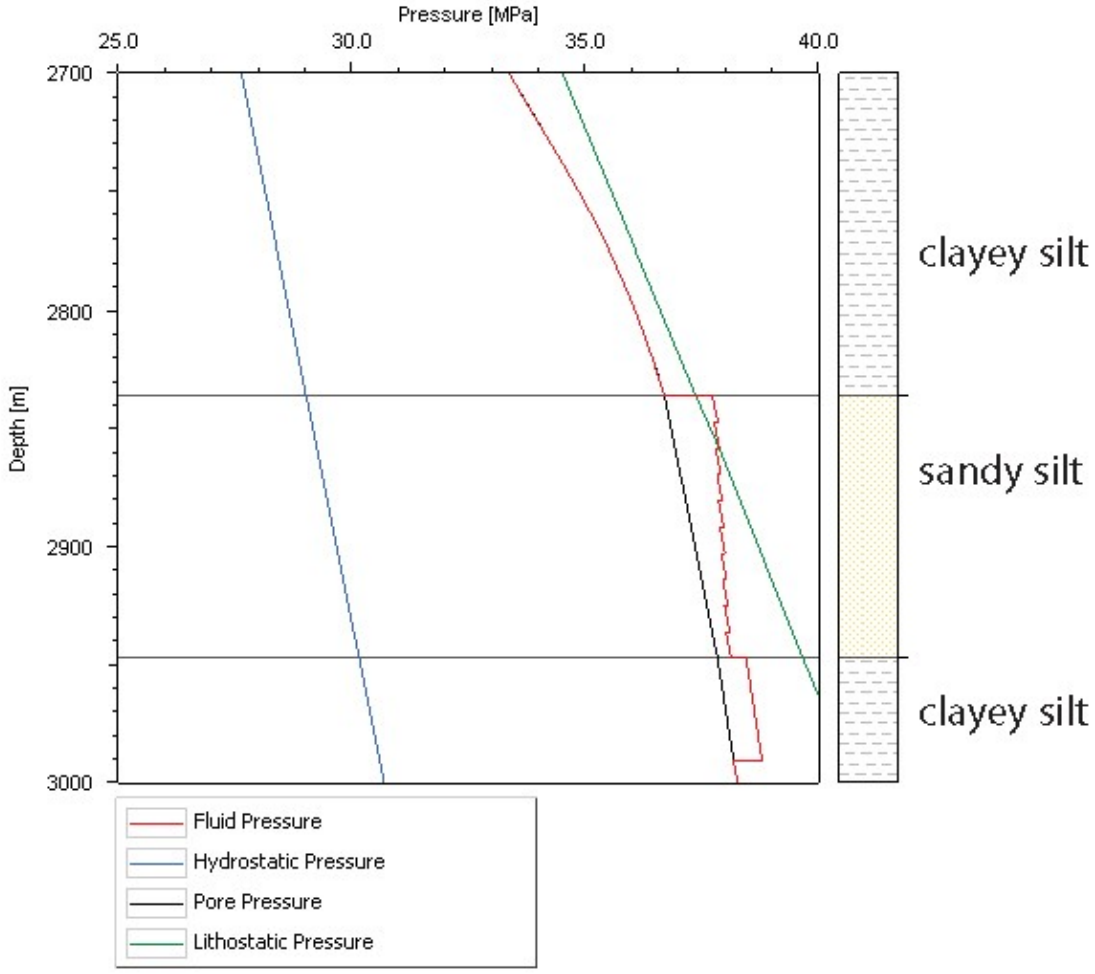

Figure 16. Pressure profile of gas trapped in sand beneath hydrate seal. The location for this profile is displayed in the inset in Figure 14.

4.6 DISCUSSION

4.6.1 Pressure

Elevated pore pressures within the shallow sands arise from a combination of effects. First, recent rapid sedimentation deposited massive amounts of mud within the northern basin (Fig 1B). The low compressibility and low permeability of the mud (Fig 4) lead to a mostly undrained basin (Fig 10).

The dipping sand layer has a profound effect on overpressure within the basin. Permeability of the sand is much higher than that of the mudrock, and an increase in effective stress has little effect on this layer (Fig 4B). The dipping sand layer maintains high permeability throughout basin evolution, and the permeable layer wicks away pressure similar to how salt wicks away heat.

High concentrations of hydrate reduce permeability in the sand. This restricts water flow, reduces drainage, thereby elevating pore pressures. Next, the buoyancy effect of free gas raises the fluid pressure (Fig 16). Finally, a hydrate seal at the BHSZ keeps the gas confined at deeper depths and higher pressures than would be possible without such seal. Rapid sedimentation of compressible mudrock increases the pore pressure by 3.7 Mpa, while the addition of gas and hydrate to the system increases the pore pressure by an additional 5.8 Mpa. In our models, gas and hydrate increase overpressure by 157% more than rapid sedimentation alone.

4.6.2 Venting locations

Seafloor venting will occur when and where the pore pressures meet the least principal stress, and effective stress is equal to or less than zero (Flemings, 2021). In the absence of pre-existing faults or fractures, venting will occur where the amount of overburden is least, which is usually at the crest of a sand body. In our basin model, we observe the position of failure not at the crest of the sand, but rather at the hydrate-gas interface at the base of the hydrate stability zone (Figure 17). This implies that the position of venting is influenced by the base of the hydrate stability zone forming an effective

hydrate seal. The position of this boundary changes, becoming progressively shallower over time (Figure 8). This in itself may lead to venting from progressively shallower positions of the sand as the geometry of the basin evolves.

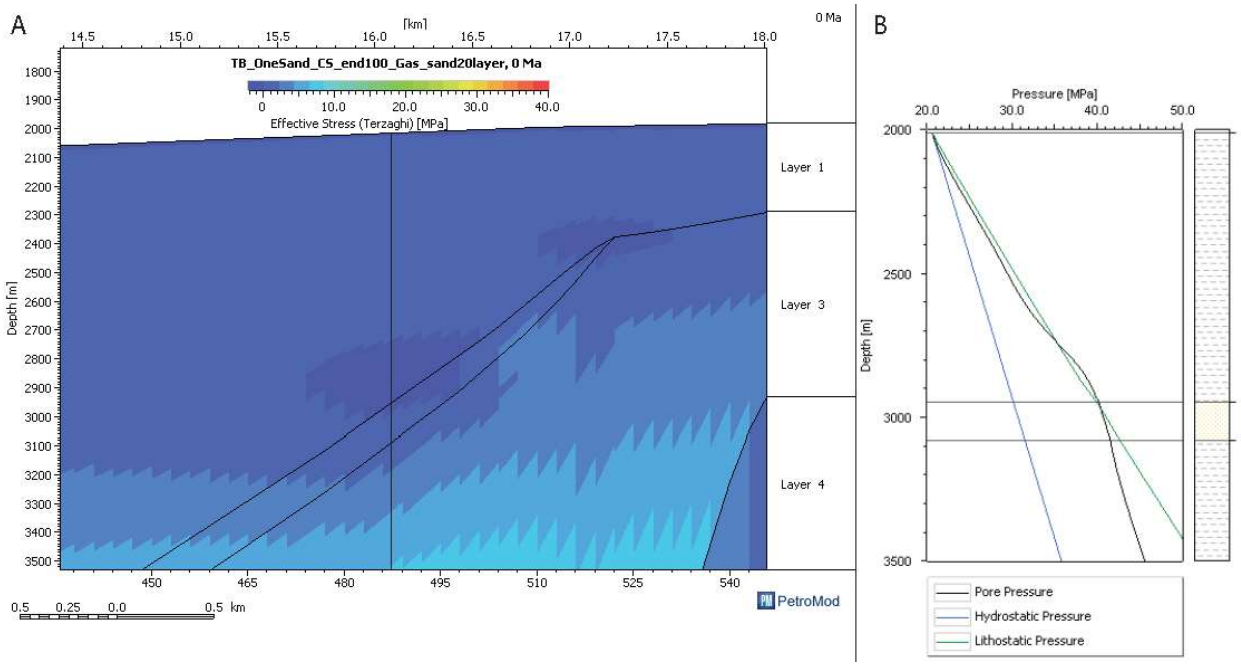

Figure 17. Effective stress. A. We observe a negative effective stress at the base of hydrate stability at the present day. B. Pore pressure profile through the zone of negative effective stress.

4.6.3 Three sands

We extend our single sand model with gas and hydrate to incorporate two additional sands in order to further explore the three sand system at Terrebonne (Fig. 18). From shallowest to deepest, the three sands represent the Blue, Orange, and Green hydrate sands of the Terrebonne basin.

The three sands are separated by 200 m of mudrock, and each sand has a different pore pressure regime. Pressure within the sands is controlled by the relative position of the gas crest of the sand to the seafloor. The BHSZ acts as a seal to trap gas within the sands

below the gas-hydrate contact. Due to the basinward dip of the sands and the shallow salt at the basin edge, the BSHZ and gas seal is deeper in the shallow sand, and shallower in the deep sand. The gas crest of the deepest sand is 600 mbsf, while the gas crest of the shallowest sand is 1000 mbsf. As a result, the we observe the highest overpressure in the stratigraphically shallowest sand, and the lowest overpressure in the stratigraphically deepest sand. This result is similar to the findings of Meazell and Flemings, (2020), where the authors used seismic data to infer fluid contacts and estimated pore pressures.

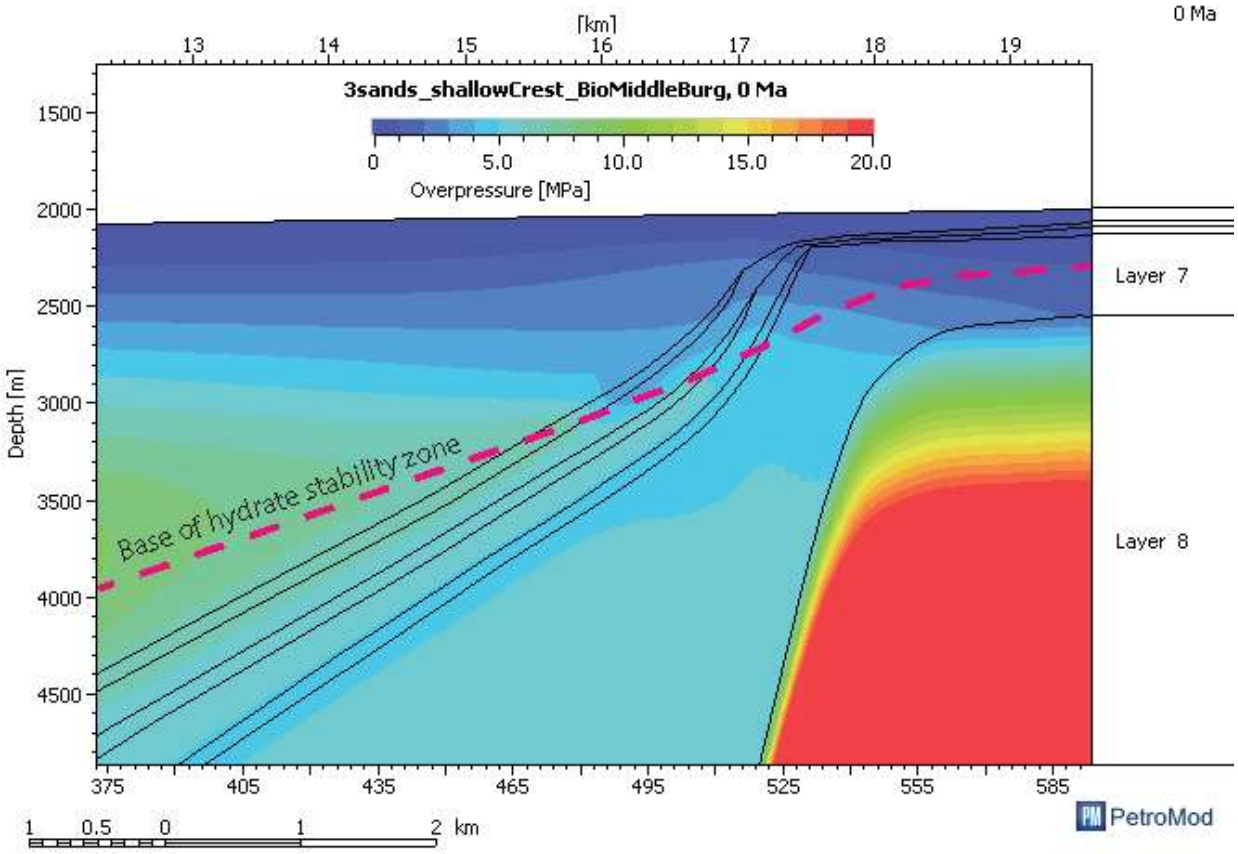

Figure 18. For the three sands model, we see observe highest overpressures at the base of the hydrate stability zone. We observe highest overpressure in the shallowest sand, and lowest overpressure in the deepest sand.

4.7 CONCLUSIONS

The Terrebonne Basin contains three major hydrate-bearing sand units that extend to the north throughout the basin, and reach depths of at least 7000 mbsl. The sands are are capped by up to five kilometers of low permeability mudrock. Overpressure within the Terrebonne basin is a result of two processes. First, recent and rapid sedimentation of compressible, low-permeability mudrock. Second, the presence of pore-clogging hydrate in dipping sands increases overpressure by restricting the drainage of water and by creating petroleum traps at the base of the hydrate stability zone. As a result of these factors, pore pressures within the sands can exceed the lithostatic stress, and are expected to be in the process of seafloor venting. This study supports the pressure estimates reported by Meazell and Flemings (In revision) and shows how the gas-to-hydrate phase boundary can control pressure and fluid flow conditions in high-relief deepwater basins.

REFERENCES

Alexander, L. L., and Flemings, P. B., 1995, Geologic evolution of a Pliocene–Pleistocene salt-withdrawal minibasin: Eugene Island Block 330, offshore Louisiana: AAPG bulletin, v. 79, no. 12, p. 1737-1756.

Boswell, R., Collett, T. S., Frye, M., Shedd, W., McConnell, D. R., and Shelander, D., 2012a, Subsurface gas hydrates in the northern Gulf of Mexico: Marine and Petroleum Geology, v. 34, no. 1, p. 4-30.

Boswell, R., Frye, M., Shelander, D., Shedd, W., McConnell, D. R., and Cook, A., 2012b, Architecture of gas-hydrate-bearing sands from Walker Ridge 313, Green canyon 955, and Alaminos canyon 21: northern deepwater Gulf of Mexico: Marine and Petroleum Geology, v. 34, no. 1, p. 134-149.

Boswell, R., Yamamoto, K., Lee, S.-R., Collett, T., Kumar, P., and Dallimore, S., 2014, Methane hydrates, Future Energy (Second Edition), Elsevier, p. 159-178.

Cartwright, J., Huuse, M., and Aplin, A., 2007, Seal bypass systems: AAPG Bulletin, v. 91, no. 8, p. 1141-1166.

Clennell, M. B., Hovland, M., Booth, J. S., Henry, P., and Winters, W. J., 1999, Formation of natural gas hydrates in marine sediments: 1. Conceptual model of gas hydrate growth conditioned by host sediment properties: Journal of Geophysical Research: Solid Earth, v. 104, no. B10, p. 22985-23003.

Crutchley, G. J., Pecher, I. A., Gorman, A. R., Henrys, S. A., and Greinert, J., 2010, Seismic imaging of gas conduits beneath seafloor seep sites in a shallow marine gas hydrate province, Hikurangi Margin, New Zealand: Marine Geology, v. 272, no. 1-4, p. 114-126.

Dewangan, P., Sriram, G., Kumar, A., Mazumdar, A., Peketi, A., Mahale, V., Reddy, S. S. C., and Babu, A., 2021, Widespread occurrence of methane seeps in deep-water regions of Krishna-Godavari basin, Bay of Bengal: Marine and Petroleum Geology, v. 124, p. 104783.

England, W. A., Mackenzie, A. S., Mann, D. M., and Quigley, T. M., 1987, The movement and entrapment of petroleum fluids in the subsurface: Journal of the Geological Society, v. 144, p. 327-347.

Fang, Y., Flemings, P. B., Daigle, H., Phillips, S. C., Meazell, P. K., and You, K., 2020, Petrophysical properties of the Green Canyon Block 955 hydrate reservoir inferred from reconstituted sediments: Implications for hydrate formation and production: AAPG Bulletin, v. 104, no. 9, p. 1997-2028.

Finkbeiner, T., Zoback, M., Flemings, P., and Stump, B., 2001, Stress, pore pressure, and dynamically constrained hydrocarbon columns in the South Eugene Island 330 field, northern Gulf of Mexico: AAPG bulletin, v. 85, no. 6, p. 1007-1031.

Flemings, P., Stump, B., Finkbeiner, T., and Zoback, M., 2002, Flow focusing in overpressured sandstones: Theory, observations, and applications: American Journal of Science, vol. 302, no. 10, p. 827-855.

Flemings, P., Long, H., Dugan, B., Germaine, J., John, C., Behrmann, J. H., Sawyer, D., and Expedition, I., 2008, Erratum to" Pore pressure penetrometers document high overpressure near the seafloor where multiple submarine landslides have occurred on the continental slope, offshore Louisiana, Gulf of Mexico"[Earth and Planetary Science Letters 269/3-4 (2008) 309-32]: Earth and Planetary Science Letters, v. 274, no. 1-2, p. 269-283.

Flemings, P. B., 2021, A Concise Guide to Geopressure: Origin, Prediction, and Applications, Cambridge University Press.

Frye, M., Shedd, W., and Boswell, R., 2012, Gas hydrate resource potential in the Terrebonne Basin, Northern Gulf of Mexico: Marine and Petroleum Geology, v. 34, no. 1, p. 150-168.

Gao, B., and Flemings, P. B., 2017, Pore pressure within dipping reservoirs in overpressured basins: Marine and Petroleum Geology, v. 80, p. 94-111.

Hillman, J. I., Cook, A. E., Daigle, H., Nole, M., Malinverno, A., Meazell, K., and Flemings, P. B., 2017, Gas hydrate reservoirs and gas migration mechanisms in the Terrebonne Basin, Gulf of Mexico: Marine and Petroleum Geology, v. 86, p. 1357-1373.

Loher, M., Marcon, Y., Pape, T., Römer, M., Wintersteller, P., dos Santos Ferreira, C., Praeg, D., Torres, M., Sahling, H., and Bohrmann, G., 2018, Seafloor sealing, doming, and collapse associated with gas seeps and authigenic carbonate structures at Venere mud volcano, Central Mediterranean: Deep Sea Research Part I: Oceanographic Research Papers, v. 137, p. 76-96.

McConnell, D. R., and Kendall, B. A., 2002, Images of the Base of Gas Hydrate Stability, Northwest Walker Ridge, Gulf of Mexico, Offshore Technology Conference: Houston, Texas, Offshore Technology Conference, p. 10.

Meazell, K., and Flemings, P. B., In revision, The evolution of seafloor venting from hydrate-sealed gas reservoirs: Earth and Planetary Science Letters.

Mello, U. T., Karner, G. D., and Anderson, R. N., 1995, Role of salt in restraining the maturation of subsalt source rocks: Marine and Petroleum Geology, v. 12, no. 7, p. 697-716.

Osborne, M., and Swarbrick, R., 1997, Mechanisms for generating overpressure in sedimentary basins: A reevaluation: AAPG Bulletin, v. 81, no. 6., p. 1023-1041.

Paganoni, M., Cartwright, J. A., Foschi, M., Shipp, C. R., and Van Rensbergen, P., 2018, Relationship between fluid-escape pipes and hydrate distribution in offshore Sabah (NW Borneo): Marine Geology, v. 395, p. 82-103.

Portnov, A., Cook, A., Heidari, M., Sawyer, D., Santra, M., and Nikolinakou, M., 2020, Salt-driven evolution of a gas hydrate reservoir in Green Canyon, Gulf of Mexico: AAPG Buletin, vol. 104, no. 9, p. 1903-1919.

Reilly, M. J., and Flemings, P. B., 2010, Deep pore pressures and seafloor venting in the Auger Basin, Gulf of Mexico: Basin Research, v. 22, no. 4, p. 380-397.

Roberts, H., Shedd, W., and Hunt Jr, J., 2010a, Dive site geology: DSV ALVIN (2006) and ROV JASON II (2007) dives to the middle-lower continental slope, northern

Gulf of Mexico: Deep Sea Research Part II: Topical Studies in Oceanography, v. 57, no. 21-23, p. 1837-1858.

Roberts, H. H., Feng, D., and Joye, S. B., 2010b, Cold-seep carbonates of the middle and lower continental slope, northern Gulf of Mexico: Deep Sea Research Part II: Topical Studies in Oceanography, v. 57, no. 21, p. 2040-2054.

Seldon, B., and Flemings, P. B., 2005, Reservoir pressure and seafloor venting: Predicting trap integrity in a Gulf of Mexico deepwater turbidite minibasin: AAPG bulletin, v. 89, no. 2, p. 193-209.

Serié, C., Huuse, M., Schødt, N. H., Brooks, J. M., and Williams, A., 2017, Subsurface fluid flow in the deep-water Kwanza Basin, offshore Angola: Basin Research, v. 29, no. 2, p. 149-179.

Sloan, E. D., and Koh, C., 2007, Clathrate hydrates of natural gases, CRC press.

Stump, B. B., and Flemings, P. B., 2002, Consolidation state, permeability, and stress ratio as determined from uniaxial strain experiments on mudstone samples from the Eugene Island 330 Area, offshore Louisiana: strain, v. 3, p. L3.

Yardley, G. S., and Swarbrick, R. E., 2000, Lateral transfer; a source of additional overpressure?: Marine and Petroleum Geology, v. 17, p. 523-537.

Appendices

APPENDIX A: GRAIN SIZE EXPERIMENT DATA

This appendix contains the results of grain size experiments conducted on depressurized and non-pressurized hydrate core samples collected from the two wells drilled in GC-955. Figure A1 shows a comparison of grain size experiments by the hydrometer method and laser diffraction via Malvern Mastersizer. The results for the sandy silt lithofacies are strikingly similar, while the results for the clayey silt differ by more than 20% clay vs silt. Figures A2-A33 are the results from the hydrometer method that were used to create the figures in Chapter 2.

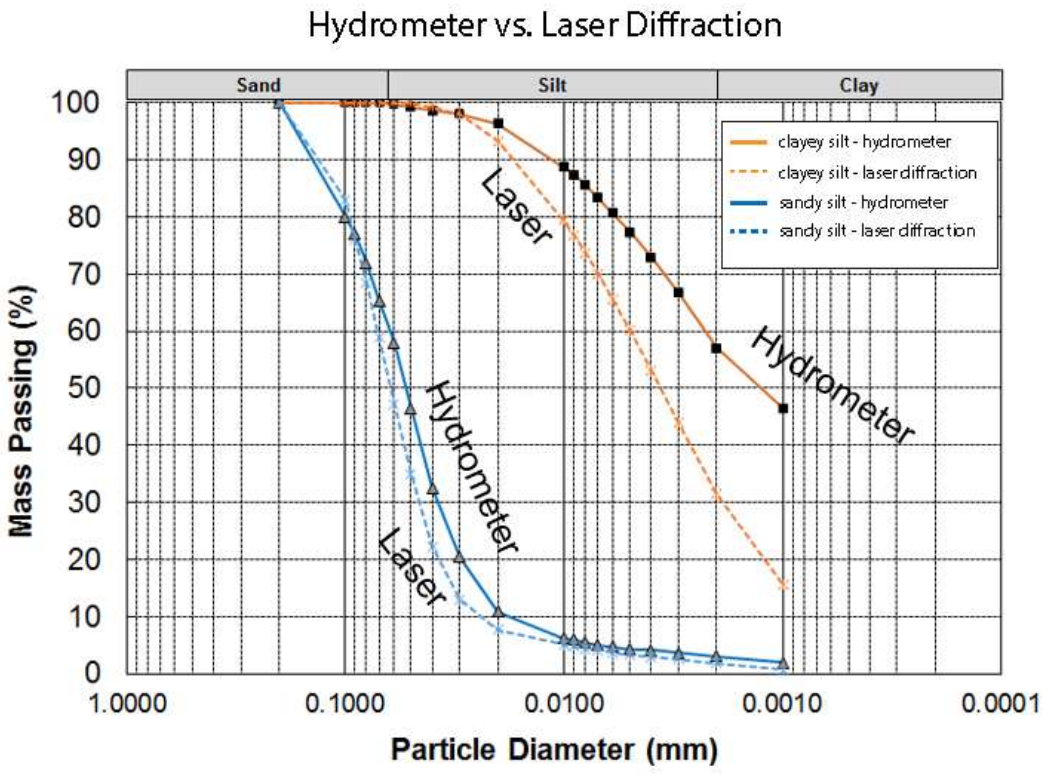

Figure A1. Comparison of results from grain size analysis via hydrometer and laser diffraction.

Hydrometer Analysis

Test No: GS054
Project : GOM2
Tested by: KM
Test Date: 10/27/2017

Boring : H002
Sample : 01CS-1
Location : GC955
Spec. Grav. = 2.65
Dry Soil Mass = 40.53 (gm)
Mass Disp. = 5.07 (gm)

Hydrometer: 151H Fisher Brand
Number = 98
Volume = 69.59 (cm^3)
Hr @ 1035 = 8.2 (cm)
Hr @ 1000 = 17.5 (cm)
Meniscus = 0.4 (gm/l)

Volumetric
Volume = 1000 (cm^3)
Area = 28.77 (cm^2)

Mass Measurement
Tare, soil, disp. = 45.20 (gm)
Tare = 0 (gm)

Note: Disp. not included in dry mass.

Note: Read hydrometer to 0.2 gm/l

Measurements					Constants		Results	
Date (mm/dd/yyyy)	Elasped Time (min)	Suspension Reading (SG*1000)	Water / Disp. Reading (SG*1000)	Temp. (C)	Viscosity (gm-sec/cm^2)	Reading Depth (cm)	Percent Finer (%)	Diameter (mm)
10/27/2017	0.16666	1030	1004.0	22.4	9.71E-06	9.4	103.0	0.09991
	0.25	1029.5	1004.0	22.4	9.71E-06	9.6	101.0	0.08215
	0.333	1029	1004.0	22.4	9.71E-06	9.7	99.0	0.07167
10/27/2017	0.5	1028.9	1004.0	22.4	9.71E-06	9.7	98.6	0.05857
	0.75	1028.4	1004.0	22.4	9.71E-06	9.8	96.6	0.04815
10/27/2017	1	1028.05	1004.0	22.4	9.71E-06	9.9	95.3	0.04189
10/27/2017	1.5	1027.4	1004.0	22.4	9.71E-06	10.1	92.7	0.03450
10/27/2017	2	1027	1004.0	22.4	9.71E-06	10.2	91.1	0.03004
10/27/2017	4	1025.2	1004.0	22.4	9.71E-06	9.5	84.0	0.02047
10/27/2017	8.0	1023.8	1004.0	22.4	9.71E-06	9.9	78.4	0.01475
10/27/2017	16	1022.3	1004.0	22.4	9.70E-06	10.3	72.5	0.01064
10/27/2017	32	1021.2	1004.0	22.5	9.69E-06	10.6	68.2	0.00762
10/27/2017	64	1020.0	1004.0	22.5	9.68E-06	10.9	63.5	0.00547
10/27/2017	134	1018.5	1004.0	22.5	9.69E-06	11.3	57.5	0.00385
10/27/2017	256	1017.6	1004.0	22.4	9.71E-06	11.5	53.8	0.00282
10/27/2017	512	1016.2	1004.0	22.4	9.71E-06	11.9	48.3	0.00202
10/27/2017	990	1015.2	1004.0	22.5	9.69E-06	12.1	44.4	0.00147
10/28/2017	1603	1015.1	1004.0	22.4	9.71E-06	12.2	44.0	0.00116
10/29/2017	3000	1013.4	1004.0	22.4	9.71E-06	12.6	37.2	0.00086

Sieve Data (wet sieved at 63 μm)
Mass retained on sieve: 0.400 (gm)
Sand-percent of dry mass: 0.99 (%)
Percent passing 63 μm: 99.01 (%)
Diameter: 0.0630 (mm)

Interpolated silt/clay boundary (at 2 μm)
Percent passing 2 μm: 48.1 (%)
Diameter: 0.002 (mm)

Remarks: For times greater than 2 minutes, an immersion correction is applied to the readings.

Figure A2. Hydrometer analysis for sample 01CS-1.

Hydrometer Analysis

Test No: GS054
Project : GOM2
Tested by: KM
Test Date: 10/23/2017

Boring : H002
Sample : 03CS-1
Location : GC955
Spec. Grav. = 2.65
Dry Soil Mass = 51.98 (gm)
Mass Disp. = 5.17 (gm)

Hydrometer: 151H Fisher Brand
Number = 98
Volume = 69.59 (cm^3)
H_r @ 1035 = 8.2 (cm)
H_r @ 1000 = 17.5 (cm)
Meniscus = 0.4 (gm/l)

Volumetric
Volume = 1000 (cm^3)
Area = 28.77 (cm^2)

Mass Measurement
fines + disp = 49.31 (gm)
Tare = 0 (gm)

Note: Disp. not included in dry mass.

Note: Read hydrometer to 0.2 gm/l

Measurements					Constants		Results	
Date (mm/dd/yyyy)	Elasped Time (min)	Suspension Reading (SG*1000)	Water / Disp. Reading (SG*1000)	Temp. (C)	Viscosity (gm-sec/cm^2)	Reading Depth (cm)	Percent Finer (%)	Diameter (mm)
10/23/2017	0.16666	1034	1004.0	22.2	9.74E-06	8.4	92.6	0.09426
	0.25	1033	1004.0	22.2	9.74E-06	8.6	89.5	0.07817
	0.333	1031.5	1004.0	22.2	9.74E-06	9.0	84.8	0.06928
10/23/2017	0.5	1030	1004.0	22.2	9.74E-06	9.4	80.2	0.05777
	0.75	1026.5	1004.0	22.2	9.74E-06	10.4	69.4	0.04944
10/23/2017	1	1024	1004.0	22.2	9.74E-06	11.0	61.7	0.04417
10/23/2017	1.5	1020	1004.0	22.2	9.74E-06	12.1	49.3	0.03777
10/23/2017	2	1017.1	1004.0	22.2	9.74E-06	12.9	40.4	0.03373
10/23/2017	4	1012.1	1004.0	22.3	9.74E-06	13.0	24.9	0.02396
10/23/2017	8.0	1010.0	1004.0	22.3	9.74E-06	13.5	18.3	0.01731
10/23/2017	16	1008.8	1004.0	22.3	9.73E-06	13.9	14.6	0.01238
10/23/2017	32.5	1008.0	1004.0	22.3	9.72E-06	14.1	12.3	0.00874
10/23/2017	64.5	1007.5	1004.0	22.4	9.70E-06	14.2	10.8	0.00623
10/23/2017	137	1007.2	1004.0	22.3	9.72E-06	14.3	9.8	0.00429
10/23/2017	257	1006.9	1004.0	22.3	9.72E-06	14.4	8.7	0.00314
10/23/2017	512	1006.8	1004.0	22.4	9.71E-06	14.4	8.6	0.00223
10/23/2017	1040	1006.7	1004.0	22.5	9.69E-06	14.4	8.4	0.00156
10/24/2017	1803	1006.0	1004.0	22.2	9.74E-06	14.6	6.1	0.00120

Sieve Data (wet sieved at 63 μm)
Mass retained on sieve: 7.840 (gm)
Sand-percent of dry mass: 15.08 (%)
Percent passing 63 μm: 84.92 (%)
Diameter: 0.0630 (mm)

Interpolated silt/clay boundary (at 2 μm)
Percent passing 2 μm: 8.5 (%)
Diameter: 0.002 (mm)

Remarks: For times greater than 2 minutes, an immersion correction is applied to the readings.

Figure A3. Hydrometer analysis for sample 03CS-1.

Hydrometer Analysis

Test No: GS054
Project : GOM2
Tested by: KM
Test Date: 11/18/2017

Boring : H005
Sample : 8CS-4
Location : GC955
Spec. Grav. = 2.65
Dry Soil Mass = 61.41 (gm)
Mass Disp. = 5.22 (gm)

Hydrometer: 151H Fisher Brand
Number = 98
Volume = 69.59 (cm^3)
H_r @ 1035 = 8.2 (cm)
H_r @ 1000 = 17.5 (cm)
Meniscus = 0.4 (gm/l)

Volumetric
Volume = 1000 (cm^3)
Area = 28.03 (cm^2)

Mass Measurement
Tare, soil, disp. = 51.61 (gm)
Tare = 0 (gm)

Note: Disp. not included in dry mass.

Note: Read hydrometer to 0.2 gm/l

Measurements					Constants		Results	
Date (mm/dd/yyyy)	Elasped Time (min)	Suspension Reading (SG*1000)	Water / Disp. Reading (SG*1000)	Temp. (C)	Viscosity (gm-sec/cm^2)	Reading Depth (cm)	Percent Finer (%)	Diameter (mm)
11/18/2017	0.16666	1036	1003.7	23.6	9.43E-06	7.8	84.4	0.08975
	0.25	1034.5	1003.7	23.6	9.43E-06	8.2	80.5	0.07512
	0.36667	1032.2	1003.7	23.6	9.43E-06	8.8	74.4	0.06429
11/18/2017	0.5	1030	1003.7	23.6	9.43E-06	9.4	68.7	0.05685
	0.75	1026.5	1003.7	23.6	9.43E-06	10.4	59.5	0.04865
11/18/2017	1	1023.5	1003.7	23.6	9.43E-06	11.1	51.7	0.04373
11/18/2017	1.5	1019.2	1003.7	23.6	9.43E-06	12.3	40.4	0.03749
11/18/2017	2	1016.5	1003.7	23.6	9.44E-06	13.0	33.4	0.03341
11/18/2017	4	1011.1	1003.7	23.6	9.43E-06	13.2	19.2	0.02379
11/18/2017	8.0	1008.8	1003.7	23.6	9.44E-06	13.8	13.2	0.01721
11/18/2017	16	1008.0	1003.8	23.5	9.45E-06	14.0	11.1	0.01227
11/18/2017	32	1007.2	1003.8	23.4	9.47E-06	14.2	9.0	0.00875
11/18/2017	64	1007.0	1003.8	23.2	9.52E-06	14.3	8.3	0.00622
11/18/2017	128	1006.9	1003.8	23.1	9.54E-06	14.3	8.0	0.00441
11/18/2017	256	1006.4	1003.9	22.8	9.60E-06	14.5	6.5	0.00314
11/18/2017	512	1006.4	1004.0	22.4	9.71E-06	14.5	6.3	0.00223
11/18/2017	1079	1006.3	1004.0	22.4	9.70E-06	14.5	6.0	0.00154
11/19/2017	1587	1006.7	1004.0	22.4	9.70E-06	14.4	7.1	0.00126
11/20/2017	2978	1006.5	1004.0	22.3	9.72E-06	14.4	6.5	0.00093

Sieve Data (wet sieved at 63 μm)
Mass retained on sieve: 15.020 (gm)
Sand-percent of dry mass: 24.46 (%)
Percent passing 63 μm: 75.54 (%)
Diameter: 0.0630 (mm)

Interpolated silt/clay boundary (at 2 μm)
Percent passing 2 μm: 6.2 (%)
Diameter: 0.002 (mm)

Remarks: For times greater than 2 minutes, an immersion correction is applied to the readings.

Figure A4. Hydrometer analysis for sample 08CS-4.

Hydrometer Analysis

Test No: GS054
Project : GOM2
Tested by: KM
Test Date: 11/18/2017

Boring : H005
Sample : 8CS-4
Location : GC955
Spec. Grav. = 2.65
Dry Soil Mass = 61.41 (gm)
Mass Disp. = 5.22 (gm)

Hydrometer: 151H Fisher Brand
Number = 98
Volume = 69.59 (cm^3)
H_r @ 1035 = 8.2 (cm)
H_r @ 1000 = 17.5 (cm)
Meniscus = 0.4 (gm/l)

Volumetric
Volume = 1000 (cm^3)
Area = 28.03 (cm^2)

Mass Measurement
Tare, soil, disp. = 51.61 (gm)
Tare = 0 (gm)

Note: Disp. not included in dry mass.

Note: Read hydrometer to 0.2 gm/l

Measurements					Constants		Results	
Date (mm/dd/yyyy)	Elasped Time (min)	Suspension Reading (SG*1000)	Water / Disp. Reading (SG*1000)	Temp. (C)	Viscosity (gm-sec/cm^2)	Reading Depth (cm)	Percent Finer (%)	Diameter (mm)
11/18/2017	0.16666	1036	1003.7	23.6	9.43E-06	7.8	84.4	0.08975
	0.25	1034.5	1003.7	23.6	9.43E-06	8.2	80.5	0.07512
	0.36667	1032.2	1003.7	23.6	9.43E-06	8.8	74.4	0.06429
11/18/2017	0.5	1030	1003.7	23.6	9.43E-06	9.4	68.7	0.05685
	0.75	1026.5	1003.7	23.6	9.43E-06	10.4	59.5	0.04865
11/18/2017	1	1023.5	1003.7	23.6	9.43E-06	11.1	51.7	0.04373
11/18/2017	1.5	1019.2	1003.7	23.6	9.43E-06	12.3	40.4	0.03749
11/18/2017	2	1016.5	1003.7	23.6	9.44E-06	13.0	33.4	0.03341
11/18/2017	4	1011.1	1003.7	23.6	9.43E-06	13.2	19.2	0.02379
11/18/2017	8.0	1008.8	1003.7	23.6	9.44E-06	13.8	13.2	0.01721
11/18/2017	16	1008.0	1003.8	23.5	9.45E-06	14.0	11.1	0.01227
11/18/2017	32	1007.2	1003.8	23.4	9.47E-06	14.2	9.0	0.00875
11/18/2017	64	1007.0	1003.8	23.2	9.52E-06	14.3	8.3	0.00622
11/18/2017	128	1006.9	1003.8	23.1	9.54E-06	14.3	8.0	0.00441
11/18/2017	256	1006.4	1003.9	22.8	9.60E-06	14.5	6.5	0.00314
11/18/2017	512	1006.4	1004.0	22.4	9.71E-06	14.5	6.3	0.00223
11/18/2017	1079	1006.3	1004.0	22.4	9.70E-06	14.5	6.0	0.00154
11/19/2017	1587	1006.7	1004.0	22.4	9.70E-06	14.4	7.1	0.00126
11/20/2017	2978	1006.5	1004.0	22.3	9.72E-06	14.4	6.5	0.00093

Sieve Data (wet sieved at 63 μm)
Mass retained on sieve: 15.020 (gm)
Sand-percent of dry mass: 24.46 (%)
Percent passing 63 μm: 75.54 (%)
Diameter: 0.0630 (mm)

Interpolated silt/clay boundary (at 2 μm)
Percent passing 2 μm: 6.2 (%)
Diameter: 0.002 (mm)

Remarks: For times greater than 2 minutes, an immersion correction is applied to the readings.

Figure A5. Hydrometer analysis for sample 08CS-4.

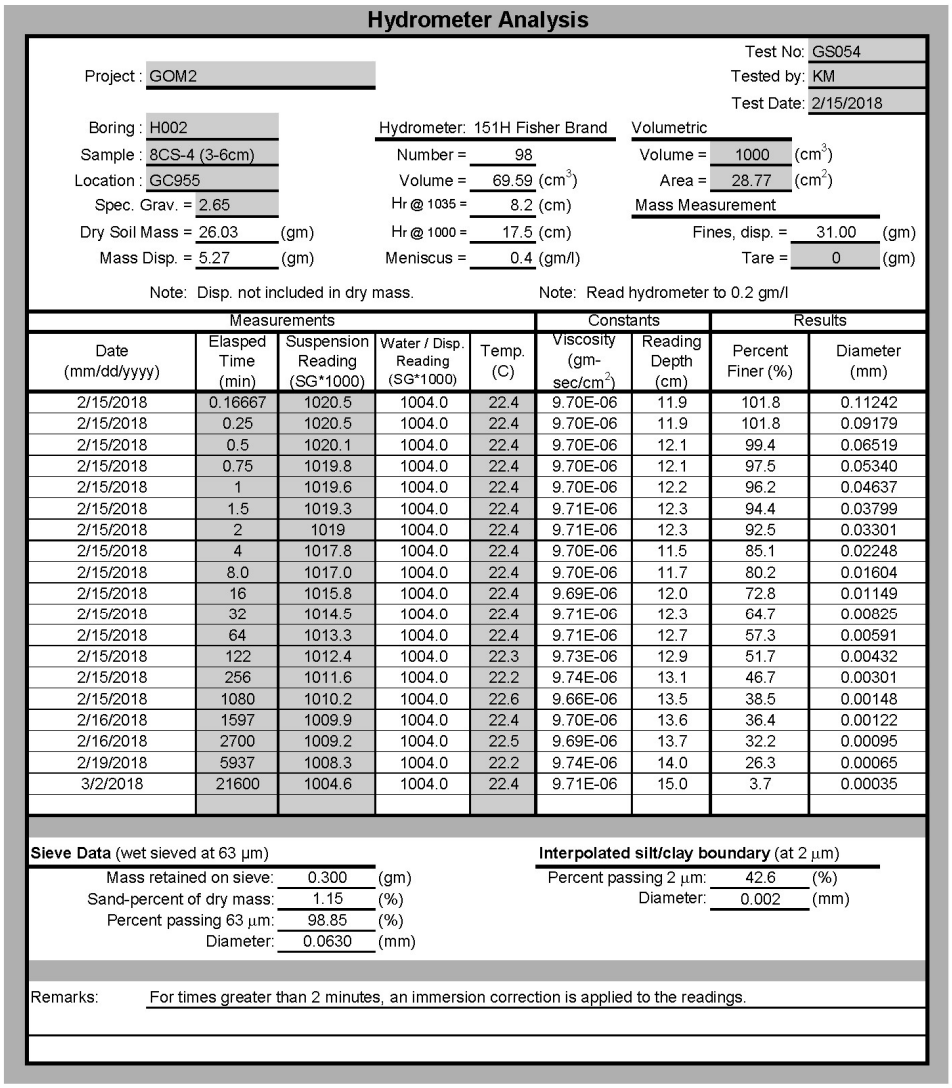

Hydrometer Analysis

Test No: GS054
Project : GOM2
Tested by: KM
Test Date: 2/15/2018

Boring : H002
Sample : 8CS-4 (3-6cm)
Location : GC955
Spec. Grav. = 2.65
Dry Soil Mass = 26.03 (gm)
Mass Disp. = 5.27 (gm)

Hydrometer: 151H Fisher Brand
Number = 98
Volume = 69.59 (cm^3)
Hr @ 1035 = 8.2 (cm)
Hr @ 1000 = 17.5 (cm)
Meniscus = 0.4 (gm/l)

Volumetric
Volume = 1000 (cm^3)
Area = 28.77 (cm^2)

Mass Measurement
Fines, disp. = 31.00 (gm)
Tare = 0 (gm)

Note: Disp. not included in dry mass.

Note: Read hydrometer to 0.2 gm/l

Measurements					Constants		Results	
Date (mm/dd/yyyy)	Elasped Time (min)	Suspension Reading (SG*1000)	Water / Disp. Reading (SG*1000)	Temp. (C)	Viscosity (gm-sec/cm^2)	Reading Depth (cm)	Percent Finer (%)	Diameter (mm)
2/15/2018	0.16667	1020.5	1004.0	22.4	9.70E-06	11.9	101.8	0.11242
2/15/2018	0.25	1020.5	1004.0	22.4	9.70E-06	11.9	101.8	0.09179
2/15/2018	0.5	1020.1	1004.0	22.4	9.70E-06	12.1	99.4	0.06519
2/15/2018	0.75	1019.8	1004.0	22.4	9.70E-06	12.1	97.5	0.05340
2/15/2018	1	1019.6	1004.0	22.4	9.70E-06	12.2	96.2	0.04637
2/15/2018	1.5	1019.3	1004.0	22.4	9.71E-06	12.3	94.4	0.03799
2/15/2018	2	1019	1004.0	22.4	9.71E-06	12.3	92.5	0.03301
2/15/2018	4	1017.8	1004.0	22.4	9.70E-06	11.5	85.1	0.02248
2/15/2018	8.0	1017.0	1004.0	22.4	9.70E-06	11.7	80.2	0.01604
2/15/2018	16	1015.8	1004.0	22.4	9.69E-06	12.0	72.8	0.01149
2/15/2018	32	1014.5	1004.0	22.4	9.71E-06	12.3	64.7	0.00825
2/15/2018	64	1013.3	1004.0	22.4	9.71E-06	12.7	57.3	0.00591
2/15/2018	122	1012.4	1004.0	22.3	9.73E-06	12.9	51.7	0.00432
2/15/2018	256	1011.6	1004.0	22.2	9.74E-06	13.1	46.7	0.00301
2/15/2018	1080	1010.2	1004.0	22.6	9.66E-06	13.5	38.5	0.00148
2/16/2018	1597	1009.9	1004.0	22.4	9.70E-06	13.6	36.4	0.00122
2/16/2018	2700	1009.2	1004.0	22.5	9.69E-06	13.7	32.2	0.00095
2/19/2018	5937	1008.3	1004.0	22.2	9.74E-06	14.0	26.3	0.00065
3/2/2018	21600	1004.6	1004.0	22.4	9.71E-06	15.0	3.7	0.00035

Sieve Data (wet sieved at 63 μm)
Mass retained on sieve: 0.300 (gm)
Sand-percent of dry mass: 1.15 (%)
Percent passing 63 μm: 98.85 (%)
Diameter: 0.0630 (mm)

Interpolated silt/clay boundary (at 2 μm)
Percent passing 2 μm: 42.6 (%)
Diameter: 0.002 (mm)

Remarks: For times greater than 2 minutes, an immersion correction is applied to the readings.

Figure A6. Hydrometer analysis f or sample 08CS-4 (3-6 cm).

Hydrometer Analysis

Test No: GS054
Project : GOM2
Tested by: KM
Test Date: 1/28/2018

Boring : H002
Sample : 8CS-4 (13-15cm)
Location : GC955
Spec. Grav. = 2.65
Dry Soil Mass = 28.40 (gm)
Mass Disp. = 4.59 (gm)

Hydrometer: 151H Fisher Brand
Number = 98
Volume = 69.59 (cm^3)
Hr @ 1035 = 8.2 (cm)
Hr @ 1000 = 17.5 (cm)
Meniscus = 0.4 (gm/l)

Volumetric
Volume = 1000 (cm^3)
Area = 28.77 (cm^2)
Mass Measurement
soil, disp. = 32.71 (gm)
Tare = 0 (gm)

Note: Disp. not included in dry mass.
Note: Read hydrometer to 0.2 gm/l

Measurements					Constants		Results	
Date (mm/dd/yyyy)	Elasped Time (min)	Suspension Reading (SG*1000)	Water / Disp. Reading (SG*1000)	Temp. (C)	Viscosity (gm-sec/cm^2)	Reading Depth (cm)	Percent Finer (%)	Diameter (mm)
1/28/2018	0.16667	1021.5	1004.0	22.3	9.72E-06	11.7	98.9	0.11129
1/28/2018	0.25	1021.5	1004.0	22.3	9.72E-06	11.7	98.9	0.09087
1/28/2018	0.5	1021	1004.0	22.3	9.72E-06	11.8	96.0	0.06462
1/28/2018	0.75	1020.8	1004.0	22.3	9.72E-06	11.9	94.9	0.05288
1/28/2018	1	1020.6	1004.0	22.3	9.72E-06	11.9	93.8	0.04590
1/28/2018	1.5	1020.1	1004.0	22.3	9.72E-06	12.1	91.0	0.03768
1/28/2018	2	1019.8	1004.0	22.4	9.71E-06	12.1	89.3	0.03273
1/28/2018	4	1018.8	1004.0	22.4	9.71E-06	11.2	83.6	0.02223
1/28/2018	8.0	1018.3	1004.0	22.4	9.71E-06	11.3	80.8	0.01581
1/28/2018	16	1017.6	1004.0	22.4	9.71E-06	11.5	76.8	0.01127
1/28/2018	32	1016.1	1004.0	22.5	9.69E-06	11.9	68.5	0.00810
1/28/2018	64	1015.1	1004.0	22.5	9.68E-06	12.2	62.9	0.00578
1/28/2018	128	1014.4	1004.0	22.5	9.67E-06	12.4	59.0	0.00412
1/28/2018	256	1013.7	1004.0	22.5	9.68E-06	12.5	55.0	0.00294
1/28/2018	527	1012.9	1004.0	22.5	9.68E-06	12.8	50.4	0.00206
1/28/2018	1059	1011.9	1004.0	22.4	9.71E-06	13.0	44.6	0.00147
1/29/2018	1734	1011.2	1004.0	22.4	9.70E-06	13.2	40.7	0.00116
1/31/2018	4360	1010.0	1004.0	22.4	9.72E-06	13.5	33.8	0.00074

Sieve Data (wet sieved at 63 μm)
Mass retained on sieve: 0.280 (gm)
Sand-percent of dry mass: 0.99 (%)
Percent passing 63 μm: 99.01 (%)
Diameter: 0.0630 (mm)

Interpolated silt/clay boundary (at 2 μm)
Percent passing 2 μm: 49.8 (%)
Diameter: 0.002 (mm)

Remarks: For times greater than 2 minutes, an immersion correction is applied to the readings.

Figure A7. Hydrometer analysis f or sample 08CS-4 (13-15 cm).

Hydrometer Analysis

Test No: GS054
Project : GOM2
Tested by: KM
Test Date: 1/28/2018

Boring : H002
Sample : 8CS-4 (18-21cm)
Location : GC955
Spec. Grav. = 2.65
Dry Soil Mass (Fine) = 27.88 (gm)
Mass Disp. = 4.27 (gm)

Hydrometer: 151H Fisher Brand
Number = 98
Volume = 69.59 (cm^3)
Hr @ 1035 = 8.2 (cm)
Hr @ 1000 = 17.5 (cm)
Meniscus = 0.4 (gm/l)

Volumetric
Volume = 1000 (cm^3)
Area = 28.77 (cm^2)

Mass Measurement
Tare, soil, disp. = 33.26 (gm)
Tare = 0 (gm)

Note: Disp. not included in dry mass.

Note: Read hydrometer to 0.2 gm/l

Measurements					Constants		Results	
Date (mm/dd/yyyy)	Elasped Time (min)	Suspension Reading (SG*1000)	Water / Disp. Reading (SG*1000)	Temp. (C)	Viscosity (gm-sec/cm^2)	Reading Depth (cm)	Percent Finer (%)	Diameter (mm)
1/28/2018	0.16667	1021	1004.0	22.3	9.74E-06	11.8	97.7	0.11202
1/28/2018	0.25	1020.5	1004.0	22.2	9.74E-06	11.9	94.8	0.09201
1/28/2018	0.3333	1020	1004.0	22.3	9.74E-06	12.1	92.0	0.08010
1/28/2018	0.5	1019	1004.0	22.3	9.74E-06	12.3	86.2	0.06611
1/28/2018	0.75	1018	1004.0	22.3	9.74E-06	12.6	80.5	0.05456
1/28/2018	1	1016.9	1004.0	22.3	9.74E-06	12.9	74.1	0.04779
1/28/2018	1.5	1014.3	1004.0	22.3	9.74E-06	13.6	59.1	0.04005
1/28/2018	2	1012.5	1004.0	22.3	9.74E-06	14.1	48.8	0.03529
1/28/2018	4	1009.3	1004.0	22.3	9.73E-06	13.7	30.3	0.02463
1/28/2018	8.0	1007.3	1004.0	22.4	9.71E-06	14.2	18.9	0.01773
1/28/2018	16	1006.9	1004.0	22.4	9.70E-06	14.4	16.7	0.01258
1/28/2018	32	1006.1	1004.0	22.4	9.69E-06	14.6	12.1	0.00896
1/28/2018	64	1006.0	1004.0	22.5	9.68E-06	14.6	11.6	0.00634
1/28/2018	128	1005.9	1004.0	22.5	9.69E-06	14.6	11.0	0.00449
1/28/2018	256	1005.5	1004.0	22.5	9.67E-06	14.7	8.8	0.00318
1/28/2018	519	1005.0	1004.0	22.5	9.67E-06	14.9	5.9	0.00224
1/28/2018	1029	1005.0	1004.0	22.5	9.69E-06	14.9	5.8	0.00160
1/29/2018	1730	1005.0	1004.0	22.5	9.69E-06	14.9	5.8	0.00123
1/31/2018	4354	1004.7	1004.0	22.4	9.71E-06	14.9	4.0	0.00078

Sieve Data (wet sieved at 63 μm)
Mass retained on sieve: 5.380 (gm)
Sand-percent of dry mass: 16.18 (%)
Percent passing 63 μm: 83.82 (%)
Diameter: 0.0630 (mm)

Interpolated silt/clay boundary (at 2 μm)
Percent passing 2 μm: 5.9 (%)
Diameter: 0.002 (mm)

Remarks: For times greater than 2 minutes, an immersion correction is applied to the readings.

Figure A8. Hydrometer analysis f or sample 08CS-4 (18-21 cm).

Hydrometer Analysis

Test No: GS054
Project : GOM2
Tested by: KM
Test Date: 2/15/2018

Boring : H002
Sample : 8CS-4 (39-41cm)
Location : GC955
Spec. Grav. = 2.65
Dry Soil Mass = 29.40 (gm)
Mass Disp. = 4.30 (gm)

Hydrometer: 151H Fisher Brand
Number = 98
Volume = 69.59 (cm^3)
Hr @ 1035 = 8.2 (cm)
Hr @ 1000 = 17.5 (cm)
Meniscus = 0.4 (gm/l)

Volumetric
Volume = 1000 (cm^3)
Area = 28.77 (cm^2)
Mass Measurement
soil, disp. = 28.31 (gm)
Tare = 0 (gm)

Note: Disp. not included in dry mass.
Note: Read hydrometer to 0.2 gm/l

Measurements					Constants		Results	
Date (mm/dd/yyyy)	Elasped Time (min)	Suspension Reading (SG*1000)	Water / Disp. Reading (SG*1000)	Temp. (C)	Viscosity (gm-sec/cm^2)	Reading Depth (cm)	Percent Finer (%)	Diameter (mm)
2/15/2018	0.16667	1020.5	1004.0	22.6	9.66E-06	11.9	90.3	0.11221
2/15/2018	0.25	1020.1	1004.0	22.6	9.66E-06	12.1	88.1	0.09203
2/15/2018	0.5	1019.6	1004.0	22.6	9.66E-06	12.2	85.4	0.06543
2/15/2018	0.75	1018.3	1004.0	22.6	9.66E-06	12.5	78.3	0.05418
2/15/2018	1	1016.9	1004.0	22.6	9.66E-06	12.9	70.7	0.04761
2/15/2018	1.5	1014.4	1004.0	22.5	9.67E-06	13.6	57.0	0.03988
2/15/2018	2	1012.4	1004.0	22.5	9.68E-06	14.1	46.0	0.03522
2/15/2018	4	1009.9	1004.0	22.5	9.68E-06	13.6	32.4	0.02442
2/15/2018	8.0	1007.6	1004.0	22.5	9.68E-06	14.2	19.8	0.01765
2/15/2018	16	1006.9	1004.0	22.5	9.69E-06	14.4	15.9	0.01257
2/15/2018	32	1006.1	1004.0	22.5	9.69E-06	14.6	11.5	0.00895
2/15/2018	64	1005.7	1004.0	22.4	9.71E-06	14.7	9.2	0.00636
2/15/2018	128	1005.7	1004.0	22.3	9.73E-06	14.7	9.1	0.00450
2/15/2018	258	1005.7	1004.0	22.4	9.70E-06	14.7	9.3	0.00317
2/15/2018	512	1005.5	1004.0	22.5	9.68E-06	14.7	8.3	0.00225
2/16/2018	1605	1005.3	1004.0	22.6	9.67E-06	14.8	7.3	0.00127
2/16/2018	2706	1005.2	1004.0	22.4	9.71E-06	14.8	6.5	0.00098

Sieve Data (wet sieved at 63 μm)
Mass retained on sieve: 5.390 (gm)
Sand-percent of dry mass: 18.33 (%)
Percent passing 63 μm: 81.67 (%)
Diameter: 0.0630 (mm)

Interpolated silt/clay boundary (at 2 μm)
Percent passing 2 μm: 8.0 (%)
Diameter: 0.002 (mm)

Remarks: For times greater than 2 minutes, an immersion correction is applied to the readings.

Figure A9. Hydrometer analysis f or sample 08CS-4 (39-41 cm).

Hydrometer Analysis

Test No: GS054
Project : GOM2-1-H005
Tested by: CAA
Test Date: 4/20/2010

Boring : H005
Sample : 1FB-1-1
Location : GC955
Spec. Grav. = 2.65
Dry Soil Mass = 31.60 (gm)
Mass Disp. = 5.02 (gm)

Hydrometer: 151H Fisher Brand
Number = 98
Volume = 69.59 (cm^3)
Hr @ 1035 = 20.2 (cm)
Hr @ 1000 = 25 (cm)
Meniscus = 0.4 (gm/l)

Volumetric
Volume = 1000 (cm^3)
Area = 28.40 (cm^2)

Mass Measurement
Tare, soil, disp. = 37.6 (gm)
Tare = 0 (gm)

Note: Disp. not included in dry mass.

Note: Read hydrometer to 0.2 gm/l

Measurements					Constants		Results	
Date (mm/dd/yyyy)	Elasped Time (min)	Suspension Reading (SG*1000)	Water / Disp. Reading (SG*1000)	Temp. (C)	Viscosity (gm-sec/cm^2)	Reading Depth (cm)	Percent Finer (%)	Diameter (mm)
8/24/2017	0.2166	1023.2	1003.8	23.2	9.52E-06	21.8	98.5	0.13185
8/24/2017	0.333	1022.9	1003.8	23.2	9.52E-06	21.8	97.0	0.10644
8/24/2017	0.5	1022.9	1003.8	23.2	9.52E-06	21.8	97.0	0.08686
8/24/2017	1	1022.75	1003.8	23.2	9.52E-06	21.8	96.2	0.06146
4/20/2010	1.5	1022.6	1003.8	23.2	9.52E-06	21.8	95.4	0.05020
4/20/2010	2	1022.5	1003.8	23.2	9.52E-06	21.9	94.9	0.04349
4/20/2010	4	1022.05	1003.8	23.2	9.53E-06	20.7	92.6	0.02993
4/20/2010	8.0	1021.3	1003.8	23.2	9.53E-06	20.8	88.8	0.02122
4/20/2010	16	1020.8	1003.8	23.2	9.53E-06	20.9	86.2	0.01503
4/20/2010	32	1020	1003.8	23.1	9.53E-06	21.0	82.1	0.01066
4/20/2010	65	1019	1003.9	22.9	9.60E-06	21.1	76.7	0.00753
4/20/2010	128	1017.9	1003.9	22.7	9.65E-06	21.3	70.9	0.00540
4/20/2010	258	1016.7	1004.0	22.5	9.69E-06	21.4	64.6	0.00382
4/20/2010	514	1015	1004.0	22.4	9.70E-06	21.7	55.9	0.00273
4/20/2010	1290	1013.7	1004.0	22.3	9.72E-06	21.8	49.2	0.00173
4/21/2010	1940	1009.5	1004.0	22.3	9.73E-06	22.4	27.8	0.00143
4/20/2010								

Sieve Data (wet sieved at 63 μm)
Mass retained on sieve: 0.040 (gm)
Sand-percent of dry mass: 0.13 (%)
Percent passing 63 μm: 99.87 (%)
Diameter: 0.0630 (mm)

Interpolated silt/clay boundary (at 2 μm)
Percent passing 2 μm: 51.0 (%)
Diameter: 0.002 (mm)

Remarks: For times greater than 2 minutes, an immersion correction is applied to the readings.

Figure A10. Hydrometer analysis f or sample 1FB-1-1.

Hydrometer Analysis

Test No: GS054
Project : GOM2
Tested by: KM
Test Date: 6/27/2017

Boring : H005
Sample : 1FB-2-TOPA
Location : GC955
Spec. Grav. = 2.65
Dry Soil Mass = 38.68 (gm)
Mass Disp. = 5.02 (gm)

Hydrometer: 151H Fisher Brand
Number = 98
Volume = 69.59 (cm^3)
Hr @ 1035 = 8.2 (cm)
Hr @ 1000 = 17.5 (cm)
Meniscus = 0.4 (gm/l)

Volumetric
Volume = 1000 (cm^3)
Area = 28.77 (cm^2)

Mass Measurement
Tare, soil, disp. = 43.67 (gm)
Tare = 0 (gm)

Note: Disp. not included in dry mass.

Note: Read hydrometer to 0.2 gm/l

Measurements					Constants		Results	
Date (mm/dd/yyyy)	Elasped Time (min)	Suspension Reading (SG*1000)	Water / Disp. Reading (SG*1000)	Temp. (C)	Viscosity (gm-sec/cm^2)	Reading Depth (cm)	Percent Finer (%)	Diameter (mm)
6/27/2017	0.25	1027.5	1004.0	22.6	9.66E-06	10.1	97.7	0.08420
6/27/2017	0.5	1027.5	1004.0	22.6	9.66E-06	10.1	97.7	0.05954
	0.75	1027.5	1004.0	22.6	9.66E-06	10.1	97.7	0.04861
6/27/2017	1	1027.5	1004.0	22.6	9.66E-06	10.1	97.7	0.04210
6/27/2017	1.5	1027.3	1004.0	22.6	9.66E-06	10.1	96.9	0.03446
6/27/2017	2	1027.1	1004.0	22.6	9.66E-06	10.2	96.1	0.02992
6/27/2017	4	1026.8	1004.0	22.6	9.66E-06	9.1	94.8	0.01995
6/27/2017	8.0	1026.5	1004.0	22.6	9.67E-06	9.1	93.6	0.01417
6/27/2017	16	1025.4	1004.0	22.5	9.68E-06	9.4	88.9	0.01019
6/27/2017	32	1024.1	1004.0	22.5	9.69E-06	9.8	83.5	0.00734
6/27/2017	64	1023.4	1004.0	22.3	9.73E-06	10.0	80.4	0.00525
6/27/2017	128	1022.0	1004.0	22.2	9.75E-06	10.3	74.5	0.00378
6/27/2017	278	1019.8	1004.0	22.3	9.72E-06	10.9	65.5	0.00264
6/27/2017	512	1018.2	1004.0	22.3	9.73E-06	11.3	58.8	0.00198
6/27/2017	1024	1016.9	1004.0	22.3	9.73E-06	11.7	53.4	0.00142
6/28/2017	2053	1015.6	1004.0	22.3	9.74E-06	12.0	48.0	0.00102

Sieve Data (wet sieved at 63 μm)
Mass retained on sieve: 0.030 (gm)
Sand-percent of dry mass: 0.08 (%)
Percent passing 63 μm: 99.92 (%)
Diameter: 0.0630 (mm)

Interpolated silt/clay boundary (at 2 μm)
Percent passing 2 μm: 59.0 (%)
Diameter: 0.002 (mm)

Remarks: For times greater than 2 minutes, an immersion correction is applied to the readings.

Figure A11. Hydrometer analysis f or sample 1FB-1-1.

Hydrometer Analysis

Test No: GS054
Project : GOM2
Tested by: KM
Test Date: 9/13/2017

Boring : H005
Sample : 1FB-3-1
Location : GC955
Spec. Grav. = 2.65
Dry Soil Mass = 47.51 (gm)
Mass Disp. = 4.96 (gm)

Hydrometer: 151H Fisher Brand
Number = 98
Volume = 69.59 (cm^3)
Hr @ 1035 = 8.2 (cm)
Hr @ 1000 = 17.5 (cm)
Meniscus = 0.4 (gm/l)

Volumetric
Volume = 1000 (cm^3)
Area = 28.77 (cm^2)

Mass Measurement
Tare, soil, disp. = 52.32 (gm)
Tare = 0 (gm)

Note: Disp. not included in dry mass.

Note: Read hydrometer to 0.2 gm/l

Measurements					Constants		Results	
Date (mm/dd/yyyy)	Elasped Time (min)	Suspension Reading (SG*1000)	Water / Disp. Reading (SG*1000)	Temp. (C)	Viscosity (gm-sec/cm^2)	Reading Depth (cm)	Percent Finer (%)	Diameter (mm)
9/13/2017	0.25	1033.5	1004.0	22.5	9.68E-06	8.5	99.8	0.07732
9/13/2017	0.5	1033.5	1004.0	22.5	9.68E-06	8.5	99.8	0.05468
	0.75	1033.3	1004.0	22.5	9.68E-06	8.5	99.1	0.04478
9/13/2017	1	1033.2	1004.0	22.5	9.68E-06	8.6	98.8	0.03884
9/13/2017	1.5	1033.1	1004.0	22.5	9.68E-06	8.6	98.4	0.03176
9/13/2017	2	1033	1004.0	22.5	9.68E-06	8.6	98.1	0.02755
9/13/2017	4	1032.4	1004.0	22.5	9.68E-06	7.6	96.1	0.01825
9/13/2017	8.0	1031.2	1004.0	22.6	9.67E-06	7.9	92.1	0.01317
9/13/2017	16	1030.1	1004.0	22.6	9.66E-06	8.2	88.3	0.00948
9/13/2017	32	1028.6	1004.0	22.5	9.68E-06	8.6	83.2	0.00687
9/13/2017	64.5	1027.0	1004.0	22.3	9.73E-06	9.0	77.5	0.00498
9/13/2017	128	1025.0	1004.0	22.3	9.72E-06	9.5	70.9	0.00363
9/13/2017	256	1023.0	1004.0	22.4	9.70E-06	10.1	64.2	0.00263
9/13/2017	512	1020.6	1004.0	22.4	9.70E-06	10.7	56.1	0.00192
9/13/2017	1008	1019.2	1004.0	22.3	9.74E-06	11.1	51.1	0.00140
9/14/2017	1666	1018.2	1004.1	22.1	9.79E-06	11.3	47.7	0.00110
9/17/2017	7095	1015.5	1004.0	22.3	9.73E-06	12.1	38.8	0.00055

Sieve Data (wet sieved at 63 μm)
Mass retained on sieve: 0.150 (gm)
Sand-percent of dry mass: 0.32 (%)
Percent passing 63 μm: 99.68 (%)
Diameter: 0.0630 (mm)

Interpolated silt/clay boundary (at 2 μm)
Percent passing 2 μm: 56.9 (%)
Diameter: 0.002 (mm)

Remarks: For times greater than 2 minutes, an immersion correction is applied to the readings.

Figure A12. Hydrometer analysis f or sample 1FB-3-1.

Hydrometer Analysis

Test No: GS054
Project : GOM2
Tested by: KM
Test Date: 6/27/2017

Boring : H005
Sample : 2FB-1-TOPA
Location : GC955
Spec. Grav. = 2.65
Dry Soil Mass = 39.58 (gm)
Mass Disp. = 5.00 (gm)

Hydrometer: 151H Fisher Brand
Number = 98
Volume = 69.59 (cm^3)
Hr @ 1035 = 8.2 (cm)
Hr @ 1000 = 17.5 (cm)
Meniscus = 0.4 (gm/l)

Volumetric
Volume = 1000 (cm^3)
Area = 28.77 (cm^2)

Mass Measurement
Tare, soil, disp. = 42.92 (gm)
Tare = 0 (gm)

Note: Disp. not included in dry mass.

Note: Read hydrometer to 0.2 gm/l

Measurements					Constants		Results	
Date (mm/dd/yyyy)	Elasped Time (min)	Suspension Reading (SG*1000)	Water / Disp. Reading (SG*1000)	Temp. (C)	Viscosity (gm-sec/cm^2)	Reading Depth (cm)	Percent Finer (%)	Diameter (mm)
6/27/2017	0.25	1028.5	1004.0	22.3	9.73E-06	9.8	99.3	0.08337
6/27/2017	0.5	1027.5	1004.0	22.3	9.73E-06	10.1	95.2	0.05975
	0.75	1027	1004.0	22.3	9.73E-06	10.2	93.2	0.04910
6/27/2017	1	1026.9	1004.0	22.3	9.73E-06	10.2	92.8	0.04258
6/27/2017	1.5	1026.2	1004.0	22.3	9.73E-06	10.4	90.0	0.03508
6/27/2017	2	1026	1004.0	22.3	9.73E-06	10.5	89.1	0.03046
6/27/2017	4	1024.5	1004.0	22.3	9.73E-06	9.7	82.9	0.02070
6/27/2017	8.0	1023.4	1004.0	22.3	9.74E-06	10.0	78.4	0.01486
6/27/2017	16	1022.5	1004.0	22.3	9.73E-06	10.2	74.7	0.01063
6/27/2017	32	1021.9	1004.0	22.3	9.73E-06	10.4	72.5	0.00757
6/27/2017	64	1020.5	1004.0	22.3	9.72E-06	10.7	66.9	0.00545
6/27/2017	150	1019.5	1004.0	22.3	9.72E-06	11.0	62.8	0.00360
6/27/2017	284	1018.1	1004.0	22.4	9.71E-06	11.4	57.2	0.00266
6/27/2017	517	1017.1	1004.0	22.3	9.72E-06	11.6	53.1	0.00199
6/27/2017	1054	1015.8	1004.0	22.2	9.75E-06	12.0	47.7	0.00142
6/29/2017	3024	1014.1	1004.0	22.3	9.72E-06	12.4	40.9	0.00085

Sieve Data (wet sieved at 63 μm)
Mass retained on sieve: 1.660 (gm)
Sand-percent of dry mass: 4.19 (%)
Percent passing 63 μm: 95.81 (%)
Diameter: 0.0630 (mm)

Interpolated silt/clay boundary (at 2 μm)
Percent passing 2 μm: 53.1 (%)
Diameter: 0.002 (mm)

Remarks: For times greater than 2 minutes, an immersion correction is applied to the readings.

Figure A13. Hydrometer analysis f or sample 02FB-1.

Hydrometer Analysis

Test No: GS054
Project : GOM2
Tested by: KM
Test Date: 6/27/2017

Boring : H005
Sample : 3FB-2-1
Location : GC955
Spec. Grav. = 2.65
Dry Soil Mass = 38.96 (gm)
Mass Disp. = 4.92 (gm)

Hydrometer: 151H Fisher Brand
Number = 98
Volume = 69.59 (cm^3)
Hr @ 1035 = 8.2 (cm)
Hr @ 1000 = 17.5 (cm)
Meniscus = 0.4 (gm/l)

Volumetric
Volume = 1000 (cm^3)
Area = 28.77 (cm^2)

Mass Measurement
Tare, soil, disp. = 43.22 (gm)
Tare = 0 (gm)

Note: Disp. not included in dry mass.

Note: Read hydrometer to 0.2 gm/l

Measurements					Constants		Results	
Date (mm/dd/yyyy)	Elasped Time (min)	Suspension Reading (SG*1000)	Water / Disp. Reading (SG*1000)	Temp. (C)	Viscosity (gm-sec/cm^2)	Reading Depth (cm)	Percent Finer (%)	Diameter (mm)
6/27/2017	0.25	1027.5	1003.8	23.5	9.45E-06	10.1	97.9	0.08327
6/27/2017	0.36666	1026.9	1003.8	23.5	9.45E-06	10.2	95.4	0.06930
	0.5	1026.2	1003.8	23.5	9.45E-06	10.4	92.5	0.05988
6/27/2017	1	1025.1	1003.8	23.5	9.45E-06	10.7	88.0	0.04293
6/27/2017	1.5	1024.1	1003.8	23.5	9.45E-06	11.0	83.9	0.03548
6/27/2017	2	1023.2	1003.8	23.5	9.45E-06	11.2	80.1	0.03106
	2.166667	1023	1003.8	23.4	9.48E-06	10.1	79.2	0.02831
6/27/2017	4	1021.6	1003.8	23.4	9.48E-06	10.4	73.4	0.02122
6/27/2017	8.0	1020.0	1003.8	23.4	9.48E-06	10.9	66.8	0.01531
6/27/2017	16	1019.0	1003.8	23.3	9.51E-06	11.1	62.6	0.01097
6/27/2017	32	1017.9	1003.8	23.2	9.53E-06	11.4	58.0	0.00786
6/27/2017	64	1017.0	1003.9	22.8	9.62E-06	11.7	53.9	0.00565
6/27/2017	128	1015.7	1004.0	22.6	9.67E-06	12.0	48.4	0.00406
6/27/2017	256	1014.5	1004.0	22.4	9.71E-06	12.3	43.2	0.00292
6/27/2017	512	1013.5	1004.0	22.3	9.73E-06	12.6	39.1	0.00209
6/27/2017	1255	1012.1	1004.0	22.3	9.74E-06	13.0	33.2	0.00135
6/28/2017	1776	1011.8	1004.0	22.4	9.70E-06	13.0	32.2	0.00114

Sieve Data (wet sieved at 63 μm)
Mass retained on sieve: 0.660 (gm)
Sand-percent of dry mass: 1.69 (%)
Percent passing 63 μm: 98.31 (%)
Diameter: 0.0630 (mm)

Interpolated silt/clay boundary (at 2 μm)
Percent passing 2 μm: 38.4 (%)
Diameter: 0.002 (mm)

Remarks: For times greater than 2 minutes, an immersion correction is applied to the readings.

Figure A14. Hydrometer analysis f or sample 3FB-2-1.

Hydrometer Analysis

Test No: GS054
Project : GOM2
Tested by: KM
Test Date: 9/27/2017

Boring : H005
Sample : 3FB-3-1
Location : GC955
Spec. Grav. = 2.65
Dry Soil Mass = 54.89 (gm)
Mass Disp. = 4.89 (gm)

Hydrometer: 151H Fisher Brand
Number = 98
Volume = 69.59 (cm^3)
Hr @ 1035 = 8.2 (cm)
Hr @ 1000 = 17.5 (cm)
Meniscus = 0.4 (gm/l)

Volumetric
Volume = 1000 (cm^3)
Area = 28.77 (cm^2)

Mass Measurement
Tare, soil, disp. = 44.07 (gm)
Tare = 0 (gm)

Note: Disp. not included in dry mass.

Note: Read hydrometer to 0.2 gm/l

Measurements					Constants		Results	
Date (mm/dd/yyyy)	Elasped Time (min)	Suspension Reading (SG*1000)	Water / Disp. Reading (SG*1000)	Temp. (C)	Viscosity (gm-sec/cm^2)	Reading Depth (cm)	Percent Finer (%)	Diameter (mm)
9/27/2017	0.25	1032	1004.0	22.4	9.71E-06	8.9	81.9	0.07924
9/27/2017	0.5	1028	1004.0	22.4	9.71E-06	10.0	70.2	0.05929
9/27/2017	0.75	1024.4	1004.0	22.4	9.71E-06	10.9	59.7	0.05068
9/27/2017	1	1021.5	1004.0	22.4	9.71E-06	11.7	51.2	0.04541
9/27/2017	1.5	1017.5	1004.0	22.4	9.71E-06	12.7	39.5	0.03873
9/27/2017	2	1015	1004.0	22.4	9.71E-06	13.4	32.2	0.03440
9/27/2017	4	1010.7	1004.0	22.4	9.72E-06	13.3	19.6	0.02427
9/27/2017	8.0	1008.3	1004.0	22.4	9.71E-06	14.0	12.4	0.01757
9/27/2017	16	1007.3	1004.0	22.4	9.71E-06	14.3	9.5	0.01254
9/27/2017	32	1007.2	1004.0	22.4	9.72E-06	14.3	9.2	0.00888
9/27/2017	64	1006.9	1004.0	22.3	9.73E-06	14.4	8.4	0.00630
9/27/2017	128	1006.8	1004.0	22.4	9.72E-06	14.4	8.1	0.00445
9/27/2017	256	1006.3	1004.0	22.4	9.71E-06	14.5	6.7	0.00316
9/27/2017	512	1006.1	1004.0	22.3	9.72E-06	14.6	6.1	0.00224
9/27/2017	1008	1005.9	1004.0	22.2	9.75E-06	14.6	5.4	0.00160
9/28/2017	1672	1005.9	1004.1	22.0	9.80E-06	14.6	5.3	0.00125

Sieve Data (wet sieved at 63 μm)
Mass retained on sieve: 15.710 (gm)
Sand-percent of dry mass: 28.62 (%)
Percent passing 63 μm: 71.38 (%)
Diameter: 0.0630 (mm)

Interpolated silt/clay boundary (at 2 μm)
Percent passing 2 μm: 5.8 (%)
Diameter: 0.002 (mm)

Remarks: For times greater than 2 minutes, an immersion correction is applied to the readings.

Figure A15. Hydrometer analysis f or sample 03FB-3-1.

Hydrometer Analysis

Test No: GS054
Project : GOM2
Tested by: KM
Test Date: 10/26/2017

Boring : H005
Sample : 04FB-1
Location : GC955
Spec. Grav. = 2.65
Dry Soil Mass = 44.02 (gm)
Mass Disp. = 5.07 (gm)

Hydrometer: 151H Fisher Brand
Number = 98
Volume = 69.59 (cm^3)
Hr @ 1035 = 8.2 (cm)
Hr @ 1000 = 17.5 (cm)
Meniscus = 0.4 (gm/l)

Volumetric
Volume = 1000 (cm^3)
Area = 28.77 (cm^2)

Mass Measurement
Tare, soil, disp. = 47.27 (gm)
Tare = 0 (gm)

Note: Disp. not included in dry mass.

Note: Read hydrometer to 0.2 gm/l

Measurements					Constants		Results	
Date (mm/dd/yyyy)	Elasped Time (min)	Suspension Reading (SG*1000)	Water / Disp. Reading (SG*1000)	Temp. (C)	Viscosity (gm-sec/cm^2)	Reading Depth (cm)	Percent Finer (%)	Diameter (mm)
10/26/2017	0.16666	1031	1004.0	22.5	9.69E-06	9.2	98.6	0.09836
	0.25	1030.5	1004.0	22.5	9.69E-06	9.3	96.7	0.08089
	0.333	1030.5	1004.0	22.5	9.69E-06	9.3	96.7	0.07009
10/26/2017	0.5	1029.5	1004.0	22.5	9.69E-06	9.6	93.1	0.05801
	0.75	1028	1004.0	22.5	9.69E-06	10.0	87.6	0.04834
10/26/2017	1	1026.2	1004.0	22.5	9.69E-06	10.4	81.0	0.04286
10/26/2017	1.5	1024.3	1004.0	22.5	9.69E-06	10.9	74.1	0.03583
10/26/2017	2	1023	1004.0	22.5	9.69E-06	11.3	69.4	0.03152
10/26/2017	4	1020.2	1004.0	22.5	9.69E-06	10.8	59.2	0.02182
10/26/2017	8.0	1018.7	1004.0	22.5	9.68E-06	11.2	53.7	0.01571
10/26/2017	16	1017.0	1004.0	22.5	9.67E-06	11.7	47.5	0.01132
10/26/2017	38	1015.5	1004.0	22.6	9.66E-06	12.1	42.1	0.00747
10/26/2017	64	1015.0	1004.0	22.6	9.65E-06	12.2	40.3	0.00578
10/26/2017	134	1014.1	1004.0	22.6	9.65E-06	12.4	37.0	0.00404
10/26/2017	256	1013.2	1004.0	22.4	9.70E-06	12.7	33.6	0.00296
10/26/2017	512	1012.2	1004.0	22.4	9.70E-06	12.9	29.9	0.00211
10/26/2017	1032	1011.7	1004.0	22.5	9.68E-06	13.1	28.2	0.00149
10/27/2017	1580	1011.5	1004.0	22.4	9.70E-06	13.1	27.4	0.00121
10/28/2017	2966	1010.4	1004.0	22.3	9.72E-06	13.4	23.3	0.00089

Sieve Data (wet sieved at 63 μm)
Mass retained on sieve: 1.820 (gm)
Sand-percent of dry mass: 4.13 (%)
Percent passing 63 μm: 95.87 (%)
Diameter: 0.0630 (mm)

Interpolated silt/clay boundary (at 2 μm)
Percent passing 2 μm: 29.6 (%)
Diameter: 0.002 (mm)

Remarks: For times greater than 2 minutes, an immersion correction is applied to the readings.
Disaggregated sample, possible drilling mud contamination.

Figure A16. Hydrometer analysis f or sample 04FB-1.

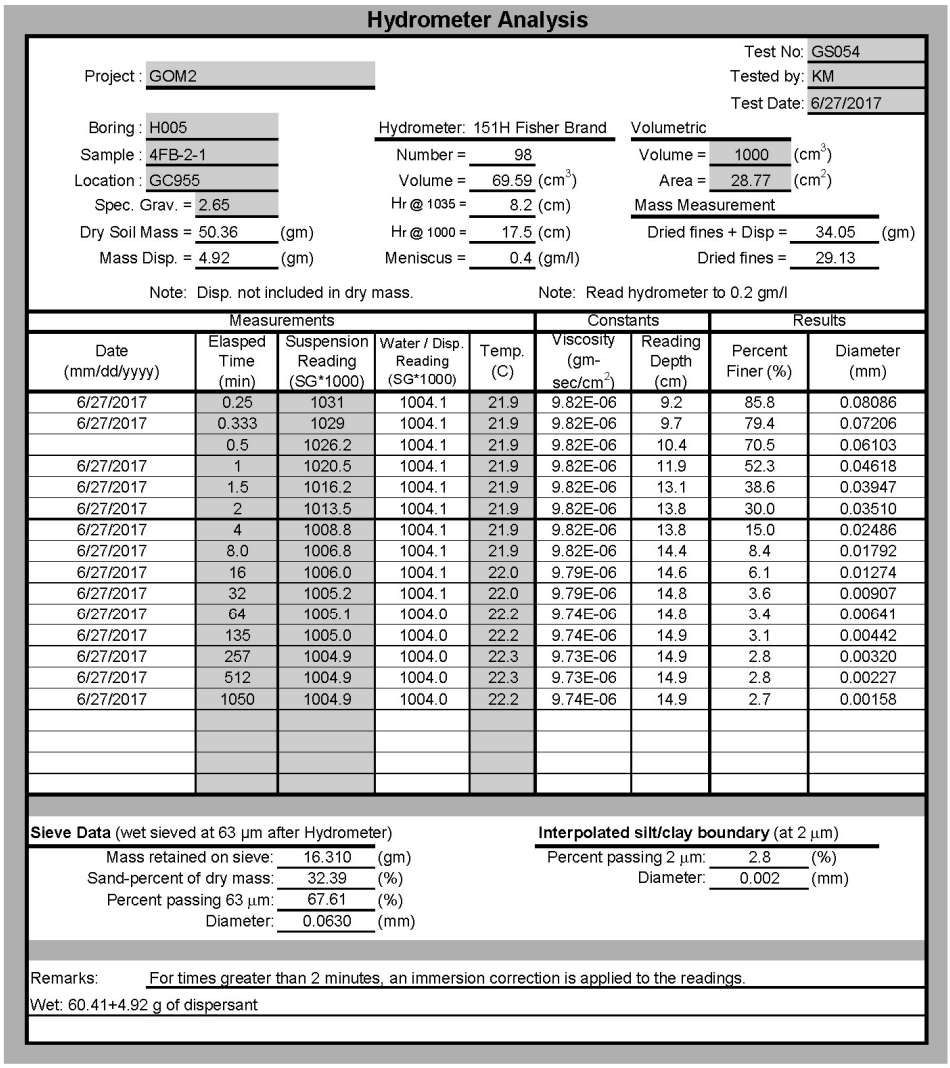

Hydrometer Analysis

Test No: GS054
Project : GOM2
Tested by: KM
Test Date: 6/27/2017

Boring : H005
Sample : 4FB-2-1
Location : GC955
Spec. Grav. = 2.65
Dry Soil Mass = 50.36 (gm)
Mass Disp. = 4.92 (gm)

Hydrometer: 151H Fisher Brand
Number = 98
Volume = 69.59 (cm^3)
Hr @ 1035 = 8.2 (cm)
Hr @ 1000 = 17.5 (cm)
Meniscus = 0.4 (gm/l)

Volumetric
Volume = 1000 (cm^3)
Area = 28.77 (cm^2)

Mass Measurement
Dried fines + Disp = 34.05 (gm)
Dried fines = 29.13

Note: Disp. not included in dry mass.

Note: Read hydrometer to 0.2 gm/l

Measurements					Constants		Results	
Date (mm/dd/yyyy)	Elasped Time (min)	Suspension Reading (SG*1000)	Water / Disp. Reading (SG*1000)	Temp. (C)	Viscosity (gm-sec/cm^2)	Reading Depth (cm)	Percent Finer (%)	Diameter (mm)
6/27/2017	0.25	1031	1004.1	21.9	9.82E-06	9.2	85.8	0.08086
6/27/2017	0.333	1029	1004.1	21.9	9.82E-06	9.7	79.4	0.07206
	0.5	1026.2	1004.1	21.9	9.82E-06	10.4	70.5	0.06103
6/27/2017	1	1020.5	1004.1	21.9	9.82E-06	11.9	52.3	0.04618
6/27/2017	1.5	1016.2	1004.1	21.9	9.82E-06	13.1	38.6	0.03947
6/27/2017	2	1013.5	1004.1	21.9	9.82E-06	13.8	30.0	0.03510
6/27/2017	4	1008.8	1004.1	21.9	9.82E-06	13.8	15.0	0.02486
6/27/2017	8.0	1006.8	1004.1	21.9	9.82E-06	14.4	8.4	0.01792
6/27/2017	16	1006.0	1004.1	22.0	9.79E-06	14.6	6.1	0.01274
6/27/2017	32	1005.2	1004.1	22.0	9.79E-06	14.8	3.6	0.00907
6/27/2017	64	1005.1	1004.0	22.2	9.74E-06	14.8	3.4	0.00641
6/27/2017	135	1005.0	1004.0	22.2	9.74E-06	14.9	3.1	0.00442
6/27/2017	257	1004.9	1004.0	22.3	9.73E-06	14.9	2.8	0.00320
6/27/2017	512	1004.9	1004.0	22.3	9.73E-06	14.9	2.8	0.00227
6/27/2017	1050	1004.9	1004.0	22.2	9.74E-06	14.9	2.7	0.00158

Sieve Data (wet sieved at 63 μm after Hydrometer)
Mass retained on sieve: 16.310 (gm)
Sand-percent of dry mass: 32.39 (%)
Percent passing 63 μm: 67.61 (%)
Diameter: 0.0630 (mm)

Interpolated silt/clay boundary (at 2 μm)
Percent passing 2 μm: 2.8 (%)
Diameter: 0.002 (mm)

Remarks: For times greater than 2 minutes, an immersion correction is applied to the readings.
Wet: 60.41+4.92 g of dispersant

Figure A17. Hydrometer analysis for sample 4FB-2-1.

Hydrometer Analysis

Test No: GS054
Project : GOM2
Tested by: KM
Test Date: 6/27/2017

Boring : H005
Sample : 4FB-3-01
Location : GC955
Spec. Grav. = 2.65
Dry Soil Mass = 43.81 (gm)
Mass Disp. = 4.94 (gm)

Hydrometer: 151H Fisher Brand
Number = 98
Volume = 69.59 (cm^3)
Hr @ 1035 = 8.2 (cm)
Hr @ 1000 = 17.5 (cm)
Meniscus = 0.4 (gm/l)

Volumetric
Volume = 1000 (cm^3)
Area = 28.77 (cm^2)

Mass Measurement
Tare, soil, disp. = 48.18 (gm)
Tare = 0 (gm)

Note: Disp. not included in dry mass.

Note: Read hydrometer to 0.2 gm/l

Measurements					Constants		Results	
Date (mm/dd/yyyy)	Elasped Time (min)	Suspension Reading (SG*1000)	Water / Disp. Reading (SG*1000)	Temp. (C)	Viscosity (gm-sec/cm^2)	Reading Depth (cm)	Percent Finer (%)	Diameter (mm)
6/27/2017	0.25	1031	1004.0	22.3	9.72E-06	9.2	98.9	0.08045
6/27/2017	0.5	1030.1	1004.0	22.3	9.72E-06	9.4	95.6	0.05762
	0.75	1029.7	1004.0	22.3	9.72E-06	9.5	94.2	0.04731
6/27/2017	1	1029.1	1004.0	22.3	9.72E-06	9.7	92.0	0.04132
6/27/2017	1.5	1028.2	1004.0	22.3	9.72E-06	9.9	88.7	0.03415
6/27/2017	2	1027.8	1004.0	22.3	9.72E-06	10.0	87.2	0.02973
6/27/2017	4	1025.9	1004.0	22.4	9.70E-06	9.3	80.1	0.02027
6/27/2017	8.0	1024.3	1004.0	22.4	9.71E-06	9.7	74.4	0.01465
6/27/2017	16	1023.6	1004.0	22.5	9.69E-06	9.9	71.9	0.01045
6/27/2017	32	1022.9	1004.0	22.4	9.70E-06	10.1	69.3	0.00746
6/27/2017	64	1021.0	1004.0	22.3	9.73E-06	10.6	62.2	0.00542
6/27/2017	156	1019.0	1004.0	22.3	9.73E-06	11.1	54.9	0.00355
6/27/2017	258	1017.9	1004.0	22.3	9.72E-06	11.4	50.9	0.00280
6/27/2017	549	1016.6	1004.0	22.4	9.71E-06	11.8	46.2	0.00195
6/27/2017	1036	1015.3	1004.0	22.3	9.72E-06	12.1	41.4	0.00144
6/28/2017	1455	1014.9	1004.0	22.2	9.74E-06	12.2	39.8	0.00122

Sieve Data (wet sieved at 63 μm)
Mass retained on sieve: 0.570 (gm)
Sand-percent of dry mass: 1.30 (%)
Percent passing 63 μm: 98.70 (%)
Diameter: 0.0630 (mm)

Interpolated silt/clay boundary (at 2 μm)
Percent passing 2 μm: 46.7 (%)
Diameter: 0.002 (mm)

Remarks: For times greater than 2 minutes, an immersion correction is applied to the readings.
Wet: 60.41+4.92 g of dispersant

Figure A18. Hydrometer analysis for sample 4FB-3-1.

Hydrometer Analysis

Test No: GS054
Project : GOM2
Tested by: KM
Test Date: 10/10/2017

Boring : H005
Sample : 4FB-4
Location : GC955
Spec. Grav. = 2.65
Dry Soil Mass = 54.16 (gm)
Mass Disp. = 5.02 (gm)

Hydrometer: 151H Fisher Brand
Number = 98
Volume = 69.59 (cm^3)
Hr @ 1035 = 8.2 (cm)
Hr @ 1000 = 17.5 (cm)
Meniscus = 0.4 (gm/l)

Volumetric
Volume = 1000 (cm^3)
Area = 28.77 (cm^2)

Fines Measurement
Tare, soil, disp. = 49.39 (gm)
Tare = 0 (gm)

Note: Disp. not included in dry mass.

Note: Read hydrometer to 0.2 gm/l

Measurements					Constants		Results	
Date (mm/dd/yyyy)	Elasped Time (min)	Suspension Reading (SG*1000)	Water / Disp. Reading (SG*1000)	Temp. (C)	Viscosity (gm-sec/cm^2)	Reading Depth (cm)	Percent Finer (%)	Diameter (mm)
10/10/2017	0.1666	1036	1004.1	21.9	9.83E-06	7.8	94.5	0.09166
10/10/2017	0.25	1034	1004.1	21.9	9.83E-06	8.4	88.6	0.07732
10/10/2017	0.3333	1032.5	1004.1	21.9	9.83E-06	8.8	84.1	0.06855
10/10/2017	0.5	1030.2	1004.1	21.9	9.83E-06	9.4	77.3	0.05788
10/10/2017	0.75	1027	1004.1	21.9	9.83E-06	10.2	67.8	0.04936
10/10/2017	1	1023.5	1004.1	21.9	9.82E-06	11.1	57.5	0.04462
10/10/2017	1.5	1019.3	1004.1	21.9	9.83E-06	12.3	45.0	0.03824
10/10/2017	2	1016	1004.1	21.9	9.83E-06	13.1	35.2	0.03428
10/10/2017	4	1010.0	1004.1	21.8	9.84E-06	13.5	17.4	0.02459
10/10/2017	8.0	1007.9	1004.1	21.8	9.84E-06	14.1	11.2	0.01775
10/10/2017	16	1007.1	1004.1	21.9	9.81E-06	14.3	8.9	0.01263
10/10/2017	34	1006.5	1004.1	22.1	9.79E-06	14.5	7.2	0.00870
10/10/2017	64	1006.0	1004.1	22.1	9.77E-06	14.6	5.7	0.00636
10/10/2017	128	1006.0	1004.1	22.1	9.78E-06	14.6	5.7	0.00450
10/10/2017	256	1005.9	1004.0	22.2	9.75E-06	14.6	5.5	0.00318
10/10/2017	512	1005.7	1004.0	22.2	9.75E-06	14.7	4.9	0.00225
10/10/2017	1069	1005.5	1004.1	22.2	9.76E-06	14.7	4.3	0.00156
10/11/2017	2670	1005.0	1004.1	22.1	9.77E-06	14.9	2.8	0.00099

Sieve Data (wet sieved at 63 μm)
Mass retained on sieve: 9.790 (gm)
Sand-percent of dry mass: 18.08 (%)
Percent passing 63 μm: 81.92 (%)
Diameter: 0.0630 (mm)

Interpolated silt/clay boundary (at 2 μm)
Percent passing 2 μm: 4.7 (%)
Diameter: 0.002 (mm)

Remarks: For times greater than 2 minutes, an immersion correction is applied to the readings.

Figure A19. Hydrometer analysis for sample 04FB-4.

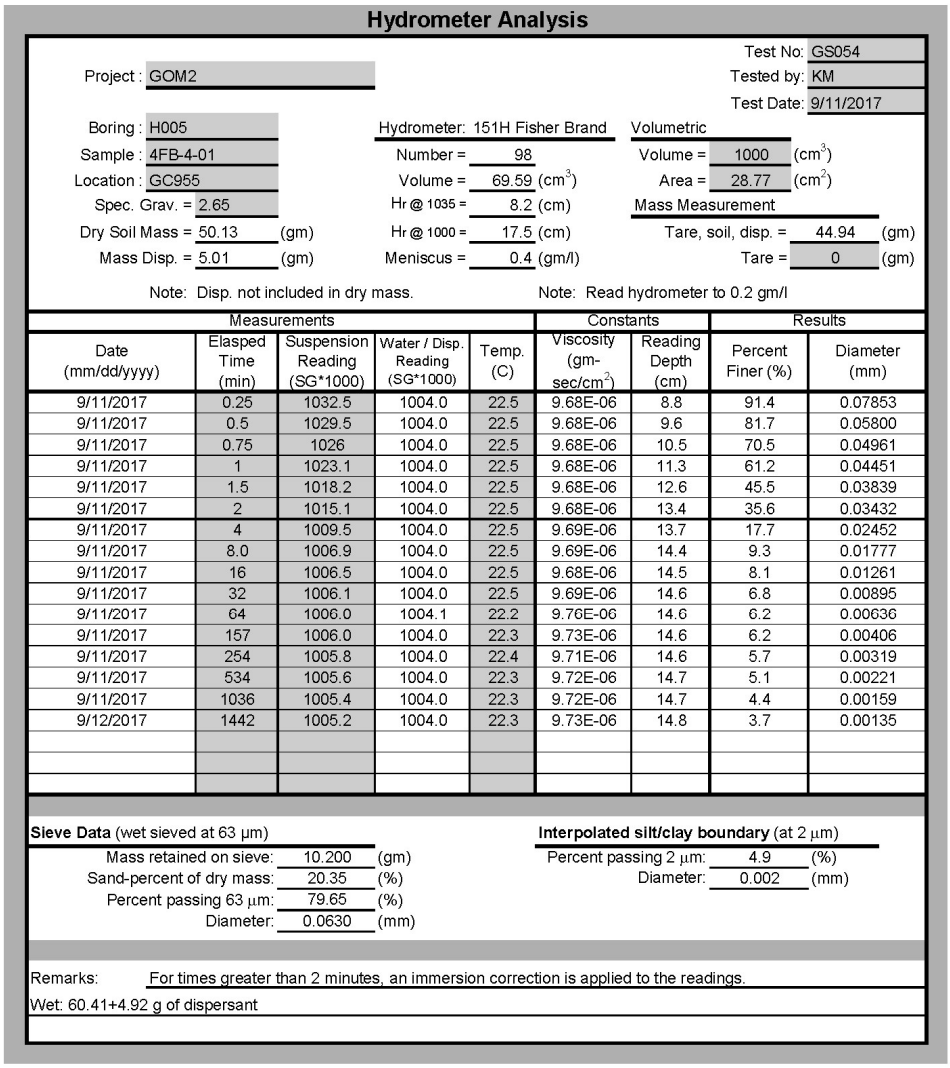

Hydrometer Analysis

Test No: GS054
Project : GOM2
Tested by: KM
Test Date: 9/11/2017

Boring : H005
Sample : 4FB-4-01
Location : GC955
Spec. Grav. = 2.65
Dry Soil Mass = 50.13 (gm)
Mass Disp. = 5.01 (gm)

Hydrometer: 151H Fisher Brand
Number = 98
Volume = 69.59 (cm^3)
Hr @ 1035 = 8.2 (cm)
Hr @ 1000 = 17.5 (cm)
Meniscus = 0.4 (gm/l)

Volumetric
Volume = 1000 (cm^3)
Area = 28.77 (cm^2)

Mass Measurement
Tare, soil, disp. = 44.94 (gm)
Tare = 0 (gm)

Note: Disp. not included in dry mass.

Note: Read hydrometer to 0.2 gm/l

Measurements					Constants		Results	
Date (mm/dd/yyyy)	Elasped Time (min)	Suspension Reading (SG*1000)	Water / Disp. Reading (SG*1000)	Temp. (C)	Viscosity (gm-sec/cm^2)	Reading Depth (cm)	Percent Finer (%)	Diameter (mm)
9/11/2017	0.25	1032.5	1004.0	22.5	9.68E-06	8.8	91.4	0.07853
9/11/2017	0.5	1029.5	1004.0	22.5	9.68E-06	9.6	81.7	0.05800
9/11/2017	0.75	1026	1004.0	22.5	9.68E-06	10.5	70.5	0.04961
9/11/2017	1	1023.1	1004.0	22.5	9.68E-06	11.3	61.2	0.04451
9/11/2017	1.5	1018.2	1004.0	22.5	9.68E-06	12.6	45.5	0.03839
9/11/2017	2	1015.1	1004.0	22.5	9.68E-06	13.4	35.6	0.03432
9/11/2017	4	1009.5	1004.0	22.5	9.69E-06	13.7	17.7	0.02452
9/11/2017	8.0	1006.9	1004.0	22.5	9.69E-06	14.4	9.3	0.01777
9/11/2017	16	1006.5	1004.0	22.5	9.68E-06	14.5	8.1	0.01261
9/11/2017	32	1006.1	1004.0	22.5	9.69E-06	14.6	6.8	0.00895
9/11/2017	64	1006.0	1004.1	22.2	9.76E-06	14.6	6.2	0.00636
9/11/2017	157	1006.0	1004.0	22.3	9.73E-06	14.6	6.2	0.00406
9/11/2017	254	1005.8	1004.0	22.4	9.71E-06	14.6	5.7	0.00319
9/11/2017	534	1005.6	1004.0	22.3	9.72E-06	14.7	5.1	0.00221
9/11/2017	1036	1005.4	1004.0	22.3	9.72E-06	14.7	4.4	0.00159
9/12/2017	1442	1005.2	1004.0	22.3	9.73E-06	14.8	3.7	0.00135

Sieve Data (wet sieved at 63 μm)
Mass retained on sieve: 10.200 (gm)
Sand-percent of dry mass: 20.35 (%)
Percent passing 63 μm: 79.65 (%)
Diameter: 0.0630 (mm)

Interpolated silt/clay boundary (at 2 μm)
Percent passing 2 μm: 4.9 (%)
Diameter: 0.002 (mm)

Remarks: For times greater than 2 minutes, an immersion correction is applied to the readings.
Wet: 60.41+4.92 g of dispersant

Figure A20. Hydrometer analysis for sample 04FB-4-01.

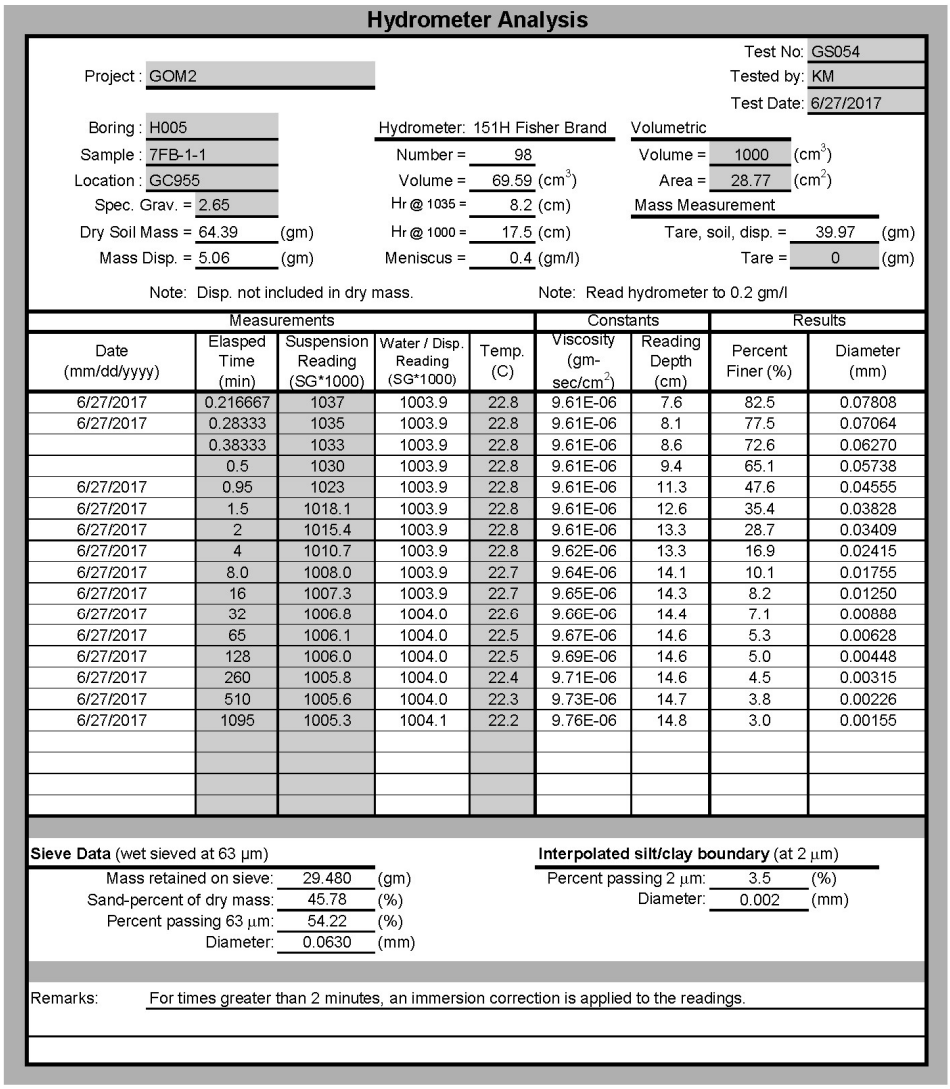

Hydrometer Analysis

Test No: GS054
Project : GOM2
Tested by: KM
Test Date: 6/27/2017

Boring : H005
Sample : 7FB-1-1
Location : GC955
Spec. Grav. = 2.65
Dry Soil Mass = 64.39 (gm)
Mass Disp. = 5.06 (gm)

Hydrometer: 151H Fisher Brand
Number = 98
Volume = 69.59 (cm^3)
Hr @ 1035 = 8.2 (cm)
Hr @ 1000 = 17.5 (cm)
Meniscus = 0.4 (gm/l)

Volumetric
Volume = 1000 (cm^3)
Area = 28.77 (cm^2)

Mass Measurement
Tare, soil, disp. = 39.97 (gm)
Tare = 0 (gm)

Note: Disp. not included in dry mass.

Note: Read hydrometer to 0.2 gm/l

Measurements					Constants		Results	
Date (mm/dd/yyyy)	Elasped Time (min)	Suspension Reading (SG*1000)	Water / Disp. Reading (SG*1000)	Temp. (C)	Viscosity (gm-sec/cm^2)	Reading Depth (cm)	Percent Finer (%)	Diameter (mm)
6/27/2017	0.216667	1037	1003.9	22.8	9.61E-06	7.6	82.5	0.07808
6/27/2017	0.28333	1035	1003.9	22.8	9.61E-06	8.1	77.5	0.07064
	0.38333	1033	1003.9	22.8	9.61E-06	8.6	72.6	0.06270
	0.5	1030	1003.9	22.8	9.61E-06	9.4	65.1	0.05738
6/27/2017	0.95	1023	1003.9	22.8	9.61E-06	11.3	47.6	0.04555
6/27/2017	1.5	1018.1	1003.9	22.8	9.61E-06	12.6	35.4	0.03828
6/27/2017	2	1015.4	1003.9	22.8	9.61E-06	13.3	28.7	0.03409
6/27/2017	4	1010.7	1003.9	22.8	9.62E-06	13.3	16.9	0.02415
6/27/2017	8.0	1008.0	1003.9	22.7	9.64E-06	14.1	10.1	0.01755
6/27/2017	16	1007.3	1003.9	22.7	9.65E-06	14.3	8.2	0.01250
6/27/2017	32	1006.8	1004.0	22.6	9.66E-06	14.4	7.1	0.00888
6/27/2017	65	1006.1	1004.0	22.5	9.67E-06	14.6	5.3	0.00628
6/27/2017	128	1006.0	1004.0	22.5	9.69E-06	14.6	5.0	0.00448
6/27/2017	260	1005.8	1004.0	22.4	9.71E-06	14.6	4.5	0.00315
6/27/2017	510	1005.6	1004.0	22.3	9.73E-06	14.7	3.8	0.00226
6/27/2017	1095	1005.3	1004.1	22.2	9.76E-06	14.8	3.0	0.00155

Sieve Data (wet sieved at 63 μm)
Mass retained on sieve: 29.480 (gm)
Sand-percent of dry mass: 45.78 (%)
Percent passing 63 μm: 54.22 (%)
Diameter: 0.0630 (mm)

Interpolated silt/clay boundary (at 2 μm)
Percent passing 2 μm: 3.5 (%)
Diameter: 0.002 (mm)

Remarks: For times greater than 2 minutes, an immersion correction is applied to the readings.

Figure A21. Hydrometer analysis for sample 07FB-1-1.

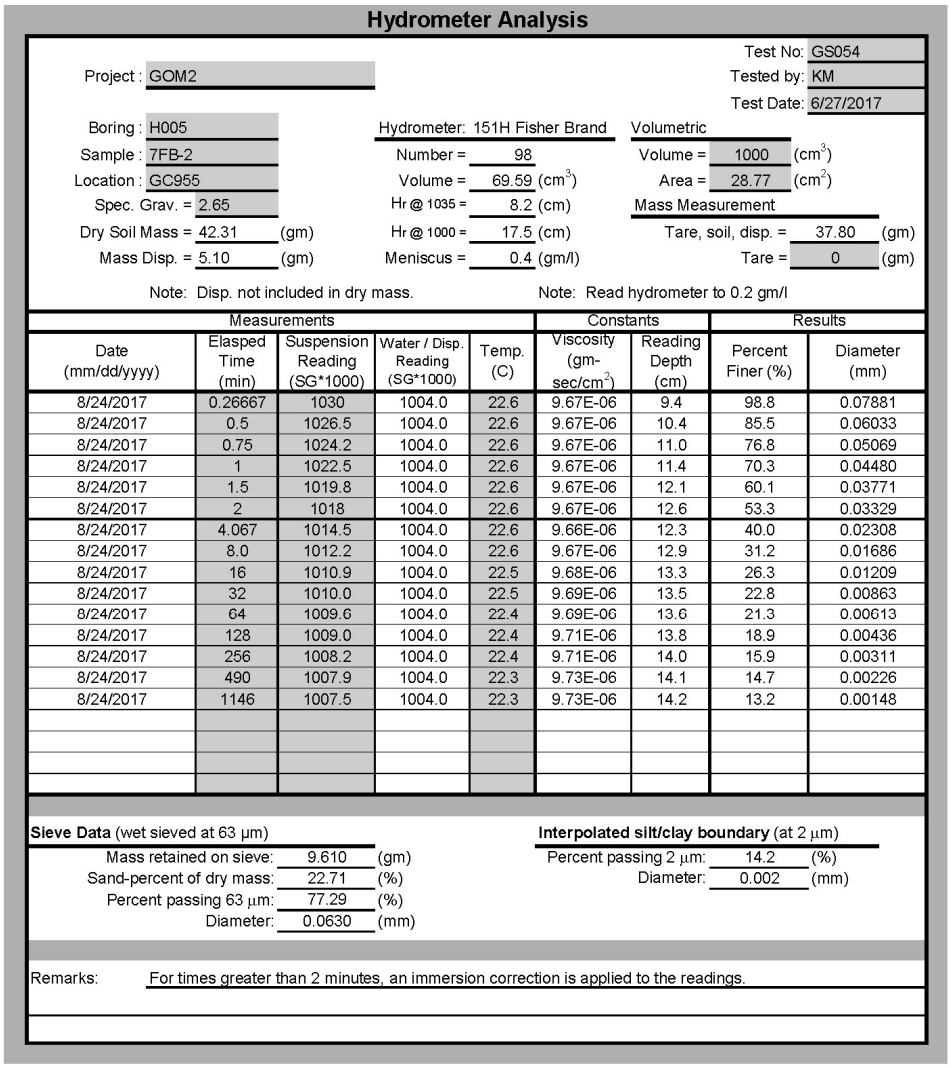

Hydrometer Analysis

Test No: GS054
Project : GOM2
Tested by: KM
Test Date: 6/27/2017

Boring : H005
Sample : 7FB-2
Location : GC955
Spec. Grav. = 2.65
Dry Soil Mass = 42.31 (gm)
Mass Disp. = 5.10 (gm)

Hydrometer: 151H Fisher Brand
Number = 98
Volume = 69.59 (cm^3)
Hr @ 1035 = 8.2 (cm)
Hr @ 1000 = 17.5 (cm)
Meniscus = 0.4 (gm/l)

Volumetric
Volume = 1000 (cm^3)
Area = 28.77 (cm^2)

Mass Measurement
Tare, soil, disp. = 37.80 (gm)
Tare = 0 (gm)

Note: Disp. not included in dry mass.
Note: Read hydrometer to 0.2 gm/l

Measurements					Constants		Results	
Date (mm/dd/yyyy)	Elasped Time (min)	Suspension Reading (SG*1000)	Water / Disp. Reading (SG*1000)	Temp. (C)	Viscosity (gm-sec/cm^2)	Reading Depth (cm)	Percent Finer (%)	Diameter (mm)
8/24/2017	0.26667	1030	1004.0	22.6	9.67E-06	9.4	98.8	0.07881
8/24/2017	0.5	1026.5	1004.0	22.6	9.67E-06	10.4	85.5	0.06033
8/24/2017	0.75	1024.2	1004.0	22.6	9.67E-06	11.0	76.8	0.05069
8/24/2017	1	1022.5	1004.0	22.6	9.67E-06	11.4	70.3	0.04480
8/24/2017	1.5	1019.8	1004.0	22.6	9.67E-06	12.1	60.1	0.03771
8/24/2017	2	1018	1004.0	22.6	9.67E-06	12.6	53.3	0.03329
8/24/2017	4.067	1014.5	1004.0	22.6	9.66E-06	12.3	40.0	0.02308
8/24/2017	8.0	1012.2	1004.0	22.6	9.67E-06	12.9	31.2	0.01686
8/24/2017	16	1010.9	1004.0	22.5	9.68E-06	13.3	26.3	0.01209
8/24/2017	32	1010.0	1004.0	22.5	9.69E-06	13.5	22.8	0.00863
8/24/2017	64	1009.6	1004.0	22.4	9.69E-06	13.6	21.3	0.00613
8/24/2017	128	1009.0	1004.0	22.4	9.71E-06	13.8	18.9	0.00436
8/24/2017	256	1008.2	1004.0	22.4	9.71E-06	14.0	15.9	0.00311
8/24/2017	490	1007.9	1004.0	22.3	9.73E-06	14.1	14.7	0.00226
8/24/2017	1146	1007.5	1004.0	22.3	9.73E-06	14.2	13.2	0.00148

Sieve Data (wet sieved at 63 μm)
Mass retained on sieve: 9.610 (gm)
Sand-percent of dry mass: 22.71 (%)
Percent passing 63 μm: 77.29 (%)
Diameter: 0.0630 (mm)

Interpolated silt/clay boundary (at 2 μm)
Percent passing 2 μm: 14.2 (%)
Diameter: 0.002 (mm)

Remarks: For times greater than 2 minutes, an immersion correction is applied to the readings.

Figure A22. Hydrometer analysis for sample 07FB-2.

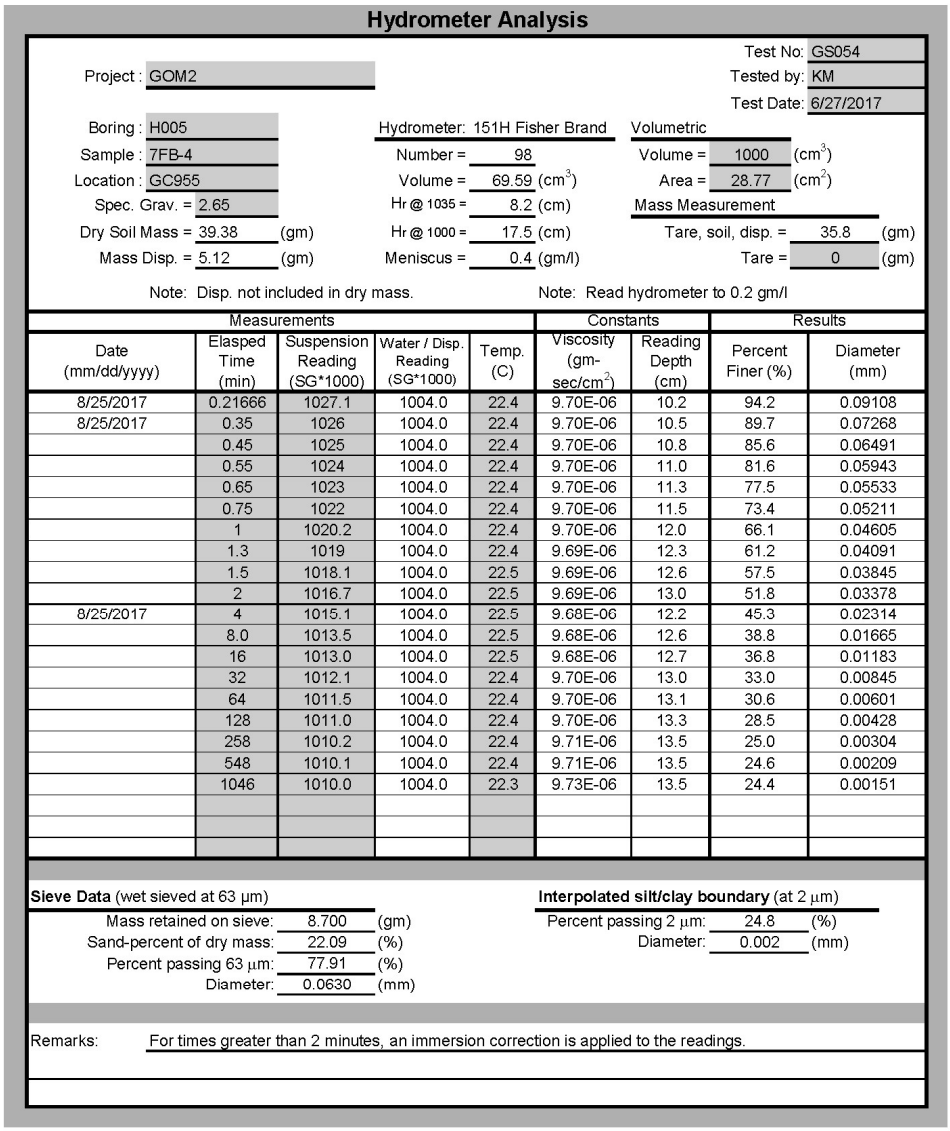

Hydrometer Analysis

Test No: GS054
Project : GOM2
Tested by: KM
Test Date: 6/27/2017

Boring : H005
Sample : 7FB-4
Location : GC955
Spec. Grav. = 2.65
Dry Soil Mass = 39.38 (gm)
Mass Disp. = 5.12 (gm)

Hydrometer: 151H Fisher Brand
Number = 98
Volume = 69.59 (cm^3)
Hr @ 1035 = 8.2 (cm)
Hr @ 1000 = 17.5 (cm)
Meniscus = 0.4 (gm/l)

Volumetric
Volume = 1000 (cm^3)
Area = 28.77 (cm^2)

Mass Measurement
Tare, soil, disp. = 35.8 (gm)
Tare = 0 (gm)

Note: Disp. not included in dry mass.

Note: Read hydrometer to 0.2 gm/l

Measurements					Constants		Results	
Date (mm/dd/yyyy)	Elasped Time (min)	Suspension Reading (SG*1000)	Water / Disp. Reading (SG*1000)	Temp. (C)	Viscosity (gm-sec/cm^2)	Reading Depth (cm)	Percent Finer (%)	Diameter (mm)
8/25/2017	0.21666	1027.1	1004.0	22.4	9.70E-06	10.2	94.2	0.09108
8/25/2017	0.35	1026	1004.0	22.4	9.70E-06	10.5	89.7	0.07268
	0.45	1025	1004.0	22.4	9.70E-06	10.8	85.6	0.06491
	0.55	1024	1004.0	22.4	9.70E-06	11.0	81.6	0.05943
	0.65	1023	1004.0	22.4	9.70E-06	11.3	77.5	0.05533
	0.75	1022	1004.0	22.4	9.70E-06	11.5	73.4	0.05211
	1	1020.2	1004.0	22.4	9.70E-06	12.0	66.1	0.04605
	1.3	1019	1004.0	22.4	9.69E-06	12.3	61.2	0.04091
	1.5	1018.1	1004.0	22.5	9.69E-06	12.6	57.5	0.03845
	2	1016.7	1004.0	22.5	9.69E-06	13.0	51.8	0.03378
8/25/2017	4	1015.1	1004.0	22.5	9.68E-06	12.2	45.3	0.02314
	8.0	1013.5	1004.0	22.5	9.68E-06	12.6	38.8	0.01665
	16	1013.0	1004.0	22.5	9.68E-06	12.7	36.8	0.01183
	32	1012.1	1004.0	22.4	9.70E-06	13.0	33.0	0.00845
	64	1011.5	1004.0	22.4	9.70E-06	13.1	30.6	0.00601
	128	1011.0	1004.0	22.4	9.70E-06	13.3	28.5	0.00428
	258	1010.2	1004.0	22.4	9.71E-06	13.5	25.0	0.00304
	548	1010.1	1004.0	22.4	9.71E-06	13.5	24.6	0.00209
	1046	1010.0	1004.0	22.3	9.73E-06	13.5	24.4	0.00151

Sieve Data (wet sieved at 63 μm)
Mass retained on sieve: 8.700 (gm)
Sand-percent of dry mass: 22.09 (%)
Percent passing 63 μm: 77.91 (%)
Diameter: 0.0630 (mm)

Interpolated silt/clay boundary (at 2 μm)
Percent passing 2 μm: 24.8 (%)
Diameter: 0.002 (mm)

Remarks: For times greater than 2 minutes, an immersion correction is applied to the readings.

Figure A23. Hydrometer analysis for sample 07FB-4.

Hydrometer Analysis

Test No: GS054
Project : GOM2
Tested by: KM
Test Date: 11/27/2018

Boring : H005
Sample : 8FB-2-1(0-4CM)
Location : GC955
Spec. Grav. = 2.65
Dry Soil Mass = 34.55 (gm)
Mass Disp. = 5.00 (gm)

Hydrometer: 151H Fisher Brand
Number = 98
Volume = 69.59 (cm^3)
Hr @ 1035 = 8.2 (cm)
Hr @ 1000 = 17.5 (cm)
Meniscus = 0.4 (gm/l)

Volumetric
Volume = 1000 (cm^3)
Area = 28.77 (cm^2)

Mass Measurement
fines, disp. = 39.33 (gm)
Tare = 0 (gm)

Note: Disp. not included in dry mass.

Note: Read hydrometer to 0.2 gm/l

Measurements					Constants		Results	
Date (mm/dd/yyyy)	Elasped Time (min)	Suspension Reading (SG*1000)	Water / Disp. Reading (SG*1000)	Temp. (C)	Viscosity (gm-sec/cm^2)	Reading Depth (cm)	Percent Finer (%)	Diameter (mm)
11/27/2018	0.16667		1006.4		1.70E-05	283.1	-4678.3	0.72496
11/27/2018	0.25	1024.9	1004.0	22.3	9.73E-06	10.8	97.0	0.08735
11/27/2018	0.5	1024.3	1004.0	22.3	9.73E-06	10.9	94.2	0.06222
11/27/2018	0.75	1024	1004.0	22.3	9.73E-06	11.0	92.8	0.05099
11/27/2018	1	1023.9	1004.0	22.3	9.73E-06	11.0	92.4	0.04421
11/27/2018	1.5	1023.5	1004.0	22.3	9.73E-06	11.1	90.5	0.03627
11/27/2018	2	1023	1004.0	22.3	9.73E-06	11.3	88.2	0.03160
11/27/2018	3	1022.5	1004.0	22.3	9.73E-06	10.2	85.9	0.02453
11/27/2018	4	1020.9	1004.0	22.3	9.73E-06	10.6	78.4	0.02169
11/27/2018	8.0	1018.7	1004.0	22.3	9.73E-06	11.2	68.2	0.01575
11/27/2018	16	1016.2	1004.0	22.3	9.73E-06	11.9	56.6	0.01146
11/27/2018	32	1014.9	1004.0	22.3	9.73E-06	12.2	50.5	0.00822
11/27/2018	64	1014.1	1004.0	22.3	9.73E-06	12.4	46.8	0.00586
11/27/2018	137	1013.1	1004.0	22.4	9.69E-06	12.7	42.3	0.00404
11/27/2018	258	1012.2	1003.9	22.7	9.64E-06	12.9	38.4	0.00297
11/27/2018	512	1011.3	1004.0	22.6	9.66E-06	13.2	34.1	0.00213
11/27/2018	1165	1010.8	1004.0	22.3	9.74E-06	13.3	31.5	0.00142
11/28/2018	2657	1009.6	1004.0	22.4	9.72E-06	13.6	26.0	0.00095

Sieve Data (wet sieved at 63 μm)
Mass retained on sieve: 0.220 (gm)
Sand-percent of dry mass: 0.64 (%)
Percent passing 63 μm: 99.36 (%)
Diameter: 0.0630 (mm)

Interpolated silt/clay boundary (at 2 μm)
Percent passing 2 μm: 33.6 (%)
Diameter: 0.002 (mm)

Remarks: For times greater than 2 minutes, an immersion correction is applied to the readings.

Figure A24. Hydrometer analysis for sample 08FB-2-1 (0-4cm).

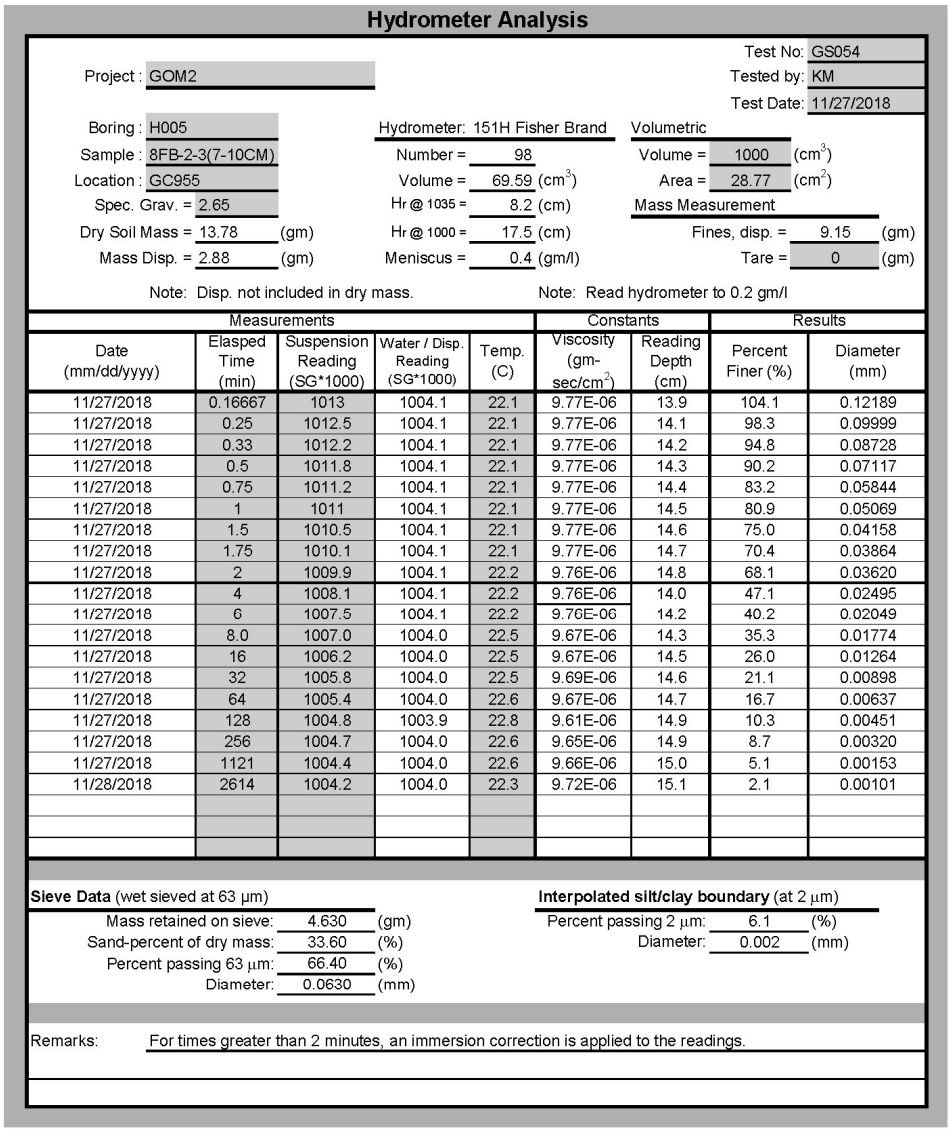

Hydrometer Analysis

Test No: GS054
Project : GOM2
Tested by: KM
Test Date: 11/27/2018

Boring : H005
Sample : 8FB-2-3(7-10CM)
Location : GC955
Spec. Grav. = 2.65
Dry Soil Mass = 13.78 (gm)
Mass Disp. = 2.88 (gm)

Hydrometer: 151H Fisher Brand
Number = 98
Volume = 69.59 (cm^3)
Hr @ 1035 = 8.2 (cm)
Hr @ 1000 = 17.5 (cm)
Meniscus = 0.4 (gm/l)

Volumetric
Volume = 1000 (cm^3)
Area = 28.77 (cm^2)

Mass Measurement
Fines, disp. = 9.15 (gm)
Tare = 0 (gm)

Note: Disp. not included in dry mass.

Note: Read hydrometer to 0.2 gm/l

Measurements					Constants		Results	
Date (mm/dd/yyyy)	Elasped Time (min)	Suspension Reading (SG*1000)	Water / Disp. Reading (SG*1000)	Temp. (C)	Viscosity (gm-sec/cm^2)	Reading Depth (cm)	Percent Finer (%)	Diameter (mm)
11/27/2018	0.16667	1013	1004.1	22.1	9.77E-06	13.9	104.1	0.12189
11/27/2018	0.25	1012.5	1004.1	22.1	9.77E-06	14.1	98.3	0.09999
11/27/2018	0.33	1012.2	1004.1	22.1	9.77E-06	14.2	94.8	0.08728
11/27/2018	0.5	1011.8	1004.1	22.1	9.77E-06	14.3	90.2	0.07117
11/27/2018	0.75	1011.2	1004.1	22.1	9.77E-06	14.4	83.2	0.05844
11/27/2018	1	1011	1004.1	22.1	9.77E-06	14.5	80.9	0.05069
11/27/2018	1.5	1010.5	1004.1	22.1	9.77E-06	14.6	75.0	0.04158
11/27/2018	1.75	1010.1	1004.1	22.1	9.77E-06	14.7	70.4	0.03864
11/27/2018	2	1009.9	1004.1	22.2	9.76E-06	14.8	68.1	0.03620
11/27/2018	4	1008.1	1004.1	22.2	9.76E-06	14.0	47.1	0.02495
11/27/2018	6	1007.5	1004.1	22.2	9.76E-06	14.2	40.2	0.02049
11/27/2018	8.0	1007.0	1004.0	22.5	9.67E-06	14.3	35.3	0.01774
11/27/2018	16	1006.2	1004.0	22.5	9.67E-06	14.5	26.0	0.01264
11/27/2018	32	1005.8	1004.0	22.5	9.69E-06	14.6	21.1	0.00898
11/27/2018	64	1005.4	1004.0	22.6	9.67E-06	14.7	16.7	0.00637
11/27/2018	128	1004.8	1003.9	22.8	9.61E-06	14.9	10.3	0.00451
11/27/2018	256	1004.7	1004.0	22.6	9.65E-06	14.9	8.7	0.00320
11/27/2018	1121	1004.4	1004.0	22.6	9.66E-06	15.0	5.1	0.00153
11/28/2018	2614	1004.2	1004.0	22.3	9.72E-06	15.1	2.1	0.00101

Sieve Data (wet sieved at 63 μm)
Mass retained on sieve: 4.630 (gm)
Sand-percent of dry mass: 33.60 (%)
Percent passing 63 μm: 66.40 (%)
Diameter: 0.0630 (mm)

Interpolated silt/clay boundary (at 2 μm)
Percent passing 2 μm: 6.1 (%)
Diameter: 0.002 (mm)

Remarks: For times greater than 2 minutes, an immersion correction is applied to the readings.

Figure A25. Hydrometer analysis for sample 08FB-2-1 (7-10 cm).

Hydrometer Analysis

Test No: GS054
Project : GOM2
Tested by: KM
Test Date: 10/10/2017

Boring : H005
Sample : 9FB-2
Location : GC955
Spec. Grav. = 2.65
Dry Soil Mass = 52.44 (gm)
Mass Disp. = 5.29 (gm)

Hydrometer: 151H Fisher Brand
Number = 98
Volume = 69.59 (cm^3)
Hr @ 1035 = 8.2 (cm)
Hr @ 1000 = 17.5 (cm)
Meniscus = 0.4 (gm/l)

Volumetric
Volume = 1000 (cm^3)
Area = 28.77 (cm^2)

Mass Measurement
Tare, soil, disp. = 44.03 (gm)
Tare = 0 (gm)

Note: Disp. not included in dry mass.

Note: Read hydrometer to 0.2 gm/l

Measurements					Constants		Results	
Date (mm/dd/yyyy)	Elasped Time (min)	Suspension Reading (SG*1000)	Water / Disp. Reading (SG*1000)	Temp. (C)	Viscosity (gm-sec/cm^2)	Reading Depth (cm)	Percent Finer (%)	Diameter (mm)
10/10/2017	0.1666	1035	1004.2	21.3	9.96E-06	8.1	94.2	0.09382
10/10/2017	0.25	1032	1004.3	21.1	1.00E-05	8.9	84.9	0.08046
10/10/2017	0.3333	1030.5	1004.3	21.1	1.00E-05	9.3	80.3	0.07123
10/10/2017	0.5	1028	1004.3	21.1	1.00E-05	10.0	72.7	0.06020
10/10/2017	0.75	1024.3	1004.3	21.1	1.00E-05	10.9	61.3	0.05152
10/10/2017	1	1021.5	1004.3	21.1	1.00E-05	11.7	52.8	0.04611
10/10/2017	1.5	1017.1	1004.3	21.1	1.00E-05	12.9	39.3	0.03949
10/10/2017	2	1014.1	1004.3	21.1	1.00E-05	13.6	30.1	0.03524
10/10/2017	4	1009.0	1004.2	21.3	9.96E-06	13.8	14.6	0.02499
10/10/2017	8.0	1007.0	1004.3	21.2	1.00E-05	14.3	8.4	0.01805
10/10/2017	16	1006.1	1004.0	22.2	9.74E-06	14.6	6.3	0.01270
10/10/2017	32	1006.0	1004.2	21.6	9.89E-06	14.6	5.6	0.00905
10/10/2017	64	1005.7	1004.1	22.1	9.77E-06	14.7	5.0	0.00638
10/10/2017	128	1005.5	1004.1	22.1	9.78E-06	14.7	4.4	0.00452
10/10/2017	256	1005.5	1004.0	22.3	9.73E-06	14.7	4.4	0.00319
10/10/2017	512	1005.3	1004.1	22.2	9.76E-06	14.8	3.8	0.00226
10/10/2017	1063	1005.3	1004.1	22.2	9.76E-06	14.8	3.7	0.00157
10/11/2017	2660	1005.0	1004.1	22.1	9.77E-06	14.9	2.9	0.00100

Sieve Data (wet sieved at 63 μm)
Mass retained on sieve: 13.700 (gm)
Sand-percent of dry mass: 26.13 (%)
Percent passing 63 μm: 73.87 (%)
Diameter: 0.0630 (mm)

Interpolated silt/clay boundary (at 2 μm)
Percent passing 2 μm: 3.8 (%)
Diameter: 0.002 (mm)

Remarks: For times greater than 2 minutes, an immersion correction is applied to the readings.

Figure A26. Hydrometer analysis for sample 09FB-2.

Hydrometer Analysis

Test No: GS054
Project : GOM2
Tested by: KM
Test Date: 6/27/2017

Boring : H005
Sample : 9FB-4-1
Location : GC955
Spec. Grav. = 2.65
Dry Soil Mass = 48.18 (gm)
Mass Disp. = 4.97 (gm)

Hydrometer: 151H Fisher Brand
Number = 98
Volume = 69.59 (cm^3)
Hr @ 1035 = 8.2 (cm)
Hr @ 1000 = 17.5 (cm)
Meniscus = 0.4 (gm/l)

Volumetric
Volume = 1000 (cm^3)
Area = 28.77 (cm^2)

Mass Measurement
Tare, soil, disp. = 50.98 (gm)
Tare = 0 (gm)

Note: Disp. not included in dry mass.

Note: Read hydrometer to 0.2 gm/l

Measurements					Constants		Results	
Date (mm/dd/yyyy)	Elasped Time (min)	Suspension Reading (SG*1000)	Water / Disp. Reading (SG*1000)	Temp. (C)	Viscosity (gm-sec/cm^2)	Reading Depth (cm)	Percent Finer (%)	Diameter (mm)
6/27/2017	0.25	1032	1004.0	22.5	9.69E-06	8.9	93.4	0.07915
6/27/2017	0.5	1030.5	1004.0	22.5	9.69E-06	9.3	88.4	0.05721
	0.75	1029.1	1004.0	22.5	9.69E-06	9.7	83.7	0.04764
6/27/2017	1	1028.1	1004.0	22.5	9.69E-06	9.9	80.4	0.04182
6/27/2017	1.5	1026.5	1004.0	22.5	9.69E-06	10.4	75.0	0.03487
6/27/2017	2	1025.3	1004.0	22.5	9.69E-06	10.7	71.0	0.03066
6/27/2017	4	1023.0	1004.0	22.3	9.73E-06	10.1	63.3	0.02110
6/27/2017	8.0	1021.1	1004.0	22.5	9.68E-06	10.6	57.1	0.01526
6/27/2017	16	1019.7	1004.0	22.4	9.70E-06	11.0	52.2	0.01099
6/27/2017	32	1018.5	1004.0	22.3	9.72E-06	11.3	48.3	0.00789
6/27/2017	64	1017.3	1004.0	22.3	9.72E-06	11.6	44.3	0.00566
6/27/2017	127	1016.3	1004.0	22.2	9.75E-06	11.9	40.9	0.00407
6/27/2017	254	1015.0	1004.0	22.4	9.71E-06	12.2	36.6	0.00291
6/27/2017	512	1014.0	1004.0	22.3	9.72E-06	12.5	33.3	0.00207
6/27/2017	1042	1012.8	1004.1	22.2	9.76E-06	12.8	29.1	0.00148
6/28/2017	1676	1012.3	1004.1	22.0	9.81E-06	12.9	27.2	0.00117

Sieve Data (wet sieved at 63 μm)
Mass retained on sieve: 2.170 (gm)
Sand-percent of dry mass: 4.50 (%)
Percent passing 63 μm: 95.50 (%)
Diameter: 0.0630 (mm)

Interpolated silt/clay boundary (at 2 μm)
Percent passing 2 μm: 32.8 (%)
Diameter: 0.002 (mm)

Remarks: For times greater than 2 minutes, an immersion correction is applied to the readings.

Figure A27. Hydrometer analysis for sample 09FB-4-1.

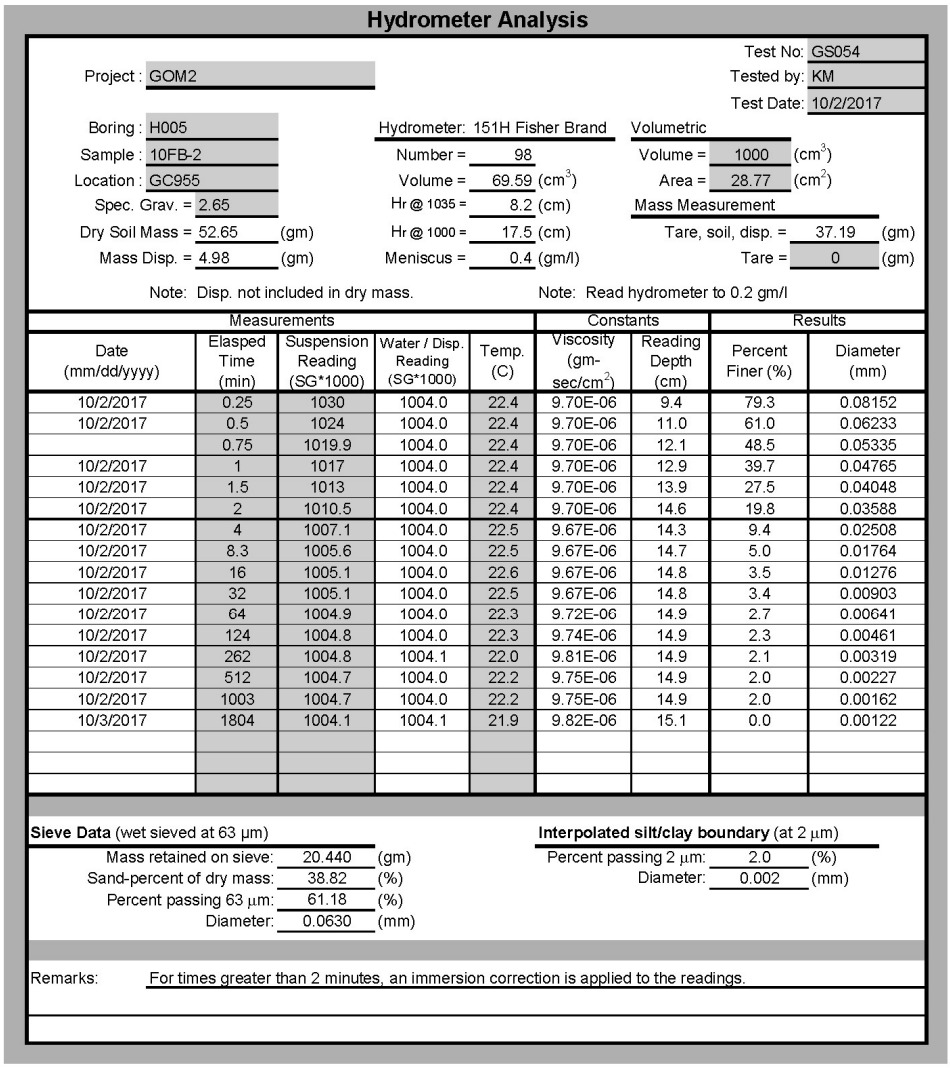

Hydrometer Analysis

Test No: GS054
Project : GOM2
Tested by: KM
Test Date: 10/2/2017

Boring : H005
Sample : 10FB-2
Location : GC955
Spec. Grav. = 2.65
Dry Soil Mass = 52.65 (gm)
Mass Disp. = 4.98 (gm)

Hydrometer: 151H Fisher Brand
Number = 98
Volume = 69.59 (cm^3)
Hr @ 1035 = 8.2 (cm)
Hr @ 1000 = 17.5 (cm)
Meniscus = 0.4 (gm/l)

Volumetric
Volume = 1000 (cm^3)
Area = 28.77 (cm^2)

Mass Measurement
Tare, soil, disp. = 37.19 (gm)
Tare = 0 (gm)

Note: Disp. not included in dry mass.

Note: Read hydrometer to 0.2 gm/l

Measurements					Constants		Results	
Date (mm/dd/yyyy)	Elasped Time (min)	Suspension Reading (SG*1000)	Water / Disp. Reading (SG*1000)	Temp. (C)	Viscosity (gm-sec/cm^2)	Reading Depth (cm)	Percent Finer (%)	Diameter (mm)
10/2/2017	0.25	1030	1004.0	22.4	9.70E-06	9.4	79.3	0.08152
10/2/2017	0.5	1024	1004.0	22.4	9.70E-06	11.0	61.0	0.06233
	0.75	1019.9	1004.0	22.4	9.70E-06	12.1	48.5	0.05335
10/2/2017	1	1017	1004.0	22.4	9.70E-06	12.9	39.7	0.04765
10/2/2017	1.5	1013	1004.0	22.4	9.70E-06	13.9	27.5	0.04048
10/2/2017	2	1010.5	1004.0	22.4	9.70E-06	14.6	19.8	0.03588
10/2/2017	4	1007.1	1004.0	22.5	9.67E-06	14.3	9.4	0.02508
10/2/2017	8.3	1005.6	1004.0	22.5	9.67E-06	14.7	5.0	0.01764
10/2/2017	16	1005.1	1004.0	22.6	9.67E-06	14.8	3.5	0.01276
10/2/2017	32	1005.1	1004.0	22.5	9.67E-06	14.8	3.4	0.00903
10/2/2017	64	1004.9	1004.0	22.3	9.72E-06	14.9	2.7	0.00641
10/2/2017	124	1004.8	1004.0	22.3	9.74E-06	14.9	2.3	0.00461
10/2/2017	262	1004.8	1004.1	22.0	9.81E-06	14.9	2.1	0.00319
10/2/2017	512	1004.7	1004.0	22.2	9.75E-06	14.9	2.0	0.00227
10/2/2017	1003	1004.7	1004.0	22.2	9.75E-06	14.9	2.0	0.00162
10/3/2017	1804	1004.1	1004.1	21.9	9.82E-06	15.1	0.0	0.00122

Sieve Data (wet sieved at 63 μm)
Mass retained on sieve: 20.440 (gm)
Sand-percent of dry mass: 38.82 (%)
Percent passing 63 μm: 61.18 (%)
Diameter: 0.0630 (mm)

Interpolated silt/clay boundary (at 2 μm)
Percent passing 2 μm: 2.0 (%)
Diameter: 0.002 (mm)

Remarks: For times greater than 2 minutes, an immersion correction is applied to the readings.

Figure A28. Hydrometer analysis for sample 10FB-2.

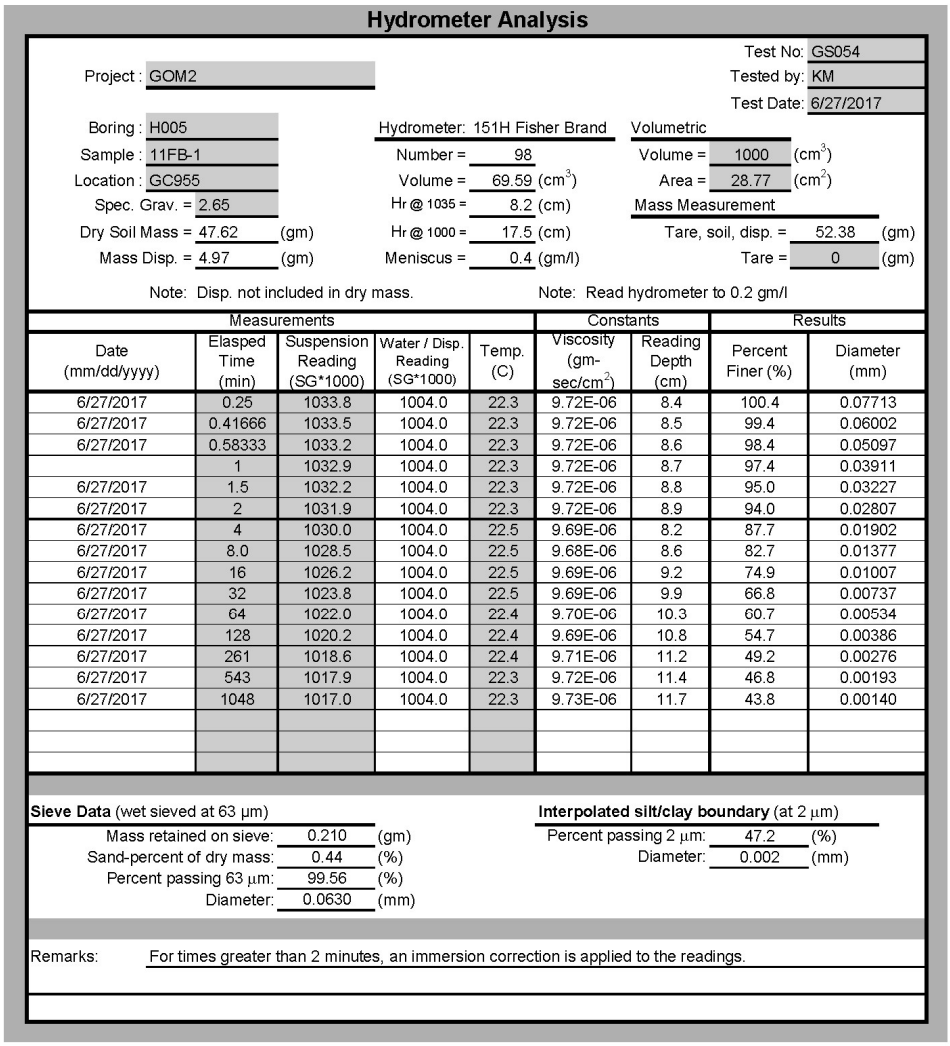

Hydrometer Analysis

Test No: GS054
Project : GOM2
Tested by: KM
Test Date: 6/27/2017

Boring : H005
Sample : 11FB-1
Location : GC955
Spec. Grav. = 2.65
Dry Soil Mass = 47.62 (gm)
Mass Disp. = 4.97 (gm)

Hydrometer: 151H Fisher Brand
Number = 98
Volume = 69.59 (cm^3)
Hr @ 1035 = 8.2 (cm)
Hr @ 1000 = 17.5 (cm)
Meniscus = 0.4 (gm/l)

Volumetric
Volume = 1000 (cm^3)
Area = 28.77 (cm^2)

Mass Measurement
Tare, soil, disp. = 52.38 (gm)
Tare = 0 (gm)

Note: Disp. not included in dry mass.

Note: Read hydrometer to 0.2 gm/l

Measurements					Constants		Results	
Date (mm/dd/yyyy)	Elasped Time (min)	Suspension Reading (SG*1000)	Water / Disp. Reading (SG*1000)	Temp. (C)	Viscosity (gm-sec/cm^2)	Reading Depth (cm)	Percent Finer (%)	Diameter (mm)
6/27/2017	0.25	1033.8	1004.0	22.3	9.72E-06	8.4	100.4	0.07713
6/27/2017	0.41666	1033.5	1004.0	22.3	9.72E-06	8.5	99.4	0.06002
6/27/2017	0.58333	1033.2	1004.0	22.3	9.72E-06	8.6	98.4	0.05097
	1	1032.9	1004.0	22.3	9.72E-06	8.7	97.4	0.03911
6/27/2017	1.5	1032.2	1004.0	22.3	9.72E-06	8.8	95.0	0.03227
6/27/2017	2	1031.9	1004.0	22.3	9.72E-06	8.9	94.0	0.02807
6/27/2017	4	1030.0	1004.0	22.5	9.69E-06	8.2	87.7	0.01902
6/27/2017	8.0	1028.5	1004.0	22.5	9.68E-06	8.6	82.7	0.01377
6/27/2017	16	1026.2	1004.0	22.5	9.69E-06	9.2	74.9	0.01007
6/27/2017	32	1023.8	1004.0	22.5	9.69E-06	9.9	66.8	0.00737
6/27/2017	64	1022.0	1004.0	22.4	9.70E-06	10.3	60.7	0.00534
6/27/2017	128	1020.2	1004.0	22.4	9.69E-06	10.8	54.7	0.00386
6/27/2017	261	1018.6	1004.0	22.4	9.71E-06	11.2	49.2	0.00276
6/27/2017	543	1017.9	1004.0	22.3	9.72E-06	11.4	46.8	0.00193
6/27/2017	1048	1017.0	1004.0	22.3	9.73E-06	11.7	43.8	0.00140

Sieve Data (wet sieved at 63 μm)
Mass retained on sieve: 0.210 (gm)
Sand-percent of dry mass: 0.44 (%)
Percent passing 63 μm: 99.56 (%)
Diameter: 0.0630 (mm)

Interpolated silt/clay boundary (at 2 μm)
Percent passing 2 μm: 47.2 (%)
Diameter: 0.002 (mm)

Remarks: For times greater than 2 minutes, an immersion correction is applied to the readings.

Figure A29. Hydrometer analysis for sample 11FB-1.

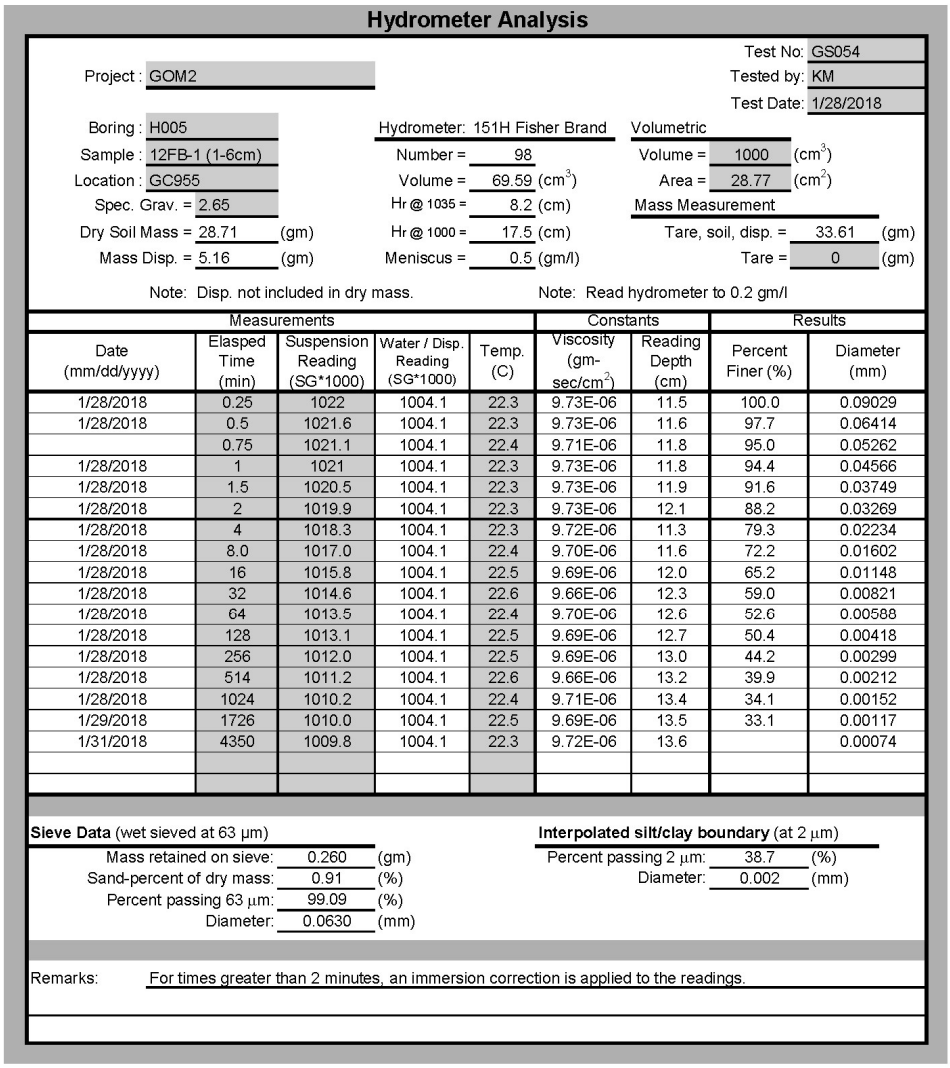

Hydrometer Analysis

Test No: GS054
Project : GOM2
Tested by: KM
Test Date: 1/28/2018

Boring : H005
Sample : 12FB-1 (1-6cm)
Location : GC955
Spec. Grav. = 2.65
Dry Soil Mass = 28.71 (gm)
Mass Disp. = 5.16 (gm)

Hydrometer: 151H Fisher Brand
Number = 98
Volume = 69.59 (cm^3)
Hr @ 1035 = 8.2 (cm)
Hr @ 1000 = 17.5 (cm)
Meniscus = 0.5 (gm/l)

Volumetric
Volume = 1000 (cm^3)
Area = 28.77 (cm^2)

Mass Measurement
Tare, soil, disp. = 33.61 (gm)
Tare = 0 (gm)

Note: Disp. not included in dry mass.

Note: Read hydrometer to 0.2 gm/l

Measurements					Constants		Results	
Date (mm/dd/yyyy)	Elasped Time (min)	Suspension Reading (SG*1000)	Water / Disp. Reading (SG*1000)	Temp. (C)	Viscosity (gm-sec/cm^2)	Reading Depth (cm)	Percent Finer (%)	Diameter (mm)
1/28/2018	0.25	1022	1004.1	22.3	9.73E-06	11.5	100.0	0.09029
1/28/2018	0.5	1021.6	1004.1	22.3	9.73E-06	11.6	97.7	0.06414
	0.75	1021.1	1004.1	22.4	9.71E-06	11.8	95.0	0.05262
1/28/2018	1	1021	1004.1	22.3	9.73E-06	11.8	94.4	0.04566
1/28/2018	1.5	1020.5	1004.1	22.3	9.73E-06	11.9	91.6	0.03749
1/28/2018	2	1019.9	1004.1	22.3	9.73E-06	12.1	88.2	0.03269
1/28/2018	4	1018.3	1004.1	22.3	9.72E-06	11.3	79.3	0.02234
1/28/2018	8.0	1017.0	1004.1	22.4	9.70E-06	11.6	72.2	0.01602
1/28/2018	16	1015.8	1004.1	22.5	9.69E-06	12.0	65.2	0.01148
1/28/2018	32	1014.6	1004.1	22.6	9.66E-06	12.3	59.0	0.00821
1/28/2018	64	1013.5	1004.1	22.4	9.70E-06	12.6	52.6	0.00588
1/28/2018	128	1013.1	1004.1	22.5	9.69E-06	12.7	50.4	0.00418
1/28/2018	256	1012.0	1004.1	22.5	9.69E-06	13.0	44.2	0.00299
1/28/2018	514	1011.2	1004.1	22.6	9.66E-06	13.2	39.9	0.00212
1/28/2018	1024	1010.2	1004.1	22.4	9.71E-06	13.4	34.1	0.00152
1/29/2018	1726	1010.0	1004.1	22.5	9.69E-06	13.5	33.1	0.00117
1/31/2018	4350	1009.8	1004.1	22.3	9.72E-06	13.6		0.00074

Sieve Data (wet sieved at 63 μm)
Mass retained on sieve: 0.260 (gm)
Sand-percent of dry mass: 0.91 (%)
Percent passing 63 μm: 99.09 (%)
Diameter: 0.0630 (mm)

Interpolated silt/clay boundary (at 2 μm)
Percent passing 2 μm: 38.7 (%)
Diameter: 0.002 (mm)

Remarks: For times greater than 2 minutes, an immersion correction is applied to the readings.

Figure A30. Hydrometer analysis for sample 12FB-1 (1-6 cm).

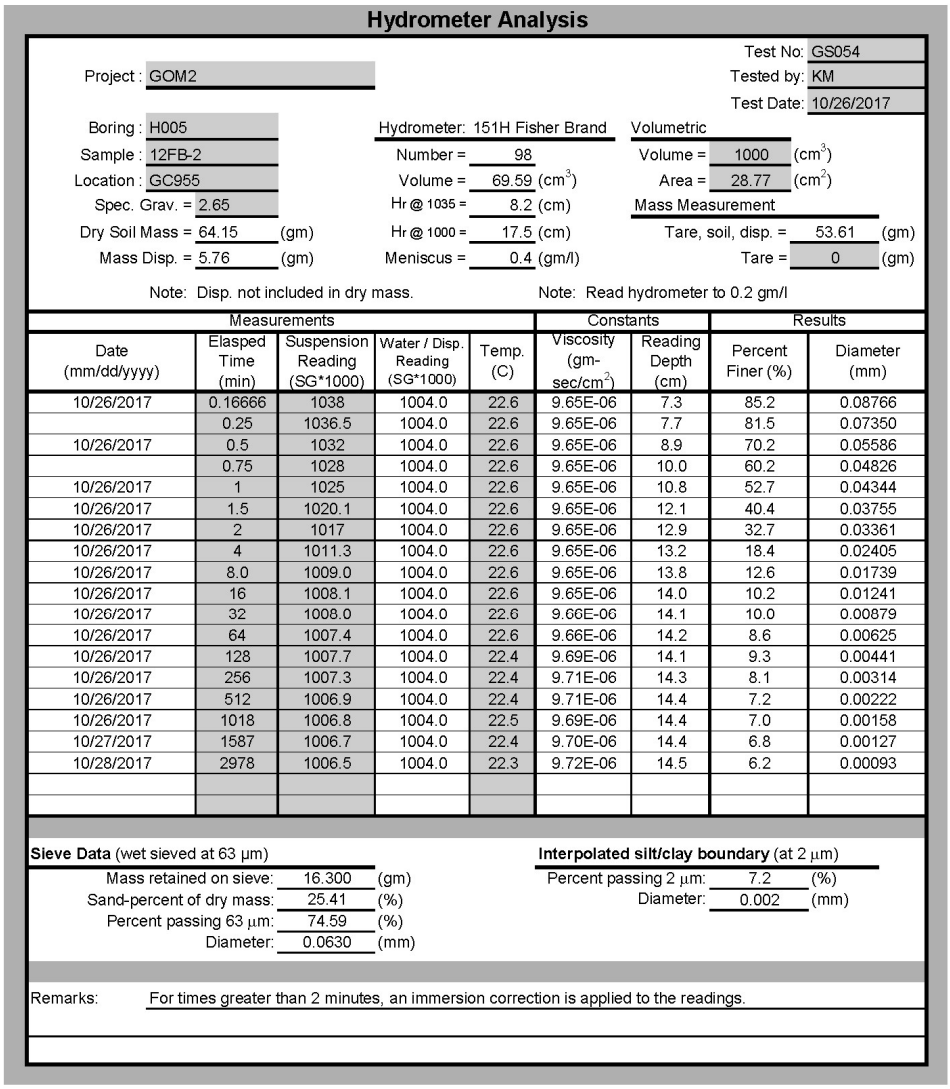

Hydrometer Analysis

Test No: GS054
Project : GOM2
Tested by: KM
Test Date: 10/26/2017

Boring : H005
Sample : 12FB-2
Location : GC955
Spec. Grav. = 2.65
Dry Soil Mass = 64.15 (gm)
Mass Disp. = 5.76 (gm)

Hydrometer: 151H Fisher Brand
Number = 98
Volume = 69.59 (cm^3)
Hr @ 1035 = 8.2 (cm)
Hr @ 1000 = 17.5 (cm)
Meniscus = 0.4 (gm/l)

Volumetric
Volume = 1000 (cm^3)
Area = 28.77 (cm^2)

Mass Measurement
Tare, soil, disp. = 53.61 (gm)
Tare = 0 (gm)

Note: Disp. not included in dry mass.

Note: Read hydrometer to 0.2 gm/l

Measurements					Constants		Results	
Date (mm/dd/yyyy)	Elasped Time (min)	Suspension Reading (SG*1000)	Water / Disp. Reading (SG*1000)	Temp. (C)	Viscosity (gm-sec/cm^2)	Reading Depth (cm)	Percent Finer (%)	Diameter (mm)
10/26/2017	0.16666	1038	1004.0	22.6	9.65E-06	7.3	85.2	0.08766
	0.25	1036.5	1004.0	22.6	9.65E-06	7.7	81.5	0.07350
10/26/2017	0.5	1032	1004.0	22.6	9.65E-06	8.9	70.2	0.05586
	0.75	1028	1004.0	22.6	9.65E-06	10.0	60.2	0.04826
10/26/2017	1	1025	1004.0	22.6	9.65E-06	10.8	52.7	0.04344
10/26/2017	1.5	1020.1	1004.0	22.6	9.65E-06	12.1	40.4	0.03755
10/26/2017	2	1017	1004.0	22.6	9.65E-06	12.9	32.7	0.03361
10/26/2017	4	1011.3	1004.0	22.6	9.65E-06	13.2	18.4	0.02405
10/26/2017	8.0	1009.0	1004.0	22.6	9.65E-06	13.8	12.6	0.01739
10/26/2017	16	1008.1	1004.0	22.6	9.65E-06	14.0	10.2	0.01241
10/26/2017	32	1008.0	1004.0	22.6	9.66E-06	14.1	10.0	0.00879
10/26/2017	64	1007.4	1004.0	22.6	9.66E-06	14.2	8.6	0.00625
10/26/2017	128	1007.7	1004.0	22.4	9.69E-06	14.1	9.3	0.00441
10/26/2017	256	1007.3	1004.0	22.4	9.71E-06	14.3	8.1	0.00314
10/26/2017	512	1006.9	1004.0	22.4	9.71E-06	14.4	7.2	0.00222
10/26/2017	1018	1006.8	1004.0	22.5	9.69E-06	14.4	7.0	0.00158
10/27/2017	1587	1006.7	1004.0	22.4	9.70E-06	14.4	6.8	0.00127
10/28/2017	2978	1006.5	1004.0	22.3	9.72E-06	14.5	6.2	0.00093

Sieve Data (wet sieved at 63 μm)
Mass retained on sieve: 16.300 (gm)
Sand-percent of dry mass: 25.41 (%)
Percent passing 63 μm: 74.59 (%)
Diameter: 0.0630 (mm)

Interpolated silt/clay boundary (at 2 μm)
Percent passing 2 μm: 7.2 (%)
Diameter: 0.002 (mm)

Remarks: For times greater than 2 minutes, an immersion correction is applied to the readings.

Figure A31. Hydrometer analysis for sample 12FB-2.

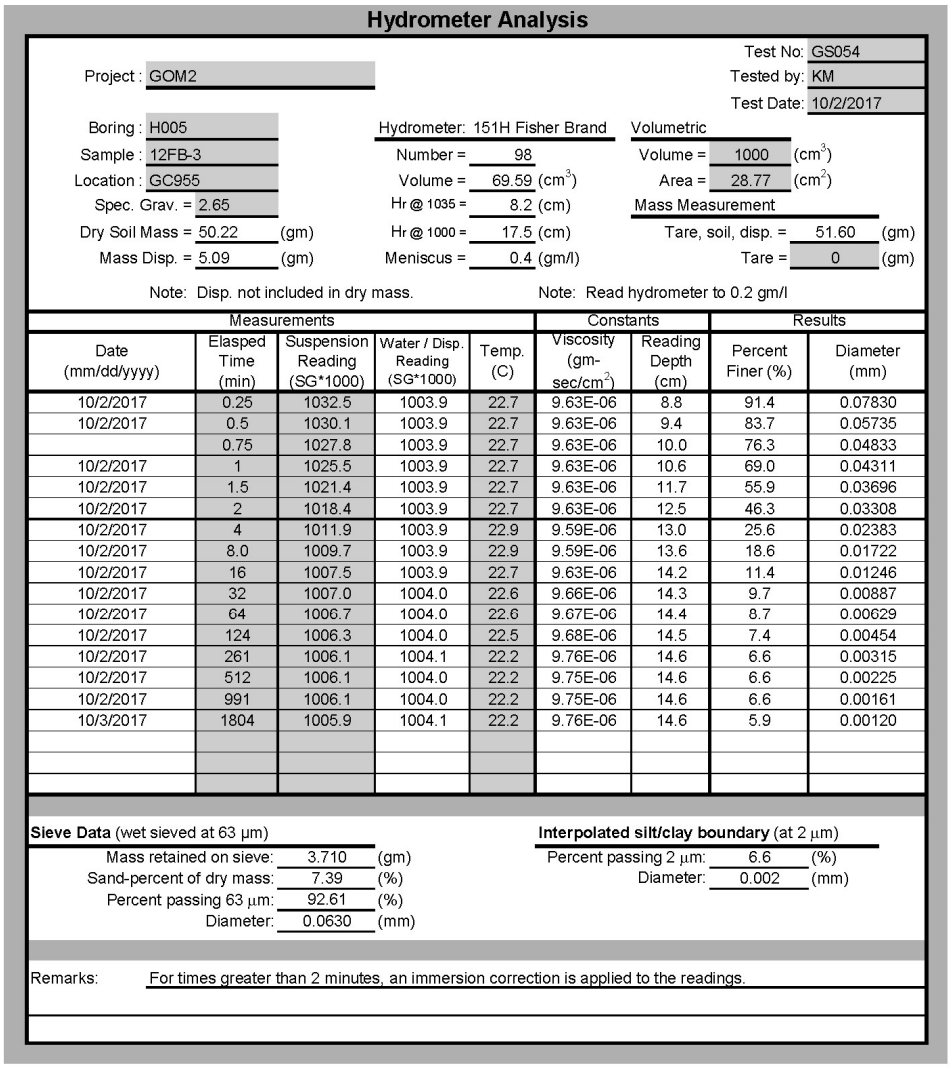

Hydrometer Analysis

Test No: GS054
Project : GOM2
Tested by: KM
Test Date: 10/2/2017

Boring : H005
Sample : 12FB-3
Location : GC955
Spec. Grav. = 2.65
Dry Soil Mass = 50.22 (gm)
Mass Disp. = 5.09 (gm)

Hydrometer: 151H Fisher Brand
Number = 98
Volume = 69.59 (cm^3)
Hr @ 1035 = 8.2 (cm)
Hr @ 1000 = 17.5 (cm)
Meniscus = 0.4 (gm/l)

Volumetric
Volume = 1000 (cm^3)
Area = 28.77 (cm^2)

Mass Measurement
Tare, soil, disp. = 51.60 (gm)
Tare = 0 (gm)

Note: Disp. not included in dry mass.

Note: Read hydrometer to 0.2 gm/l

Measurements					Constants		Results	
Date (mm/dd/yyyy)	Elasped Time (min)	Suspension Reading (SG*1000)	Water / Disp. Reading (SG*1000)	Temp. (C)	Viscosity (gm-sec/cm^2)	Reading Depth (cm)	Percent Finer (%)	Diameter (mm)
10/2/2017	0.25	1032.5	1003.9	22.7	9.63E-06	8.8	91.4	0.07830
10/2/2017	0.5	1030.1	1003.9	22.7	9.63E-06	9.4	83.7	0.05735
	0.75	1027.8	1003.9	22.7	9.63E-06	10.0	76.3	0.04833
10/2/2017	1	1025.5	1003.9	22.7	9.63E-06	10.6	69.0	0.04311
10/2/2017	1.5	1021.4	1003.9	22.7	9.63E-06	11.7	55.9	0.03696
10/2/2017	2	1018.4	1003.9	22.7	9.63E-06	12.5	46.3	0.03308
10/2/2017	4	1011.9	1003.9	22.9	9.59E-06	13.0	25.6	0.02383
10/2/2017	8.0	1009.7	1003.9	22.9	9.59E-06	13.6	18.6	0.01722
10/2/2017	16	1007.5	1003.9	22.7	9.63E-06	14.2	11.4	0.01246
10/2/2017	32	1007.0	1004.0	22.6	9.66E-06	14.3	9.7	0.00887
10/2/2017	64	1006.7	1004.0	22.6	9.67E-06	14.4	8.7	0.00629
10/2/2017	124	1006.3	1004.0	22.5	9.68E-06	14.5	7.4	0.00454
10/2/2017	261	1006.1	1004.1	22.2	9.76E-06	14.6	6.6	0.00315
10/2/2017	512	1006.1	1004.0	22.2	9.75E-06	14.6	6.6	0.00225
10/2/2017	991	1006.1	1004.0	22.2	9.75E-06	14.6	6.6	0.00161
10/3/2017	1804	1005.9	1004.1	22.2	9.76E-06	14.6	5.9	0.00120

Sieve Data (wet sieved at 63 μm)
Mass retained on sieve: 3.710 (gm)
Sand-percent of dry mass: 7.39 (%)
Percent passing 63 μm: 92.61 (%)
Diameter: 0.0630 (mm)

Interpolated silt/clay boundary (at 2 μm)
Percent passing 2 μm: 6.6 (%)
Diameter: 0.002 (mm)

Remarks: For times greater than 2 minutes, an immersion correction is applied to the readings.

Figure A32. Hydrometer analysis for sample 12FB-3.

Hydrometer Analysis

Test No: GS054
Project : GOM2
Tested by: KM
Test Date: 1/28/2018

Boring : H005
Sample : 12FB-3 (30-37cm)
Location : GC955
Spec. Grav. = 2.65
Dry Soil Mass = 33.19 (gm)
Mass Disp. = 4.30 (gm)

Hydrometer: 151H Fisher Brand
Number = 98
Volume = 69.59 (cm^3)
Hr @ 1035 = 8.2 (cm)
Hr @ 1000 = 17.5 (cm)
Meniscus = 0.4 (gm/l)

Volumetric
Volume = 1000 (cm^3)
Area = 28.77 (cm^2)

Mass Measurement
Tare, soil, disp. = 23.96 (gm)
Tare = 0 (gm)

Note: Disp. not included in dry mass.

Note: Read hydrometer to 0.2 gm/l

Measurements					Constants		Results	
Date (mm/dd/yyyy)	Elasped Time (min)	Suspension Reading (SG*1000)	Water / Disp. Reading (SG*1000)	Temp. (C)	Viscosity (gm-sec/cm^2)	Reading Depth (cm)	Percent Finer (%)	Diameter (mm)
1/28/2018	0.16667	1022	1004.0	22.3	9.72E-06	11.5	87.0	0.11066
1/28/2018	0.25	1020	1004.0	22.3	9.72E-06	12.1	77.3	0.09241
1/28/2018	0.5	1017.5	1004.0	22.3	9.72E-06	12.7	65.2	0.06712
1/28/2018	0.75	1014.5	1004.0	22.3	9.73E-06	13.5	50.7	0.05651
1/28/2018	1	1012.7	1004.0	22.3	9.73E-06	14.0	42.0	0.04979
1/28/2018	1.5	1010	1004.0	22.4	9.72E-06	14.7	29.0	0.04166
1/28/2018	2	1007.7	1004.0	22.4	9.71E-06	15.3	17.9	0.03680
1/28/2018	4	1006.0	1004.0	22.4	9.71E-06	14.6	9.6	0.02537
1/28/2018	8.0	1005.1	1004.0	22.4	9.69E-06	14.8	5.3	0.01808
1/28/2018	16	1004.3	1004.0	22.4	9.71E-06	15.0	1.4	0.01288
1/28/2018	32	1004.1	1004.0	22.4	9.70E-06	15.1	0.5	0.00912
1/28/2018	53	1004.0	1004.0	22.4	9.71E-06	15.1	0.0	0.00710
1/28/2018	128	1004.1	1004.0	22.5	9.69E-06	15.1	0.6	0.00456
1/28/2018	256	1004.0	1004.0	22.5	9.69E-06	15.1	0.0	0.00323
1/28/2018	497	1003.8	1004.0	22.6	9.66E-06	15.2	-0.8	0.00232
1/28/2018	1025	1003.8	1004.0	22.5	9.68E-06	15.2	-0.9	0.00161
1/29/2018	1735	1004.0	1004.0	22.5	9.68E-06	15.1	0.1	0.00124
1/31/2018	4340	1003.4	1004.0	22.4	9.71E-06	15.3	-3.0	0.00079

Sieve Data (wet sieved at 63 μm)
Mass retained on sieve: 13.530 (gm)
Sand-percent of dry mass: 40.77 (%)
Percent passing 63 μm: 59.23 (%)
Diameter: 0.0630 (mm)

Interpolated silt/clay boundary (at 2 μm)
Percent passing 2 μm: -0.8 (%)
Diameter: 0.002 (mm)

Remarks: For times greater than 2 minutes, an immersion correction is applied to the readings.

Figure A33. Hydrometer analysis for sample 12FB-3 (30-37 cm).

APPENDIX B: SUPPLEMENTAL FIGURES FROM CHAPTER 3

This appendix contains additional figures from Chapter 3. These figures were included in the appendix of the manuscript due to figure limits in the journal Earth and Science Planetary Letters.

The well logs for WR313-G and WR313-H show very high sonic velocities, high resistivities, and reduced density (interpreted as pore-filling hydrate) in the sands above the BSR. In seismic data, the hydrate-bearing sands are imaged by a positive reflection. Below the BSR, the sands have a reduced velocity, resistivity, and density, that we interpret as the presence of pore-filling water. The sands below the BSR are imaged by a trough-leading reflection. The most striking example of this is the Orange sand, where we observe a strong, peak-leading reflection above the BSR in WR313-H (Fig. B1; interpreted as hydrate-bearing sand), and a trough-leading reflection below the BSHZ in WR313-G (Fig. B2; interpreted as water-bearing sand). We observe similar response with the Blue sand interpreted as hydrate bearing and imaged by a peak-leading reflection above the BSR/BHSZ at WR313-H and WR313-G (Fig. B1 & B2), and the Green sand imaged by a trough-leading reflection below the BSR in WR313-H (Fig. B1).

Appendix B1. Well logs for WR313-H

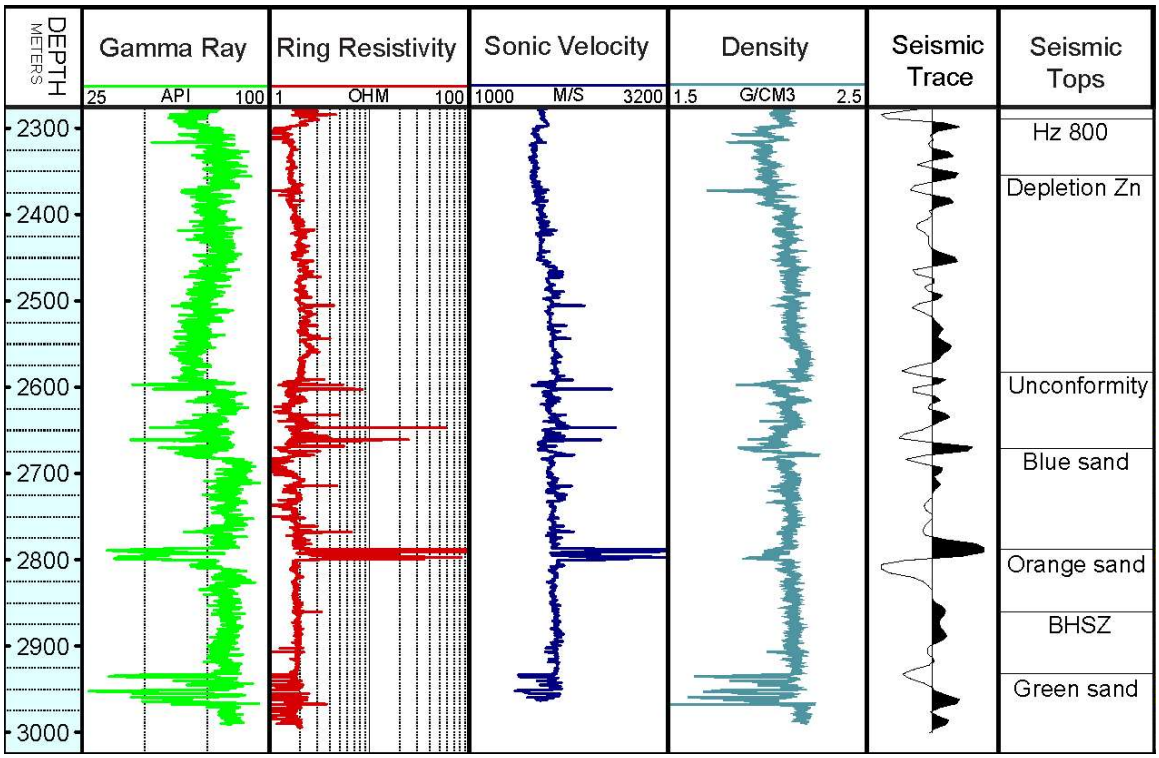

Figure B 1. Well logs for WR313-H. At this position, the Blue sand and the Orange sand are interpreted as saturated with hydrate based on the high resistivity, high sonic velocity, and low density responses. The Green sand is interpreted as saturated with water based on the low resistivity and low sonic velocity responses.

Appendix B2. Well logs for WR313-G

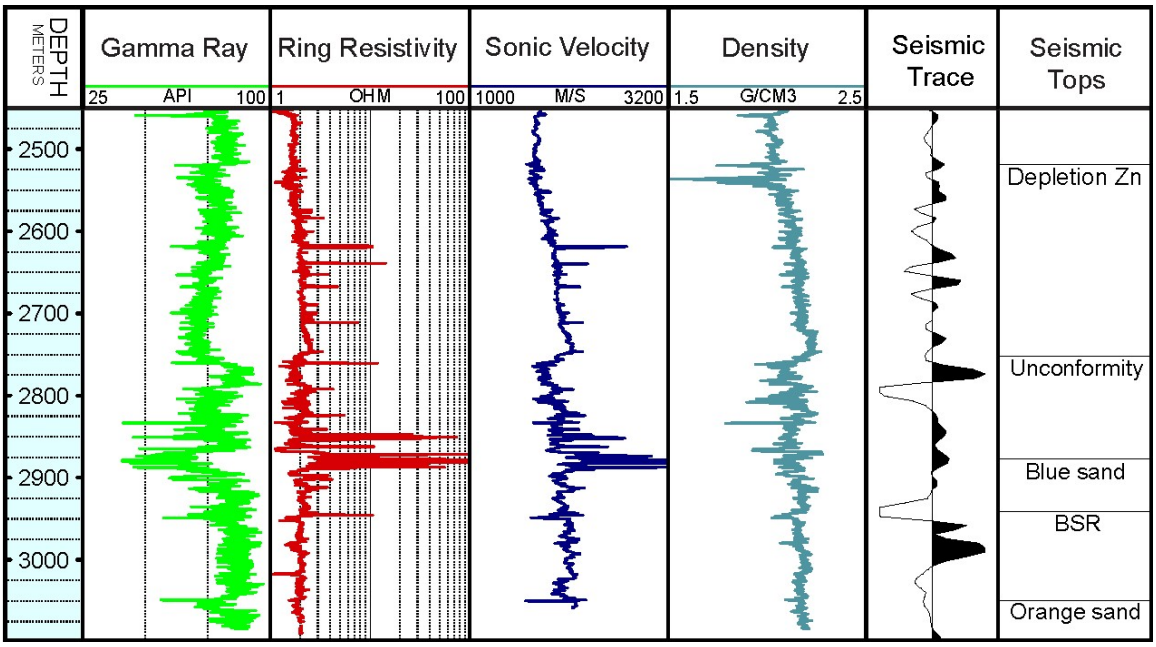

Figure B 2. Well logs for WR313-G. At this position, the Blue sand is interpreted as saturated with hydrate based on the high resistivity, high sonic velocity, and low density responses. The Orange sand is interpreted as saturated with water based on the low resistivity and low sonic velocity responses.

Appendix B3. Seismic profile of the Blue row of gas mounds

This appendix contains a seismic line across the western-most gas mounds, B1-B4. We include this figure to illustrate the inter-mound relationships and the pluming BSR beneath the southernmost B4 mound.

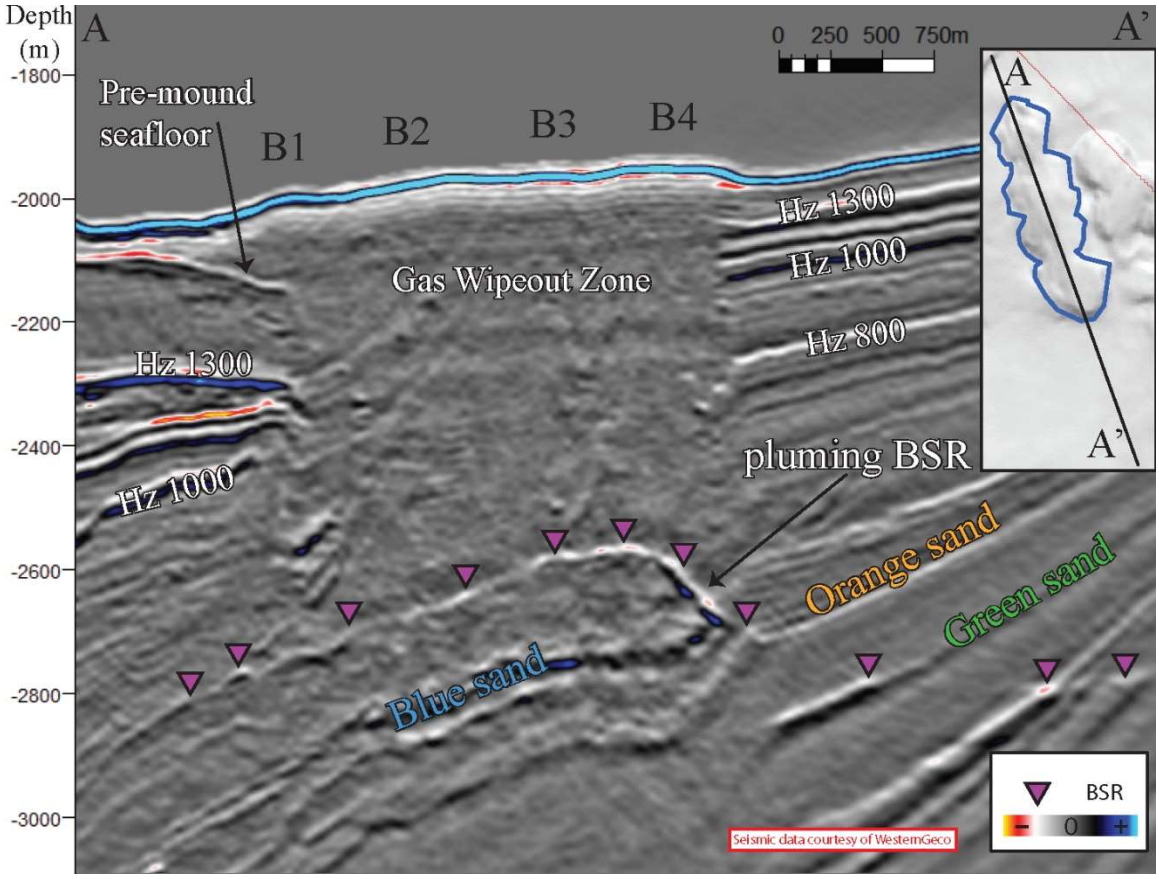

Figure B 3. Seismic profile of the Blue row of gas mounds, B1 – B4. The strong seafloor reflection does now show any apparent onlapping that may suggest an age relationship between the mounds. The internal structure of the gas mounds is obscured by the Gas Wipeout Zone between the seafloor and the BSR, which rises and reaches nearest the seafloor beneath mound B4.

Bibliography

Alexander, L. L., and Flemings, P. B., 1995, Geologic evolution of a Pliocene–Pleistocene salt-withdrawal minibasin: Eugene Island Block 330, offshore Louisiana: AAPG bulletin, v. 79, no. 12, p. 1737-1756.

Andresen, K. J., 2012, Fluid flow features in hydrocarbon plumbing systems: What do they tell us about the basin evolution?: Marine Geology, v. 332, p. 89-108.

Benjamin, U. K., and Huuse, M., 2017, Seafloor and buried mounds on the western slope of the Niger Delta: Marine and Petroleum Geology, v. 83, p. 158-173.

Beaubouef, R., 2004, Deep-water leveed-channel complexes of the Cerro Toro Formation, Upper Cretaceous, southern Chile: AAPG bulletin, v. 88, p. 1471-1500.

Boswell, R., T. S. Collett, M. Frye, W. Shedd, D. R. McConnell, and D. Shelander, 2012a, Subsurface gas hydrates in the northern Gulf of Mexico: Marine and Petroleum Geology, v. 34, p. 4-30.

Boswell, R., M. Frye, D. Shelander, W. Shedd, D. R. McConnell, and A. Cook, 2012b, Architecture of gas-hydrate-bearing sands from Walker Ridge 313, Green canyon 955, and Alaminos canyon 21: northern deepwater Gulf of Mexico: Marine and Petroleum Geology, v. 34, p. 134-149.

Boswell, R., K. Yamamoto, S.-R. Lee, T. Collett, P. Kumar, and S. Dallimore, 2014, Methane hydrates, Future Energy (Second Edition), Elsevier, p. 159-178.

Boswell, R., J. Yoneda, and W. F. Waite, 2018, India National Gas Hydrate Program Expedition 02 summary of scientific results: Evaluation of natural gas-hydrate-bearing pressure cores: Marine and Petroleum Geology http://doi.org/10.1016/j.marpetgeo.2018.10.020.

Browne, G. H., and R. M. Slatt, 1997, Thin-bedded slope fan (channel-levee) deposits from New Zealand: an outcrop analog for reservoirs in the Gulf of Mexico.

Cartwright, J., Huuse, M., and Aplin, A., 2007, Seal bypass systems: AAPG Bulletin, v. 91, no. 8, p. 1141-1166.

Cartwright, J., and Santamarina, C., 2015, Seismic characteristics of fluid escape pipes in sedimentary basins: Implications for pipe genesis: Marine and Petroleum Geology, v. 65, p. 126-140.

Ceramicola, S., Dupré, S., Somoza, L., and Woodside, J., 2018, Cold seep systems, Submarine geomorphology, Springer, p. 367-387.

Chand, S., T. A. Minshull, D. Gei, and J. M. Carcione, 2004, Elastic velocity models for gas-hydrate-bearing sediments—A comparison: Geophysical Journal International, v. 159, p. 573-590.

Clemenceau, G. R., 1995, Ram/Powell Field: Viosca Knoll Block 912, Deepwater Gulf of Mexico, *in* R. D. J. Winn, J. M. Armentrout, ed., Turbidites and associated deep-water facies: SEPM Core Workshop 20, p. 95-129.

Clemenceau, G. R., J. Colbert, and D. Edens, 2000, Production Results from Levee-Overbank Turbidite Sands at Ram/Powell Field, Deepwater Gulf of Mexico, *in* P. Weimer, ed., Deep-Water Reservoirs of the World, SEPM Society for Sedimentary Geology.

Clennell, M. B., Hovland, M., Booth, J. S., Henry, P., and Winters, W. J., 1999, Formation of natural gas hydrates in marine sediments: 1. Conceptual model of gas hydrate growth conditioned by host sediment properties: Journal of Geophysical Research: Solid Earth, v. 104, no. B10, p. 22985-23003.

Collett, T. S., and R. Boswell, 2012, Resource and hazard implications of gas hydrates in the Northern Gulf of Mexico: Results of the 2009 Joint Industry Project Leg II Drilling Expedition: Marine and Petroleum Geology, v. 34, p. 1-3.

Collett, T. S., R. Boswell, J. R. Cochran, P. Kumar, M. Lall, A. Mazumdar, M. V. Ramana, T. Ramprasad, M. Riedel, K. Sain, A. V. Sathe, and K. Vishwanath, 2014, Geologic implications of gas hydrates in the offshore of India: Results of the National Gas Hydrate Program Expedition 01: Marine and Petroleum Geology, v. 58, p. 3-28.

Collett, T. S., M. Riedel, J. R. Cochran, R. Boswell, P. Kumar, and A. Sathe, 2008, Indian continental margin gas hydrate prospects: results of the Indian National Gas Hydrate Program (NGHP) expedition 01: Proc. 6 th Int. Conf. Gas Hydrates, Vancouver. https://circle.ubc.ca/bitstream/handle/2429/1035/5365.pdf.

Cook, A. E., Anderson, B. I., Rasmus, J., Sun, K., Li, Q., Collett, T. S., and Goldberg, D. S., 2012, Electrical anisotropy of gas hydrate-bearing sand reservoirs in the Gulf of Mexico: Marine and Petroleum Geology, v. 34, no. 1, p. 72-84.

Covault, J. A., and S. A. Graham, 2010, Submarine fans at all sea-level stands: Tectono-morphologic and climatic controls on terrigenous sediment delivery to the deep sea: Geology, v. 38, p. 939-942.

Cronin, B. T., A. Hurst, H. Celik, and I. Türkmen, 2000, Superb exposure of a channel, levee and overbank complex in an ancient deep-water slope environment: Sedimentary Geology, v. 132, p. 205-216.

Crutchley, G. J., Kroeger, K. F., Pecher, I. A., and Gorman, A. R., 2018, How tectonic folding influences gas hydrate formation: New Zealand's Hikurangi subduction margin: Geology, v. 47, no. 1, p. 39-42.

Crutchley, G. J., Pecher, I. A., Gorman, A. R., Henrys, S. A., and Greinert, J., 2010, Seismic imaging of gas conduits beneath seafloor seep sites in a shallow marine gas hydrate province, Hikurangi Margin, New Zealand: Marine Geology, v. 272, no. 1-4, p. 114-126.

Deptuck, M. E., G. S. Steffens, M. Barton, and C. Pirmez, 2003, Architecture and evolution of upper fan channel-belts on the Niger Delta slope and in the Arabian Sea: Marine and Petroleum Geology, v. 20, p. 649-676.

Dewangan, P., Sriram, G., Kumar, A., Mazumdar, A., Peketi, A., Mahale, V., Reddy, S. S. C., and Babu, A., 2021, Widespread occurrence of methane seeps in deep-water regions of Krishna-Godavari basin, Bay of Bengal: Marine and Petroleum Geology, v. 124, p. 104783.

Di Stefano, C., V. Ferro, and S. Mirabile, 2010, Comparison between grain-size analyses using laser diffraction and sedimentation methods: Biosystems engineering, v. 106, p. 205-215.

England, W. A., Mackenzie, A. S., Mann, D. M., and Quigley, T. M., 1987, The movement and entrapment of petroleum fluids in the subsurface: Journal of the Geological Society, v. 144, p. 327-347.

Enunwa, C., J. L. Razzano III, A. Ramgulam, P. B. Flemings, T. Ertekin, and Z. T. Karpyn, 2005, Tahoe Field Case Study—Understanding Reservoir Compartmentalization in a Channel-Levee System: Gulf Coast Association of Geologic Societies Transactions, v. 55, p. 152-162.

Etiope, G., 2012, Climate science: Methane uncovered: Nat. Geosci., v. 5, p. 373-374.

Evans, R. J., Davies, R. J., and Stewart, S. A., 2007, Internal structure and eruptive history of a kilometre-scale mud volcano system, South Caspian Sea: Basin Research, v. 19, no. 1, p. 153-163.

Fang, Y., Flemings, P. B., Daigle, H., Phillips, S. C., Meazell, P. K., and You, K., 2020, Petrophysical properties of the Green Canyon Block 955 hydrate reservoir inferred from reconstituted sediments: Implications for hydrate formation and production: AAPG Bulletin, v. 104, no. 9, p. 1997-2028.

Ferro, V., and S. Mirabile, 2009, Comparing particle size distribution analysis by sedimentation and laser diffraction method: Journal of Agricultural Engineering, v. 40, p. 35-43.

Figueiredo, J. J., D. M. Hodgson, S. S. Flint, and J. P. Kavanagh, 2010, Depositional environments and sequence stratigraphy of an exhumed Permian mudstone-dominated submarine slope succession, Karoo Basin, South Africa: Journal of Sedimentary Research, v. 80, p. 97-118.

Finkbeiner, T., Zoback, M., Flemings, P., and Stump, B., 2001, Stress, pore pressure, and dynamically constrained hydrocarbon columns in the South Eugene Island 330 field, northern Gulf of Mexico: AAPG bulletin, v. 85, no. 6, p. 1007-1031.

Flemings, P. B., 2021, A Concise Guide to Geopressure: Origin, Prediction, and Applications, Cambridge University Press.

Flemings, P. B., R. Boswell, T. S. Collett, A. E. Cook, D. Divins, M. Frye, G. Guerin, D. S. Goldberg, A. Malinverno, and K. Meazell, 2017, GOM2: Prospecting, Drilling and Sampling Coarse-Grained Hydrate Reservoirs in the Deepwater Gulf of Mexico: Proceeding of ICGH-9, p. 10.

Flemings, P. B., Liu, X., and Winters, W. J., 2003, Critical pressure and multiphase flow in Blake Ridge gas hydrates: Geology, v. 31, no. 12, p. 1057-1060.

Flemings, P., Long, H., Dugan, B., Germaine, J., John, C., Behrmann, J. H., Sawyer, D., and Expedition, I., 2008, Erratum to" Pore pressure penetrometers document high overpressure near the seafloor where multiple submarine landslides have occurred on the continental slope, offshore Louisiana, Gulf of Mexico"[Earth and Planetary Science Letters 269/3-4 (2008) 309-32]: Earth and Planetary Science Letters, v. 274, no. 1-2, p. 269-283.

Flemings, P. B., S. Phillips, R. Boswell, T. S. Collett, A. Cook, T. Dong, M. Frye, G. Guerin, D. Goldberg, M. Holland, J. Jang, P. Meazell, J. Morrison, J. O'Connell, T. Pettigrew, E. Petrou, P. Polito, A. Portnov, M. Santra, P. Schultheiss, Y. Seol, W. Shedd, E. Solomon, C. Thomas, W. F. Waite, and K. You, 2020, Pressure coring a high-saturation coarse-grained methane hydrate reservoir in the northern Gulf of Mexico: AAPG bulletin.

Flemings, P. B., S. Phillips, T. S. Collett, A. Cook, R. Boswell, and t. U.-G.-E. Scientists, 2018, Expedition Summary, UT-GOM2-1 Hydrate Pressure Coring Expedition Report, Austin, TX, University of Texas Institute for Geophysics, TX.

Flemings, P., Stump, B., Finkbeiner, T., and Zoback, M., 2002, Flow focusing in overpressured sandstones: Theory, observations, and applications: American Journal of Science, vol. 302, no. 10, p. 827-855.

Folk, R. L., 1980, Petrology of sedimentary rocks, Hemphill Publishing Company.

Foschi, M., Cartwright, J. A., MacMinn, C. W., and Etiope, G., 2020, Evidence for massive emission of methane from a deep-water gas field during the Pliocene: Proceedings of the National Academy of Sciences, v. 117, no. 45, p. 27869-27876.

Frye, M., W. Shedd, and R. Boswell, 2012, Gas hydrate resource potential in the Terrebonne Basin, Northern Gulf of Mexico: Marine and Petroleum Geology, v. 34, p. 150-168.

Fujii, T., T. Saeki, T. Kobayashi, T. Inamori, M. Hayashi, O. Takano, T. Takayama, T. Kawasaki, S. Nagakubo, and M. Nakamizu, 2008, Resource assessment of methane hydrate in the eastern Nankai Trough, Japan: Offshore technology conference.

Gao, B., and Flemings, P. B., 2017, Pore pressure within dipping reservoirs in overpressured basins: Marine and Petroleum Geology, v. 80, p. 94-111.

Gardner, M. H., J. M. Borer, J. J. Melick, N. Mavilla, M. Dechesne, and R. N. Wagerle, 2003, Stratigraphic process-response model for submarine channels and related features from studies of Permian Brushy Canyon outcrops, West Texas: Marine and Petroleum Geology, v. 20, p. 757-787.

Gay, A., Lopez, M., Berndt, C., and Séranne, M., 2007, Geological controls on focused fluid flow associated with seafloor seeps in the Lower Congo Basin: Marine Geology, v. 244, no. 1, p. 68-92.

Germaine, J. T., and A. V. Germaine, 2009, Geotechnical laboratory measurements for engineers, John Wiley & Sons.

Guerin, G., A. Cook, S. Mrozewski, T. Collett, and R. Boswell, 2010, Gulf of Mexico Gas Hydrate Joint Industry Project Leg II: Green Canyon 955 LWD operations and results.

Gupta, L. P., W. Tanikawa, Y. Hamada, T. Hirose, N. Ahagon, T. Sugihara, N. Abe, S. Nomura, Y. Masaki, and H. Y. Wu, 2018, Examination of gas hydrate-bearing deep ocean sediments by X-ray Computed Tomography and verification of physical property measurements of sediments: Marine and Petroleum Geology.

Hackbarth, C. J., and R. D. Shew, 1994, Morphology and stratigraphy of a Mid-Pleistocene turbidite leveed channel from seismic, core and log data, northeastern Gulf of Mexico, *in* P. Weimer, A. H. Bouma, and B. F. Perkins, eds., Submarine Fans and Turbidite Systems—Sequence Stratigraphy, Reservoir Architecture and Production Characteristics Gulf of Mexico and International, Houston, Texas, SEPM Society for Sedimentary Geology, v. 15, p. 127 - 133, doi: https://doi.org/10.5724/gcs.94.15.

Hagedorn, A. R., and R. J. Blackwell, 1972, Summary of Experience with Pressure Coring, Fall Meeting of the Society of Petroleum Engineers of AIME, San Antonio, Texas, Society of Petroleum Engineers, p. 10.

Hansen, L., R. Callow, I. Kane, and B. Kneller, 2017a, Differentiating submarine channel-related thin-bedded turbidite facies: Outcrop examples from the Rosario Formation, Mexico: Sedimentary Geology, v. 358, p. 19-34.

Hansen, L., M. Janocko, I. Kane, and B. Kneller, 2017b, Submarine channel evolution, terrace development, and preservation of intra-channel thin-bedded turbidites: Mahin and Avon channels, offshore Nigeria: Marine Geology, v. 383, p. 146-167.

Hansen, L. A., R. H. Callow, I. A. Kane, F. Gamberi, M. Rovere, B. T. Cronin, and B. C. Kneller, 2015, Genesis and character of thin-bedded turbidites associated with submarine channels: Marine and Petroleum Geology, v. 67, p. 852-879.

Heggland, R., 2004, Definition of geohazards in exploration 3-D seismic data using attributes and neural-network analysis: AAPG bulletin, v. 88, p. 857-868.

Hillman, J. I., Cook, A. E., Daigle, H., Nole, M., Malinverno, A., Meazell, K., and Flemings, P. B., 2017, Gas hydrate reservoirs and gas migration mechanisms in the Terrebonne Basin, Gulf of Mexico: Marine and Petroleum Geology, v. 86, p. 1357-1373.

Hiscott, R. N., F. R. Hall, and C. Pirmez, 1997, Turbidity-current overspill from the Amazon Channel: texture of the silt/sand load, paleoflow from anisotropy of magnetic susceptibility, and implications for flow processes: Proceedings -Ocean Drilling Program Scientific Results, p. 53-78.

Hodgson, D. M., C. N. Di Celma, R. L. Brunt, and S. S. Flint, 2011, Submarine slope degradation and aggradation and the stratigraphic evolution of channel–levee systems: Journal of the Geological Society, v. 168, p. 625-628.

Holland, M., P. Schultheiss, and J. Roberts, 2019, Gas hydrate saturation and morphology from analysis of pressure cores acquired in the Bay of Bengal during expedition NGHP-02, offshore India: Marine and Petroleum Geology, v. 108, p. 407-423.

Holland, M., P. Schultheiss, J. Roberts, and M. Druce, 2008, Observed gas hydrate morphologies in marine sediments: 6th International Conference on Gas Hydrates, Chevron, Vancouver, BC, Canada, p. 6-10.

Hovland, M., Gallagher, J., Clennell, M., and Lekvam, K., 1997, Gas hydrate and free gas volumes in marine sediments: Example from the Niger Delta front: Marine and Petroleum Geology, v. 14, no. 3, p. 245-255.

Hutchinson, D., R. Boswell, T. Collett, J. C. Dai, O. Dugan, M. Frye, D. Mcconnell, K. Rose, W. Shedd, and D. Shel, 2009, Gulf of Mexico gas hydrate joint industry project leg II: green canyon 955 site selection.

Hutchinson, D. R., D. Shelander, J. Dai, D. McConnell, W. Shedd, M. Frye, C. Ruppel, R. Boswell, E. Jones, and T. Collett, 2008, Site selection for DOE/JIP gas hydrate drilling in the northern Gulf of Mexico: International Conference on Gas Hydrates.

Inada, N., and K. Yamamoto, 2015, Data report: Hybrid Pressure Coring System tool review and summary of recovery result from gas-hydrate related coring in the Nankai Project: Marine and Petroleum Geology, v. 66, p. 323-345.

Ito, T., Y. Komatsu, T. Fujii, K. Suzuki, K. Egawa, Y. Nakatsuka, Y. Konno, J. Yoneda, Y. Jin, M. Kida, J. Nagao, and H. Minagawa, 2015, Lithological features of hydrate-bearing sediments and their relationship with gas hydrate saturation in the eastern Nankai Trough, Japan: Marine and Petroleum Geology, v. 66, p. 368-378.

Jobe, Z. R., 2010, Multi-scale architectural evolution and flow property characterization of channelized turbidite systems, Doctoral dissertation: Stanford University, Stanford, California, 218 p.

Jobe, Z. R., D. R. Lowe, and W. R. Morris, 2012, Climbing-ripple successions in turbidite systems: depositional environments, sedimentation rates and accumulation times: Sedimentology, v. 59, p. 867-898.

Judd, A., and Hovland, M., 2009, Seabed fluid flow: the impact on geology, biology and the marine environment, Cambridge University Press.

Kane, I. A., and D. M. Hodgson, 2011, Sedimentological criteria to differentiate submarine channel levee subenvironments: exhumed examples from the Rosario Fm.(Upper Cretaceous) of Baja California, Mexico, and the Fort Brown Fm.(Permian), Karoo basin, S. Africa: Marine and Petroleum Geology, v. 28, p. 807-823.

Kane, I. A., D. T. McGee, and Z. R. Jobe, 2012, Halokinetic effects on submarine channel equilibrium profiles and implications for facies architecture: conceptual model illustrated with a case study from Magnolia Field, Gulf of Mexico: Geological Society, London, Special Publications, v. 363, p. 289-302.

Kendrick, J. W., 2000, Turbidite Reservoir Architecture in the Northern Gulf of Mexico Deepwater: Insights from the Development of Auger, Tahoe, and Ram/Powell Fields, *in* P. Weimer, ed., Deep-Water Reservoirs of the World, Houston, Texas, SEPM Society for Sedimentary Geology, p. 450-468.

Kopf, A. J., 2008, Making calderas from mud: Nature Geoscience, v. 1, no. 8, p. 500-501.

Kvenvolden, K. A., 1988, Methane hydrate—a major reservoir of carbon in the shallow geosphere?: Chemical geology, v. 71, p. 41-51.

Kvenvolden, K. A., and Rogers, B. W., 2005, Gaia's breath—global methane exhalations: Marine and Petroleum Geology, v. 22, no. 4, p. 579-590.

Lee, M. W., and T. S. Collett, 2012, Pore- and fracture-filling gas hydrate reservoirs in the Gulf of Mexico Gas Hydrate Joint Industry Project Leg II Green Canyon 955 H well: Marine and Petroleum Geology, v. 34, p. 62-71.

Liu, X., and Flemings, P. B., 2006, Passing gas through the hydrate stability zone at southern Hydrate Ridge, offshore Oregon: Earth and Planetary Science Letters, v. 241, no. 1-2, p. 211-226.

Loher, M., Marcon, Y., Pape, T., Römer, M., Wintersteller, P., dos Santos Ferreira, C., Praeg, D., Torres, M., Sahling, H., and Bohrmann, G., 2018, Seafloor sealing, doming, and collapse associated with gas seeps and authigenic carbonate structures at Venere mud volcano, Central Mediterranean: Deep Sea Research Part I: Oceanographic Research Papers, v. 137, p. 76-96.

McCarthy, P., J. Brand, B. Paradiso, J. Ezekwe, N. Wiltgen, A. Bridge, R. Willingham, and M. Bogaards, 2005, Using Geostatistical Inversion of Seismic And Borehole Data to Generate Reservoir Models For Flow Simulations of Magnolia Field, Deepwater Gulf of Mexico, SEG Technical Program Expanded Abstracts, Houston, Texas, Society of Exploration Geophysicists, p. 1351-1354.

McConnell, D. R., 2000, Optimizing deepwater well locations to reduce the risk of shallow-water-flow using high-resolution 2D and 3D seismic data. Proceedings of Offshore Technology Conference, Houston, Texas, USA, OTC-11973, DOI: 10.4043/11973-MS.

McConnell, D. R., T. S. Collett, R. Boswell, M. Frye, W. W. Shedd, R. S. Dufrene, P. D. Godfriaux, S. Mrozewski, G. Guerin, A. Cook, and E. Jones, 2010, Gulf of Mexico Gas Hydrate Joint Industry Project Leg II: Initial Results from the Green Canyon 955 Site, Proceedings of Offshore Technology Conference, Houston, Texas, USA, OTC-20801-MS, DOI: 10.4043/20801-MS.

McConnell, D. R., and Kendall, B. A., 2002, Images of the Base of Gas Hydrate Stability, Northwest Walker Ridge, Gulf of Mexico, Offshore Technology Conference: Houston, Texas, Offshore Technology Conference, p. 10.

McConnell, D. R., Zhang, Z., and Boswell, R., 2012, Review of progress in evaluating gas hydrate drilling hazards: Marine and Petroleum Geology, v. 34, no. 1, p. 209-223.

Meazell, P. K., and Flemings, P. B., In revision, The evolution of seafloor venting from hydrate-sealed gas reservoirs: Earth and Planetary Science Letters.

Meldahl, P., R. Heggland, B. Bril, and P. de Groot, 2001, Identifying faults and gas chimneys using multiattributes and neural networks: The Leading Edge, v. 20, p. 474-482.

Mello, U. T., Karner, G. D., and Anderson, R. N., 1995, Role of salt in restraining the maturation of subsalt source rocks: Marine and Petroleum Geology, v. 12, no. 7, p. 697-716.

Morris, E. A., D. M. Hodgson, R. L. Brunt, and S. S. Flint, 2014, Origin, evolution and anatomy of silt-prone submarine external levées: Sedimentology, v. 61, p. 1734-1763.

Naruk, S. J., Solum, J. G., Brandenburg, J. P., Origo, P., and Wolf, D. E., 2019, Effective stress constraints on vertical flow in fault zones: Learnings from natural CO2 reservoirs: AAPG Bulletin, v. 103, no. 8, p. 1979-2008.

Noguchi, S., N. Shimoda, O. Takano, N. Oikawa, T. Inamori, T. Saeki, and T. Fujii, 2011, 3-D internal architecture of methane hydrate-bearing turbidite channels in the eastern Nankai Trough, Japan: Marine and Petroleum Geology, v. 28, p. 1817-1828.

Osborne, M., and Swarbrick, R., 1997, Mechanisms for generating overpressure in sedimentary basins: A reevaluation: AAPG Bulletin, v. 81, no. 6., p. 1023-1041.

Oshima, M., K. Suzuki, J. Yoneda, A. Kato, M. Kida, Y. Konno, M. Muraoka, Y. Jin, J. Nagao, and N. Tenma, 2019, Lithological properties of natural gas hydrate–

bearing sediments in pressure-cores recovered from the Krishna–Godavari Basin: Marine and Petroleum Geology, v. 108, p. 439-470.

Paganoni, M., Cartwright, J. A., Foschi, M., Shipp, C. R., and Van Rensbergen, P., 2018, Relationship between fluid-escape pipes and hydrate distribution in offshore Sabah (NW Borneo): Marine Geology, v. 395, p. 82-103.

Peakall, J., B. McCaffrey, and B. Kneller, 2000, A process model for the evolution, morphology, and architecture of sinuous submarine channels: Journal of Sedimentary Research, v. 70, p. 434-448.

Pettijohn, F. J., P. E. Potter, and R. Siever, 2012, Sand and sandstone, New York, Springer Science & Business Media, 553 p.

Phillips, S., P. Flemings, M. Holland, P. Schultheiss, W. F. Waite, J. Jang, E. Petrou, and H. Hammon, 2020, Extremely high concentrations of methane hydrate in a deepwater silt reservoir from the northern Gulf of Mexico (Green Canyon 955): AAPG bulletin.

Pickering, K., J. Coleman, M. Cremer, L. Droz, B. Kohl, W. Normark, S. O'Connell, D. Stow, and A. Meyer-Wright, 1986, A high sinuosity, laterally migrating submarine fan channel-levee-overbank: results from DSDP Leg 96 on the Mississippi Fan, Gulf of Mexico: Marine and Petroleum Geology, v. 3, p. 3-18.

Piper, D. J., and M. Deptuck, 1997, Fined-grained turbidites of the Amazon Fan: facies characterization and interpretation: PROCEEDINGS-OCEAN DRILLING PROGRAM SCIENTIFIC RESULTS, p. 79-108.

Piper, D. J., and W. R. Normark, 2001, Sandy fans-from Amazon to Hueneme and beyond: AAPG bulletin, v. 85, p. 1407-1438.

Portnov, A., A. E. Cook, M. Heidari, D. E. Sawyer, M. Santra, and M. Nikolinakou, 2018, Salt-driven evolution of a gas hydrate reservoir in Green Canyon, Gulf of Mexico: AAPG Bulletin, this volume.

Prather, B. E., C. Pirmez, C. D. Winker, M. Deptuck, and D. Mohrig, 2012, Stratigraphy of linked intraslope basins: Brazos-Trinity system western Gulf of Mexico: Application of the principles of seismic geomorphology to continental-slope and base-of-slope systems: Case studies from seafloor and near-seafloor analogues: SEPM, Special Publication, v. 99, p. 83-109.

Reilly, M. J., and Flemings, P. B., 2010, Deep pore pressures and seafloor venting in the Auger Basin, Gulf of Mexico: Basin Research, v. 22, no. 4, p. 380-397.

Roberts, H., Shedd, W., and Hunt Jr, J., 2010a, Dive site geology: DSV ALVIN (2006) and ROV JASON II (2007) dives to the middle-lower continental slope, northern Gulf of Mexico: Deep Sea Research Part II: Topical Studies in Oceanography, v. 57, no. 21-23, p. 1837-1858.

Roberts, H. H., Feng, D., and Joye, S. B., 2010b, Cold-seep carbonates of the middle and lower continental slope, northern Gulf of Mexico: Deep Sea Research Part II: Topical Studies in Oceanography, v. 57, no. 21, p. 2040-2054.

Ruppel, C., R. Boswell, and E. Jones, 2008, Scientific results from Gulf of Mexico gas hydrates Joint Industry Project Leg 1 drilling: introduction and overview: Marine and Petroleum Geology, v. 25, p. 819-829.

Ruppel, C. D., and Kessler, J. D., 2017, The interaction of climate change and methane hydrates: Reviews of Geophysics, v. 55, no. 1, p. 126-168.

Ryu, B.-J., T. S. Collett, M. Riedel, G. Y. Kim, J.-H. Chun, J.-J. Bahk, J. Y. Lee, J.-H. Kim, and D.-G. Yoo, 2013, Scientific results of the Second Gas Hydrate Drilling Expedition in the Ulleung Basin (UBGH2): Marine and Petroleum Geology, v. 47, p. 1-20.

Sain, K., Minshull, T. A., Singh, S. C., and Hobbs, R. W., 2000, Evidence for a thick free gas layer beneath the bottom simulating reflector in the Makran accretionary prism: Marine Geology, v. 164, no. 1, p. 3-12.

Santra, M., P. Flemings, and K. Meazell, 2020, Evolution of Gas Hydrate-bearing Deepwater Channel-Levee System in Abyssal Gulf of Mexico – Levee Growth and Deformation: AAPG bulletin.

Sawyer, D. E., P. B. Flemings, R. C. Shipp, and C. D. Winker, 2007, Seismic geomorphology, lithology, and evolution of the late Pleistocene Mars-Ursa turbidite region, Mississippi Canyon area, northern Gulf of Mexico: AAPG bulletin, v. 91, p. 215-234.

Sawyer, D. E., R. Jacoby, P. Flemings, and J. T. Germaine, 2009, Data report: Particle size analysis of sediments in the Ursa Basin, IODP Expedition 308 Sites U1324 and U1322, northern Gulf of Mexico: Proc. IODP| Volume, p. 2.

Schultheiss, P., M. Holland, J. Roberts, Q. Huggett, M. Druce, and P. Fox, 2011, PCATS: pressure core analysis and transfer system: Proceedings of the 7th International Conference on Gas Hydrates (ICGH 2011), Edinburgh, UK, p. 17-21.

Seldon, B., and Flemings, P. B., 2005, Reservoir pressure and seafloor venting: Predicting trap integrity in a Gulf of Mexico deepwater turbidite minibasin: AAPG bulletin, v. 89, no. 2, p. 193-209.

Serié, C., Huuse, M., Schødt, N. H., Brooks, J. M., and Williams, A., 2017, Subsurface fluid flow in the deep-water Kwanza Basin, offshore Angola: Basin Research, v. 29, no. 2, p. 149-179.

Shedd, W., Boswell, R., Frye, M., Godfriaux, P., and Kramer, K., 2012, Occurrence and nature of "bottom simulating reflectors" in the northern Gulf of Mexico: Marine and Petroleum Geology, v. 34, no. 1, p. 31-40.

Shepard, F. P., 1954, Nomenclature based on sand-silt-clay ratios: Journal of Sedimentary Research, v. 24, p. 151-158.

Shukla, K., T. Collett, P. Kumar, U. Yadav, R. Boswell, M. Frye, M. Riedel, I. Kaur, and K. Vishwanath, 2018, National Gas Hydrate Program expedition 02: Identification of gas hydrate prospects in the Krishna-Godavari Basin, offshore India: Marine and Petroleum Geology, v. 108, p. 167-184.

Sloan, E. D., 2003, Fundamental principles and applications of natural gas hydrates: Nature, v. 426, p. 353.

Sloan, E. D., and Koh, C. A., 2007, Clathrate hydrates of natural gases, CRC press.

Smith, A. J., Flemings, P. B., Liu, X., and Darnell, K., 2014, The evolution of methane vents that pierce the hydrate stability zone in the world's oceans: Journal of Geophysical Research: Solid Earth, v. 119, no. 8, p. 6337-6356.

Stow, D. A. V., and A. J. Bowen, 1978, Origin of lamination in deep sea, fine-grained sediments: Nature, v. 274, p. 324.

Stow, D. A. V., and A. J. Bowen, 1980, A physical model for the transport and sorting of fine-grained sediment by turbidity currents: Sedimentology, v. 27, p. 31-46.

Straub, K. M., and D. Mohrig, 2008, Quantifying the morphology and growth of levees in aggrading submarine channels: Journal of Geophysical Research: Earth Surface, v. 113.

Straub, K. M., D. Mohrig, J. Buttles, B. McElroy, and C. Pirmez, 2011, Quantifying the influence of channel sinuosity on the depositional mechanics of channelized turbidity currents: A laboratory study: Marine and Petroleum Geology, v. 28, p. 744-760.

Stump, B. B., and Flemings, P. B., 2002, Consolidation state, permeability, and stress ratio as determined from uniaxial strain experiments on mudstone samples from the Eugene Island 330 Area, offshore Louisiana: strain, v. 3, p. L3.

Tamaki, M., T. Fujii, and K. Suzuki, 2017, Characterization and prediction of the gas hydrate reservoir at the second offshore gas production test site in the eastern Nankai trough, Japan: Energies, v. 10, p. 1678.

Talukder, A. R., 2012, Review of submarine cold seep plumbing systems: leakage to seepage and venting: Terra Nova, v. 24, no. 4, p. 255-272.

Tréhu, A. M., Flemings, P. B., Bangs, N. L., Chevallier, J., Gràcia, E., Johnson, J. E., Liu, C. S., Liu, X., Riedel, M., and Torres, M. E., 2004, Feeding methane vents and gas hydrate deposits at south Hydrate Ridge: Geophysical Research Letters, v. 31, no. 23.

Thomas, C., S. Phillips, P. Flemings, M. Santra, H. Hammon, T. S. Collett, A. Cook, T. Pettigrew, M. Holland, and P. Schultheiss, 2020, Pressure-coring operations durin Expedition UT-GOM2-1 in Green Canyon Block 955, northern Gulf of Mexico: AAPG bulletin.

Tréhu, A. M., F. R. Rack, and M. E. Torres, 2003, Proceedings of the Ocean Drilling Program [electronic resource].: drilling gas hydrates on Hydrate Ridge, Cascadia Continental Margin; covering leg 204 of the cruises of the drilling vessel JOIDES Resolution; Victoria, British Columbia, Canada, to Victoria, British Columbia, Canada; 7 July-2 September 2002. Initial reports, Texas A&M University.

Van Rensbergen, P., Depreiter, D., Pannemans, B., Moerkerke, G., Van Rooij, D., Marsset, B., Akhmanov, G., Blinova, V., Ivanov, M., and Rachidi, M., 2005, The El Arraiche mud volcano field at the Moroccan Atlantic slope, Gulf of Cadiz: Marine Geology, v. 219, no. 1, p. 1-17.

Walker, R. G., 1978, Deep-water sandstone facies and ancient submarine fans: models for exploration for stratigraphic traps: AAPG Bulletin, v. 62, p. 932-966.

Weimer, P., 1990, Sequence stratigraphy, facies geometries, and depositional history of the Mississippi Fan, Gulf of Mexico (1): AAPG bulletin, v. 74, p. 425-453.

Weissenburger, K., and T. Borbas, 2004, Fluid properties, phase and compartmentalization: Magnolia field case study, deepwater Gulf of Mexico, USA: Geological Society, London, Special Publications, v. 237, p. 231-255.

Wen, B., A. Aydin, and N. S. Duzgoren-Aydin, 2002, A comparative study of particle size analyses by sieve-hydrometer and laser diffraction methods: Geotechnical Testing Journal, v. 25, p. 434-442.

Wentworth, C. K., 1922, A scale of grade and class terms for clastic sediments: The journal of geology, v. 30, p. 377-392.

Winters, W. J., W. F. Waite, D. Mason, L. Gilbert, and I. Pecher, 2007, Methane gas hydrate effect on sediment acoustic and strength properties: Journal of Petroleum Science and Engineering, v. 56, p. 127-135.

Yardley, G. S., and Swarbrick, R. E., 2000, Lateral transfer; a source of additional overpressure?: Marine and Petroleum Geology, v. 17, p. 523-537.